



# Magnetization dynamics in magnetic nanostructures

Dana Elena Sorea Stanescu

## ► To cite this version:

Dana Elena Sorea Stanescu. Magnetization dynamics in magnetic nanostructures. Condensed Matter [cond-mat]. Université Joseph-Fourier - Grenoble I, 2003. English. NNT: . tel-00006021v1

**HAL Id: tel-00006021**

**<https://theses.hal.science/tel-00006021v1>**

Submitted on 7 May 2004 (v1), last revised 7 May 2004 (v2)

**HAL** is a multi-disciplinary open access archive for the deposit and dissemination of scientific research documents, whether they are published or not. The documents may come from teaching and research institutions in France or abroad, or from public or private research centers.

L'archive ouverte pluridisciplinaire **HAL**, est destinée au dépôt et à la diffusion de documents scientifiques de niveau recherche, publiés ou non, émanant des établissements d'enseignement et de recherche français ou étrangers, des laboratoires publics ou privés.

# THÈSE

présentée par

**Dana Elena SOREA STANESCU**

pour obtenir le titre de

DOCTEUR DE L'UNIVERSITE JOSEPH FOURIER – GRENOBLE 1

spécialité: **PHYSIQUE**

---

## **MAGNETIZATION DYNAMICS**

### **IN MAGNETIC NANOSTRUCTURES**

---

Date de soutenance: 1 décembre 2003

#### **COMPOSITION DU JURY :**

Theo RASING	Rapporteur
Claude CHAPPERT	Rapporteur / Président du jury
Jean-Louis PORTESEIL	Examineur
Eric BEAUREPAIRE	Examineur
Pascal XAVIER	Invité
Ursula EBELS	Invité
Kamel OUNADJELA	Directeur de thèse

Thèse préparée au sein des laboratoires :  
CNRS/IPCMS – Strasbourg et CEA-Grenoble/DRFMC/SPINTEC



---

## REMERCIEMENTS

---

Ce travail de thèse a été réalisé dans le *Département de Recherche Fondamentale sur la Matière Condensée* (DRFMC) du CEA/Grenoble, dans le laboratoire SPINTEC.

Mes remerciements s'adressent tout d'abord aux membres du jury : à M. Claude Chappert qui a accepté de présider le jury de thèse et d'en être rapporteur ; à M. Theo Rasing pour avoir accepté d'en être rapporteur, à M. Jean Louis Porteseil et M. Eric Beaurepaire d'avoir participé à ce jury de thèse comme examinateurs, à M. Pascal Xavier et Mme. Ursula Ebels d'avoir participé comme invités et à mon directeur de thèse, M. Kamel Ounadjela.

Je voudrais remercier M. Kamel Ounadjela pour m'avoir proposé ce sujet de thèse. Je témoigne ma gratitude à Mme. Ursula Ebels qui a encadré ce sujet de thèse et qui a montré beaucoup de patience pour corriger ce manuscrit.

Un GRAND MERCI à Alexandre Viegas pour son aide et soutien tout au long de ma thèse. J'ai beaucoup apprécié toutes les discussions scientifiques que nous avons eues, même celles contradictoires. Merci encore une fois, Alexandre, et bonne continuation.

Je tiens à remercier M. Jean-Pierre Nozières pour m'avoir accueillie à SPINTEC et pour sa disponibilité et son soutien pendant ma thèse.

J'ai poursuivi les deux premières années de ma thèse à l'*Institut de Physique et Chimie de Matériaux à Strasbourg* (IPCMS). Je ne pourrais pas oublier les personnes qui m'ont encadrée et encouragée pendant ce temps. Tout d'abord je voudrais remercier M. Eric Beaurepaire pour m'avoir donnée les premières leçons sur l'effet Kerr et pour m'apprendre à faire le premier alignement, ce qui m'a beaucoup aidée pour les expériences qui ont suivi. Un grand merci à Victor da Costa et Coriolan Tiusan pour le temps qu'ils ont passé afin de m'apprendre à utiliser la machine de dépôt de couches minces, et à m'initier à la physique des vannes de spin et des jonctions tunnel. J'aimerais également remercier Theo Dimopoulos qui m'a initiée aux techniques de lithographie optique à Siemens/Erlangen.

Un GRAND MERCI à toute l'équipe de Siemens qui m'a toujours accueillie très chaleureusement pendant mes stages à Erlangen. Particulièrement, je remercie M. Ludwig

Baer, M. Hugo van den Berg, Daniela et Elena. Je n'oublierai jamais leur hospitalité, leur sens de l'humour et leur bonne volonté.

Mes remerciements s'adressent à tous mes collègues de SPINTEC, permanents, doctorants, stagiaires et post-doctorants. La démarche scientifique peut sembler parfois très complexe et rude et il est difficile d'y voir le but. Pendant ces moments on a besoin de « lumière » pour éclairer notre chemin, « lumière » apportée dans mon cas par les discussions que j'ai eues avec M Anatoli Vedyayev et M. Bernard Dieny. Je tiens à les remercier pour leur aide et leur confiance. Merci également aux personnes de C5, M. Stéphane Auffret, M. Bernard Rodmacq, M. Gérard Casali pour leur aide et leur disponibilité. Merci Emmanuelle, Yann, Vincent, Catherine, Claire, Gilles, Ahmad, Olivier, Bernard, Adriana, Alina, Marta, Lili, Lucian, Sandra, Isabel, Christophe, Virgil, Fabrice, Hanna pour les moments de bonne humeur et amitié que j'ai partagés avec vous. Merci Ioana, pour m'avoir supportée pendant la rédaction de ma thèse.

J'aimerais remercier M. Pascal Xavier et M. Jacques Richard du laboratoire CRTBT/CNRS – Grenoble pour m'avoir conseillée lors des mesures de hautes fréquences et pour avoir corrigé une partie du manuscrit. J'exprime également ma gratitude à M. Thierry Fournier et M. Thierry Crozes qui m'ont aidée dans la micro-fabrication des échantillons dans la salle blanche de Nanofab/CNRS – Grenoble. J'aimerais également remercier Mme. Claudine Lacroix, la directrice du Laboratoire Louis Néel, pour nous avoir accueillis pendant les quelques mois suivant le déménagement de notre groupe de Strasbourg à Grenoble.

Un GRAND MERCI à tous mes amis qui m'ont soutenue et encouragée pendant toute ma thèse. Merci à Alina et Ovidiu, Cristi, Simona, Antoine, Vasile, Claudia et Cyril, Adriana, Alina, Ioana, Monica et Vali.

Merci beaucoup à ma sœur, Sorina, pour m'avoir toujours soutenue et encouragée.

Un TRES GRAND MERCI à Stefan, mon mari, qui a été toujours présent pour m'écouter, m'écouter et encore m'écouter, pour me soutenir, encourager et pour m'aider à traverser les moments les plus difficiles de ces dernières années.

Le tout dernier GRAND MERCI appartient à mes parents qui ont été les premiers qui m'ont initiée aux secrets des sciences exactes (mathématique et physique). Je les remercie du fond de mon cœur et je leurs dédie ce manuscrit.

*The only reason for time is so that  
everything doesn't happen at once.*

*[Albert Einstein]*



## **TABLE OF CONTENTS**

<b>GENERAL INTRODUCTION</b> .....	11
<b>CHAPTER 1: STATIC AND DYNAMIC ASPECTS OF MICROMAGNETISM</b> .....	19
1.1. Magnetic moments .....	22
1.2. Energy and magnetic fields of a magnetic system .....	24
1.3. Landau-Lifshitz-Gilbert equation .....	26
1.4. Small angle magnetization deviation .....	28
1.5. Magnetic length-scales .....	31
1.6. Domain walls .....	32
1.7. Magnetization reversal mechanisms .....	33
1.7.1. Domain wall dynamics .....	34
1.7.2. Coherent magnetization reversal – Stoner-Wolfarth model .....	37
1.7.3. Precessional reversal .....	41
<b>CHAPTER 2: THE STROBOSCOPIC PUMP-PROBE TECHNIQUE; DESIGN DEVELOPMENT AND EXPERIMENTAL SETUP</b> .....	45
2.1. Pump-probe technique .....	49
2.2. Pump and probe requirements .....	50
2.3. Transmission line theory .....	51
2.3.1. Telegrapher equations of transmission lines .....	54
2.3.2. The terminated lossless transmission line .....	55
2.3.3. Scattering matrix .....	57
2.3.4. Types of transmission line: striplines, micro-striplines, waveguides .....	58
2.4. Experimental solutions for the pump .....	60
2.4.1. Voltage pulse characteristics .....	60
2.4.2. Rectangular micro-stripline .....	62
2.4.3. The signification of 3dB attenuation limit .....	65
2.4.4. Transmission lines design and characterization .....	67
2.4.5. Conclusions .....	75
2.5. The PROBE .....	76
2.5.1. The Magneto-Optic PROBE .....	77



2.5.1.1. Magneto – Optical Effects .....	74
2.5.1.2. Magneto-Optical Kerr Effect .....	77
2.5.1.3. Longitudinal Kerr effect configuration .....	85
2.5.1.4. Transversal Kerr effect configuration .....	88
2.5.1.5. MOKE experimental setup .....	90
2.5.1.6. Dynamic MOKE experiment .....	93
2.5.2. The magneto – resistive PROBE.....	95
2.5.2.1. Magneto-Resistive Effects .....	95
2.5.2.2. Magneto-Resistive experimental Setup .....	97
2.5.3. The inductive PROBE .....	99
2.5.3.1. Inductive Effect .....	99
2.5.3.2. Experimental setup .....	100
2.6. Pump-Probe technique – state-of-art .....	102

### **CHAPTER 3: EXPERIMENTAL TECHNIQUES**

FOR SAMPLE PREPARATION AND CHARACTERIZATION .....	105
3.1. Introduction .....	108
3.2. Sample preparation techniques .....	109
3.2.1. Sputtering technique .....	109
3.2.2. Optical lithography technique .....	111
3.2.3. Ion Beam Etching (IBE) .....	114
3.2.4. Reactive Ion Etching (RIE) .....	115
3.3. Sample characterization techniques .....	116
3.3.1. Atomic Force Microscopy (AFM) .....	116
3.3.2. Magnetic Force Microscopy (MFM) .....	118
3.3.3. Conductive AFM .....	118
3.3.4. Scanning Electron Microscopy (SEM) .....	119
3.4. Sample preparation and characterization .....	120
3.4.1. Coplanar wave- guides preparation .....	120
3.4.2. Magnetic sample elaboration .....	121
3.4.3. Samples preparation for dynamic MR measurements .....	128
3.4.4. First alternative preparation process for dynamic MR devices .....	134
3.4.5. Second alternative preparation process for dynamic MR devices .....	134

<b>CHAPTER 4: MAGNETIZATION DYNAMICS IN SPIN-VALVES MICRON-SIZED ELEMENTS</b>	
AND CONTINUOUS FILMS .....	135
4.1. Introduction .....	138
4.2. Static MOKE measurements of NiO-based spin valves .....	139
4.2.1. Micron-sized ( $20 \times 40\mu\text{m}^2$ ) rectangular elements .....	140
4.2.2. Static MFM characterization .....	142
4.2.3. Static MOKE measurements .....	143
4.3. Dynamic MOKE studies of NiO-based spin valves.....	145
4.3.1. FMR type measurements in the time domain .....	146
4.3.2. Hysteresis loops in the presence of sharp magnetic field pulses .....	148
4.3.3. Magnetization large-angle deviations observed with the time-resolved stroboscopic MOKE .....	153
4.3.4. Precessional reversal .....	157
4.3.4.1. Experimental evidence for precessional reversal .....	157
4.3.4.2. Reduced remanence .....	160
4.3.4.3. Magnetization trajectory .....	162
4.3.4.4. Macrospin simulations .....	164
4.3.4.5. Precessional magnetization switching – conclusions .....	178
4.4. Precessional reversal on micron-sized IrMn-based spin valves .....	181
4.4.1. Static magneto-resistive characterization .....	182
4.4.2. The characterization of the electronic device .....	184
4.4.3. Remanence magneto-resistive measurements .....	188
4.4.4. Dynamic magneto-resistive measurements .....	192
4.5. Precessional reversal on continuous magnetic films- preliminary results .....	197
<b>CONCLUSIONS AND PERSPECTIVES .....</b>	<b>201</b>
<b>REFERENCES .....</b>	<b>205</b>
 <b>ANNEXE 1: ANALYTICAL CALCULATION OF THE MAGNETIC FIELD INDUCED BY A DC- CURRENT</b> <b>IN A RECTANGULAR STRIPLINE.....</b>	 <b>213</b>
<b>ANNEXE 2: FOURIER TRANSFORM OF DISCRETELY SAMPLED DATA.....</b>	<b>219</b>
<b>ANNEXE 3: MACROSPIN SIMULATIONS .....</b>	<b>221</b>
<b>ANNEXE 4: MOKE SIMULATIONS.....</b>	<b>223</b>
<b>ANNEXE 5: DIELECTRIC TENSOR.....</b>	<b>228</b>



# **GENERAL INTRODUCTION**



Each magnetic system is characterized by *equilibrium and metastable magnetic states*, corresponding to global respective local minima of the total energy of the magnetic system. The transition of the magnetization from one state to another, under the influence of an external magnetic field, temperature or a spin polarized current is a dynamic process, called **the magnetization dynamics**, whose characteristic time depends on the type of excitation, the material parameters as well as the spatial dimensions of the magnetic system.

In order to describe the dynamics of the magnetization processes Landau and Lifshitz were the first to derive a mathematical expression in the form of a non-linear differential equation. It has been later extended by Gilbert and the corresponding equation of motion for the magnetization dynamics is nowadays known nowadays as the *Landau-Lifshitz-Gilbert equation* [Landau & Lifshitz1935, Gilbert1955]. Modifications of LLG are currently under discussion in order to include the action of a spin polarized current on the magnetization dynamics.

Since 1940, the studies of the magnetization dynamics in different magnetic systems have become of large interest, in particular with respect to the industrial applications such as magnetic memories. One of the first magnetic recording devices based on the magnetization dynamics used ferrite heads to *write* and *read* the information. Because the ferrite permeability falls above 10 MHz [Doyle 1998], the read/write process was possible only with a reduced rate. An important improvement (i.e. decreased response time) was obtained using magnetic thin film heads. Upon reduction of the dimensions of the magnetic system (i.e. reduced film thickness compared to the other two dimensions) strong demagnetizing fields will be induced, and thus a high value of the demagnetizing factor ( $\sim 1$ ) creating a large anisotropy field perpendicular to the film surface. In this way, reasonable permeabilities for applied frequencies larger than 300 MHz were obtained in thin magnetic films devices [Doyle1998].

Both the increase of the data storage capacity (decreasing the magnetic unit dimensions down to micro- or nano- meters) and the decrease of the access times (of nanoseconds and sub nanoseconds for MRAM devices), are the major challenges of current research work.

Consequently, one has to be concerned in a first step by the dependence of the magnetic properties upon reducing the sample dimensions. Figure I.1 gives a classification of the characteristic magnetic processes as a function of the magnetic system dimensions (or the spins number  $S$  of the magnetic system). From the hysteresis curves presented in figure I.1 the different magnetization reversal processes can be investigated such as: *the nucleation, the propagation and the annihilation of domain walls* for multi-domain particles, *the uniform*

rotation of the magnetization for single-domain particles and *quantum phenomena* for one magnetic moment particle.

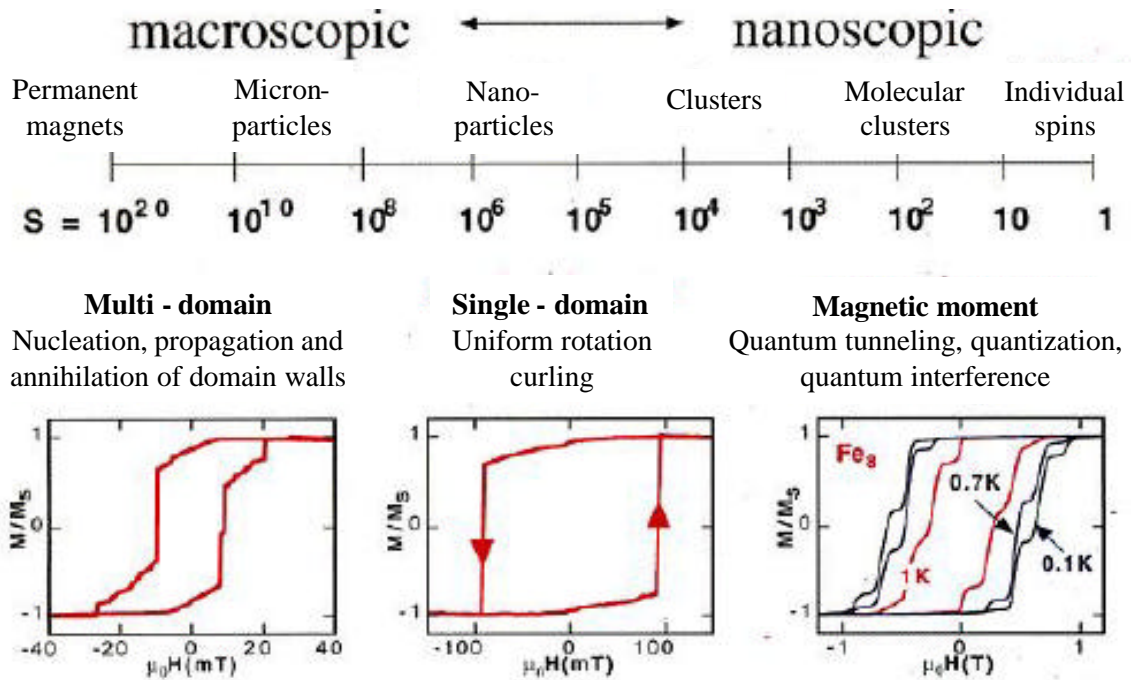


Figure I.1:

Mesoscopic physics: from macroscopic to nanoscopic magnetic systems [Wernsdorfer 2001]

In the second step, one has to consider the time scale of the different processes, some of which are indicated in figure I.2.

On the **femtosecond time scale**, the characteristic processes correspond to the relaxation of the *electron system* [Beaurepaire1996, Beaurepaire1998, Guidoni2002].

The **picosecond time scale** corresponds to the precession frequencies of a metallic ferromagnetic system (typical GHz). Back et al. [Back1998, Siegmann1995] have demonstrated for the first time experimentally a new concept based on the reversal by precession for perpendicularly magnetized Co/Pt multilayers using strong in plane magnetic field pulses of 2 – 4.4 ps duration obtained at the Stanford Linear Accelerator Center. This has then been followed by time-resolved pump-probe experiments on the laboratory scale by [Freeman1992, Doyle 1993, He 1994, Doyle 1998, Hiebert 1997, Freeman 1998, Stankiewicz 1998, Zhang 1997, Koch 1998] for in-plane magnetized soft magnetic materials. Later, in 2002-2003, [Gerrits2002, Schumacher2002, Schumacher 2002B, Schumacher 2003, Schumacher2003B] have shown as well that it is possible to suppress the ringing effect after the precessional reversal of the magnetization which is an important condition for the application in MRAM devices. Besides the studies on the reversal mechanism, these time-

resolved dynamic measurement techniques yield also the free-oscillations of the magnetization after pulsed- or stepped- magnetic field excitation from which the ferromagnetic resonance frequency and information on the damping can be obtained [Silva1999].

Magnetization reversal process that occur over a time of **nanoseconds** and above, include the coherent rotation and reversal by domain wall nucleation and propagation, as well as associated relaxation processes [Freeman1991, Russek 2000, Russek 2000B, Binns2003, Williams 1950, Slonczewski 1991].

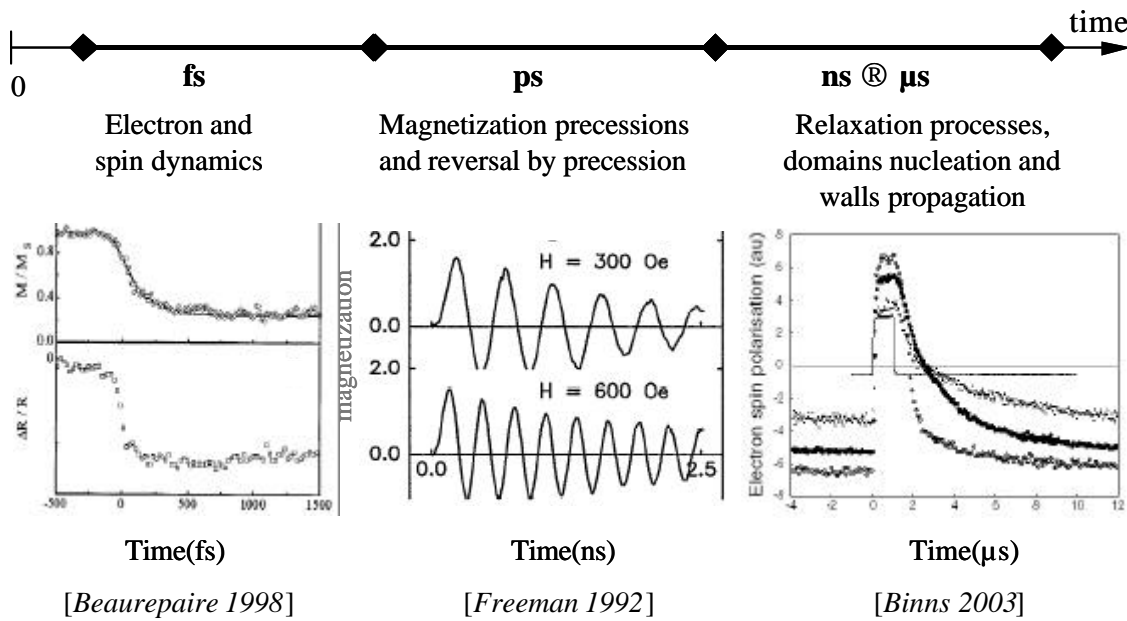


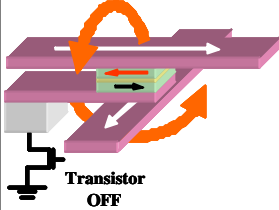
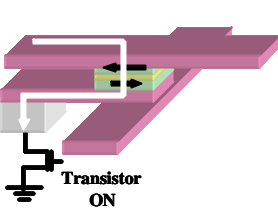
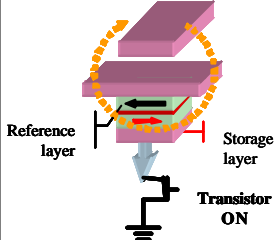
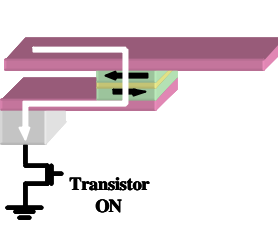
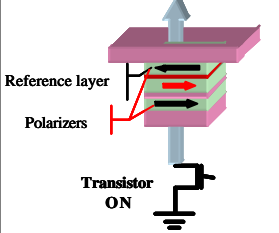
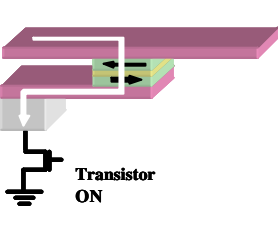
Figure I.2:  
Characteristic time scales for the magnetization dynamics

Due to the characteristic times of the *magnetization reversal by precession*, which are of some hundreds of picoseconds, this process has been considered as a promising concept to be used in magnetic random access memories (MRAM). It will allow to reduce the response time of the devices from some nanoseconds (in the present devices) to some hundreds of picoseconds. However, several limitations will occur for this so-called *Field Induced Magnetic Switching (FIMS) concept (precessional and Stoner Wohlfahrt)*, when scaling the system size.

Therefore other concepts have been proposed such as the *Thermally Assisted Switching (TAS)* and the *Current Induced Magnetic Switching (CIMS)*. The corresponding MRAM cell design of these processes are presented in figure I.3. Current realizations of *FIMS* devices use two orthogonal pulsed magnetic fields generated by two conductors. These devices were



intended to induce the Stoner-Wolfarth reversal but they can be also used to induce the precessional reversal using shorter magnetic field pulses. The *TAS* uses the temperature dependence of the write field by sending current pulses through a tunnel junction while applying a magnetic field pulse through the word/bit lines. The *CIMS* uses a high density, spin polarized current that passes through the tunnel junction to switch the storage layer. In this case, no magnetic field is required.

MRAM	WRITING	READING
<b>FIMS</b> Field Induced Magnetic Switching		
<b>TAS</b> Thermally Assisted Switching		
<b>CIMS</b> Current Induced Magnetic Switching		

*Figure I.3*  
MRAM – switching processes in applications

In January 2000, when this PhD work started, the precessional reversal was already evidence by Back and al. [Back1998] in systems with perpendicular anisotropy (Co/Pt multi-layers) using synchrotron radiation techniques, at the Stanford Linear Accelerator Center. Therefore, one of the challenges was to reach similar results on magnetic samples with *planar anisotropy* using laboratory facilities.

In this context, my work was aimed at establishing a high-frequency measurement technique to characterize the magnetization reversal processes and the magnetization dynamics with a resolution on the picosecond time-scale. This technique has been used to characterize the precessional reversal process in different magnetic systems such as

continuous films and patterned single- and multi- layer structures, which have applications in MRAM devices. My work focused on the realization of an experimental set-up and on the realization of the samples, adapted to high-frequency experiments, using different preparation techniques such as magnetic thin film sputtering, ultra-violet lithography as well as different etching techniques.

This manuscript is structured as follows:

- i) In the first chapter, I give a short introduction of some static and dynamic aspects of micromagnetism.
- ii) The second chapter is focused on the pump-probe measurement technique. Several fundamental aspects related to the transmission line theory are described, which are important for the design of the pump part. Furthermore, the basic concepts of the probe technique such as the magneto-optical Kerr effect, the magneto-resistive effect and the inductive effect are presented. The experimental setup used in my work will then be described based on these theoretical considerations.
- iii) In the third chapter the sample preparation and characterization are detailed.
- iv) The experimental results related to the magnetization dynamics (precessional reversal, small angle oscillations) both in magnetic micron-sized samples and continuous magnetic thin films are given in the fourth chapter. For a complete interpretation and understanding of the experimental data, the results are compared to macrospin simulations.

Four annexes are available at the end of this manuscript:

Annexe 1: *The calculation of the magnetic field induced by a DC-current that traverses a conductor of rectangular section*

Annexe 2: *The calculation of the Fourier transform of discretely sampled data*

Annexe 3: *The macrospin simulation code*

Annexe 4: *Jones Matrices for optical components and simulations of the magneto-optic Kerr effect*

Annexe 5: *The dielectric tensor that defines the Fresnel coefficients corresponding to the Kerr reflected signal.*



**CHAPTER 1:**  
**STATIC AND DYNAMIC ASPECTS OF**  
**MICROMAGNETISM**



## ***Abstract***

*The first chapter is dedicated to the presentation of some aspects of micromagnetism. After a brief recall of notions related to the magnetic moments of an electron, the characteristic energies and the associated magnetic fields in a continuous ferromagnetic material are presented. The equilibrium and metastable magnetic states correspond to global respective local minima of the total energy. The transition from one stable state to another or the relaxation from an out-of-equilibrium state towards the nearest minimum is given by the Landau-Lifshitz-Gilbert equation, which describes the magnetization dynamics. Its solution, for given boundary conditions will yield the magnetization trajectory (evolution of  $\vec{M}$  in time). Here, both, small angle magnetization perturbations that correspond to linear solutions, as well as the magnetization reversal (Stoner-Wolfarth and precessional reversal), will be addressed.*

## ***Résumé***

*Le premier chapitre est dédié à la présentation de certains aspects de la théorie du micro-magnétisme et des notions de base reliées au moment magnétique de l'électron. Nous présentons des détails concernant les concepts micro-magnétiques appliqués dans les matériaux ferromagnétiques en introduisant les énergies caractéristiques et les champs magnétiques associées. Les états magnétiques d'équilibre sont dérivés de la minimisation de l'énergie totale du matériau ferromagnétique.*

*La deuxième partie est dédiée à l'équation Landau-Lifshitz qui définit la variation temporelle de l'aimantation. Nous discutons ses applications dans la théorie du micro-magnétisme et en particulier les solutions linéaires qui correspondent aux faibles perturbations de l'aimantation ainsi que le renversement de l'aimantation (model Stoner-Wolfarth et précessionnel).*

## 1.1. MAGNETIC MOMENTS

The electron in an atom has two angular momenta: i) the orbital angular momentum,  $\vec{L}$ , and ii) the spin angular momentum  $\vec{S}$ . The corresponding magnetic moments,  $\vec{\mu}_L$  or  $\vec{\mu}_S$  are respectively:

$$\begin{aligned}\vec{\mu}_L &= -g_L \vec{L} \\ \vec{\mu}_S &= -g_S \vec{S}\end{aligned}\quad (1.1)$$

where  $g_L$  and  $g_S$  represent the orbital and respective the spin gyromagnetic factors. They are given by Planck's constant,  $\hbar$ , Bohr magneton,  $\mu_B$ <sup>1</sup>, and the gyromagnetic splitting factor,  $g_L$  or  $g_S$ :

$$g_{L,S} = g_{L,S} \frac{\mu_B}{\hbar}; \quad \mu_B = \frac{|e|\hbar}{2m} \quad (1.2)$$

In the spin-orbit coupling cases the total angular momentum is given by:  $\vec{J} = \vec{L} + \vec{S}$ , and the corresponding total magnetic momentum by  $\vec{\mu}_J = -g_J \vec{J}$ . Here the gyromagnetic factor can be expressed in a similar way as in equation 1.2. Neglecting the orbital contribution to the total angular momentum,  $L = 0$  and  $J = S$ , the Landé factor ( $g_{L,S}$ ) is equal to 2, while in the case with  $S = 0$  and  $J = L$ , the Landé factor is equal to 1 [Ashcroft1976, Kittel1966].

Considering an arbitrary external magnetic field,  $\vec{H}$ , the evolution in time of the magnetic momentum  $\mu_J$  of an electron (fig.1.1), is defined by the angular momentum – type equation of motion:

$$\frac{d\vec{\mu}_J}{dt} = -g_J (\vec{\mu}_J \times \mu_0 \vec{H}), \quad g_J > 0 \quad (1.3)$$

where  $\mu_0 = 4\pi 10^{-7}$  H/m. This equation describes a precessional motion of the magnetic moment around the external magnetic field characterized by the frequency,  $f$ :

$$f = \frac{1}{2\pi} \cdot \frac{e\mu_0 H}{m_e} = \text{const.} * H \quad (1.4)$$

$f$  is called the Larmor frequency. The constant in equation 1.4 has in SI<sup>2</sup> units the value  $3.52 * 10^4$  Hz/(A/m). This value corresponds to one precession period of 357 ns for a magnetic field equal to 1 Oe. The Larmor frequency increases and in consequence, the precession time decreases with increasing magnetic field.

<sup>1</sup>  $\mu_B = |e|\hbar / 2m_e$  where  $e$  and  $m_e$  is the charge and the mass of the electron

<sup>2</sup>  $e = 1.6 * 10^{-19}$  C;  $\mu_0 = 4\pi * 10^{-7}$  T\*m/A;  $m_e = 9.1 * 10^{-31}$  Kg;  $H(\text{A/m}) = H(\text{Oe}) * 79.58$

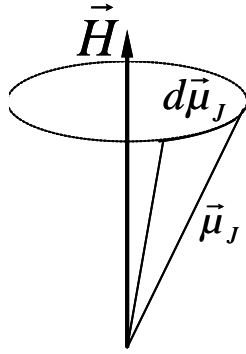


Figure 1.1  
Precessional motion of a magnetic moment around an arbitrary external magnetic field  $\vec{H}$ , determining its frequency  $f$ .

In ferromagnetic materials, the spins are strongly coupled by the exchange interaction. Therefore, there is no strong variation of the orientation of the magnetic moments  $\vec{\mu}_j$  from one lattice site to the next. This allows the introduction of an average magnetic moment, called magnetization,  $\vec{M}$ :

$$\vec{M} = \frac{\sum_j \vec{\mu}_j}{V} \quad (1.5)$$

for which a similar equation to 1.3 can be derived to describe the magnetization precession around an effective field in a continuum theory [Chikazumi1997]. It is the basis of Brown's equations [Brown1963] as well as the Landau-Lifshitz-Gilbert equation [Landau & Lifshitz1935, Gilbert1955]:

$$\frac{d\vec{M}}{dt} = -\mathbf{g}(\vec{M} \times \mu_0 \vec{H}_{eff}) \quad (1.6)$$

where  $\mathbf{g} = g \cdot \frac{|e|}{2m_e} = 87.91 \cdot 10^9 \cdot g (Oe^{-1} \cdot Hz)$ . One basic assumption of the theory of micromagnetism is the existence of a spontaneous magnetization vector that has a constant amplitude:  $|\vec{M}| = const$ .

The effective magnetic field in equation 1.6 is given by the derivative of the total energy of the ferromagnetic system:

$$\vec{H}_{eff} = -\nabla_{\vec{M}} E \quad (1.7)$$

In the following, the total energy,  $E$ , is derived.



## 1.2. ENERGY AND MAGNETIC FIELDS OF A MAGNETIC SYSTEM

The total energy of a magnetic system has different contributions coming from exchange energy ( $E_{ex}$ ), magneto-crystalline anisotropy energy ( $E_u$ ), dipolar energy ( $E_{dip}$ ), and Zeeman energy ( $E_z$ ):

$$E = E_{ex} + E_u + E_{dip} + E_{zeeman} \quad (1.8)$$

Hence, the corresponding effective magnetic field has four contributions:

$$\vec{H}_{eff} = -\nabla_{\vec{M}} E = \vec{H}_{ex} + \vec{H}_u + \vec{H}_{dip} + \vec{H}_{zeeman} \quad (1.9)$$

### i) The exchange energy

The exchange energy in a system of  $N$  spins is defined as:

$$E_{ex} = -\frac{1}{2} \sum_{i=1}^N \sum_{j=1}^N J_{ij} (\vec{\mu}_i \cdot \vec{\mu}_j) \quad (1.10)$$

where  $J_{ij}$  is a positive parameter (in ferromagnetic systems) that represents the exchange integral corresponding to the interaction between the magnetic moments  $i$  and  $j$ . This interaction is strongest for adjacent moments and therefore local. In ferromagnetic materials, it favors parallel alignment of the spins. In continuous media, of volume  $V$ , the exchange energy is expressed as:

$$E_{ex} = \int_V A_{ex} \left\{ [\nabla m_x(\vec{r})]^2 + [\nabla m_y(\vec{r})]^2 + [\nabla m_z(\vec{r})]^2 \right\} dV, \quad \vec{m}(m_x, m_y, m_z) = \frac{\vec{M}}{M_s} \quad (1.11)$$

where  $A_{ex}$  is the exchange constant that is proportional to the exchange integral  $J_{ij}$ ,  $\nabla m_{x,y,z}$  is the spatial gradient ( $\nabla_{\vec{r}}$ ) of the magnetization normalized components corresponding to the  $ox$ ,  $oy$  and  $oz$  axis. The exchange interaction is isotropic, resulting in no preferential orientation of the magnetization with respect to the crystal axis.

### ii) The magneto-crystalline energy

Due to the interaction between the magnetic moments and the crystalline lattice via spin-orbit interaction, the orientation of the magnetic moments has preferential directions given by the underlying symmetry of the lattice. The deviation of the magnetic moments from this direction increases the system energy that is called magneto-crystalline anisotropy energy.

In the case of a uniaxial magnetic anisotropy, the energy takes the form:

$$E_u = K_u \left| 1 - \left( \vec{u} \cdot \frac{\vec{M}}{M_s} \right)^2 \right| \quad (1.12)$$

where  $\vec{u}$  is the unit vector, along the direction of the uniaxial easy axis,  $K_u$  is the uniaxial anisotropy energy constant, and  $M_s$  is the magnetization modulus.

From 1.7 and 1.12 the uniaxial anisotropy magnetic field is expressed as a function of the unitary vector  $\vec{m}$ :

$$H_u = \frac{2K_u}{\mu_0 M_s} \cdot \vec{u} (\vec{u} \cdot \vec{m}) \quad (1.13)$$

### iii) The magnetostatic energy

For a uniformly magnetized sample, magnetic poles appear on its surface, giving rise to a demagnetizing field,  $\vec{H}_d$ . The corresponding energy is expressed as:

$$E_{dip} = -\frac{1}{2} \mu_0 \int_V \vec{M}(\vec{r}) \cdot \vec{H}_d(\vec{r}) \cdot d\vec{r} \quad (1.14)$$

This energy is small compared to the exchange energy between neighboring moments thus it has no direct influence on the parallel alignment of neighboring spins. However, it is of long range and therefore will influence the spatial distribution of the magnetization vector.

The corresponding demagnetizing field is equal to:

$$\vec{H}_d = -\vec{\overline{N}} \cdot \vec{M} \quad (1.15)$$

where  $\vec{\overline{N}}$  is the demagnetizing tensor, which in its most general case is position dependent  $\vec{\overline{N}}(\vec{r})$ .

In homogeneously magnetized samples, the demagnetizing field is opposed to the magnetization vector  $\vec{M}$  for which the tensor  $\vec{\overline{N}}$  takes the form of:

$$\vec{\overline{N}} = \begin{bmatrix} N_x & 0 & 0 \\ 0 & N_y & 0 \\ 0 & 0 & N_z \end{bmatrix}, N_x + N_y + N_z = I \quad (1.16)$$

A consequence of the demagnetizing energy is the non-uniform magnetization distribution, such as magnetic domains. These are created to avoid surface and volume magnetic charges.

iv) Zeeman energy

The energy determined by the interaction between the magnetization  $\vec{M}$  and an external magnetic field is called Zeeman energy. In order to minimize this energy, defined by:

$$E_{zeeman} = -\mu_0 \vec{M} \cdot \vec{H}_{ext} \quad (1.17)$$

every magnetic moment of the magnetic system tends to align parallel to the external magnetic field,  $\vec{H}_{ext}$ . The external magnetic field can include a static bias field ( $H_{bias}$ ) as well as a time varying field pulse ( $h_p$ ) or a harmonic high frequency field ( $h_{rf}$ ).

**1.3. LANDAU-LIFSHITZ-GILBERT EQUATION**

The evolution of the magnetization in time and space under a local effective field  $\vec{H}_{eff}(\vec{r}, t)$  is described by the Landau-Lifshitz (LL) equation proposed in 1935 [Landau & Lifshitz 1935]. This equation is similar to equation 1.6 but with a supplementary damping term:

$$\frac{\partial \vec{M}}{\partial t} = -\mathbf{g} (\vec{M} \times \mu_0 \vec{H}_{eff}) - \frac{\lambda}{M_s^2} (\vec{M} \times (\vec{M} \times \mu_0 \vec{H}_{eff})) \quad (1.18a)$$

Here, the parameter  $\lambda$  expresses the magnitude of the damping, and is called the relaxation frequency. The first term corresponds to the torque on the magnetization vector exerted by the effective field  $\vec{H}_{eff}$  and describes the Larmor precession of the magnetization vector around  $\vec{H}_{eff}$ . The second term corresponds to the phenomenological damping torque, which is responsible for the reorientation of the magnetization vector towards the effective field.

An alternative equation has been proposed by Gilbert in 1955 [Gilbert 1955]:

$$\frac{\partial \vec{M}}{\partial t} = -\mathbf{g} (\vec{M} \times \mu_0 \vec{H}_{eff}) + \frac{\alpha}{M_s} \left( \vec{M} \times \frac{\partial \vec{M}}{\partial t} \right) \quad (1.18b)^3$$

---

<sup>3</sup> Here  $\mathbf{g} = g \cdot \frac{|e|}{2m_e}$

where  $\alpha$  is the damping constant of positive value,  $\alpha > 0$ . The precessional term:  $(\vec{M} \times \mu_0 \vec{H}_{eff})$  is here replaced by  $\partial \vec{M} / \partial t$ . In this way, the damping leads not only to the realignment of the magnetization towards the effective field but it acts also on the precessional motion itself.

The Landau-Lifshitz-Gilbert equation 1.18b can be transformed into the Landau-Lifshitz form (1.18a) when using  $\mathbf{g}' = \mathbf{g} / (1 + \mathbf{a}^2)$  and  $\mathbf{l} = \mathbf{a} \mathbf{g} M_s / (1 + \mathbf{a}^2)$  [Mallinson1987]. We have  $\mathbf{g}' = \mathbf{g}$  and  $\mathbf{l} = \mathbf{a} \mathbf{g} M_s$  in the condition of small damping ( $\mathbf{a} \ll 1$ ).

In the Landau-Lifshitz-Gilbert equation the damping constant  $\mathbf{a}$  appears as the parameter responsible for the magnetization relaxation toward the equilibrium state (or the closest minimum) [Miltat2002]. In absence of damping ( $\mathbf{a} = 0$ ) the magnetization  $\vec{M}$  precesses indefinitely around the effective field  $\vec{H}_{eff}$  and will never align parallel to the effective field. The damping mechanism is associated to the coupling between the magnetic spins and other degrees of freedom (phonons, electrons) as well as impurities and defects) [Miltat2002, Bailleul2002]. For  $\mathbf{a} \neq 0$  the magnetization executes precessions around the effective field as shown in figure 1.2, which are characterized by an angle that is exponentially attenuated.

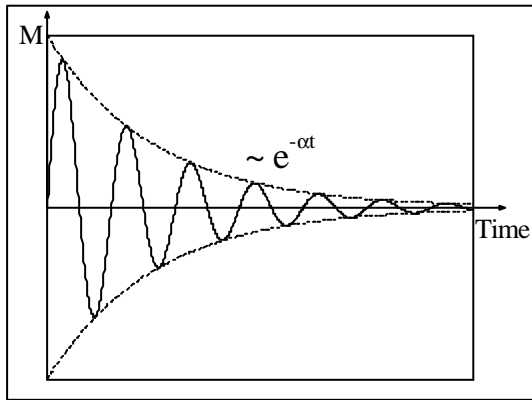


*Figure 1.2*  
Attenuated magnetization precessions around the effective field, for  $\mathbf{a} > 0$

The value of the damping factor is a material property. In literature, values are given ranging between  $\mathbf{a} = 0.005$  up to  $0.1$  [Miltat2002], for instance:  $\mathbf{a} = 0.008$  for a NiFe sphere [Bauer2000], or  $\mathbf{a} = 0.031$  for a thin bi-layer of CoFe/NiFe of a spin valve [Schumacher2002].

The LLG equation is a coupled non-linear second order differential equation that describes the static magnetization distribution as well as its dynamics. The latter contains the small and larger angle deviations of the magnetization from its equilibrium state. Only for few situations, analytical solutions to the LLG equation can be obtained, in the static as well as in the dynamic case. One analytic solution of the dynamic case can be obtained for small amplitude oscillations around equilibrium upon linearization of the LLG equation. This case will be considered in section 1.4. In general cases, the solutions to the LLG equation are obtained by numerical simulations, which have been intensively developed in the past 5-10 years as an important tool for the understanding of micro-magnetism.

One simplified approach to solving the Landau-Lifshitz-Gilbert equation numerically is the representation of the total system by a single macroscopic spin. In this case, the LLG equation can be solved relatively easily by common numerical integration methods such as Runge Kutta [Numerical\_Recipes]. This approach has been used in this work as described in Annexe 4.

If one is only interested in the static magnetization distribution, the equilibrium/metastable states of a ferromagnetic system can be obtained from the variational principle for the energy [Brown1963, Miltat1994]:

$$\begin{aligned} dE(\vec{M}) &= 0 \\ d^2E(\vec{M}) &> 0 \end{aligned} \quad (1.19)$$

where  $E(\vec{M})$  represents the total energy of the system. These lead to Brown's equations:

$$\begin{aligned} \vec{m} \times \vec{H}_{eff} &= 0 \text{ in the bulk and} \\ \vec{m} \times \partial \vec{m} / \partial n &= 0 \text{ at the surface} \end{aligned} \quad (1.20)$$

#### 1.4. SMALL ANGLE MAGNETIZATION DEVIATION

##### Spin waves

The general solutions of the linearized LLG equation are spin waves that correspond to the propagation of “small perturbations” through sample. These perturbations are characterized by a well-defined spatial correlation of the phase  $\mathbf{j}$  and of the deviation angle or spin wave amplitude  $\mathbf{q}$  (fig.1.3). In the particular case, when the magnetic moments precess in phase in the entire magnetic system, the precession mode is uniform ( $\mathbf{j} = 0$ ,  $\mathbf{q} = \text{const.}$ ) (fig.1.3b).

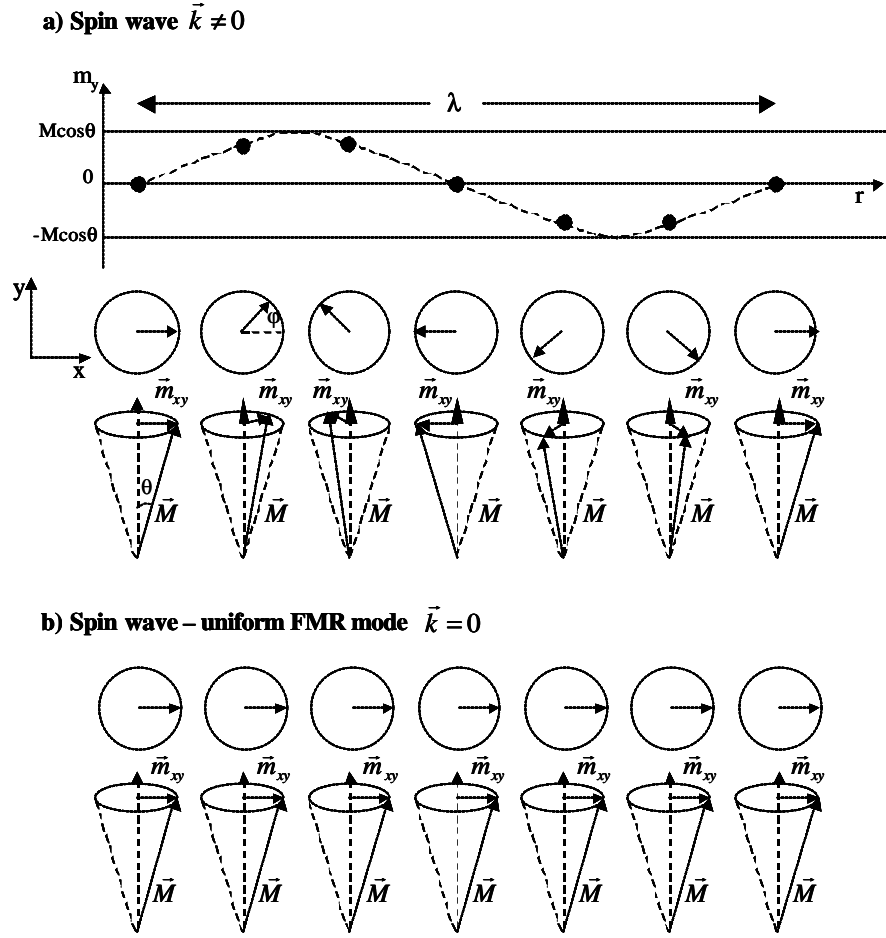


Figure 1.3: Spin wave mode of wave vector  $\vec{k}$ : a) Finite wavelength  $\vec{k} \neq 0$  and b) uniform precession mode  $\vec{k} = 0$  ( $L = \infty$ ).

The spin wave frequency carries information about system energy such as the anisotropy energy, the external magnetic fields or the saturation magnetization ( $M_S$ ). Therefore, measurements of spin wave frequencies are an important tool to characterize magnetic systems. There are two complementary types of experiments that are commonly used to study spin waves, **Brillouin Light Scattering** (BLS) [Cochran1995, Hillebrands1995] and **FerroMagnetic Resonance** (FMR) [Heinrich1995, Celinski1997, and Farle1998]. In the BLS spin waves of wave vector  $\vec{k}$  can be created or annihilated in contrast to the FMR excitations in which no momentum is transferred and only those modes are excited for which the total momentum is zero,  $\vec{k} = 0$ .

Besides those conventional measurements, recently new types of measurement techniques in the time domain have been presented in the literature [Silva1999, Celinski1997, Crawford1999, Freeman1992, Russek2000B], similar to the one described in this thesis. They are based on a pump-probe technique, which employs coplanar wave-guide devices and

allows one to determine the natural precession frequency from the damped oscillations measured in the time domain (see chapter 2).

Because, for magnetization dynamics experiments, the natural frequencies set the time-scale, we will derive in the following the uniform mode frequencies for a continuous thin film.

### Uniform Ferro-Magnetic Resonance mode

The FMR technique consists of the measurement of the absorption of the microwave energy when a spatially uniform microwave (*rf*) magnetic field excites the magnetic moments in a system. A minimum in the microwave spectrum occurs when the *rf*-frequency coincides with the magnetization precession frequency.

The equation of motion of the magnetization for small amplitude precessions is obtained from the linearized Landau-Lifshitz-Gilbert equation (eq.1.18b) in the lossless case ( $\alpha = 0$ ) [Kittel 1947].

Solutions of the linearized equation yield the precession frequency as a function of the second derivate of the energy [Farle1998, Miltat2002]:

$$\frac{\omega}{g} = \frac{g}{M \sin q} \sqrt{\frac{\partial^2 E}{\partial q^2} \frac{\partial^2 E}{\partial j^2} - \left( \frac{\partial^2 E}{\partial q \partial j} \right)^2} \quad (1.21)$$

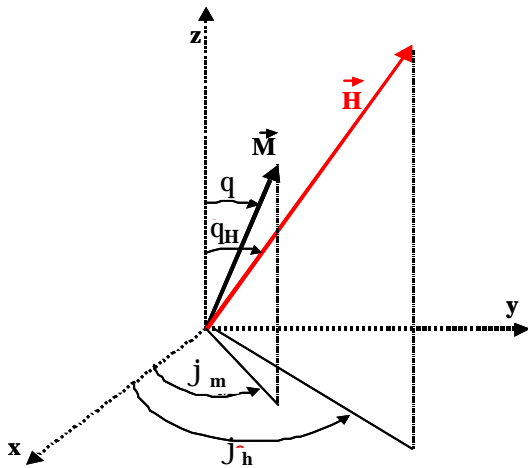


Figure 1.4:  
Spherical coordinates for the magnetization and magnetic field vectors used in the calculation of the ferromagnetic resonance frequency

Using the energy expression of a continuous film of uniaxial in-plane anisotropy, one obtains the Kittel equation:

$$\frac{\omega}{g} = \frac{1}{\sin q} \sqrt{[H \cos(j_m - j_H) + H_u \cos^2 j_m + 4pM_s][H \cos(j_m - j_H) + H_u \cos 2j_m]} \quad (1.22)$$

where the angles  $q$ ,  $j_m$  and  $j_H$  are defined in figure 1.4.  $H$  represents the external magnetic field whose orientation is defined by the angles  $j_H$  and  $q_H$  (here the external field is

considered in the film plane,  $\theta_H=90^\circ$ ),  $H_u$  represents the uniaxial anisotropy field and its orientation is defined by  $\mathbf{q}$  and  $\mathbf{j}_m$ . The microwave field is considered to be perpendicular to the external field.

Considering the particular case of a magnetic thin film in (x,y) plane excited by a rf-magnetic field,  $H_{rf}$ , parallel to the ox-axis, in an external magnetic field,  $H$ , parallel to oy-axis, the magnetic susceptibility associated to the rf-magnetic field is defined as:

$$\mathbf{c}_{rf} = \frac{M_x}{H_{rf}} = \frac{\mathbf{c}_H}{1 - \left( \frac{\mathbf{w}}{\mathbf{w}_0} \right)^2} \quad (1.23)$$

where  $\mathbf{c}_H = \frac{M_y}{H}$ . We observe that the variation of the magnetic susceptibility as a function of  $\mathbf{w}$ , has a maximum for  $\mathbf{w} = \mathbf{w}_0$ . The imaginary parts of the magnetic susceptibility,  $\text{Im}(\mathbf{c}_m)$  characterize the energy absorption that appears in the magnetic system due to excitation by an rf-magnetic field. The absorbed microwave power,  $P_{rf}$ , in a magnetic thin film, is defined as [Celinski 1997]:

$$P_{rf} = \frac{1}{2} \mathbf{w} \text{Im}[\mathbf{c}_{rf}] \cdot |H_{rf}|^2 \quad (1.24)$$

For an external rf-magnetic field of frequency  $f = \mathbf{w}/2\mathbf{p}$  equal to the frequency  $f_0 = \mathbf{w}_0/2\mathbf{p}$  of the magnetization precessions, the rf-energy is entirely absorbed by the magnetic system. The frequency  $f_0$  is called the ferromagnetic resonance frequency. Ferromagnetic resonance occurs for the frequency value for which the absorbed power in the thin film (eq.1.24) is at maximum value.

## 1.5. MAGNETIC LENGTHSCALES

Coming back to the static magnetization distribution, there exist different magnetic length scales that characterize the magnetic static distribution. These length scales are derived from the competition between the internal energies of the system (defined in section 1.2), the exchange, magnetostatic, and magneto-crystalline energies.

- The competition between the exchange energy and the anisotropy energy defines the width of a domain wall, given by the Bloch wall parameter:



$$\Delta_0 = \sqrt{\frac{A_{ex}}{K}} \quad (1.25)$$

- The competition between the exchange energy and the magnetostatic energy defines the exchange length:

$$l_{ex} = \sqrt{\frac{2A_{ex}}{\mu_0 M_s^2}} \quad (1.26)$$

- The quality factor compares the magneto-crystalline to the magnetostatic energy:

$$Q = \frac{2K}{\mu_0 M_s^2} \quad (1.27)$$

## 1.6. DOMAIN WALLS

Barkhausen found the first experimental confirmation of the magnetic domain concept in 1919 [Barkhausen1919]. He discovered that the magnetization process in an applied field contains discontinuous variations named Barkhausen jumps, which he explained as magnetic domain switching<sup>4</sup>. Further analysis of the dynamics of this process [Sixtus 1931] led to the conclusion that such jumps can occur by the propagation of the boundary between domains of opposite magnetization.

In 1932, Bloch [Bloch1932] analyzed the spatial distribution of the magnetization,  $M$ , in the boundary regions between domains, finding that they must have a width of several hundred lattice constants, since an abrupt transition (over one lattice constant) would be in conflict with the exchange interaction. Two basic modes of the rotation of the magnetization vector can be defined for domain walls:

i) The three dimensional (3D) rotation of the magnetization from one domain through a  $180^\circ$  wall to the other domain, determining a Bloch wall (fig.1.5a). Here the magnetization rotates in a plane parallel to the wall plane. This wall is characteristic to bulk materials or thick films.

ii) The two dimensional (2D) rotation of the magnetization from one domain through a  $180^\circ$  wall to the other domain, determining a Néel wall. Here the magnetization rotates perpendicular to the wall plane. This type of walls appears in thin magnetic films, where the in-plane rotation of the magnetization has a lower energy than in the classical Bloch wall

---

<sup>4</sup> Interpretation considered not valid today

mode (fig.1.5b). This is due to the demagnetizing field produced by the Bloch wall spins that point perpendicular to the film surface. In order to reduce these fields, the magnetization starts to rotate in-plane.

The transition from a Bloch wall to a Néel wall occurs roughly when the film thickness,  $t$ , becomes comparable to the wall width,  $\delta_w$ . (Hubert1998).

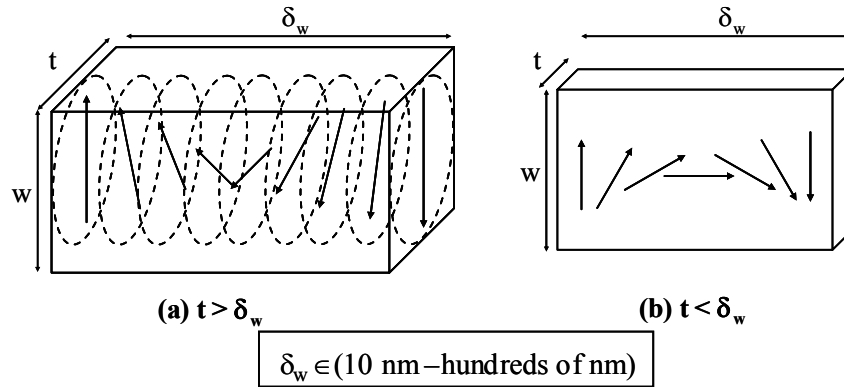


Figure 1.5:

180° magnetic domains walls:

(a) Bloch walls in a bulk material (b) Néel walls in a thin magnetic film

The width of a domain wall ( $\delta_w$ ) is proportional to Bloch parameter, ( $\Delta_0$ ) defined in equation 1.25. The Néel wall is thinner than the Bloch walls  $\delta_w^{Néel} < \delta_w^{Bloch}$  where the width of a Bloch wall can be estimated by:

$$\delta_w^{Bloch} = \pi \Delta_0 \quad (1.28)$$

## 1.7. MAGNETIZATION REVERSAL MECHANISMS

As a function of the sample dimensions and the type of excitation fields (static or pulsed, of variable sweep rate –  $dH/dt$ , of different orientations with respect to the uniaxial anisotropy) one distinguishes between different classes for the magnetization reversal processes, for which the most important ones are detailed below:

- i) Reversal obtained by nucleation and domain wall propagation
- ii) Reversal by uniform rotation of the magnetization
- iii) Reversal by magnetization precession

### 1.7.1. DOMAIN WALL DYNAMICS

The first magnetization curve and the hysteresis loop of an extended ferromagnetic material (note: this does not hold necessarily for nanomagnets) characterize the quasi-static reversal of its magnetization (fig1.6) in a varying external magnetic field. On the first magnetization curve (fig.1.6), the magnetization alignment parallel to the external field is realized by reversible wall displacements and non-coherent rotation from point A to point B and then by coherent rotation from B to the saturation point C [Kittel1966]. Wall displacement increases the magnetic domain surface that has the magnetization parallel to the external magnetic field and consequently, decreases the magnetic domain with the magnetization anti-parallel to the external magnetic field [Koch1998, Choi2001].

On the hysteresis curve, decreasing the external field from positive saturation (point C), the nucleation of reversed magnetic domains sets in at a certain value of the magnetic field as we can observe in point D on figure 1.6. Depending on the sample type and magnetic homogeneity, the dynamics from the point D to F may include domain wall displacements, and non-coherent or coherent magnetization rotations.

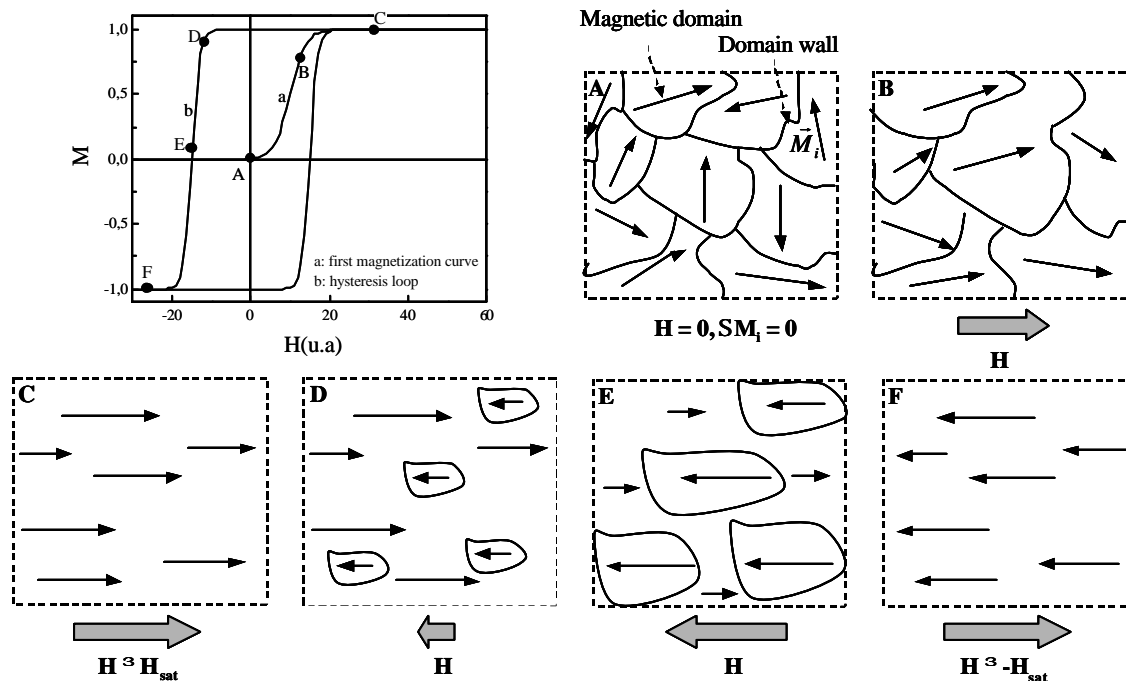


Figure 1.6

Magnetic domain configuration corresponding to different points on the first magnetization curve and hysteresis loop

One important parameter that characterizes the domain wall propagation in the presence of an external magnetic field is the wall velocity,  $v$ . This velocity can be deduced by integrating the Landau-Lifshitz-Gilbert equation (1.18b) over the domain wall width [Malozemoff1979, Hubert1998]. Since the displacement mechanism of a Bloch wall has some similarities to the precessional reversal process (detailed in section 1.7.3) it will be detailed in the following.

We suppose two neighboring magnetic domains with their magnetizations “up” and “down” separated by a  $180^\circ$  Bloch domain wall. The Bloch wall magnetization is oriented in the wall plane and perpendicular to the domain magnetization. An “up” magnetic field exerts no torque on the domain magnetization since the angles between the field and the domain magnetization vectors are  $0^\circ$  and  $180^\circ$ , respectively. Contrary, the torque between the domain wall magnetization and the external field ( $\vec{M}_{wall} \times \vec{H}$ ) rotates the magnetization out of the wall plane by an angle  $\mathbf{j}_{wall}$ , from point 1 to point 2 as shown in the figure 1.7. This creates a strong demagnetizing field,  $h_d$ , perpendicular to the wall plane, which induces a precession of the magnetization around  $h_d$ , rotating the magnetization from point 2 to point 3. Consequently, the wall magnetization aligns with the domain magnetization that is parallel to the external field. This is equivalent to a wall propagation from left to right in figure 1.7 with the velocity  $v$ .

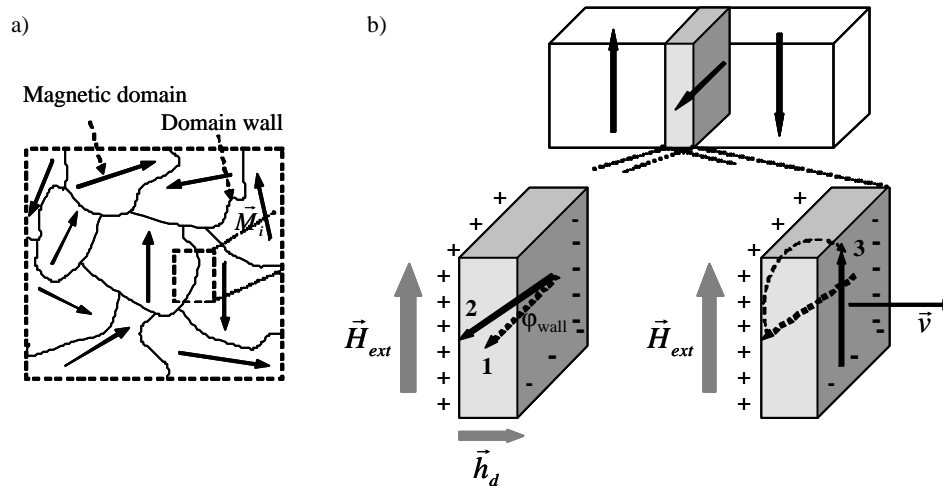


Figure 1.7

- a) Ferromagnetic structure composed of magnetic domains and domain walls;
- b) Bloch wall displacement mechanism

The domain wall velocity,  $v$ , is proportional to the difference between the external field,  $H_A$ , and the coercive field,  $H_C$ , to the sample magnetization,  $M_S$ , to the wall width

( $\approx \sqrt{A_{ex}/K}$ ), to the gyromagnetic factor,  $\gamma$ , and is inversely proportional to the damping parameter  $\lambda$  [Doyle 1998]:

$$v \propto \frac{gM_S}{I} \sqrt{\frac{A_{ex}}{K}} \cdot \mu_0 (H_A - H_C) \quad (1.29)$$

Equation 1.29 can be rewritten to obtain a more general expression for the reversal time,  $\tau$ :

$$\begin{aligned} \frac{1}{t} &= \frac{v}{L} \\ &\propto \frac{gM_S}{IL} \sqrt{\frac{A_{ex}}{K}} \cdot \mu_0 (H_A - H_C) \\ &= \frac{\mu_0}{S_w} (H_A - H_C); \\ \text{with } S_w &= \frac{IL}{gM_S} \sqrt{\frac{K}{A_{ex}}} = \frac{L}{\mu} \end{aligned} \quad (1.30)$$

The parameter  $S_w$  represents the switching coefficient and it is defined as the ratio between the sample length,  $L$ , and the effective wall mobility,  $\mu$ . These relations have been verified by numerous experiments in the past for larger (bulk) samples [Rado 1963].

It is noted that the reversal mechanism depends on the external magnetic field sweep rate ( $dH/dt$ ). For example, Camarero et al [Camarero2001] studied the influence of the external field sweep rate ( $dH/dt$ ) on the magnetization reversal dynamics. They revealed that the magnetization reversal is dominated by domain wall displacements for low  $dH/dt$  values and by nucleation processes for higher  $dH/dt$  values in exchange coupled NiO-Co bilayers.

A nice parallel between the reversal of cluster particles of variables densities on the substrate and the reversal dominated by domain dynamics in thin films [Ferre1997] was experimentally realized in 2003 by Binns et al. [Binns2003]. He showed that *at low coverage* of the substrate with clusters, the switching dynamics of the sample remains the same as in the clean substrate while *above a certain limit of coverage*, a significant acceleration of the magnetic reversal was observed with a fast component due to a reversal propagating through the cluster film. Its conclusion was that the velocity of the propagation, rather than the rate of reverse magnetization nuclei, dominates the reversal through the cluster film, the average switching time for a cluster in this case being about 10ns.

### 1.7.2. COHERENT MAGNETIZATION REVERSAL – STONER-WOLFARTH MODEL

The coherent rotation model was developed by Stoner-Wolfarth [St.-W. 1948] and Louis Néel [Néel 1947]. This model considers the magnetization reversal of a mono-domain particle in an external magnetic field,  $H$ . In this case, the rotation of the magnetic moments increases the anisotropy energy while the exchange energy remains constant.

Figure 1.8 shows the evolution of the mono-domain particle energy as a function of the applied magnetic field,  $H$ , which defines the equilibrium angle  $\mathbf{q}$  of the magnetization direction with respect to the uniaxial anisotropy easy axis. The total energy of the particle is the sum over three terms: the demagnetization, Zeeman, and magneto-crystalline energies. The normalized energy is written as [Wernsdorfer 1996]:

$$E = \sin^2(\mathbf{q}) - 2h \cos(\mathbf{q} - \mathbf{j}) \quad (1.31)$$

where the angles  $\mathbf{q}$  and  $\mathbf{j}$  are specified in figure 1.8, and  $h$  represents the ratio between the external field energy and the magneto-crystalline anisotropy energy constant,  $K$ :

$$h = \frac{H}{H_K} = \frac{\mu_0 M H}{2K} \quad (1.32)$$

We consider the particle to be in one of the energy minima at zero field, as shown in figure 1.8 on the symmetric curve for  $h = 0$ . This corresponds to the magnetization parallel to the easy axis of the particle where the first derivate of the energy function is zero:

$$\partial_q E = 0 \quad (1.33)$$

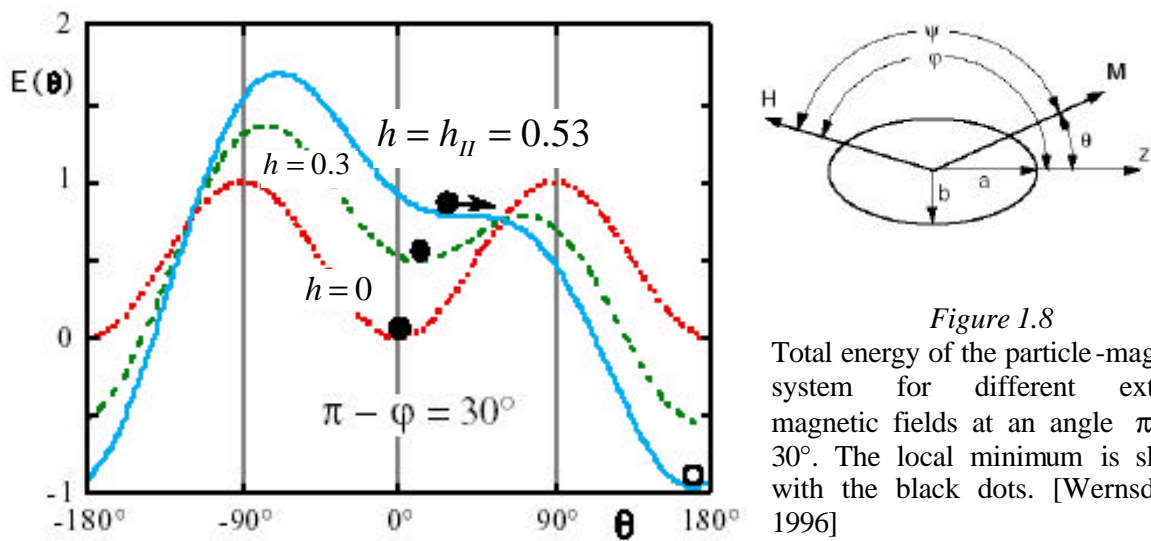


Figure 1.8

Total energy of the particle-magnetic system for different external magnetic fields at an angle  $\pi - \phi = 30^\circ$ . The local minimum is shown with the black dots. [Wernsdorfer 1996]

Applying a magnetic field into the opposite direction of the magnetization the symmetric curve becomes asymmetric and the local energy minimum moves toward positive

angles  $\mathbf{q}$ . Increasing the field values, the difference between the energy minimum and energy maximum is decreasing going to zero at a critical magnetic field,  $h_c$ . This corresponds to a saddle point where the second derivate of the energy is zero:

$$\partial_q^2 E = 0 \quad (1.34)$$

From (1.31 – 1.33) we obtain an expression of the critical reversal field,  $h_c$ , as a function of the angle  $\mathbf{j}$  between the direction of the applied field and the uniaxial anisotropy direction:

$$h_c = \frac{1}{(\sin^{2/3} \mathbf{j} + \cos^{2/3} \mathbf{j})^{3/2}} \quad (1.35)$$

The angle  $\mathbf{q}_0$  defined as the angle between the magnetization  $\vec{M}$  and the direction  $oz$ , for which the magnetization reversal occurs, can be expressed as:

$$\tan \mathbf{q}_0 = -\tan^{1/3} \mathbf{j} \quad (1.36)$$

The critical field,  $h_c$ , for which the reversal occurs as a function of the angle  $\mathbf{j}$ , (eq.1.36) is presented by the Stoner-Wolfarth astroid in figure 1.9. The curve  $\vec{h} = \vec{h}_0(\mathbf{j})$  delimitates the region of reversal ( $\vec{h} \geq \vec{h}_0(\mathbf{j})$ ) from the region of non-reversal ( $\vec{h} < \vec{h}_0(\mathbf{j})$ ).

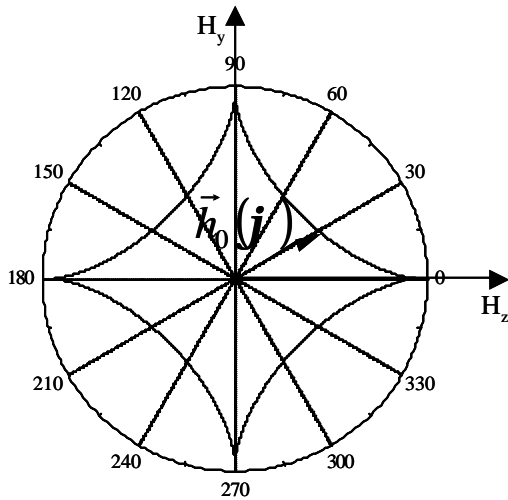


*Figure 1.9*  
Stoner-Wolfarth astroid that defines the limit between the non-reversal (inner region) and reversal (outer region) regions.

Referring to figure I.1 from the general introduction, this process appears in single-domain magnetic systems, where quasi-static external fields are applied parallel to the direction to which the magnetization should be reversed.

Wernsdorfer et al. experimentally verified the Stoner-Wolfarth model on magnetic nanoparticles of 50-150nm dimensions. Despite a clear single-domain character of the particles, they showed that a distribution of switching field exists, whose width increases by decreasing the temperature and becomes constant at very low temperatures [Wernsdorfer

1995]. For non-zero temperatures, the switching field becomes a stochastic variable and the magnetization switching takes place before the energy barrier goes to zero [Bonet 1999, Thirion 2002].

Stoner-Wolfarth reversal is actually used in MRAM applications (see FIMS – fig.I.3 – general introduction), the magnetic memory being reversed by the total field obtained with two magnetic field pulses ( $H_y$  and  $H_z$  in figure 1.9) obtained with two conductor lines perpendicular to each other. The time scales, characteristic to this reversal, are in the nanosecond range.

In order to understand the time limits that occur during the coherent rotation reversal, we consider a Stoner-Wolfarth particle represented by an ellipsoid with the long axis parallel to the  $oy$ -axis. We will analyze the details that appear during the coherent rotation of the magnetization toward an external magnetic field applied parallel to this  $oz$ -axis as shown in figure 1.10. We suppose that the amplitude of the external magnetic field is slowly increased up to the anisotropy field value ( $H_k$ ). This means that for each value of the external magnetic field (7 values on figure 1.10) the magnetization “has the time” to relax parallel to its current effective magnetic field.

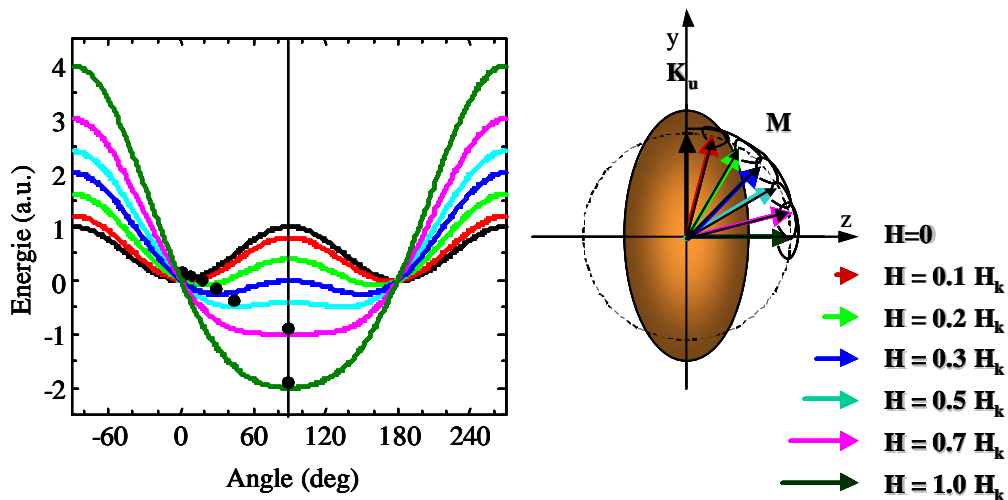


Figure 1.10

Quasi-static relaxation of the magnetization during its reversal by coherent rotation in a Stoner-Wolfarth particle

For  $H = 0$  the magnetization is parallel to the  $oy$ -axis position that corresponds to one local minimum of the symmetric curve from figure 1.10. Increasing the magnetic field from zero to  $0.1H_k$  (applied parallel to  $+oz$  axis) the angle corresponding to the local minimum varies from  $0^\circ$  to about  $10^\circ$ , corresponding to the new orientation of the effective field. The magnetization relaxes into this new local minimum executing a small-angle precessional



motion around the effective field. Equivalent relaxation processes are obtained increasing the external field up to the value equal to  $0.7H_K$ , value for which the local minimum is obtained for an angle of  $90^\circ$ . In this case, the maximum and the two minimum points confound in a minimum point. Further increasing of the external magnetic field values decrease the energy of the minimum but leaves the angle constant at  $90^\circ$ .

The sweep rate of the magnetic field ( $dH/dt$ ) has an important influence on the magnetization rotation in a macrospin particle. As in the example given above, for small values of the sweep rate, the magnetization relaxes parallel to the intermediate effective field. If the value of  $dH/dt$  is large enough, an adiabatic excitation of the macrospin system can be induced. For this the corresponding rise-time needs to be smaller than the characteristic precession time ( $\sim 100\text{ps}$ ).

Several studies have been performed in order to characterize the magnetization reversal induced by variable magnetic fields of frequencies more or less important (from MHz to tens of GHz). Recently, Bauer et al [Bauer2000] analyzed the response of a mono-domain particle of ellipsoidal shape to magnetic pulses of variable duration, amplitude and shape. Two switching mechanisms were evidenced: one corresponding to the uniform rotation obtained for long pulses (2.75ns – figure 1.11a) and the other to the precessional reversal for shorter pulses (0.25ns – figure 1.11b). The former mechanism was described in this section while the latter one will be detailed in the following.

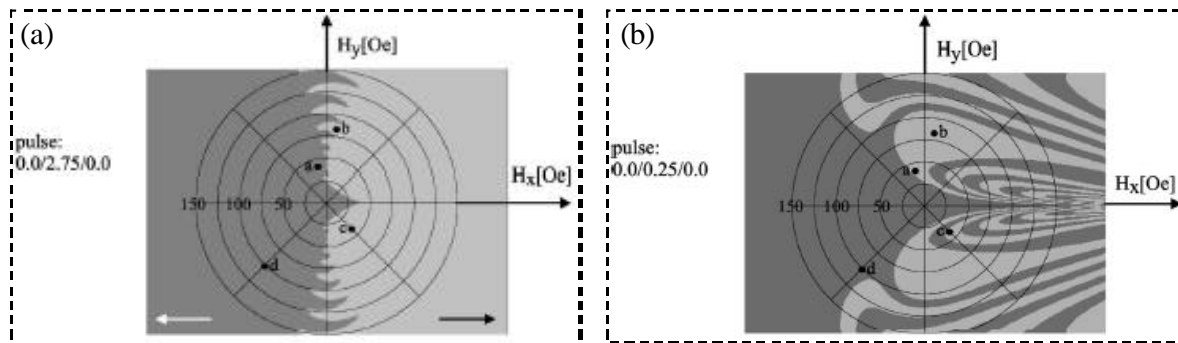


Figure 1.11: Switching diagrams corresponding to the a) Stoner-Wolfarth and b) precessional reversal [Bauer 2000] of an ellipsoidal shape particle characterized by  $N_x = 0.008$ ,  $N_y = 0.012$  and  $N_z = 0.98$ .

### 1.7.3. PRECESSIONAL REVERSAL

The magnetization switching by precession is obtained by applying very fast rising magnetic field pulse perpendicular to the initial magnetization direction stabilized by the uniaxial anisotropy [Bauer2000, Miltat2002]. The excitation rise-time should be in the sub-nanosecond range in order to realize adiabatic excitation. Larger rise-times (about some ns) would determine the magnetization to continuously relax parallel to the intermediate effective fields (that correspond to intermediate magnetic field values in the pulse rise-time interval). The switching is obtained in half a precession period of the magnetization, corresponding to about some hundreds of picoseconds. Comparing to the Stoner-Wolfarth reversal, the precessional reversal is characterized by shorter switching times. It is the fastest switching process known until today, being characterized by switching times of the same order as the precession period, and relaxation processes or thermal fluctuations do not influence the reversal since the excitation is adiabatic.

The excitation field induces a large demagnetizing field perpendicular to the film surface that results in a mostly in-plane magnetization precession. The origin of the strong demagnetizing field perpendicular to the film surface and the precessional reversal steps will be detailed in the following.

*Precessional reversal – step no. I: Out-of-plane motion of the magnetization (figure 1.12.I)*

We consider the initial magnetization orientation in the plane of the thin film (point 1 on figure 1.12.I). A pulsed magnetic field is applied perpendicular to the magnetization direction and in the film plane, determining a new effective field ( $\vec{h}_{eff} = \vec{h}_p + \vec{H}_u + \vec{h}_d$ ) in the film plane. In this case  $h_d$  has a negligible value since the magnetization lies in the film plane and  $N_{||}$  is almost zero. This will give rise to a precessional motion of the magnetization around the in-plane effective field, and lead to an out-of-plane component of the magnetization  $M^\perp \neq 0$ . As thin films are characterized by a very large demagnetizing field perpendicular to the film plane ( $N^\perp \approx 1$ ), the demagnetizing field increases its value very rapidly ( $h_d^\perp = -N^\perp M^\perp$ ) and will oppose the out-of-plane motion of the magnetization, this movement being slowed down. The new effective magnetic field is now quasi-perpendicular to the film surface and has a relatively large value ( $\vec{h}_{eff} = \vec{h}_p + \vec{H}_u + \vec{h}_d^\perp$ ). For instance an out of plane deviation of  $1^\circ$  of the magnetization corresponds to  $m_z = 0.0175$  that determines a demagnetizing field

perpendicular to the film plane:  $h_d^\perp = -N_z m_z = 183 \text{ Oe}$  for  $M_S^{\text{NiFe}} = 853 \text{ emu/cm}^3$ . This value is much larger than the anisotropy field value ( $H_u$ ) or the external pulsed magnetic field ( $\sim 10 \text{ Oe} - 100 \text{ Oe}$ ).

*Precessional reversal – step no. II: Magnetization precession in the film plane* (figure 1.12.II)

The magnetization continues its motion with an in-plane precession around the effective field (curve defined by points 2 and 3 on figure 1.12.II), which is quasi-perpendicular to the film plane. The precession time is about some hundreds of picoseconds and thus, this process is characterized by frequencies in the GHz range.

*Precessional reversal – step no. III: Magnetization precession stopped in a switched position* (figure 1.12.III)

Choosing the right parameters for the magnetic field pulses (amplitude, rise-time, width) and the magnetic material (damping parameter, sample dimensions, internal fields) the magnetization relaxes parallel to the reversed position (point 3 on the figure 1.12.III) after executing half ( $1/2$ ), one and a half ( $3/2$ ), two and a half ( $5/2$ ), ... precession cycles. The minimum switching time is obtained after half a precession. Usually each reversal by precession is followed by small precessions of the magnetization around the effective field called *ringing* that is a source of noise in MRAM devices and increases the effective switching time. The precessional reversal that has no ringing is called a *ballistic reversal*. In 2002/2003, Gerrits et al and Schumacher et al. [Gerrits2002, Schumacher2002, Schumacher2002B] presented the magnetization reversal in half a precession period by coherent rotation of the magnetization avoiding ringing.

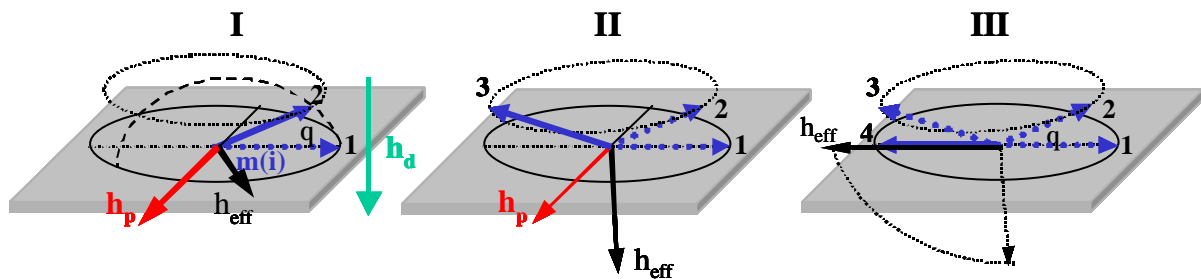


Figure 1.12:  
Precessional switching mechanism

In reality, macrospin systems are difficult to be experimentally obtained and in consequence, it is desirable to apply this concept of precessional reversal to micron-sized magnetic particles.

This was the challenge of this work. As we will see in chapter 4, the precessional reversal was evidenced both in micron-sized samples and continuous magnetic thin films, characterized by an in-plane uniaxial easy axis. Furthermore, we evidenced the stochastic character of the dynamics, which is related to the dynamic processes that are not-correlated for different regions of the sample and to the stroboscopic nature of the measurement technique.



## **CHAPTER 2**

### **THE STROBOSCOPIC PUMP-PROBE TECHNIQUE: DESIGN, DEVELOPMENT AND EXPERIMENTAL SETUP**



**Abstract:**

*Depending on the properties to be investigated, there are a variety of techniques to probe the magnetic state as a function of some given external parameters (e.g. the applied field). Most of these techniques probe a stable, equilibrium or metastable state (such as magnetometric techniques) when the system has relaxed. Others, probe the stationary dynamic states such as FerroMagnetic Resonance (FMR). Most of these techniques are “slow” and require several milliseconds to probe the magnetic states. These techniques cannot be used to follow the transition between different equilibrium states (such as domain wall propagation or magnetization oscillations), induced by the variation of the external parameters.*

*In order to access these transient states, time-resolved measurements are required with sub-nanosecond time resolution. One powerful technique is the stroboscopic pump-probe technique where the delay between the pump and the probe is adjusted depending on the time scale of the event to capture. Here we are interested in registering the magnetization evolution during precessional motion, whose precession period lies in the range of 100 – 1000 ps. Thus, sub-nanosecond time resolution is required. In this chapter, we describe the pump-probe technique developed during my thesis work.*

*As PUMP, we have used the magnetic field of an electromagnetic wave induced in a transmission line onto which the magnetic sample is placed. These magnetic fields are produced by applying voltage signals on the transmission line, which can be either short pulses or steps delivered by a commercial pulse generator or a continuous wave of high frequency delivered by a signal generator integrated in a network analyzer.*

*The magnetization evolution in time is stroboscopically PROBED using three physical effects: the Magneto-Optical Kerr Effect (MOKE), the Magneto-Resistive (MR) Effect, and the Inductive Effect. These different techniques are adapted to measure different processes. FMR type experiments were realized using the MOKE experiments and the inductive technique and the magnetization reversal was evidenced using the Magneto-Optical Kerr and Magneto-Resistive effects.*

*In this chapter, the basic designs as well as the realization of such experiments are described. The propagation of high-frequency voltage signals in a conducting wire requires specially designed transmission lines. Therefore, a brief review of the transmission line theory is presented in section 2.3. The different probe techniques and the corresponding experimental realization are presented in section 2.5.*



## Résumé

*Il existe une variété des différentes techniques pour sonder l'état magnétique en fonction des paramètres externes (ex. le champ magnétique appliqué). La plupart de ces techniques permettent l'étude d'un état magnétique stable (techniques magnétométriques). D'autres techniques, comme la Résonance Ferro-Magnétique (RFM), sondent les états dynamiques stationnaires. La majorité de ces techniques nécessitent des temps de mesure de l'ordre de plusieurs millisecondes. Elles ne peuvent pas être utilisées pour mesurer les états transitoires induits par la variation relativement abrupte des paramètres externes dans des petites échelles de temps (ps, ns).*

*Pour accéder à l'aimantation caractéristique des états transitoires, qui décrivent l'évolution du système d'un état d'équilibre vers un autre (propagation des parois, oscillations de l'aimantation), des mesures résolues en temps sont nécessaires. Un exemple correspond à la technique stroboscopique pompe-sonde, où, le délai entre la pompe et la sonde est ajusté en fonction de l'échelle temporelle du processus à mesurer.*

*Dans notre cas, l'intérêt est de mesurer la dynamique de l'aimantation pendant le mouvement précessionnel, qui a des temps caractéristiques dans la gamme 100 – 1000ps. En conséquence, des résolutions temporelles inférieures à la nanoseconde sont demandées.*

*Dans ce chapitre, nous présentons la technique pompe-sonde développée pendant ma thèse. La pompe correspond aux impulsions de champ magnétique de haute fréquence induites dans des guides d'onde coplanaires sur lesquelles les échantillons magnétiques ont été lithographiés. L'évolution temporelle de l'aimantation est étudiée en utilisant : l'effet Kerr magnéto-optique, l'effet magnéto-résistif et l'effet inductif. Nous présentons la réalisation expérimentale des mesures résolues en temps et, en particulier, de la partie pompe (l'adaptation de la ligne de transmission) et de la partie sonde (des différentes configurations de mesure pour accéder aux différentes composantes de l'aimantation).*

## 2.1. PUMP – PROBE TECHNIQUE

Töpler performed the first pump-probe experiment in 1867 [Töpler1867]. He used a  $2\mu\text{s}$  spark to initiate a sound wave and then photographed the propagation using a second spark triggered with an electrical delay. The first pump-probe experiment using an ultrashort *laser pulse* and an *optical delay* was used to measure the transient response of a germanium sample subjected to a 10ps pulse [Auston1974]. A detailed chronology of the origin of the pump-probe experimental technique is provided by Ippen and Shank, along with other methods using ultrashort light pulses [Shapiro1977].

A schematic of the pump-probe technique is presented in figure 2.1.

We consider a magnetic system that is characterized by the dynamic response  $M(t)$  as given in figure 2.1b induced by the pump excitation shown in figure 2.1a. Here, the pump is represented by magnetic field pulses that carry frequencies in the same interval as the natural frequencies of the magnetic sample.

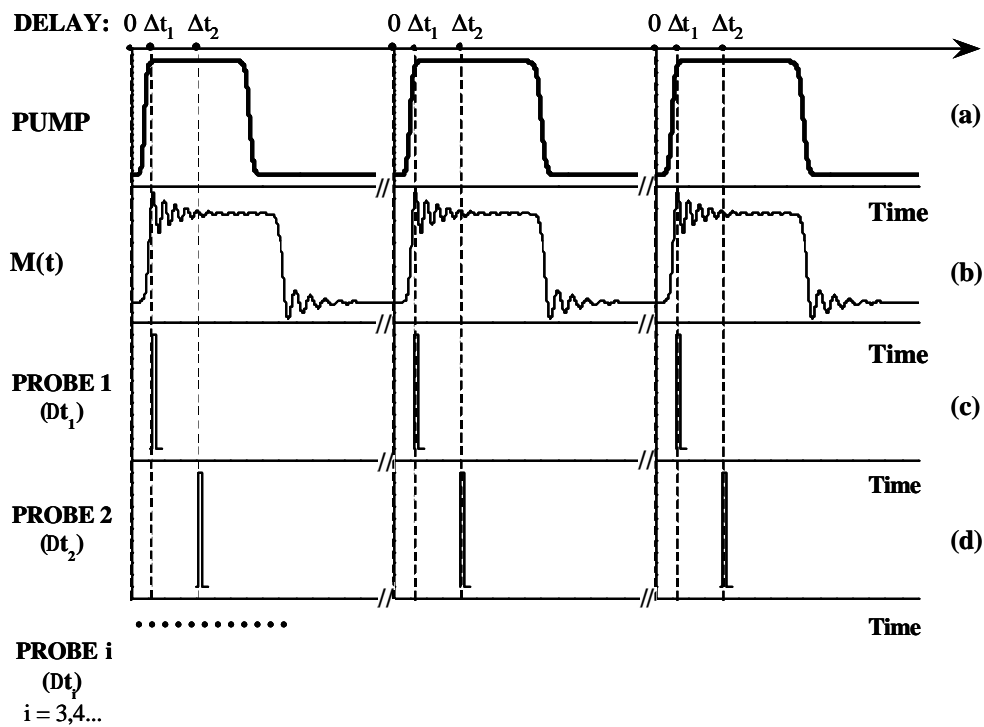


Figure 2.1

Schematics of the synchronized “pump-probe” technique

The measurement of the magnetization dynamic response,  $M(t)$ , with a high time resolution is realized using a short-duration PROBE signal (fig.2.1c, d). This probe is delayed with respect to the pump (with the delay  $\Delta t_1$ ,  $\Delta t_2$ , ...) in order to measure successive points,  $M(\Delta t_1)$ ,  $M(\Delta t_2)$ , ... of the dynamic response,  $M(t)$ .

In these type of experiments, the time resolution is determined by three elements: i) the probe signal duration, ii) the time interval between two successive delay values and iii) the jitter<sup>1</sup> of the pump, probe or delay, that defines the synchronization between the pump and the probe signals.

In our experiments a common pump has been used, composed of an impedance matched coplanar waveguide onto which the magnetic sample is positioned. Depending on the sample size and structure to be measured, we have used three different types of probes. Figure 2.2 presents the experimental techniques used to pump and probe the magnetization dynamics in micron-sized samples using MOKE, MR and the inductive effect in time and frequency domain.

In the following three sections (2.2 – 2.4) we will first concentrate on the requirements and realization of the pump and then we will discuss in section 2.5 the different probe techniques.

## 2.2. PUMP AND PROBE REQUIREMENTS

For the realization of such a pump-probe experiment one may define a number of requirements. Studies of the magnetization precessional motion are possible if the excitation signal contains frequencies in the same interval as the frequencies to be excited in the magnetic sample (about 1-10GHz in the case of metallic magnetic samples). This requires either high frequencies for a sinusoidal excitation signal delivered by the network analyzer or short rise-times (30-100ps) for the voltage pulse as delivered by a pulse generator. Short rise-times of the pump pulses correspond to an adiabatic excitation (see sections 1.7.2. and 1.7.3. from chapter 1) of the magnetic systems where the thermal fluctuations can be neglected [Back1998]. In order to cover the various dynamical processes to be studied, a voltage source needs to be defined, that has a variable output voltage as well as variable field pulse lengths.

The transmission lines into which the voltage pulse are delivered (pump) or which are used to capture a fast changing voltage signal (probe) need to be designed such that sub-nanosecond time voltage pulses (or GHz continuous wave voltages) propagate with minimum attenuation. This means that they have to be impedance matched all over their length.

There are two critical points along the transmission which we would like to point out:

---

<sup>1</sup> The jitter of a signal is defined as the width at half-amplitude of the gaussian function, centered in  $t_0$ , which defines the probability to trigger a signal at the moment  $t_0$ .

- i) the contacts between the line and the electronic equipment delivering or registering the high frequency signals,
- ii) the widths of the transmission line. This varies from the contact region (100 $\mu\text{m}$ ) towards the micron-sized sample (few  $\mu\text{m}$ ), where the line width determines the amplitude of the magnetic excitation field. For example, for magnetization reversal studies, the applied field pulses should be larger than the anisotropy field value which is of the order of a few tens of Oe.

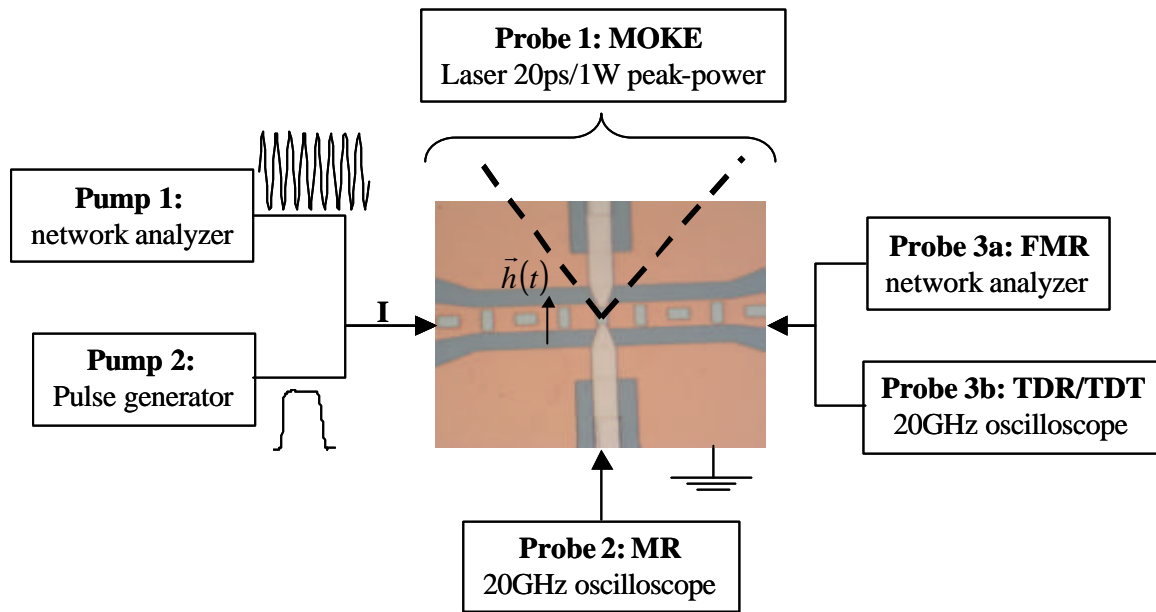


Figure 2.2  
“Pump-probe” experimental techniques

An analysis of the transmission line theory is presented in the following section in order to establish the detailed requirements necessary to impedance match the pump and probe lines in high frequency experiments.

### 2.3. TRANSMISSION LINE THEORY

The propagation of an electromagnetic wave in a medium is defined as a problem with boundary conditions. In our case, this is given by a conducting line surrounded by a ground plane. Two equivalent approaches are used to describe such wave propagation: i) electromagnetic wave propagation theory (Maxwell’s theory) and ii) transmission line theory.

The first theory is a general approach to the electromagnetic wave propagation in space and time based on Maxwell's equations. The propagation velocity of the electromagnetic wave in the dielectric of the line, characterized by the dielectric relative permittivity,  $\epsilon_r$ , and the magnetic relative permeability,  $\mu_r$ , has a smaller value with respect to the electromagnetic wave velocity in air:  $c = 3 \cdot 10^8 \text{ m/s}$ . It is expressed as:

$$v = \frac{c}{\sqrt{\epsilon_r \cdot \mu_r}} \quad (2.1)$$

When the surrounding dielectric is composed of different materials with different  $\epsilon_r$  and  $\mu_r$ , (for example a layered structure or different materials on the top and bottom of the metallic line) the velocity is given by the effective parameters:

$$v = \frac{c}{\sqrt{\epsilon_{eff} \cdot \mu_{eff}}} \quad (2.2)$$

where  $\epsilon_{eff}$  and  $\mu_{eff}$  are the effective constants.

The transmission line theory was initially developed to solve the problem of signal transfer over long distances in telecommunications. Its principal result is the telegrapher equation. In this theory the spatial distribution of the current and voltage along the transmission line is considered, as well as their time dependence:

$$\begin{aligned} V(x,t) &= V(x) \cdot \exp(j\omega t + j_1) \\ I(x,t) &= I(x) \cdot \exp(j\omega t + j_2), \omega = 2\pi f \end{aligned} \quad (2.3)$$

To give an idea of the relevant length-scale, figure 2.3 presents the wavelengths corresponding to the frequency range of 1-15 GHz.

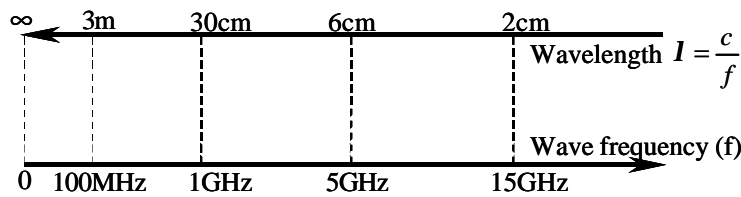


Figure 2.3:  
Scale of wavelength and the  
corresponding frequencies in air  
( $c = 3 \cdot 10^8 \text{ m/s}$ )

We distinguish two cases depending on the relative ratio between the system size,  $L$ , to be studied and the wavelength,  $\lambda$ :

- For  $L \ll \lambda$  there is no propagation between two points of the circuit at a given moment  $t$ . For example, this would be the case for a circuit smaller than some millimeters at 10GHz (corresponding to  $\lambda = 3\text{cm}$ ). As the voltage and current are constant, all over the circuit length, at a moment in time,  $t$ , Kirchoff's laws can then be applied to the overall

transmission line represented by the equivalent circuit in figure 2.4. It consists of three resistances in series corresponding to the line resistance ( $R_1$  and  $R_2$ ) and the load resistance  $R_0$ .

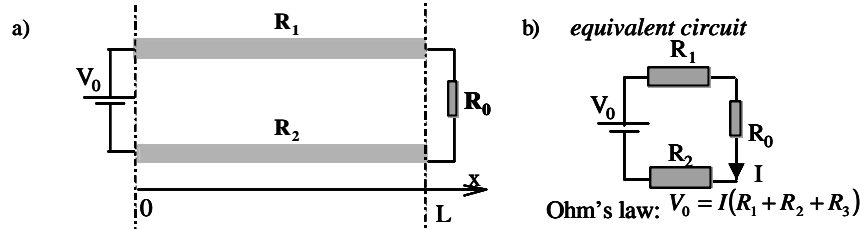


Figure 2.4:  $L \ll \lambda$

a) Simple circuit representation; b) equivalent circuit

- For  $L > \lambda$ , the circuit dimensions become comparable to the wavelength and the application of the Kirchhoff's laws on the overall circuit is not sufficient, since there is a propagation delay between two points of the circuit. The time-dependent phenomena along the circuit are described as a distributed-parameter network, where voltages and currents can vary in their magnitude and phase over the lengths.

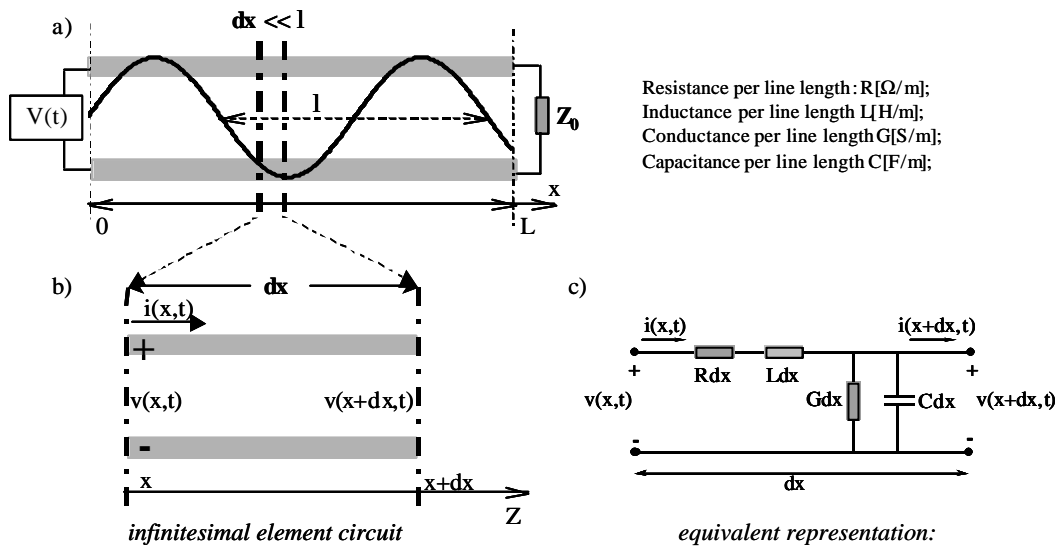


Figure 2.5:  $L \gg \lambda$

a) Transmission line of a length comparable with the wavelength; b) The infinitesimal circuit element ( $dx \ll \lambda$ ); c) The equivalent circuit of the lumped element.

The lumped circuit of a transmission line (fig.2.5) is represented by an infinitesimal element of the line characterized by  $dx \ll \lambda$  that can be solved by Kirchhoff's laws. The dielectric capacity,  $C \cdot dx$ , and the dielectric conductance,  $G \cdot dx$  define the capacitive and resistive properties of the dielectric between the two conductors represented in figure 2.5 by

(+) and (-). The resistance,  $R \cdot dx$ , and the inductance,  $L \cdot dx$ , define the conductor properties as the resistive losses, and respective the electromagnetic induction.

### 2.3.1. TELEGRAPHER EQUATIONS OF TRANSMISSION LINES

Kirchhoff's voltage and current laws applied to the equivalent lumped element circuit of infinitesimal length ( $dx \rightarrow 0$ ), which is represented in figure 2.5, lead to the time-domain form of the *transmission line, or telegrapher, equations*:

$$\begin{aligned}\frac{\partial v(x,t)}{\partial x} &= -R \cdot i(x,t) - L \frac{di(x,t)}{dt} \\ \frac{\partial i(x,t)}{\partial x} &= -G \cdot v(x,t) - C \frac{dv(x,t)}{dt}\end{aligned}\quad (2.4)$$

Considering the sinusoidal steady-state condition, with cosine-based phasors (eq.2.3), the equations 2.4 become:

$$\begin{aligned}\frac{d^2 V(x)}{dx^2} - \mathbf{g}^2 \cdot V(x) &= 0 \\ \frac{d^2 I(x)}{dx^2} - \mathbf{g}^2 \cdot I(x) &= 0\end{aligned}\quad (2.5)$$

where

$$\mathbf{g} = \mathbf{a} + j\mathbf{b} = \sqrt{(R + j\omega L)(G + j\omega C)} \quad (2.6)$$

is the complex propagation constant.

The solutions of the electromagnetic wave equations 2.5 are:

$$\begin{aligned}V(x) &= V_0^+ e^{-\mathbf{g}x} + V_0^- e^{\mathbf{g}x} \\ I(x) &= \frac{V_0^+}{Z_0} e^{-\mathbf{g}x} - \frac{V_0^-}{Z_0} e^{\mathbf{g}x}\end{aligned}\quad (2.7)$$

where the  $e^{-\mathbf{g}x}$  term represents wave propagation in the positive  $x$ -direction; the  $e^{\mathbf{g}x}$  term, stands for the wave propagation in the negative  $x$ -direction, and  $Z_0$  represents *the characteristic impedance* of the transmission line that is defined as:

$$Z_0 = \frac{V_0^+}{I_0^+} = -\frac{V_0^-}{I_0^-} = \sqrt{\frac{R + j\omega L}{G + j\omega C}} \quad (2.8)$$

The *characteristic impedance* (eq. 2.8) is a complex variable that is linked to the voltage and current phase-changes introduced in the circuit by the inductive ( $Ldx$ ) and capacitive ( $Cdx$ ) elements. In the case of real transmission lines, the characteristic impedance value

depends also on the line series resistance ( $R$ ) and on the shunt conductance ( $G$ ) of the dielectric medium between the line and the ground plane. In this case, the losses introduced by the Joule effect in the conductor line and by the conduction in the dielectric have to be considered for the evaluation of the characteristic impedance. In several practical cases, the transmission line losses can be neglected ( $R = G = 0$ ) resulting in a simplification of the above results. In this case, the characteristic impedance reduces to the frequency independent relation its value being dependent only on the values of  $L$  and  $C$ :

$$\begin{aligned} \mathbf{g} &= \mathbf{a} + j\mathbf{b} = j\mathbf{w}\sqrt{LC} \\ Z_0 &= \sqrt{\frac{L}{C}} \end{aligned} \quad (2.9)$$

Some others parameters of the wave propagation in transmission lines in the lossless case ( $R = G = 0$ ) are:

- the electromagnetic wavelength: 
$$l = \frac{2p}{b} = \frac{2p}{w\sqrt{LC}} \quad (2.10)$$

- the electromagnetic wave phase velocity: 
$$v_p = \frac{w}{b} = \frac{1}{\sqrt{LC}} \quad (2.11)$$

In practical cases, transmission lines are used to transmit electromagnetic energy to an arbitrary device, characterized by the load impedance  $Z_L$ . As a function of the values of the load impedance  $Z_L$ , three special cases of the terminated lossless transmission lines can be distinguished as described in the following.

### 2.3.2. THE TERMINATED LOSSLESS TRANSMISSION LINE

We assume that an incident wave of the form  $V_0^+ e^{-jbx}$  is applied to a transmission line at  $x < 0$  and that the line is terminated with an arbitrary load impedance  $Z_L$  as shown in figure 2.6.

In this case the characteristic impedance expressed by equation (2.8) for  $x = 0$  becomes:

$$Z_L = \frac{V(0)}{I(0)} = \frac{V_0^+ + V_0^-}{V_0^+ - V_0^-} Z_0 \quad (2.12)$$

From here the *voltage reflection coefficient* is:

$$\Gamma = \frac{V_0^-}{V_0^+} = \frac{Z_L - Z_0}{Z_L + Z_0} \quad (2.13)$$



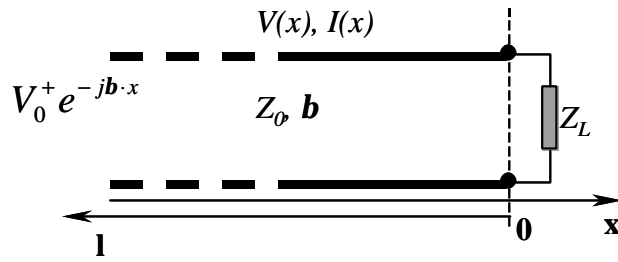


Figure 2.6:  
Transmission line terminated in a  
load impedance  $Z_L$

We consider a step voltage signal, applied on a  $Z_L$ -terminated transmission line, and different terminations. The short circuit ( $Z_L = 0$ ) determines a negative reflection of the voltage step ( $\Gamma = -1$ ). The impedance matching to the circuit ( $Z_L = 50\Omega$ ) determines no-reflection of the voltage ( $\Gamma = 0$ ). The open circuit ( $Z_L = \infty$ ) induces a positive reflection of the voltage step ( $\Gamma = +1$ ). All three cases are presented in figure 2.7. The reflection appears after a time  $t_r = D/v$  necessary for the wave to return, defined as the ratio between the total distance,  $D$ , crossed by the wave before and after reflection and the wave velocity,  $v$ .

The total voltage and current waves can be written as a function of the voltage reflection coefficient:

$$\begin{aligned} V(x) &= V_0^+ (e^{-jb x} + \Gamma e^{jb x}) \\ I(x) &= \frac{V_0^+}{Z_0} (e^{-jb x} - \Gamma e^{jb x}) \end{aligned} \quad (2.14)$$

In equations 2.14, we observe that a positive reflected voltage,  $\Gamma > 0$ , corresponds to a negative reflected current. In this context, it is important to mention that the magnetic field polarity is the same as the current polarity.

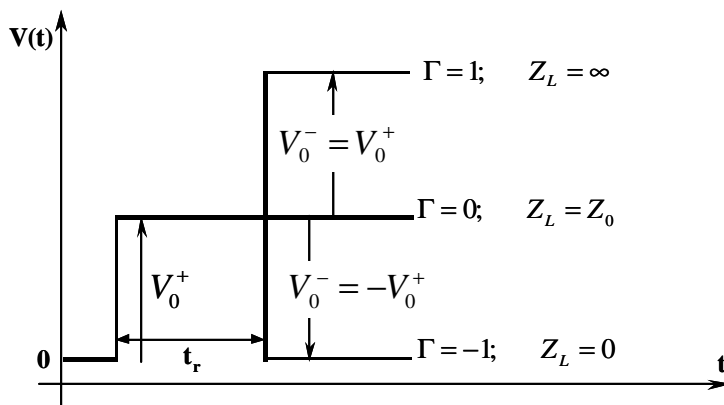


Figure 2.7:  
 $Z_L$ -terminated transmission line  
reflections

In summary, the voltage and the current are described as a sum of the incident and reflected wave giving rise to interferences. For a zero reflection ( $\Gamma = 0$  on figure 2.7), the load impedance  $Z_L$  is *matched* to the transmission line, i.e.  $Z_L = Z_0$ . In this case, there is no interference and all the incident power is absorbed by the load. If the load is mismatched to

the transmission line,  $Z_L \neq Z_0$ , only a part of the available power of the generator is delivered to the load impedance, giving rise to a reflected wave or a Reflected “Loss” (RL) which, in decibels (dB), is defined as:

$$RL(dB) = -20 \log |\Gamma| \quad (2.15)$$

In high-frequency electronics the *conventional value* for the characteristic impedance of a matched transmission line is  $Z_0 = 50\Omega$ .

### 2.3.3. SCATTERING MATRIX

In practice, a complete characterization in the frequency domain of a transmission line is realized by measuring the scattering matrix using a network analyzer (N.A.) as shown in figure 2.8. The N.A. delivers at port 1 a sinusoidal signal in a large range of frequencies and measures the transmitted power at port 2 or the reflected power at port 1. We can consider the transmission line as a “black box” which will be connected at two ports 1 and 2 as shown in figure 2.8.

Applying an incident power  $P_0$  to port 1, we obtain a standing wave composed by two waves, which propagate into the positive and the negative  $x$ -direction respectively. The transmitted power will be measured at port 2 ( $P_{12}$ ) and the reflected one at port 1 ( $P_{11}$ ). In the same way, by applying the incident power to port 2 we will measure the transmission at port 1 ( $P_{21}$ ) and the reflection at port 2 ( $P_{22}$ ).



Figure 2.8: Schematics of the two port transmission line

The scattering matrix is defined as:

$$S = \begin{bmatrix} S_{11} & S_{12} \\ S_{21} & S_{22} \end{bmatrix} \quad (2.16)$$

where the transmission parameters are<sup>1</sup>:

---

<sup>1</sup> These definitions are valid supposing that the load impedances for port 1 and port 2 are both  $Z_0$ .

$$S_{12} = \sqrt{\frac{P_{12}}{P_0}} \text{ and } S_{21} = \sqrt{\frac{P_{21}}{P_0}} \quad (2.17a)$$

and the reflection parameters are related to the parameter  $\mathbf{G}$  defined above:

$$S_{11} = \sqrt{\frac{P_{11}}{P_0}} \text{ and } S_{22} = \sqrt{\frac{P_{22}}{P_0}} \quad (2.17b)$$

For dB values of the scattering parameters, we use an equivalent expression to (2.15).

A symmetrical transmission line has a symmetrical scattering matrix. If the transmission line is perfectly matched to  $Z_0$  there will be no reflection and the scattering matrix will be equal to the identity matrix:  $\begin{bmatrix} 1 & 0 \\ 0 & 1 \end{bmatrix}$ . A lossless transmission line is characterized by:

$$S_{11}^2 + S_{12}^2 = S_{21}^2 + S_{22}^2 = 1 \quad (2.18)$$

#### 2.3.4. TYPES OF TRANSMISSION LINE: STRIPLINES, MICRO-STRIPLINES, WAVEGUIDES

As a function of the ground plane geometry with respect to the centerline of a transmission line, one can distinguish between several transmission line types. The coaxial cable represents the ideal transmission line where the ground plane surrounds perfectly the center-conductor of the cable. In practical cases, one uses cuts of the coaxial cable for which electromagnetic field configurations are shown in figure 2.9. In each case, approximate analytical equations can be obtained in order to estimate the distribution of the vectors  $\vec{E}$  and  $\vec{H}$ , and implicitly the electromagnetic wave propagation conditions [Pozar1998, Gupta1996].

The coplanar wave-guide, grounded or not, is obtained by a horizontal cut of the coaxial cable. A planar conductor line placed between two horizontal metallic planes (the ground plane) represents the Coplanar Wave-Guide (CPW). Another metallic plane placed at a certain distance under the wave-guide, transforms it in a Grounded Coplanar Wave-Guide (GCPW). A vertical cut of a coaxial cable determines the Strip-Line (SL) and the Micro-Strip-Line (MS). In all cases, a planar conductor line is placed at a certain distance with respect to the ground plane. In addition, the SL contains one more ground plane fixed above the conductor line.

Transmission lines of micron-sized dimensions are necessary in memory devices, which are usually patterned by lithographical techniques. The transmission lines presented in figure

2.9 have advantages and disadvantages with respect to (i) the facility of the patterning process, (ii) the possibility of integrating them in electronic devices, and (iii) the field homogeneities.

One of the advantages of MS lines or CPW with respect to SL is their planar geometry. Photolithographic processes in a single step can easily pattern them, while a stripline would demand a minimum of two-steps.

One of the disadvantages of MS with respect to CPW is that, in a MS, the distance between the two conductors is fixed as determined by the dielectric layer thickness, while in CPW, the gap between the centerline and the ground plane can be varied, leaving the possibility to match the transmission line over all its length. For electronic devices the MS are preferred over CPW because of their reduced surface. In our experiment, this is not important since we use one single device to realize the measurement and, for the moment, we are not interested in the increase of the density of such devices on a wafer.

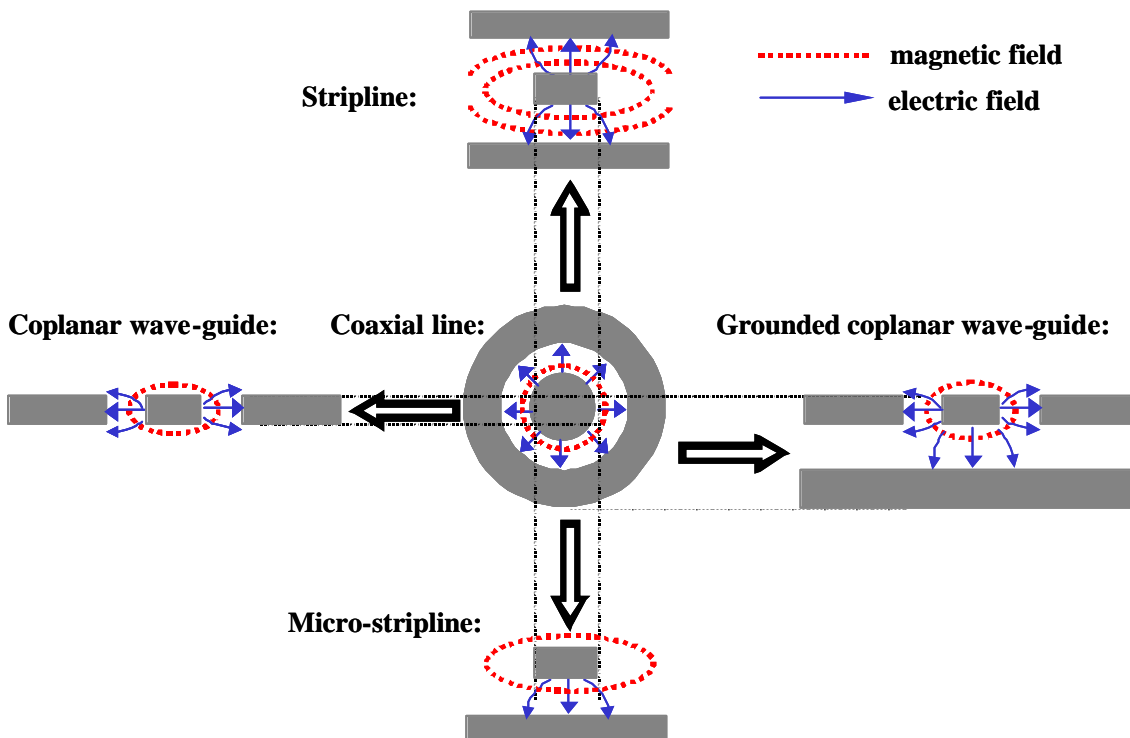


*Figure 2.9:*  
Transmission line examples:  
striplines, micro-striplines, coplanar and grounded coplanar wave-guides

## 2.4. EXPERIMENTAL SOLUTIONS FOR THE PUMP

Section 2.3 presented the theoretical aspects of the transmission line theory and the advantages and disadvantages of different geometries. In the following, we present the experimental realization of the transmission line, which is a compromise of the equipment available, and the ideal requirements from the theory.

Firstly, we detail the characteristics of the electric pulse delivered by a commercial pulse generator. Secondly, we present estimations on the magnetic field and electric resistance values for rectangular conductor lines. Thirdly, we present the transmission line design and characterization focusing on the choices of the substrate material, the metallic material as well as the geometric shape.

### 2.4.1. VOLTAGE PULSE CHARACTERISTICS

The pump consists of the pulsed magnetic field created around a  $50\Omega$ -matched coplanar wave-guide, into which voltage pulses are delivered by a commercial pulse generator. Two pulse generators were available, at the beginning of my thesis: the model 10060 delivered by Picosecond Pulse Labs and the model Avtech. The most important parameters for the incident pulse are its rise-time, pulse width, pulse amplitude, and the pulse shape quality (small overshoots amplitudes).

#### Rise-time

The rise-time is defined by the time interval when the pulse amplitude varies between 10% and 90% from its maximum value. These values determine the maximum frequencies that are induced in the magnetic system that is measured. Since the characteristic frequencies of the magnetization oscillations to be studied are in the 1-10GHz range, rise-times smaller than 100ps, are needed.

#### Width and amplitude

The pulse width and amplitude have to be variable (from 100ps to 10ns and respective from 1mV to larger than 10V) to study different processes characterized by different characteristic times (e.g. for the relaxation processes in the ns time scale) and to control the oscillations induced in the magnetic system.

### Overshoot and the oscillations just after the pulse rise-time

The overshoot (positive voltage peak that appears just after the pulse rise-time) and the voltage oscillations that follow it are represented on figure 2.10. In order to minimize parasitic effects on the magnetic response, it is desirable to keep the overshoots smaller than 5% from the maximum pulse amplitude. The presence of the overshoots on the incident pulse creates supplementary oscillations of the magnetization that superpose on the magnetization oscillations due to the pulse rise-time.

### Trigger

Further requirements concern the pulse generator trigger. The internal and external triggers are used in the stroboscopic measurement (*internal* when the pulse generator trigger dictates the trigger of an other apparatus, and, *external* when the pulse generator is triggered by one of the other apparatus). The manual trigger is useful in quasi-static measurements when we are interested in the magnetic state of the sample after one single magnetic field pulse. The pulse repetition rate should be adjustable between 1Hz and some hundreds of kHz.

The pulses delivered by the Avtech pulse generator have as properties: amplitude variable between 0 and 20V, pulse width between 0.3 and 2ns, rise-time and fall-time in 100/200 ps range, and jitter<sup>2</sup> of  $\pm 15$ ps. These parameters were not satisfying for our purposes.

For our study we have chosen the PICOSECOND PULSE LABS PULSE GENERATOR MODEL 10060A with parameters of 55ps rise-time, 100ps – 10ns pulse width, 10V maximum amplitude and overshoots smaller than 5%. The trigger repetition rate for this model can be varied from 1Hz to 100kHz.

The high-frequency magnetic responses and the pulses delivered by the Picosecond Pulse Labs pulse generator were visualized on a high frequency oscilloscope fabricated by Agilent. The oscilloscope parameters are: 20GHz bandwidth, maximum noise smaller than 1mVrms, and vertical resolution of 12bits (15 with averaging).

In figure 2.10, we present the incident voltage pulses of 2ns width, 55ps rise-time and 0.15V amplitude delivered by Picosecond Pulse Labs pulse generator model 10060A, measured on the 20-GHz bandwidth Agilent oscilloscope.

---

<sup>2</sup> The jitter of the pulse generator characterizes the probability to deliver a pulse at the moment  $T_0$ , which is fixed by the trigger. A jitter of  $\pm 15$ ps means that there is a non-zero probability to have pulses delivered at  $(T_0 \pm 15$ ps).

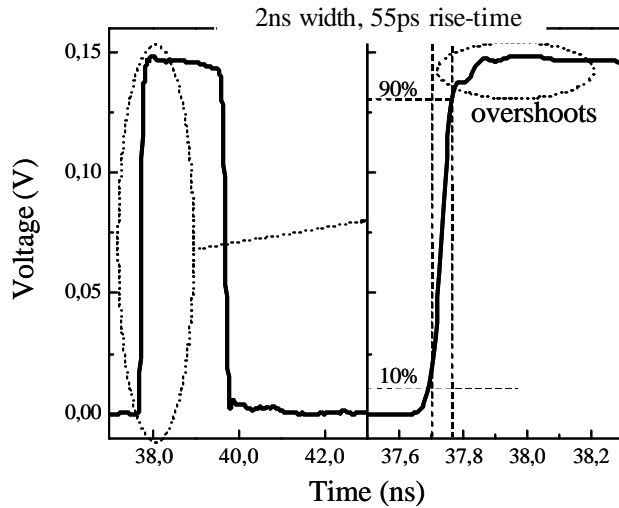


Figure 2.10:  
Voltage pulse of 2ns duration,  
55ps rise-time and 0.15V  
amplitude visualized on a  
20GHz oscilloscope

### 2.4.2. RECTANGULAR MICRO-STRIPLINE

For pulse amplitudes of voltage  $U$ , the current value in a line of resistance  $R$  is equal to  $U/R$ . The current that traverses the line determines the amplitude of the magnetic field pulse obtained around the line ( $B \sim I$ ). Both the magnetic field and the electrical resistance vary as a function of the conductor line dimensions. In the following, we discuss the dependence of both the magnetic field and electrical resistance on the width, length, and thickness of a conductor line of rectangular section.

#### Magnetic fields calculation

We use the Biot-Savart law:

$$\vec{B}(\vec{r}) = \nabla_{\vec{r}} \times \vec{A} = \frac{\mu_0 J}{4\pi} \int_{V'} (\nabla_{\vec{r}} \times \vec{i}) \frac{d\vec{r}'}{|\vec{r} - \vec{r}'|} \quad (2.19)$$

to calculate magnetic field values in different points defined by the vector  $\vec{r}$ , induced by the constant current density,  $J$ , that goes through the conductor line of rectangular section defined by the vector  $\vec{r}'$ . The vector  $\vec{A}$  represents the vector potential associated to the magnetic induction  $\vec{B}$ . The details concerning the analytical calculus are presented in annexe 1.

The magnetic field vectors are represented in figure 2.11 as a function of the coordinates  $y$  and  $z$  parallel to the conductor width and thickness, respectively. Different field amplitudes are represented with different colors. The magnetic fields were calculated at a distance of 77.5 nm with respect to the surface of the conductor line of 275 nm thickness (fig.2.11 a, b, c,

and f) for a 66 mA current value<sup>3</sup>. Three values for the line width ( $2\text{ }\mu\text{m}$ ,  $5\text{ }\mu\text{m}$  and  $10\text{ }\mu\text{m}$ ) were considered. Increasing five times the width from  $2\text{ }\mu\text{m}$  up to  $10\text{ }\mu\text{m}$ , we observe a decrease of the magnetic field values by 4.3 times (from about 182 Oe down to 42 Oe in the middle of the line where  $y = 0$ ). Large magnetic fields (180 Oe – 190 Oe) are obtained for very reduced widths of the conductor line ( $2\text{ }\mu\text{m}$ ).

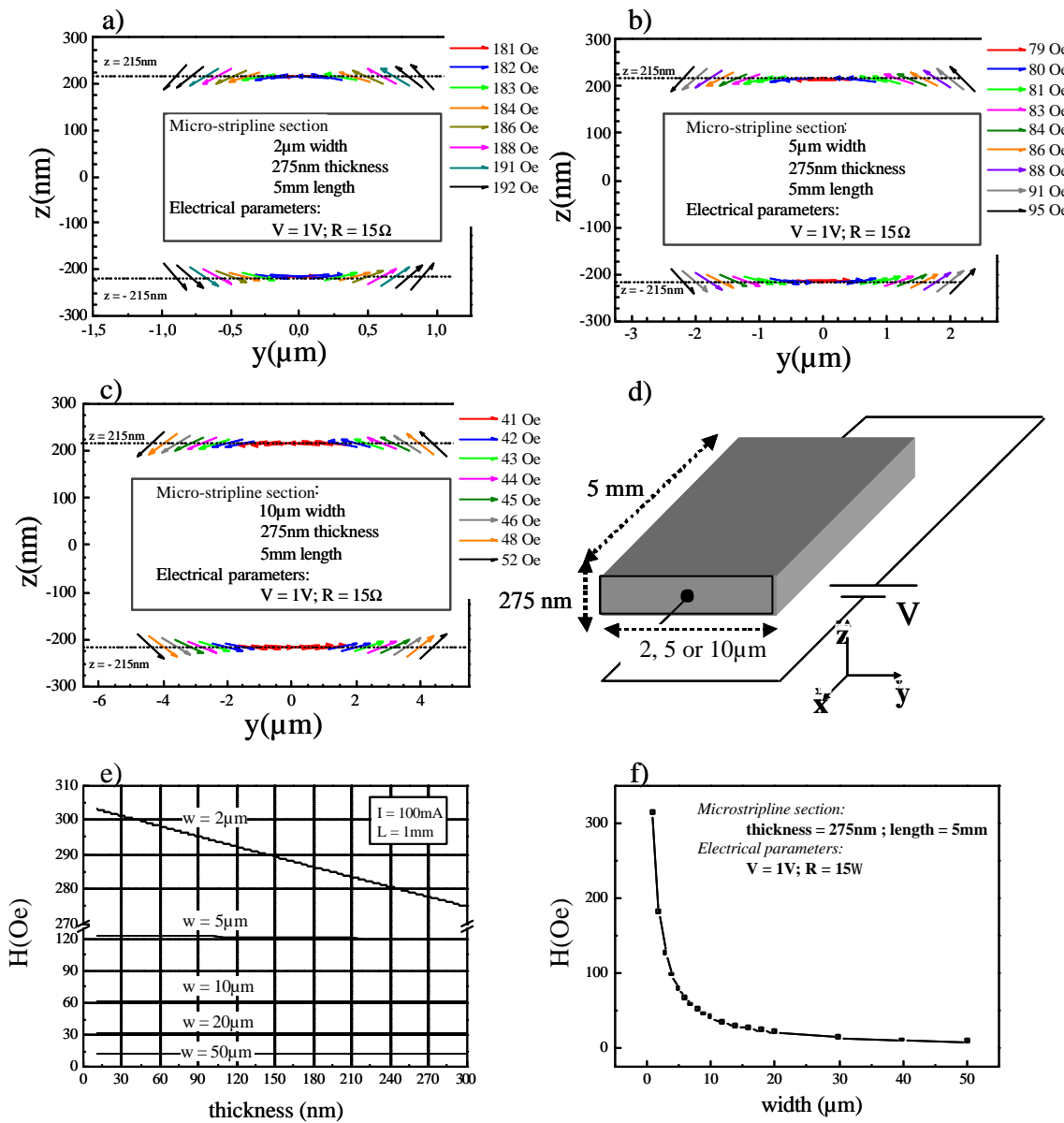


Figure 2.11:

Magnetic field configuration for different values of the line widths:  $2\text{ }\mu\text{m}$  (a),  $5\text{ }\mu\text{m}$  (b), and  $10\text{ }\mu\text{m}$  (c) for a rectangular conductor line (d). Magnetic field values as a function of the line thickness (e) and width (f)

<sup>3</sup> The magnetic field calculations were realized in the absence of a ground plane near the stripline.



As we can see in figure 2.11e, the field is quasi-independent of the line thickness for widths larger than  $5\mu\text{m}$ . Smaller values of the line width ( $2\mu\text{m}$ ) determine a strong decrease of the field values, upon increasing the line thickness. In figure 2.11e, the field calculation was realized for a current value of 100 mA.

In conclusion, the magnetic field decreases by increasing the conductor line width and increasing thickness. Hence, relatively small sections of the conductor lines are required in order to obtain magnetic fields larger than for example the internal magnetic fields of a few tens of Oe. This leads to the condition of:

$$w < 50 \mu\text{m} \quad (2.20)$$

Here we have to mention that conductor line widths of  $50 \mu\text{m}$  were used in the dynamic measurements obtaining magnetic field amplitudes about 25 Oe for maximum amplitude of the voltage pulse of 10V. This value was large enough to observe the magnetization reversal by precession in a sample characterized by an anisotropy field about 20Oe but higher order excitations require larger magnetic fields.

### Electrical resistance

From the transmission line theory (section 2.3), the transmission of the electromagnetic wave is optimum for small values of the line resistance. Ideally, the resistance should be neglected but, in the real case, it has to be minimized. The electrical resistance of the line is directly proportional to the metal resistivity,  $r$ , (e.g.  $r_{Cu} = 1.7E-8 \text{ } \Omega\text{m}$ ), and the line length,  $L$ , and is inversely proportional to the line width,  $w$ , and thickness,  $t$ :

$$R[\Omega] = r \frac{L}{w \cdot t} \quad (2.21)$$

We observe that to decrease the resistance value the thickness,  $t$ , and the width,  $w$ , should be increased. Figure 2.12 presents the electrical resistance values as a function of the conductor thickness,  $t$ , and the width,  $w$ . We observe that resistance values smaller than  $15\Omega$  (for which the line is considered lossless in a first approximation) are obtained for:

$$\begin{aligned} w &= 50\mu\text{m}; & t &> 30\text{nm}; \\ w &= 20\mu\text{m}; & t &> 70\text{nm}; \\ w &= 10\mu\text{m}; & t &> 150\text{nm}; \\ \mathbf{w} &= \mathbf{5\mu\text{m}}; & \mathbf{t} &> \mathbf{270\text{nm}}; \\ \mathbf{w} &= \mathbf{2\mu\text{m}}; & \mathbf{t} &\gg \mathbf{300\text{nm}}; \end{aligned} \quad (2.22)$$

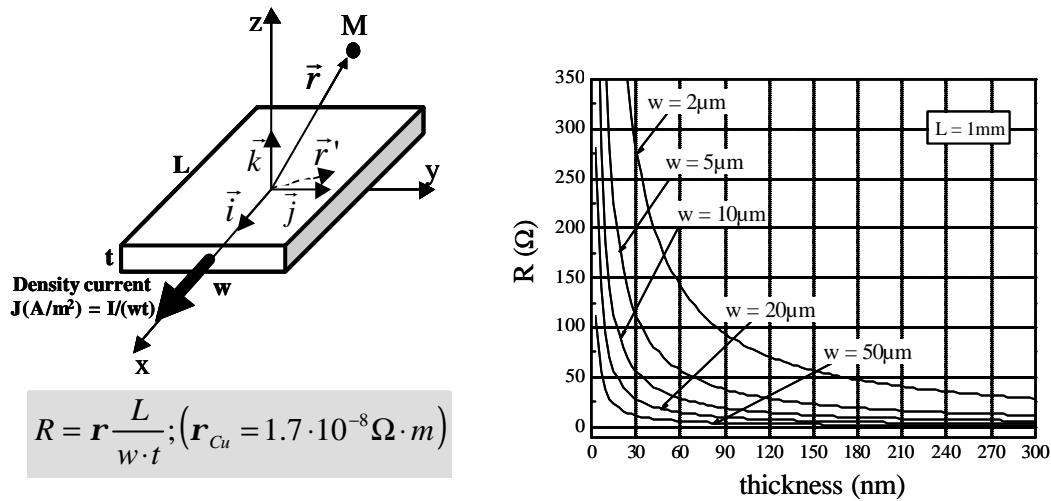


Figure 2.12:

Resistance values for a rectangular conductor line as a function of the line thickness and width

In conclusion, we observe that the conditions 2.21 and 2.22 are opposed and the experimental solution should contain a compromise between them. Comparing figure 2.11, and 2.12, we observe that for metallic layer thickness values between 10 nm and 300 nm and width between 2  $\mu\text{m}$  up to 50  $\mu\text{m}$  the magnetic field values vary between the 10 Oe up to 305 Oe. Increasing the layer thickness, in order to minimize the resistance, the field values decreases. For our purposes – the magnetization dynamics study in samples characterized by internal fields in the range of 30-300 Oe, magnetic fields of 100 Oe are sufficiently high. Thus, acceptable resistance values ( $\sim 15\Omega$ ) are obtained for layer thickness larger than 250 nm. In this interval, the values of the magnetic field are smaller than 280 Oe.

In this work, the metallic layer thickness was chosen to be 275nm, while the widths varied between 10 $\mu\text{m}$  and 50 $\mu\text{m}$  over a length of 5mm for realizing the transmission lines for the magnetization dynamic study.

### 2.4.3. THE SIGNIFICATION OF 3dB ATTENUATION LIMIT

Once a transmission line is realized, its properties can be characterized with respect to its attenuation of the transmitted power as well as to its bandwidth. The attenuation in transmission lines can be characterized both in the time and the frequency domain. The characterization of a device in the frequency domain is realized by comparing the measured transmission and reflection parameters with the 3-dB bandwidth limit.

### What is the 3dB limit?

Let us suppose a theoretical example with an electric pulse of 50ps rise-time applied on five different Devices Under Test ( $DUT_i$ ,  $i = 1,5$ ). Each device represents a frequency filter and we suppose that they attenuate differently the high frequency components of the incident pulse. This is equivalent to an increase of the rise-time values of the transmitted pulses. Figure 2.13 presents the incident pulse and the five different transmitted pulses characterized by the rise-time values: 50ps, 55ps, 60ps, 65ps, and 70ps.

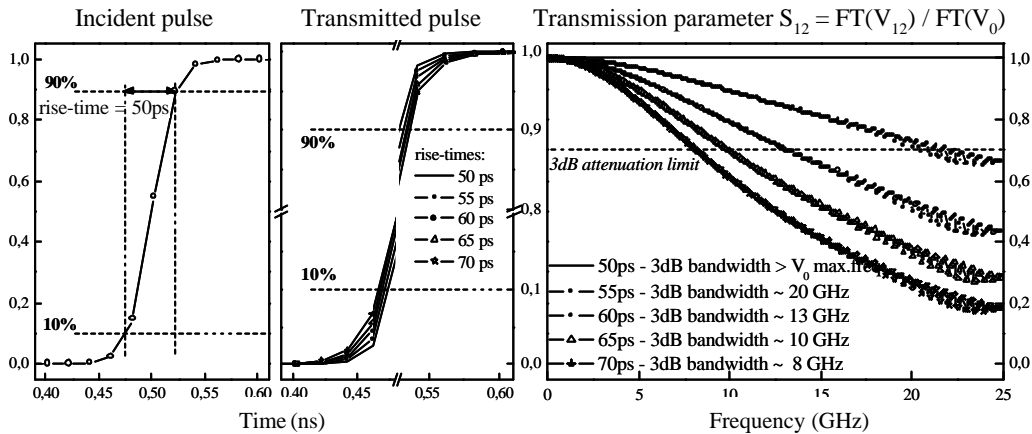


Figure 2.13:

Calculated transmission parameter supposing an incident pulse rise-time of 50ps and several transmitted pulse rise-times: 50, 55, 60, 65, 70ps

The transmission scattering parameter  $S_{12}$  is calculated as the square root of the ratio between the transmitted and the incident power (see equation 2.17). Figure 2.13 presents the parameter  $S_{12}$  that corresponds to each transmitted pulse. In the first case, the transmitted pulse rise-time of 50ps corresponds to a total transmission of the incident power and the 3dB-bandwidth of the device is larger than the maximum frequency that characterizes the incident pulse. Rise-times of 55ps, 60ps, 65ps and 70ps for the transmitted pulses, in the 2<sup>nd</sup>, 3<sup>rd</sup>, 4<sup>th</sup> and 5<sup>th</sup> cases, larger than the incident pulse rise-time of 50ps, correspond to the 3dB-bandwidths of devices around 20GHz, 13GHz, 10GHz and 8GHz, respectively.

#### 2.4.4. TRANSMISSION LINE DESIGN AND CHARACTERIZATION

##### *Transmission line design*

The first step in the transmission line preparation is the realization of their design, respecting high frequency properties and impedance matching all over the line length. For this, line dimensions, metallic material, and substrate material parameters play an important role in the value of the characteristic impedance of the line that has to be matched to  $50\Omega$ .

The geometries for two types of transmission lines: MS and CPW were estimated using the Txline [Txline], Serenade, and Ensemble software available at CRTBT/CNRS laboratory.

In both cases, the line widths, necessary to create high magnetic field pulses (see section 2.4.2), should have about tens of micrometer values. Electrical contacts, which use the bonding technique, the silver painting or high frequency contacts (as we will see in the following), need larger contact surfaces with widths about some hundreds of micrometers.

In consequence, the line width has to be varied between hundreds of micrometers in the contact regions and tens of micrometers in the center.

Variable width over the line length results in a variable impedance that may induce reflections of the incident electromagnetic wave that propagates through the transmission line [Pozar1998]. The modality chosen to match the line geometry to no-reflection transmission of the high frequency signal will be discussed in the following for two types of transmission lines: MS and CPW.

##### *The MS matching*

The MS matching can be realized by varying its width ( $w$ ) and the substrate thickness ( $h$ ) in order to obtain a characteristic impedance of  $50\Omega$ . For the same value of the thickness, larger line widths determine larger impedance values. For the MS that demand variable width dimensions over its length, the reflections minimization can be realized using an exponential dependence for the line characteristic impedance. This technique is named “taperisation” and the corresponding impedance can be written as:

$$Z = Z_0 e^{ax} \quad \text{where} \quad Z_0 = 50\Omega \quad \text{and} \quad a = \frac{1}{L} \ln \left( \frac{Z_L}{Z_0} \right) \quad (2.23)$$

In this case, we have an exponential variation of the line width over the line length that minimizes the reflections over a certain bandwidth. Figure 2.14a presents the exponential tapering for a MS of  $275\mu\text{m}$  width at the contact region and  $20\mu\text{m}$  in the middle over a length

$L$  of about 1 mm, width values for which the characteristic impedances are  $50\ \Omega$  and  $112\ \Omega$ , respectively. The dimensions were estimated using the Txline software [Txline] for 20GHz wave frequencies, for Si dielectric of  $300\ \mu\text{m}$  thickness, 11.3 dielectric constant, and 0.003 loss tangent and for Cu conductor of 275nm thickness.

Finally, the MS design was not used because of the impossibility to realize the contacts on the lower ground plane and on the line, using a SMA connector fixed on the line with silver painting.

### The CPW matching

The CPW design represents an alternative for the transmission line to use in our experiment. Even if the centerline of the CPW presents variation of the width over the line length, the advantage of the CPW with respect to the MS is that the CPW can be matched to  $50\Omega$  all over its length by choosing the correct values for the gap between the centerline and the horizontal ground plane. Figure 2.14b presents the design of the  $50\Omega$ -matched CPW. The dimensions were estimated using the Txline software [Txline] for 20GHz wave frequencies, with the following parameters: Si dielectric of  $300\mu\text{m}$  thickness, and of 12.9 dielectric constant, and a Cu conductor of 300nm thickness.

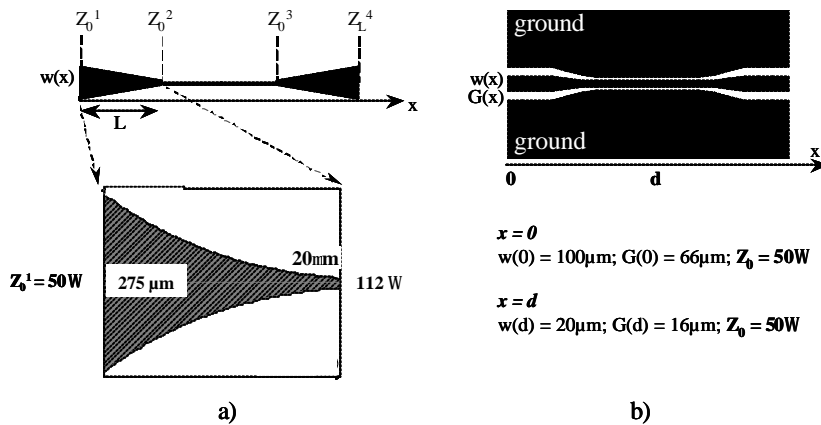


Figure 2.14:

a) Exponential tapered micro-stripline and  
 b)  $50\Omega$ -matched coplanar wave-guide

In our experiment, we have chosen the CPW as transmission line to generate the high frequency pulsed magnetic field. From an experimental point of view, this geometry was advantageous with respect to the MS because of the modality to realize the electrical contacts.

In the following, we detail this aspect by presenting some results on the characterization in the frequency and the time domain of different devices, which have been realized at the beginning of my thesis. The differences between them consists in i) the modality to realize the

electrical contacts, ii) different geometries of the transmission lines, iii) different substrates and iv) different metallic composition of the multilayers used in the patterned transmission lines.

### Frequency-domain characterization

In the frequency domain the quality of the entire device (fig.2.15), that contains the transmission line, the contacts, the connectors and the cables, is characterized by measuring its scattering matrix using the network analyzer (see section 2.3).

The first device (fig.2.15A) corresponds to a MS deposited on the top of a Si substrate of low resistivity ( $5 \Omega\text{cm}$ ) with sharp variations of the width along the line length onto which the contacts were realized by bonding. The scattering transmission parameters  $S_{12}$  or  $S_{21}$  are smaller than the 3dB limit\* and we observe very large reflections (scattering parameters:  $S_{11}$  or  $S_{22}$ ) for a large number of frequencies in the interval from 150MHz up to 20GHz. These results can be explained by the presence of abrupt variations of the MS width (from  $1000\mu\text{m}$  down to  $65\mu\text{m}$ ) that induce important reflections in our device. In this example, the contacts made by bonding are un-matched for high-frequency experiments. They behave as perturbing transmission lines in cascade with the one we want to test.

The second one (fig.2.15B) corresponds to the same MS but with contacts realized using coaxial-SMA connectors and Ag painting on the metal surface. The transmission in the line has losses less than 3dB for frequencies below 10GHz. We obtained an improvement of the transmission in this device characterized by a 3dB-bandwidth, much larger than in the first example (about 10GHz).

Besides unmatched line dimensions and contacts further criteria to consider is the substrate. The dielectric permittivity,  $\epsilon$ , and the loss tangent,  $d$  represent two parameters of importance for the electromagnetic wave propagation in transmission lines.

In the examples presented in figures 2.15A and 2.15B, the relatively important conductivity of the doped Si-substrate, equivalent to large values of the substrate loss tangent, determines dielectric losses in the electromagnetic wave transmission.

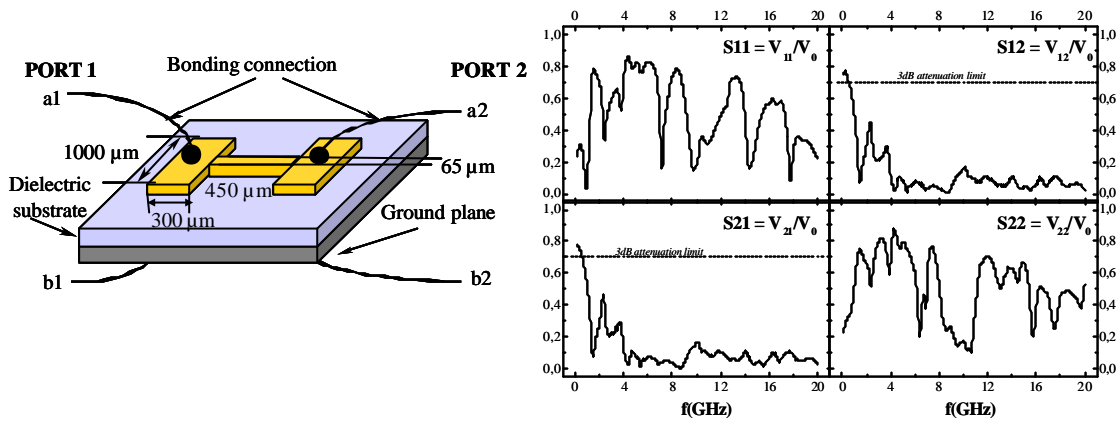
The un-doped Si is characterized by tabulated small values of the loss tangent ( $d = 10^{-3} - 3 \cdot 10^{-3}$ ) and high values for the dielectric permittivity ( $\epsilon = 11.7 - 12.9$ ), values that are of interest for lossless high-frequency experiments, as we have realized in this work. The third example (fig.2.15C) represents a  $50\Omega$ -matched CPW patterned on a Si substrate of very high

---

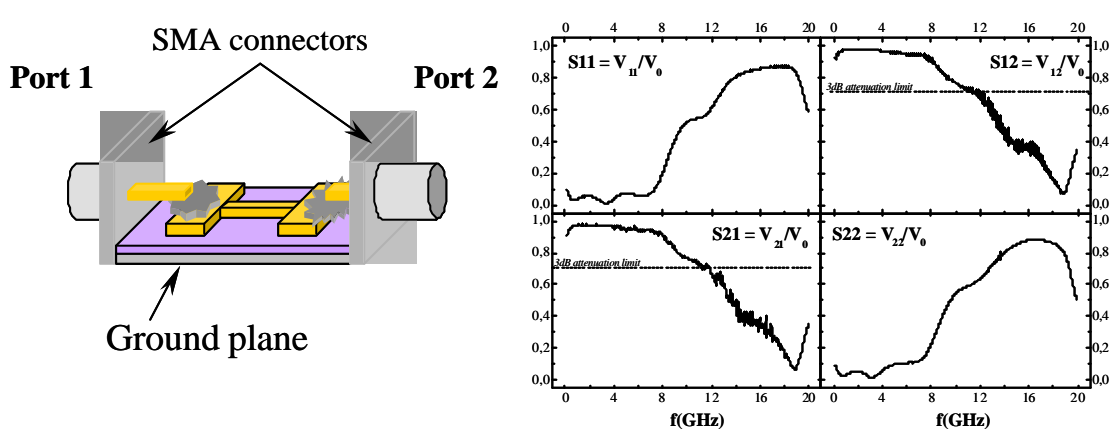
\* The 3dB attenuation corresponds to a voltage ration:  $V_{\text{Transmitted}}/V_{\text{incident}} = 0,708$ .

resistivity (between  $5E+3$  and  $1E+4 \text{ } \Omega\text{cm}$ ) onto which the electrical contacts were realized using  $50\Omega$  matched high frequency connectors. The results reveal a good transmission ( $S_{12}$  and  $S_{21} > -3\text{dB}$ ) in a large interval of frequencies (up to 20 GHz) and implicitly the reflection parameters are very reduced with respect to the previous two cases in the same frequency range.

### A) Bonding connection on the micro-stripline:



### B) Direct contact on the micro-stripline using SMA connectors:



### C) Direct contact on a coplanar wave-guide using 50W matched pico-probes connectors:

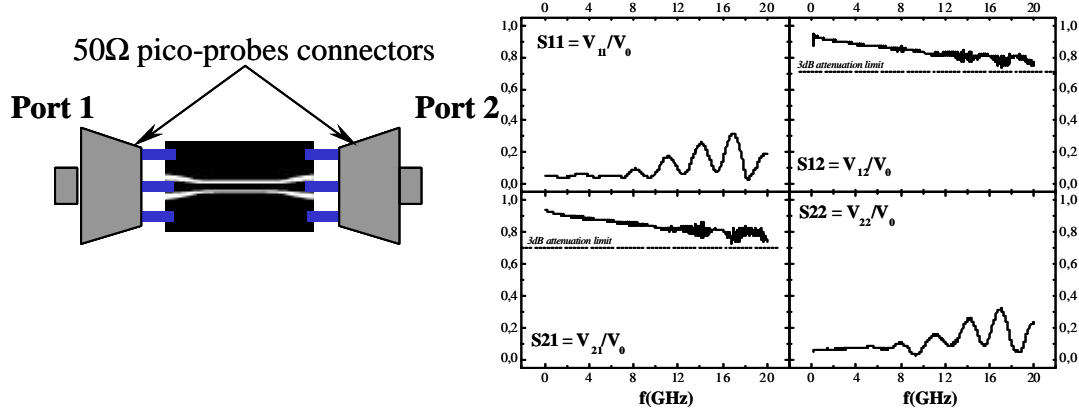


Figure 2.15:

MS and CPW frequency-domain characterization using the network analyzer

Alternatives to the Si substrates are  $\text{Al}_2\text{O}_3$  ( $d = 5 \cdot 10^{-4} - 2 \cdot 10^{-3}$ ,  $\epsilon = 9.6 - 10.1$ ), and GaAs ( $d = 5 \cdot 10^{-4} - 1 \cdot 10^{-3}$ ,  $\epsilon = 1.9$ ) [Txline].

In conclusion:

- The substrate should have good dielectric properties (high resistivity, high dielectric constant, small loss tangent);
- The entire circuit, from the source generator (network analyzer, pulse generator, oscilloscope) to the device and then the measuring apparatus (network analyzer, oscilloscope), composed by: cables, connectors, bias T, etc. has to be matched to  $50\Omega$ -impedance. This excludes from the beginning the connection types such as bonding or with silver painting, the SMA connectors and coaxial cables of reduced 3dB-bandwidth.
- The CPW has to be matched to  $50\Omega$  all over its length by adjusting the gap between the ground and the centerline. The  $50\Omega$ -matching of the MS is realized using the “taperisation” technique.
- Considering the 3dB-bandwidth values of 10GHz and 20GHz respectively, for the devices presented in figures 2.15B and respective 2.15C, the rise-time of the transmitted pulse will be equal to 65ps or respective 55ps, for an incident pulse with 50ps rise-time. The 3dB-bandwidth of the MS represented in figure 2.15A has a very small value, which means that it can be used in DC-experiments or low-frequency experiments but not in high-frequency studies.
- The disadvantage of the device presented in the figure 2.15B, are the contact quality since the contacts between the SMA connectors and the metallic surface through the silver painting are not characterized by good properties at high-frequency and their properties change from one contact to another.

Considering all the disadvantages and the advantages of the devices that have been already tested, with respect to the purpose of our study (the magnetization dynamics characterization in a high bandwidth), we have chosen the device presented in the figure 2.15C, i.e.  $50\Omega$ -matched CPW lithographically patterned on a Si-substrate of high resistivity with contacts realized directly on the line surface with  $50\Omega$ -microprobes flexible connectors.



### *High frequency connectors*

#### A) SMA connectors <sup>4</sup> (fig.2.16A)

The first characterization measurements were realized using SMA or coaxial connectors of bandwidth in the 20 GHz range. Two examples of connectors used in our experiment are presented in the figure 2.16A. These connectors were not adapted to our experiment because of the low bandwidth ( $< 10\text{GHz}$ ) of the connections between the connectors and the transmission lines. In consequence, we used the microprobes connectors, matched to high-frequency experiments, that will be described in the following.

#### B) Microprobes connectors <sup>5</sup>(fig.2.16B)

They were used to realize high-frequency measurements and their properties are:

- $50\Omega$ -impedance matching in a large bandwidth up to  $40\text{GHz}$ ;
- Three micron-sized contacts ( $50\times 50\mu\text{m}^2$ ) providing contact to the centerline and to the ground plane of the CPW;
- The distances between contacts are fixed to  $300\mu\text{m}$ ,  $200\mu\text{m}$ ,  $150\mu\text{m}$ , etc.
- The contacts are flexible;
- The connections realized with these connectors are characterized by a higher quality (high bandwidth –  $20\text{GHz}$  that determines quasi-identical pulse shapes from one experiment to another).

In order to realize good contacts the microprobes were fixed on x, y, z motion stages<sup>6</sup> characterized by micron-sized values of the displacement step, in order to realize a correct alignment between the sample contact regions and the connectors. The contact is realized by visualizing the sample with a stereoscope, and moving the connectors on vertical direction with oz-displacement stage. Figure 2.16 presents the image on a monitor of the three contacts of a microprobe aligned and contacted with the CPW. The flexibility of the microprobes is a parameter that becomes very important during the contact operation since a good contact is obtained after exerting a small pressure on the microprobes once it is in contact with the metallic surface.

---

<sup>4</sup> Fabricated by RADIOSPARE

<sup>5</sup> Fabricated by CASCADE MICROTECH

<sup>6</sup> Fabricated by MELLES GRIOT

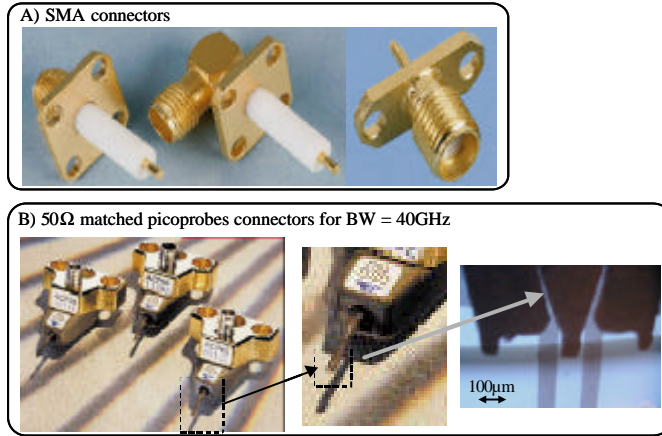


Figure 2.16

A) SMA connectors and B) Microprobes connectors (Cascade - Microtech)

### Time-domain characterization

As a final point, we compare three CPW of different metallic compositions.

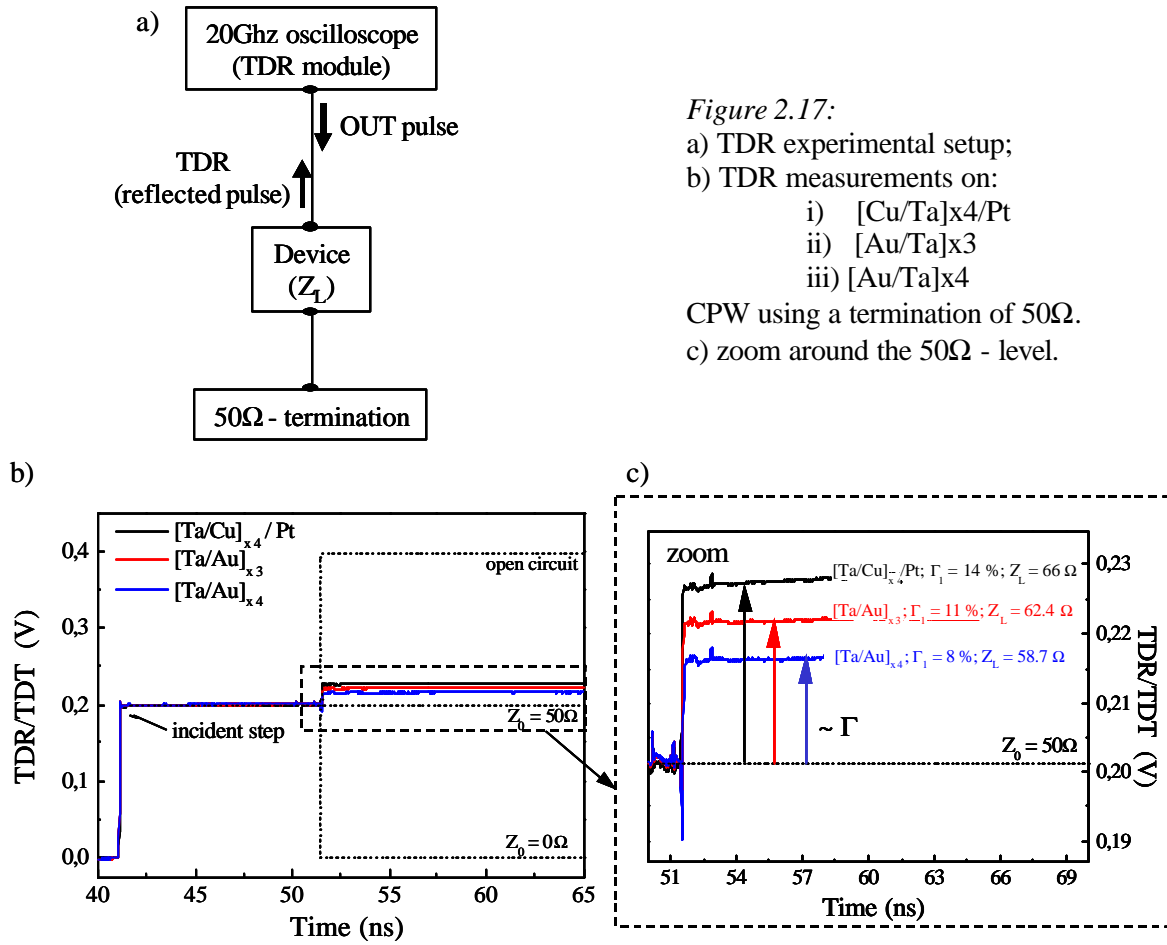
The transmitted and reflected signals measured using the time domain reflectometry (TDR) and the time domain transmission (TDT) modulus of a specific digital oscilloscope of 20GHz bandwidth, revealed informations on the device electrical resistance ( $R_D$ ) and characteristic impedance ( $Z_D$ ). Here, three types of CPW were measured, both of the same geometry, deposited on the same substrate but of different metallic composition: one with Cu and the other two with Au of two different thicknesses. The lithographically patterned CPW were composed by metallic multilayers of structures: i)[Cu/Ta]x4/Pt; ii)[Au/Ta]x3 and iii)[Au/Ta]x4. The measurements were performed using the experimental setup presented in figure 2.17a using a 50Ω termination. The role of the Ta layer is to increase the metallic layer adherence to the Si substrate. We have experimentally observed that during the contact realization on one single metallic layer of Cu, of 300nm thickness with the microprobes, the metallic layer is damaged. This is due to the poor adherence of thick metallic layers to the Si substrate. Using the Ta layer between Cu and Si substrate and dividing Cu or Au thickness in several layers ( $n^\circ$  of layers = 4, 5, ...) the line adherence was improved.

Figure 2.17b presents the TDR results obtained on three CPW that are compared to the three reference levels that correspond to the 50Ω-termination, short - or open – circuit. For a 50Ω-terminated line we observe small positive reflections from which the reflection coefficient can be estimated:

$G = 14\%$  for [Cu(50nm)/Ta(5nm)]x4/Pt(5nm) structure,

$G = 11\%$  for [Au(50nm)/Ta(5nm)]x3 structure and

$G = 8\%$  for [Au(50nm)/Ta(5nm)]x4 structure.



The centerline width values are 100μm on the contacts regions and 10μm in the center. The metallic thickness was 275nm and the gap was calculated [Txline] to match the CPW impedance to 50Ω over all the line length. The reflection coefficient is defined by equation 2.13 where  $Z_0 = 50\Omega$  and  $Z_L$  represents the device characteristic impedance. As the CPW geometry was calculated in order to have  $Z_L = \sqrt{L/C} = 50\Omega$  in the lossless approximation, the fact that  $G$  is larger than zero leads us to the conclusion that the line resistance is not negligible and the total impedance becomes larger than 50Ω. From 2.13 we deduce the formula:

$$Z_L = Z_0 \frac{1 + \Gamma}{1 - \Gamma} \quad (2.24)$$

and we obtain 66,3Ω, 62,4Ω and 58.7Ω for the characteristic impedance of [Cu(50nm)/Ta(5nm)]<sub>x4</sub>/Pt(5nm), [Au(50nm)/Ta(5nm)]<sub>x3</sub> and [Au(50nm)/Ta(5nm)]<sub>x4</sub> structure, respectively.

The characteristic impedance for a transmission line (eq.2.8), characterized by a lossless dielectric,  $G = 0$  (high resistivity Si-substrate), is expressed by:

$$Z_0 = \sqrt{\frac{R + j\omega L}{j\omega C}} \quad (2.25)$$

Increasing the resistance values,  $R$ , the impedance  $Z_0$  increases also. This explains the larger impedance of the Cu line ( $66\Omega$ ) with respect to the Au line ( $58.7\Omega$ ) since the Cu resistivity is larger than Au resistivity. A larger section of the line obtained with 4x Au-layers with respect to only 3x Au-layers determines a decrease of the electrical resistance, and in consequence, the electric losses are reduced. Nevertheless, because of the lack of Au target in the sputtering machine, during this study we used CPW composed of Cu and Ta layers.

#### 2.4.5. CONCLUSIONS

Magnetic field pulses of high frequencies can be obtained in  $50\Omega$ -matched transmission lines whose geometries are calculated using the transmission line theory and the telegrapher equations. There are four particular types of transmission lines that represent cuts from the coaxial cable: i) the stripline, ii) the micro-stripline, iii) the coplanar wave-guide, and iv) the grounded coplanar wave-guide.

The experimental devices characterization was realized in frequency- and time- domain, using the 20GHz – network analyzer and the 20GHz – oscilloscope, respectively. They revealed a large bandwidth (20GHz) and reduced reflections due to the electrical resistance of the line for  $50\Omega$  - CPW lithographically patterned on the surface of a Si-substrate of high resistivity using as contacts  $50\Omega$ -microprobes flexible connectors directly on the line surface.

The metal thickness value is chosen in order to have small resistance values and sufficiently high magnetic fields. The width was varied in the dynamic study between maximum  $50\mu\text{m}$  down to  $2\mu\text{m}$ .

As a function of the CPW termination, one ( $50\Omega$  termination) or two voltage pulses can be obtained of the same (open circuit) or opposite polarity (short circuit) (fig.2.7), which will be used for realizing different types of experiments (magnetization reversal experiments using two magnetic field pulses of the same polarity and FMR types measurements using one single magnetic field pulse).

## 2.5. THE PROBE

Time-resolved measurements of the magnetization dynamics can be realized using different probe techniques. Among them, we mention the magneto-optic Kerr and Faraday effect [Freeman1991-2000, Gerrits2002, Crawford1996-2000], magneto-resistive [Russek2000, Schumacher2002-2003] and inductive effects [Silva1999], X-ray Magnetic Circular Dichroism (XMCD) or Magnetic Linear Dichroism in the Angular Distribution (MLDAD) [Binns 2003, Bonfim2001, Back1998]. In addition to the time resolution, spatial resolution can be obtained with the magneto-optic effect or the XMCD where the optical or X-ray beam is focused onto the sample surface up to micron-sized dimensions. Furthermore, all three components of the magnetization vector can be measured using the MOKE for appropriate choice of the measurement geometry. Samples of dimensions smaller than the beam spot dimensions cannot be measured easily with these probe techniques. In these cases, we can use the magneto-resistive or inductive effects, at the cost of performing a *global* measurement of the magnetization dynamics.

During this work we have developed three probe techniques, namely, the time resolved magneto-optic Kerr effect, the magneto-resistive effect as well as the inductive technique. The theoretical background and the experimental setup of the three types of probes are described in the next sections.

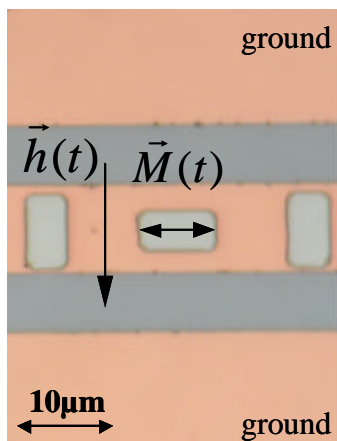


Figure 2.18:  
Magnetic samples  $(4 \times 8)\mu\text{m}^2$  lithographically  
patterned on the centerline of a coplanar wave-guide

The device consisted of the CPW (the pump line) to induce the excitation field  $\vec{h}(t)$ , and the magnetic sample patterned on top of the pump line, characterized by the magnetization  $\vec{M}(t)$  (see sample preparation in chapter 3). Figure 2.18 presents  $4 \times 8\mu\text{m}^2$  magnetic samples on top of the centerline of the CPW of  $10\mu\text{m}$  width.

### 2.5.1. THE MAGNETO-OPTIC PROBE

The magneto-optic probe uses the interaction between the electric field of a laser beam,  $\vec{E}$ , incident on the magnetic sample and the electrons of the sample which feel the sample magnetization,  $\vec{M}$  via the spin-orbit interaction. Among the magneto-optic effects, we mention Faraday, Kerr, and Voigt effects. They will be discussed in the following but we will focus on the Magneto-Optic Kerr Effect (MOKE) that will be used as magneto-optic probe in the dynamic experiments.

#### 2.5.1.1. MAGNETO – OPTICAL EFFECTS

The non-symmetric binding of the outermost electrons of their constitutive ions causes optical anisotropy in crystals. As a result, the electron displacements, under the action of the harmonic electric field of a light wave,  $\vec{E}(\vec{r}, t)$ , depends on the field direction, as given by the permittivity tensor,  $\overline{\overline{\epsilon}}_r$ . When a magnetic induction,  $\vec{B}$ , is applied to an isotropic dielectric, the medium becomes electrically anisotropic for electromagnetic waves, giving rise to so-called magneto-optical effects. An appropriate expression of the tensor  $\overline{\overline{\epsilon}}_r$  can be derived in a molecular approach, by considering the motion of bound electrons in the presence of both a harmonic field,  $\vec{E}(\vec{r}, t) = \vec{E}e^{-i\omega t}$  and a static field  $\vec{B}$ , as described by the Lorentz force law. [Palmer1996] (see Annexe 6).

As a function of the orientation of the light propagation,  $\vec{k}_{incident}$  with respect to the magnetic induction,  $\vec{B}$  one distinguishes between two magneto-optical effects:

- a) *The Faraday rotation* for  $\vec{k}_{incident} \parallel \vec{H}_e$  (fig.2.19a);
- b) *The Cotton-Mouton or Voigt effect* for  $\vec{k}_{incident} \perp \vec{H}_e$  (fig.2.19b).

#### *Faraday effect*

This effect corresponds to a circular birefringence in an isotropic dielectric by a magnetic field along the direction of propagation  $\vec{k}_{incident} \parallel \vec{H}_e$  [Palmer1996, Vonsovskii1974]. This phenomenon is defined by two different refraction indices ( $n^+$  and  $n^-$ ) for right- respectively left- circularly polarized light. For a given direction of the external magnetic field  $\vec{H}_e$ , a variation of the sign of  $\vec{k}$  (propagation vector) will reverse the sense of

rotation of the incident wave polarization (clockwise  $\Leftrightarrow$  counterclockwise). The relation between the Faraday rotation angle  $q_F$  and the magnetic field intensity  $H_e$ , was established experimentally by Faraday in 1846 and can be written in the form:

$$q_F = R_V H_e l \propto (n^+ - n^-) \quad (2.26)$$

where  $R_V$  is known as the Verdet constant and  $l$  is the medium length. The Faraday rotation is a linear effect in the field  $H_e$ , with a constant of proportionality given by Verdet constant.

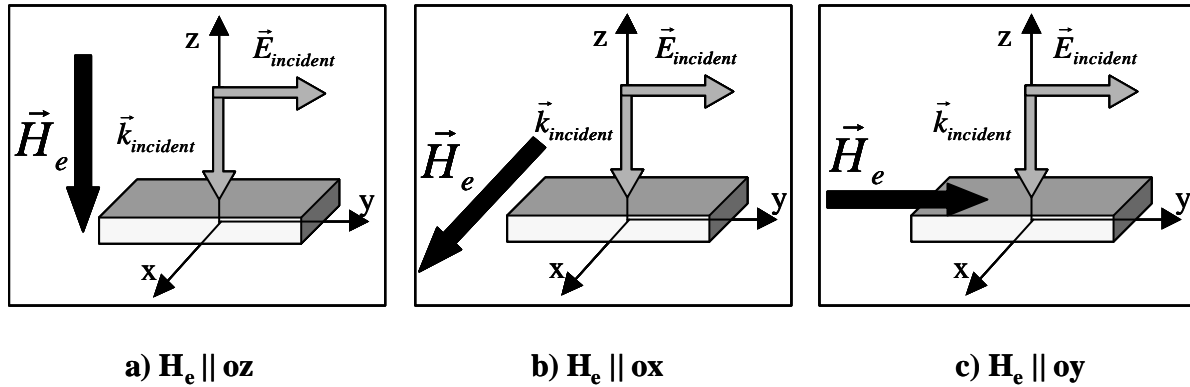


Figure 2.19:

Faraday effect (a) and Cotton-Mouton or Voigt effect (extra-ordinary refraction – b – and ordinary refraction – c)

### The Cotton – Mouton or Voigt effect

This effect corresponds to the linear magnetic birefringence of an incident light that traverses a medium that behaves as a biaxial crystal if it is placed in an external magnetic field perpendicular to the light propagation direction.

If the magnetic field is perpendicular to the wave propagation direction, the medium is characterized by two refraction indices named: *the ordinary* ( $n_o$ ) and *the extraordinary* ( $n_e$ ) refraction indices. The two refraction indices determine two refracted beams: *the ordinary beam* that corresponds to the electric vector of the wave parallel to the external magnetic field,  $\vec{E}_{wave} \parallel \vec{H}_e$ , and *the extraordinary beam* when the two vectors are perpendicular to each other,  $\vec{E}_{wave} \perp \vec{H}_e$ . This phenomenon is known as *the linear magnetic birefringence*. The difference between the phases of the two beams can be expressed empirically as:

$$\Delta = (n_o - n_e) \frac{\omega}{2pc} l = A_{CM} H_e l \quad (2.27)$$

where  $\omega$  is the light frequency,  $A_{CM}$  is the Cotton – Mouton constant and  $l$  is the medium length. In general, this constant is a function of the nature of the substance, the light wavelength, and the temperature [Vonsovskii1974]. This effect is smaller compared to the

Faraday rotation and its measurement requires magnetic inductions of the order of a few *Tesla* [Palmer1996].

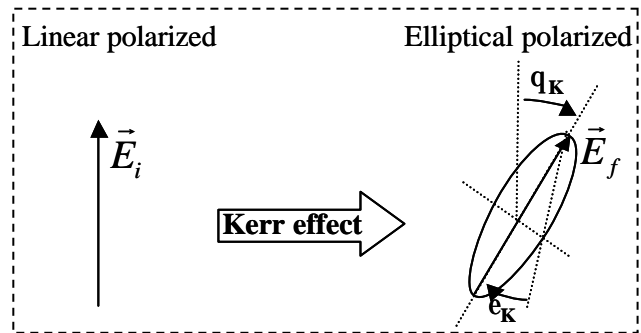
Similar effects are observed in the reflection of electromagnetic wave on the ferromagnetic metallic surfaces. They correspond to the Magneto-Optical Kerr Effect (MOKE) which will be detailed in the following.

### *The Kerr effect*

The Magneto-Optical Kerr Effect (MOKE) consists in a non-zero rotation angle ( $q_K$ ) or ellipticity ( $e_K$ ) of the electric vector of a linearly polarized light after its reflection from magnetic and non-magnetic sample surfaces.

In ferromagnetic metals, the interaction between the vector  $\vec{E}$  of the incident electromagnetic wave and the electrons can qualitatively be described as a linear oscillating motion of the electrons due to the electric field  $\vec{E}$ , and a superposed perpendicular oscillating motion due to the Lorentz force induced by the magnetization,  $\vec{M}$ , of the magnetic medium. The result of this interaction is a rotation of the initial polarization which transforms the *linearly polarized* wave into an *elliptically polarized* wave. The Kerr rotation has a complex value and is defined as:

$$\tilde{q}_K = q_K + j e_K \quad (2.28)$$



Typical values of the real part of the Kerr rotation,  $q_K$ , are e.g. for Fe  $q_K^{NiFe}(30^\circ C) = 0.013\text{deg}$  and for Co  $q_K^{Co}(30^\circ C) = -0.016\text{deg}$  [Kim2002]<sup>1</sup>. Typical values for the imaginary part (ellipticity  $e_K$ ) of the Kerr rotation are e.g.  $e_K^{NiFe}(30^\circ C) = 0.010\text{deg}$  and  $e_K^{Co}(30^\circ C) = 0.088\text{deg}$  [Kim 2002]<sup>1</sup>.

<sup>1</sup> Measurement configuration is specified in the reference: [Lee2000]



The Kerr effect is a linear magneto-optic effect, i.e. the rotation of the light polarization is linearly proportional to the magnetization value ( $q_K \sim M$ ). The interaction of the electromagnetic wave with the magnetic medium is described by the wave equation [Atkinson]:

$$\Delta \vec{E}(\vec{r}, \mathbf{w}) - \nabla^2 \vec{E}(\vec{r}, \mathbf{w}) = k_0^2 \hat{\epsilon}(\mathbf{w}) \vec{E}(\vec{r}, \mathbf{w}) \quad (2.29)$$

where  $\vec{E}(\vec{r}, \mathbf{w})$  represents the electric field vector,  $k_0$  the wave vector amplitude and  $\hat{\epsilon}(\mathbf{w})$  the electrostatic permittivity tensor corresponding to the magnetic medium. The permittivity tensor is written as a function of the complex refractive index  $n$ , the complex Voigt constant  $Q$  and of the magnetization components  $m_1$ ,  $m_2$  and  $m_3$ , as:

$$\hat{\epsilon}(\mathbf{w}) = n^2 \begin{bmatrix} 1 & -im_3Q & im_2Q \\ im_3Q & 1 & -im_1Q \\ -im_2Q & im_1Q & 1 \end{bmatrix}, \quad n = n(\mathbf{w}), \quad Q = Q(\mathbf{w}, M_s) \quad (2.30)$$

The Kerr effect is used to study the surface magnetization (more exactly from the sample surface down to approximately 30nm depth) of ferromagnetic materials since it is obtained by reflection on metallic samples.

In a MOKE experiment, superposed to the Kerr effect may occur the Faraday or the Voigt effect. The Faraday effect appears when the light passes transparent media of the experimental setup (lenses or glass substrates), which are submitted to a magnetic field. The Faraday rotation,  $q_{Faraday}$ , adds to the total angle of rotation. In the MOKE measurements, where one measures the intensities corresponding to the electric fields of the wave ( $I = E \cdot E^*$ ), the Faraday effect appears as a parabolic dependence of  $I$  as a function of the external field,  $H_e$  for high magnetic fields.

Details on the experimental configurations used in MOKE measurements, are described in the following sections.

### 2.5.1.2. MAGNETO-OPTICAL KERR EFFECT

#### *Experimental Kerr configurations*

One distinguishes three different experimental Kerr configurations, *polar*, *longitudinal* and *transversal*, as shown in figure 2.20:

- i) In the *polar configuration*, one measures the magnetization component parallel to the plane of incidence and perpendicular to the magnetic film surface.
- ii) The *longitudinal configuration* is generally used to measure the magnetization component parallel to the plane of incidence and oriented in the plane of the magnetic film.
- iii) In the *transversal configuration*, we are mostly sensitive to the magnetization component perpendicular to the plane of incidence and oriented in the plane of the magnetic film.

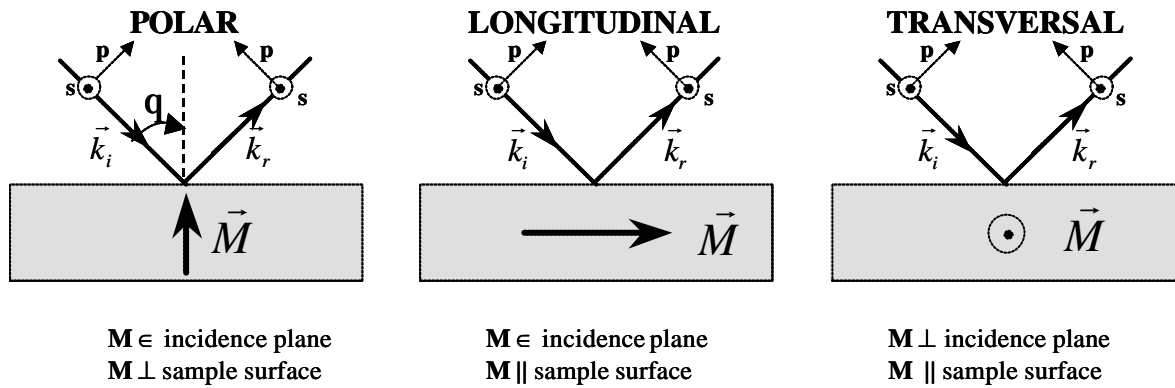


Figure 2.20:  
MOKE experimental configurations: *polar*, *longitudinal*, and *transversal*

The electric vector,  $\vec{E}$ , is decomposed into two orthogonal basic components  $E_p$  and  $E_s$ , which are perpendicular to the wave-vector,  $\vec{k}$ . The  $E_p$ -component is parallel to the plane of incidence, while the  $E_s$ -component is perpendicular to the plane of incidence (fig. 2.20). Thus, the vector  $\vec{E}$  is written as:

$$\vec{E} = \begin{bmatrix} E_p \\ E_s \end{bmatrix} \quad (2.31)$$

The Kerr rotation and ellipticity are defined as a function of the electric field components defined in the  $E_P$ - $E_S$  coordinate system [Atkinson]. Several experimental configurations have been used to measure the magnetization components or the Kerr rotation. All of them have been deduced from the calculations of the electric field components parallel to  $E_P$  and  $E_S$ . In the following, we present the schematics of a basic MOKE experiment.

### *Schematics of a MOKE experiment*

The experimental MOKE setup used in our experiment is presented in figure 2.21. For the light source, a laser is used since it is characterized by a *coherent* and a *monochromatic* light emission. The polarizer is used to obtain an incident linearly polarized light that is focused on the sample with a lens (fig.2.21). After the reflection from the magnetic sample, the divergent beam is focused by a second lens onto the analyzer, which “analyzes” the reflected beam by separating its  $P$  and  $S$  components. The detector is represented by one or several photodiodes that are sensitive to the light wavelength. In special experimental situations that will be detailed in section 2.5.1.3. and 2.5.1.4, a half-wave plate is inserted between the second lens and the analyzer.

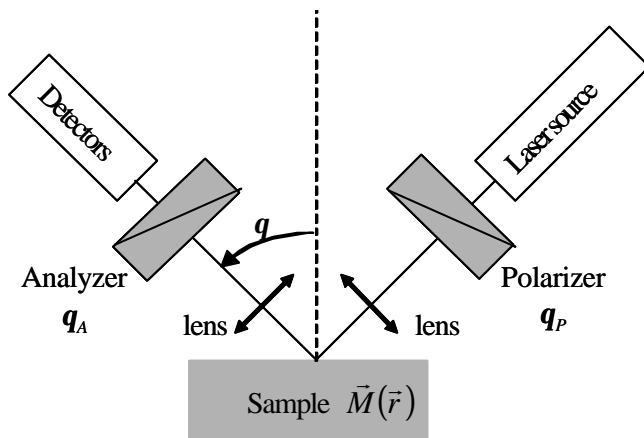


Figure 2.21  
MOKE general schematics

The intensity of the light measured by the detectors is equal to the square of the modulus of the complex value of the wave electric vector  $E$ :

$$I = |E|^2 = E \cdot E^* \quad (2.32)$$

where  $E^*$  is the conjugate of the electric field,  $E$ .

The calculation of the electric vector after the interaction of the light with the optical components, the polarizer, the lenses, the magnetic sample, the analyzer and eventually the half-wave plate is realized using the Jones matrix formalism.

### Jones matrix formalism

A formalism that calculates the electric field vector of the light passing through optical components uses the Jones 4x4 matrices,  $[JM]$ , as a mathematical representation of lenses, polarizers, samples, etc. The electric vector,  $\vec{E}^2$ , corresponding to the light after its interaction with a system, is expressed as a function of the electric vector of the incident light,  $\vec{E}^1$ , using the equation:

$$\vec{E}^2 = [JM]_{system} \vec{E}^1 \quad (2.33)$$

where the matrix  $[JM]_{system}$  represents the Jones matrix associated to the optical system.

The Jones matrix of the entire system can be decomposed into the Jones matrices corresponding to each optical component:

$$[JM]_{system} = [JM]_{analyzer} \cdot [JM]_{I/2} \cdot [JM]_{sample} \cdot [JM]_{polarizer} \quad (2.34)$$

Here, we neglect the Faraday effect in lenses.

The Jones matrices for the polarizer (analyzer), magnetic samples, and half-wave plate will be presented in the following.

### Polarizer (analyzer) Jones matrix

The polarizers used, consists of birefringent media, which refract differently the polarization parallel respectively perpendicular to the polarizer/analyzer axes, obtaining two different beams (fig.2.22). These systems are equally used to analyze the light polarization after its reflection from the magnetic sample. In this case, they are called analyzers.

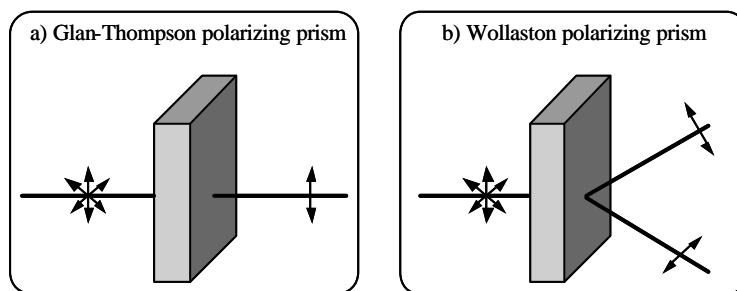


Figure 2.22  
a) Glan-Thompson and b) Wollaston polarizing prisms

In certain cases, only one beam is transmitted (the second one being absorbed) (e.g. Glan-Thompson polarizing prism in figure 2.22a) and other cases, both beams are transmitted (e.g. Wollaston polarizing prism in figure 2.22b). The Jones matrices for the two cases are:

$$JM_1 = \begin{bmatrix} \cos^2 \mathbf{q}_p & \sin \mathbf{q}_p \cdot \cos \mathbf{q}_p \\ \sin \mathbf{q}_p \cdot \cos \mathbf{q}_p & \sin^2 \mathbf{q}_p \end{bmatrix} \text{ (Glan-Thompson polarizing prism)} \quad (2.35a)$$

$$JM_2 = \begin{bmatrix} \cos \mathbf{q}_P & -\sin \mathbf{q}_P \\ \sin \mathbf{q}_P & \cos \mathbf{q}_P \end{bmatrix} \text{ (Wollaston polarizing prism)} \quad (2.35b)$$

where  $\mathbf{q}_P$  is the angle between the polarizing prism axis and  $P$ -axis of the system.

### Half-wave plate Jones matrix

The half-wave plate rotates the polarization plane by an angle  $2\gamma$  (fig.2.34). The bisectrix of this angle is called the *half-wave plate axis*. The corresponding Jones matrix is:

$$JM_{1/2} = \begin{bmatrix} \cos(2\mathbf{q}_L) & -\sin(2\mathbf{q}_L) \\ \sin(2\mathbf{q}_L) & \cos(2\mathbf{q}_L) \end{bmatrix} \quad (2.36)$$

where  $\mathbf{q}_L$  is the angle between the half wave plate axis and the  $P$ -axis.

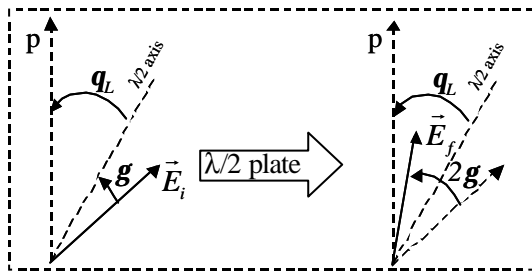


Figure 2.23  
Rotation induced by a half-wave plate

### Magnetic sample Jones matrix

The interaction between the incident vector,  $\vec{E}^i$ , and the magnetic sample is described by a matrix that contains as parameters the *Fresnel coefficients* ( $r_{ij}^2$ ) :

$$\begin{bmatrix} E_P^r \\ E_S^r \end{bmatrix} = \begin{bmatrix} r_{PP} & r_{PS} \\ r_{SP} & r_{SS} \end{bmatrix} \begin{bmatrix} E_P^i \\ E_S^i \end{bmatrix} \quad (2.37)$$

The Fresnel coefficients are complex numbers which depend on the optical properties of the sample such as the complex refractive index  $\mathbf{n}$ , the angle of incidence  $\mathbf{q}$  (fig2.20), the complex Voigt constant  $\mathbf{Q}$ , and the polar, longitudinal and transversal magnetization components:  $\mathbf{m}_p$ ,  $\mathbf{m}_l$  and  $\mathbf{m}_t$  respectively. The  $r_{ij}$  coefficients can be written as a function of two coefficients which are magnetization independent ( $r_{PP}^0$  or  $r_{SS}^0$ ) and five coefficients, which depend on the transversal ( $r_{PP}^t$ ), longitudinal ( $r_{PS}^l$  or  $r_{SP}^l$ ) or polar ( $r_{PS}^p$  or  $r_{SP}^p$ ) magnetization component [Atkinson, Kang2000, Wilkes2000]:

<sup>2</sup> For Fresnel coefficients we use the reference axis of the light beam :  $P$  and  $S$  as presented in figure 2.20.

$$\begin{cases}
r_{PP} = \frac{n^2 \cos \mathbf{q} - \mathbf{g}}{n^2 \cos \mathbf{q} + \mathbf{g}} + j \frac{m_t n^2 Q \sin(2\mathbf{q})}{(n^2 \cos \mathbf{q} + \mathbf{g})^2} = r_{PP}^0 + r_{PP}^t \\
r_{PS} = j n^2 Q \cos \mathbf{q} \frac{\left[ m_p - m_l \frac{\sin \mathbf{q}}{\mathbf{g}} \right]}{(\cos \mathbf{q} + \mathbf{g})(n^2 \cos \mathbf{q} + \mathbf{g})} = r_{PS}^P - r_{PS}^l \\
r_{SP} = j n^2 Q \cos \mathbf{q} \frac{\left[ m_p + m_l \frac{\sin \mathbf{q}}{\mathbf{g}} \right]}{(\cos \mathbf{q} + \mathbf{g})(n^2 \cos \mathbf{q} + \mathbf{g})} = r_{SP}^P + r_{SP}^l \\
r_{SS} = \frac{\cos \mathbf{q} - \mathbf{g}}{\cos \mathbf{q} + \mathbf{g}} = r_{SS}^0
\end{cases} \quad (2.38)$$

where  $\mathbf{g} = \sqrt{n^2 - \sin^2 \mathbf{q}}$ .

As it can be observed in (2.38), for a given material (fixed  $n$ ,  $Q$  constants), the Fresnel coefficients depend strongly on the incidence angle,  $\mathbf{q}$ , of the incoming polarized light and of the three magnetization components.

The interest is to find particular experimental configurations for which one measures only one component of the magnetization.

Figure 2.24 presents the dependences of the modulus,  $|r_{ij}|$ , and the phase,  $\delta$ , of the complex Fresnel coefficients as a function of the angle of incidence  $\mathbf{q}$  using the following complex values for  $n$  and  $Q$ :  $n = 3.05 + j \cdot 1.236$ ;  $Q = -0.0376 + j \cdot 0.0066$ .

For  $\mathbf{q} = 0$ ,  $r_{PP}$  depends only on the polar magnetization component,  $m_p$ . For larger values of the angle  $\mathbf{q}$ , the reflected light contains information on all magnetization components:  $m_p$ ,  $m_l$  and  $m_t$ .

To measure separately each component of the magnetization (longitudinal, transversal or polar) particular geometries of the experimental setup can be used. Perpendicular incidence ( $\mathbf{q} = 0$ ) is generally used to measure the polar magnetization component. The others two components of the magnetization (longitudinal or transversal) can be measured for incidence angles  $\mathbf{q} > 0$  by choosing special angles on the polarizer ( $\mathbf{q}_P$ ) and analyzer ( $\mathbf{q}_A$ ) settings. The values of the angles  $\mathbf{q}_P$  and  $\mathbf{q}_A$  for a longitudinal or respective transversal MOKE experiment can be deduced by analyzing the mathematical expression of the beam intensity recorded by the detectors (fig.2.21). Several detection mechanisms have been envisaged for different MOKE experiments. Among them we can mention: i) *the single detection* where the beam refracted by the analyzer is recorded on one single detector ( $I_{MOKE} = I_D$ ) and ii) *the differential*

detection where we measure the difference between the intensities of two detectors ( $I_{MOKE} = I_{D1} - I_{D2}$ ).

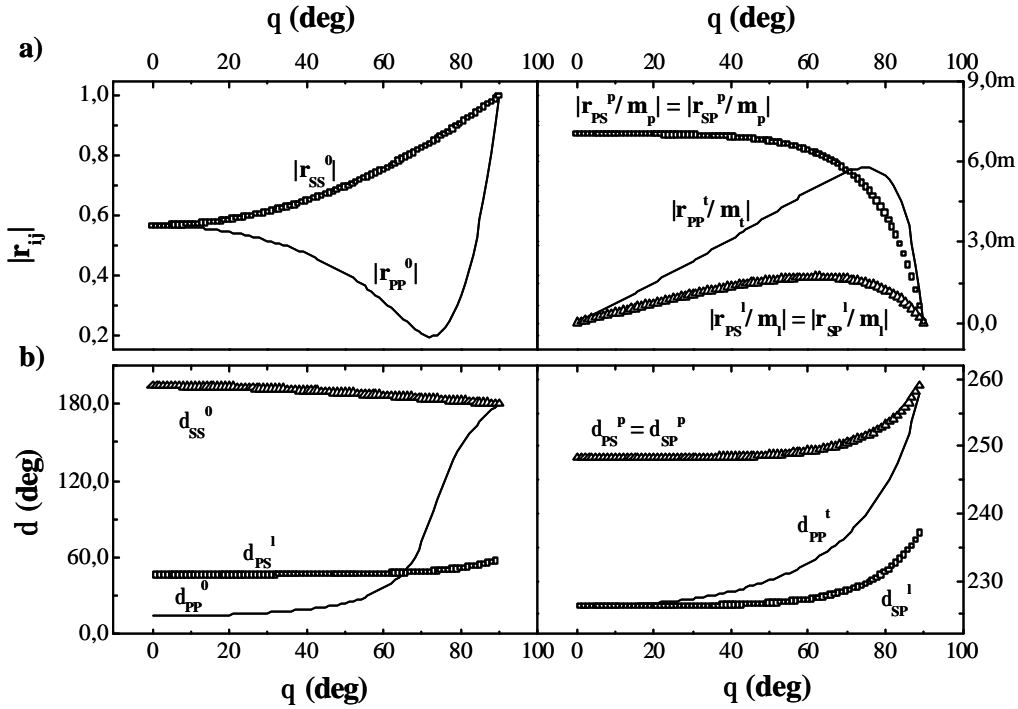


Figure 2.24:

Variation of the modules (a) and phases (b) of the complex Fresnel coefficients, function of the incidence angle on the sample  $q$

In the following we present the single detection mode for the light reflected by the magnetic sample for two polarizations of the incident light and ( $P$  and respectively  $S$ ). Considering a magnetic sample represented by a magnetic thin film with a uniaxial anisotropy, the stable magnetic states of the sample are characterized by an in-plane direction of the magnetization vector. In this case the polar component is zero ( $m_p = 0$ ).

### Single detection mode

i) For an  $S$ -polarized incident light ( $q_p = 90^\circ$ ), the reflected signal ( $E^r$ ) is proportional to Fresnel coefficients  $r_{PS}^l$  and  $r_{SS}^0$  (from equation 2.37), and thus indirectly to the longitudinal magnetization component,  $m_l$ :

$$\vec{E}^r = \begin{bmatrix} E_P^r \\ E_S^r \end{bmatrix} = \begin{bmatrix} r_{PP} & r_{PS} \\ r_{SP} & r_{SS} \end{bmatrix} \begin{bmatrix} 0 \\ E_S^i \end{bmatrix} = \begin{bmatrix} -r_{PS}^l \\ r_{SS}^0 \end{bmatrix} E_S^i \quad (2.39)$$

In this configuration, one can realize a longitudinal MOKE measurement choosing an angle close to zero on the analyzer (e.g. Glan-Thompson polarizing prism – see figure 2.22)

and measuring the intensity of the refracted light ( $E_p^r$ ) that is proportional to  $m_l$  in a single detection mode.

ii) For a  $P$ -polarized incident light ( $q_p = 0^\circ$ ), the reflected signal ( $E^r$ ) is proportional to Fresnel coefficients  $r_{pp}$  and  $r_{sp}^l$  (from equation 2.37), which are proportional both to the longitudinal and transversal magnetization components:

$$\begin{bmatrix} E_p^r \\ E_s^r \end{bmatrix} = \begin{bmatrix} r_{pp} & r_{ps} \\ r_{sp} & r_{ss} \end{bmatrix} \begin{bmatrix} E_p^i \\ 0 \end{bmatrix} = \begin{bmatrix} r_{pp}^0 + r_{pp}^t \\ r_{sp}^l \end{bmatrix} E_p^i \quad (2.40)$$

Depending on the analyzer setting, close to  $0^\circ$  or to  $90^\circ$ , we can obtain a signal proportional to  $m_t$  and  $m_l$  respectively. For an analyzer angle close to  $0^\circ$ , we measure the  $E_p^r$  component. In this case the signal is composed of an offset of large value ( $r_{pp}^0 \sim 0.2 - 1$  on figure 2.24) and a much smaller term proportional to the transversal magnetization component ( $r_{pp}^t \sim 0 - 0.006$  on figure 2.24). In our experimental set-up it turned out that the second term is of the order of the experimental noise and thus not measurable. At an angle close to  $90^\circ$ , on the analyzer (e.g. Glan-Thompson polarizing prism – see figure 2.22) the refracted beam corresponding to  $E_s^r$ , is proportional to  $r_{sp}^l$  and with this to the longitudinal component of the magnetization,  $m_l$  in a single detection mode.

The two experimental configurations presented above, were characterized by reduced ratios *signal / noise*. Using these configurations, we obtained a signal/noise ratio about 13 for a NiFe continuous thin film of 5nm thickness. Furthermore, since the magnetic systems to study have micron-sized dimensions, the signal/noise becomes even more reduced<sup>3</sup>, and, thus, a new detection setup is required.

To optimize the measurement sensitivity (to minimize the noise with respect to Kerr signal), we used a differential detection.

### Differential detection mode

We will show that for certain values of the angles of the polarizer and analyzer settings (see configurations given below) the difference between the light intensities of the two beams refracted from the analyzer is proportional more or less to the longitudinal or transversal components of the magnetization.

---

<sup>3</sup> The reflections of the light (spot of 15μm diameter) on the boards of micron-sized sample (20 x 40 μm<sup>2</sup>) determine a supplementary noise



These configurations are:

*Longitudinal configuration:*  $q_P = 0^\circ$ ,  $q_A = 45^\circ$

*Transversal configuration:*  $q_P = 45^\circ$ ,  $q_A = 90^\circ$

In the two cases, we used as analyzer a Wollaston prism (fig.2.22). Each rotation of the analyzer axis corresponds to different positions for the two detectors used in the differential detection. Experimentally it is less convenient to change the detector position for each rotation of the analyzer. In consequence, we used a half wave plate between the sample and the analyzer in order to rotate the reflected beam before its incidence on the analyzer.

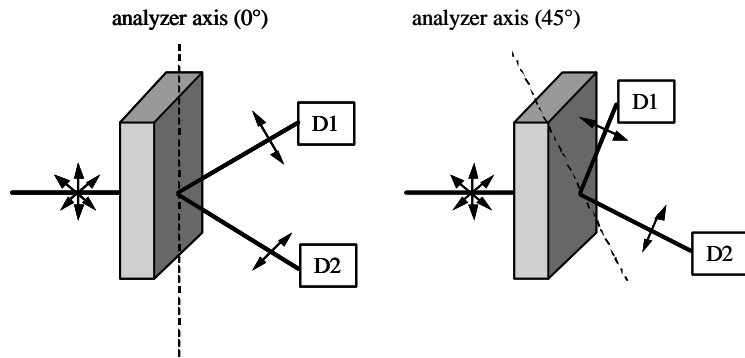


Figure 2.25

The rotation of the analyzer axis determines the rotation of the detector positions

Using the expressions presented above for the Jones matrices for the Wollaston prism used as analyzer (eq.2.35b) and for the half-wave plate (eq.2.36), for  $q_A = 2q_L$  we have the equivalence:

$$[JM]_{Wollaston}^{q_A} = [JM]_{I/2}^{2q_L} [JM]_{Wollaston}^{0^\circ} \quad (2.41)$$

In consequence, using a half wave plate and maintaining the analyzer at  $0^\circ$ , the two configurations have the angle parameters:

*Longitudinal configuration:*  $q_P = 0^\circ$ ,  $q_L = 22.5^\circ$ ,  $q_A = 0^\circ$ ;

*Transversal configuration:*  $q_P = 45^\circ$ ,  $q_L = 45^\circ$ ,  $q_A = 0^\circ$ .

In the following, we detail the longitudinal and the transversal configurations as these have been used during this work.

### 2.5.1.3. LONGITUDINAL KERR EFFECT CONFIGURATION

The longitudinal configuration measurement, in our case, was realized using:

- i) Incident light  $P$ -polarized ( $\mathbf{q}_P = 0^\circ$ )
- ii) Angle on the analyzer equal to  $\mathbf{q}_A = 45^\circ$ .

We measured the difference between the intensities recorded on the two detectors:

$$\Delta I = I_{D1} - I_{D2}.$$

Using the Jones matrix of the polarizer for  $\mathbf{q}_P = 0^\circ$  the transmitted electric field vector  $\vec{E}^2$  is given by:

$$\begin{bmatrix} E_P^2 \\ E_S^2 \end{bmatrix} = \begin{bmatrix} 1 & 0 \\ 0 & 0 \end{bmatrix} \begin{bmatrix} E_P^1 \\ E_S^1 \end{bmatrix} = \begin{bmatrix} E_P^1 \\ 0 \end{bmatrix} \quad (2.42)$$

After the reflection from the magnetic sample, taking all magnetization contributions into account (polar, longitudinal and transversal) the electric field is expressed as:

$$\begin{bmatrix} E_P^3 \\ E_S^3 \end{bmatrix} = \begin{bmatrix} r_{PP}^0 + r_{PP}^t & r_{PS}^p - r_{PS}^l \\ r_{SP}^p + r_{SP}^l & r_{SS}^0 \end{bmatrix} \begin{bmatrix} E_P^2 \\ 0 \end{bmatrix} \quad (2.43)$$

Using a Jones matrix for a Wollaston prism (2.35b), for  $\mathbf{q}_A = 45^\circ$ , we obtain the electric field  $P$  and  $S$  components:

$$\begin{bmatrix} E_P^4 \\ E_S^4 \end{bmatrix} = \frac{\sqrt{2}}{2} \begin{bmatrix} 1 & -1 \\ 1 & 1 \end{bmatrix} \begin{bmatrix} E_P^3 \\ E_S^3 \end{bmatrix} \quad (2.44)$$

The intensities of the two beams incident on the two detectors are calculated as:

$$\begin{aligned} I_P^4 &= (E_P^4) \cdot (E_P^4)^* = \frac{1}{2} (E_P^3 - E_S^3) \cdot (E_P^3 - E_S^3)^* = \frac{I_P^1}{2} (r_{PP} - r_{SP}) \cdot (r_{PP} - r_{SP})^* \\ I_S^4 &= (E_S^4) \cdot (E_S^4)^* = \frac{1}{2} (E_P^3 + E_S^3) \cdot (E_P^3 + E_S^3)^* = \frac{I_P^1}{2} (r_{PP} + r_{SP}) \cdot (r_{PP} + r_{SP})^* \end{aligned} \quad (2.45)$$

where  $I_P^1 = (E_P^1) \cdot (E_P^1)^*$

Considering the complex form for the Fresnel coefficients:

$$r_{ij} = |r_{ij}| \exp(j\mathbf{d}_{ij}) \quad ij=pp, sp \quad (2.46)$$

we obtain:

$$\begin{aligned} I_P^4 &= [|r_{PP}|^2 - 2|r_{PP}||r_{SP}|\cos \mathbf{d} + |r_{SP}|^2] \frac{I_P^1}{2} \\ I_S^4 &= [|r_{PP}|^2 + 2|r_{PP}||r_{SP}|\cos \mathbf{d} + |r_{SP}|^2] \frac{I_P^1}{2} \end{aligned} \quad (2.47)$$

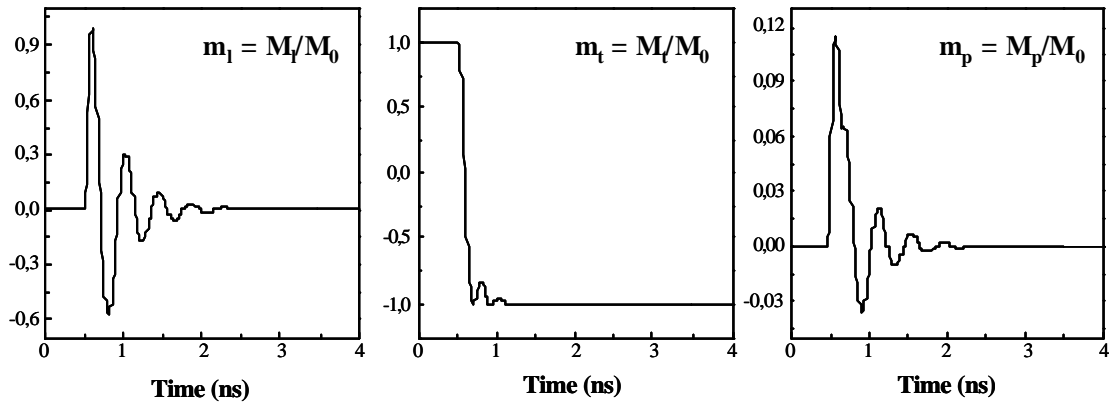
where  $\mathbf{d} = \mathbf{d}_{PP} - \mathbf{d}_{SP}$ .

The difference  $DI$  corresponding to the differential detection is expressed as:

$$\Delta I = I_S^4 - I_P^4 = I_P^1 \cdot 2|r_{PP}|r_{SP}|\cos \mathbf{d}| \quad (2.48)$$

The expression (2.48) contains all three-magnetization components:  $m_p$ ,  $m_l$  and  $m_t$  in the coefficients:  $r_{PP}$  and  $r_{SP}$ . Introducing the analytical expressions of Fresnel coefficients (eq.2.38) in the  $DI$  form (2.48) we obtain a complex analytical expression for  $DI$  from where the contribution of each component of the magnetization is difficult to obtain.

#### A) $m_l, m_p, m_t$ time dependence :



#### B) $DI$ dependence and fit parameters

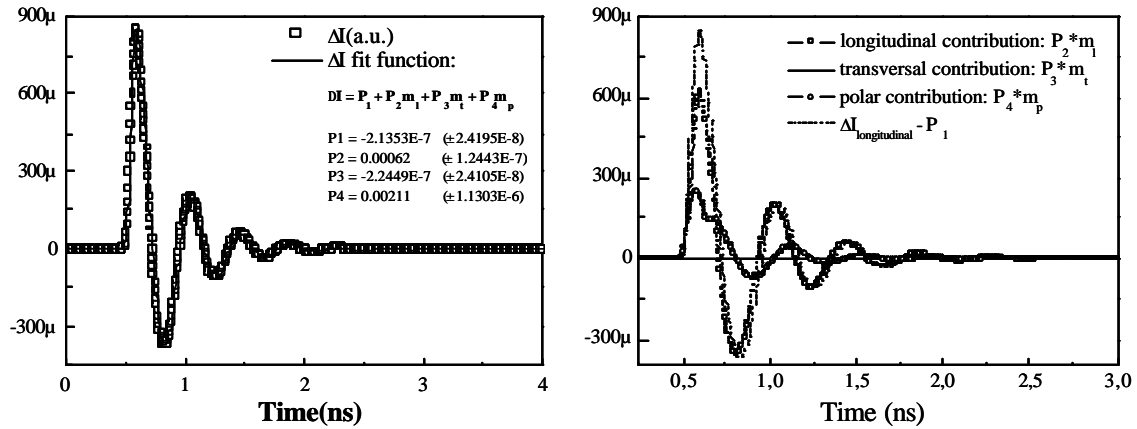


Figure 2.26:<sup>4</sup>

Longitudinal configuration:  $q_P = 0^\circ$ ,  $q_A = 45^\circ$

In consequence, we have realized a numerical fitting of the calculated  $DI$ <sup>5</sup> as a function of the values of  $m_l$ ,  $m_t$  and  $m_p$ . We used the time-dependence of  $m_l$ ,  $m_t$  and  $m_p$  resulting from macrospin simulations (see Annexe 3 and chapter 4 – section 4.2.7.4). The macrospin results were obtained using the parameters: damping parameter  $\alpha = 0.03$ , magnetization value  $M_S =$

<sup>4</sup> Attention to the scale in the polar component representation

<sup>5</sup> MOKE simulations are detailed in Annexe 4

$860 \text{ emu/cm}^3$ , and demagnetizing parameters:  $N_L = 0.0067$ ,  $N_T = 0$ ,  $N_P = 0.9933$ . The magnetization, initially oriented parallel to the transversal direction (in the sample plane and perpendicular to the plane of incidence), will reverse under an applied pulsed magnetic field of 155 Oe amplitude, parallel to the longitudinal direction (in the sample plane and parallel to the plane of incidence). Details concerning the magnetization reversal will be discussed in chapter 4.

Figure 2.26B represents the calculated  $\mathbf{DI}$  values for the configuration: polarizer  $\mathbf{q}_P = 0^\circ$ , analyzer  $\mathbf{q}_A = 45^\circ$  and angle of incidence  $\mathbf{q} = 45^\circ$ . We used the following complex values for  $n$  and  $Q$ :  $n_{Fe} = 3.05 + j \cdot 1.236$ ;  $Q_{Fe} = -0.0376 + j \cdot 0.0066$ . As we can observe in equations 2.47,  $I_P$  and  $I_S$  contain an important contribution due to the transversal magnetization component. By measuring the difference between them, we should expect a quasi-zero contribution of the transversal component to  $\mathbf{DI}$ . If we suppose that we have a linear variation of  $\mathbf{DI}$  with  $m_p$ ,  $m_l$  and  $m_t$  as expressed in the next formula:

$$\Delta I = P_1 + P_2 m_l + P_3 m_t + P_4 m_p \quad (2.49)$$

by fitting this function to the calculated curve, we obtained the values for the parameters:  $P_1 = -2.13 \cdot 10^{-7}$ ,  $P_2 = 6.2 \cdot 10^{-4}$ ,  $P_3 = -2.24 \cdot 10^{-7}$  and  $P_4 = 2.11 \cdot 10^{-3}$ . We observe that  $P_4$  and  $P_2$  are three or four orders of magnitude larger than  $P_1$  and  $P_3$ , which demonstrate that the polar and longitudinal contributions are more important than the transversal ones. Because the polar magnetization component during the reversal is smaller with respect to the longitudinal or transversal magnetization values, the polar part in the final Kerr result has a reduced contribution. This is clearly demonstrated by representing the curves of the products  $P_2 m_l$ ,  $P_3 m_t$  and  $P_4 m_p$  as a function of time (fig.2.26B). We observe that the transverse contribution can be neglected while the polar and longitudinal components have  $\sim 25\%$  respective  $\sim 75\%$  contribution to the total result respectively. This configuration is named “longitudinal” because, in general, in static MOKE measurements on magnetic samples with planar anisotropy, the polar component can be neglected. In dynamic MOKE measurements, (characteristic times of sub-nanoseconds) the magnetization vector gains a non-zero polar component and its contribution to the final result should be considered.

In conclusion in a dynamic or static “longitudinal Kerr effect configuration” when using an angle of incidence of  $\mathbf{q} = 45^\circ$ , the measured signal contains negligible information on the transversal magnetization component ( $m_t$ ). The most important part of the signal

contains information about the longitudinal component of the magnetization ( $m_l$ ) but also on the polar component ( $m_p$ ).

*Note:* the parameters used in the MOKE calculations were:  $Q_{Fe} = 0.0376 + i \cdot 0.0066$  and  $n_{Fe} = 3.05 + i \cdot 1.236$ .

#### 2.5.1.4. TRANSVERSAL KERR EFFECT CONFIGURATION

The transversal configuration measurement, in our case, was realized using:

- i) Polarizer angle of  $q_p = 45^\circ$ ;
- ii) Analyzer angle of  $q_A = 90^\circ$ .

The difference between the intensities is measured on the two detectors:  $\Delta I = I_{D1} - I_{D2}$ .

With a  $45^\circ$  angle on the polarizer ( $q_p = 45^\circ$ ), the  $E_p$  and  $E_s$  components of the incident polarization are equal:

$$\begin{bmatrix} E_p^2 \\ E_s^2 \end{bmatrix} = \frac{1}{2} \begin{bmatrix} 1 & 1 \\ 1 & 1 \end{bmatrix} \begin{bmatrix} E_p^1 \\ E_s^1 \end{bmatrix} = \begin{bmatrix} E_0 \\ E_0 \end{bmatrix} \quad (2.50)$$

After the reflection from the magnetic sample, the  $E_p^3$  and  $E_s^3$  components can be calculated as shown in equation 2.43.

For an analyzer angle of  $90^\circ$  ( $q_A = 90^\circ$ ) the electric field components  $E_p^4$  and  $E_s^4$  are:

$$\begin{bmatrix} E_p^4 \\ E_s^4 \end{bmatrix} = \begin{bmatrix} 0 & -1 \\ 1 & 0 \end{bmatrix} \begin{bmatrix} E_p^3 \\ E_s^3 \end{bmatrix} \quad (2.51)$$

Taking the complex form for the Fresnel coefficients as in equation 2.46 we obtain:

$$\begin{aligned} I_p^4 &= (E_p^4) \cdot (E_p^4)^* = I_0 \left[ |r_{SP}|^2 + 2|r_{SP}||r_{SS}^0| \cos \mathbf{d}_s + |r_{SS}^0|^2 \right] \text{ where } \mathbf{d}_s = \mathbf{d}_{SP} - \mathbf{d}_{SS}^0 \\ I_s^4 &= (E_s^4) \cdot (E_s^4)^* = I_0 \left[ |r_{PP}|^2 - 2|r_{PP}||r_{PS}| \cos \mathbf{d}_p + |r_{PS}|^2 \right] \text{ where } \mathbf{d}_p = \mathbf{d}_{PP} - \mathbf{d}_{PS} \end{aligned} \quad (2.52)$$

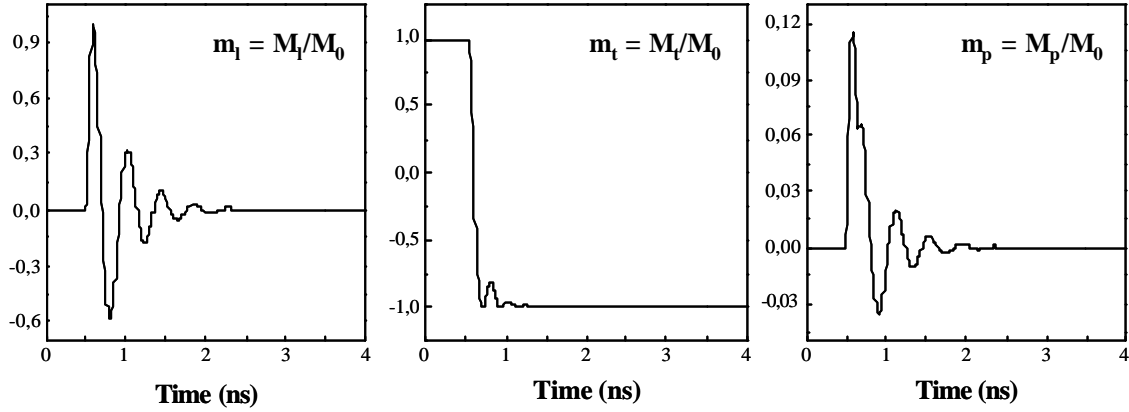
The difference between the two intensities is:

$$\Delta I = I_p^4 - I_s^4 = I_0 \cdot \left[ |r_{SP}|^2 + 2|r_{SP}||r_{SS}^0| \cos \mathbf{d}_s + |r_{SS}^0|^2 - |r_{PP}|^2 + 2|r_{PP}||r_{PS}| \cos \mathbf{d}_p - |r_{PS}|^2 \right] \quad (2.53)$$

Figure 2.27B represents the calculated differential intensity  $\Delta I$  for the configuration: polarizer  $q_p = 45^\circ$ , analyzer  $q_A = 90^\circ$  and angle of incidence  $q = 45^\circ$ . As we can observe in equations 2.52 and 2.53 both the  $I_p$  and  $I_s$  intensities but also the difference  $\Delta I$ , contain contributions due to all magnetization components. Supposing the same linear variation of  $\Delta I$

as expressed in the formula 2.49, by fitting this function to the calculated curve (fig.2.27B) we obtain the following values for the parameters:  $P_1 = 0.1235$ ,  $P_2 = 2.2 \cdot 10^{-4}$ ,  $P_3 = 1.41 \cdot 10^{-3}$  and  $P_4 = 4.71 \cdot 10^{-3}$ . We notice that all parameters have comparable values.

#### A) $m_l$ , $m_t$ , $m_p$ time dependence :



#### B) DI dependence and fit parameters

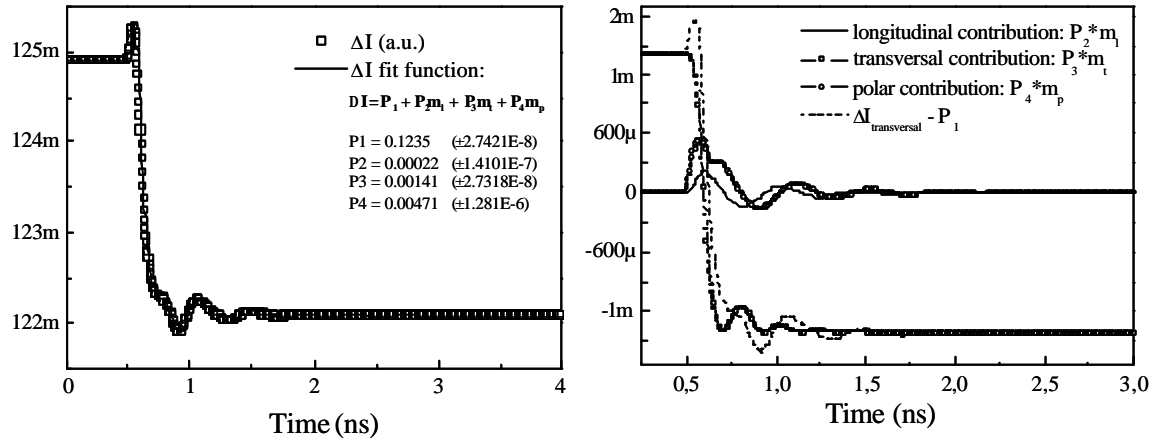


Figure 2.27:  
Transversal configuration:  $q_p = 45^\circ$ ,  $q_A = 90^\circ$

To better visualize the contribution of each component to the final result we have traced the variation of the products:  $P_2 m_l$ ,  $P_3 m_t$  and  $P_4 m_p$  as a function of time (fig.2.27B). We observe that the dominant contribution comes from the transverse magnetization component, while the polar and longitudinal components have small but non-negligible contributions to the total result.

In conclusion, in a transversal Kerr effect configuration, the measured signal contains information of all the three components of the magnetization: transversal, longitudinal, and polar. The dominant contribution of the signal is proportional to the transversal component of

the magnetization ( $m_t$ ) but there are non-negligible contributions that come from the polar ( $m_p$ ) and longitudinal magnetization components ( $m_l$ ).

### 2.5.1.5. EXPERIMENTAL MOKE SETUP

The MOKE measurements were realized using the so-called “longitudinal” and “transversal” experimental configurations, already described in the previous section. They required as components: a light source, a polarizer, the magnetic sample to study, a half-wave plate, an analyzer, and the two detectors used in the differential detection. Furthermore, we added a chopper, microscope objective, and focusing lens, as is shown on the picture in figure 2.28. The optical components are detailed in the following.

#### Light source

The light source corresponds to an infrared (IR) laser diode fabricated by *Advanced Photonic Systems*. It delivers partially polarized laser pulses characterized by the wavelength  $\lambda = 810 \text{ nm}$ , pulse duration:  $20 \text{ ps}$ , pulse peak power:  $1 \text{ W}$ , variable pulse repetition frequency (we used a frequency of  $100 \text{ KHz}$ ). It is used in both dynamic and static MOKE measurements.

#### Polarizer

The polarizer is a Glan-Thompson polarizing prism and it is used to linearly polarize the incident light beam (fig.2.22).

#### Microscope objective

The light is focused onto the magnetic sample using a 20x, 16 mm working distance microscope objective. The minimum spot dimension obtained during this study was of about  $15 \text{ }\mu\text{m}$  diameter.

#### Focusing lens

After the reflection from the magnetic sample, the beam is focused onto the detectors (through a half-wave plate) using a convergent lens.

### Half-wave plate and analyzer

The half wave plate rotates the polarization of the reflected beam and the analyzer (Wollaston prism) separates the beam in two beams, with two orthogonal polarizations using a Wollaston prism (fig.2.22).

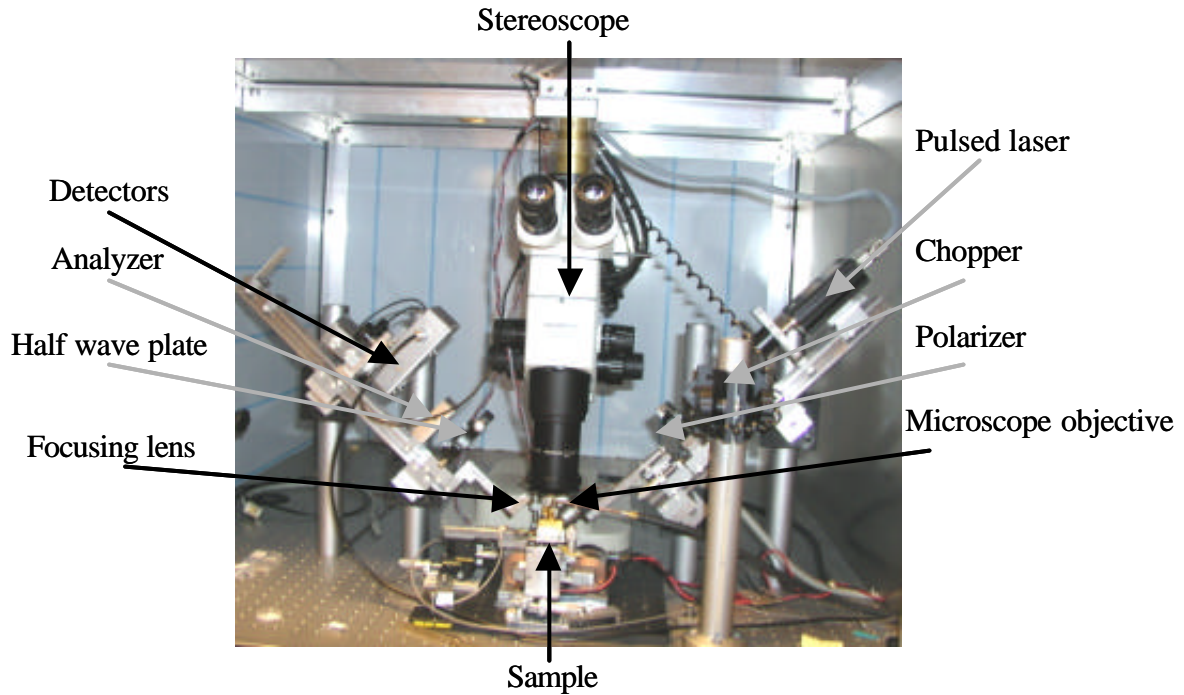


Figure 2.28  
MOKE experimental setup

### Detectors

The two beams refracted by the analyzer (fig. 2.22) are captured by two silicon photodetectors characterized by a detection window centered on the laser wavelength. The differential detection consists on measuring the difference between the intensities of the two beams ( $DI = I_{D1} - I_{D2}$ ).

### Stereoscope

A stereoscope fabricated by Olympus with a 1.2 x objective and 10x ocular, is used to visualize the laser spot on the sample and the high frequency microprobes connections to electrically contact the coplanar waveguide.

The experiments realized using the differential detection have shown that the noise was reduced from 20 $\mu$ V to about 5 $\mu$ V. With our experiment, we obtained a *signal/noise* ratio about 30 on a NiFe sample of 20 x 40 $\mu$ m<sup>2</sup> (5 $\mu$ V noise for a signal variation of 150 $\mu$ V).



To further improve the signal/noise ratio, the Kerr signals corresponding to voltage signals about  $200 \mu\text{V}$  have been measured using a lock-in detection scheme. This uses a modulation technique that will be detailed in the following.

#### *Laser modulation in a MOKE experiment*

The incident light delivered by the laser is characterized by two frequencies i) the wave frequency  $370 \cdot 10^{12} \text{ Hz}$ ; and ii) the pulse frequencies – about  $100 \text{ KHz}$ . These frequencies are too high for a lock-in amplifier, which measures signals of reduced amplitude characterized by frequencies of several hundreds of  $\text{Hz}$ .

The modulation of the incident light is realized using a chopper. In this way one obtains a light intensity modulation for frequencies about some hundreds of  $\text{Hz}$ . Figure 2.29 compares the non-modulated with the modulated laser signal. For a pulse repetition rate of  $100 \text{ KHz}$ , the time interval between two consecutive pulses is  $10 \mu\text{s}$ . After the modulation realized by the chopper, laser pulses are transmitted to the sample only in a time-window of  $4 \text{ ms}$  duration from the full interval of about  $7 \text{ ms}$  that corresponds to the chopper modulation frequency of  $140 \text{ Hz}$  (see figure 2.29B). The lock-in measures the light intensity,  $DI$ , that is proportional to the Kerr effect integrated over the entire time interval  $\tau$  of measurement (time constant). In our case the time constant was set on the lock-in to  $300 \text{ ms}$ .

In a static measurement, the external magnetic field is maintained constant for a time larger than  $300 \text{ ms}$  and the result characterizes the equilibrium magnetic state that corresponds to the external field value.

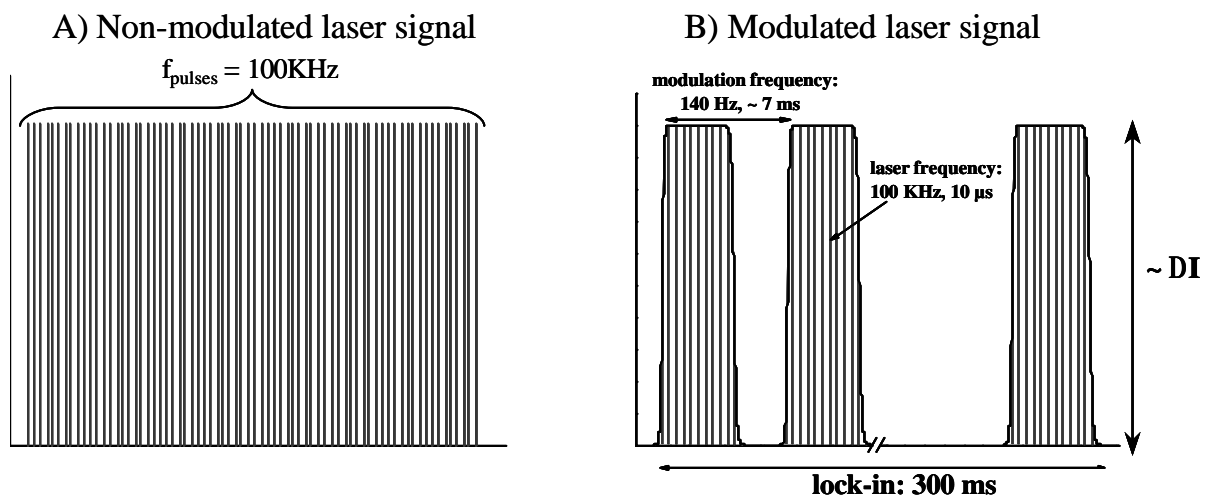


Figure 2.29  
The modulation of the incident laser

We use the same measurement technique in the dynamic measurements. The details of this measurement will be presented in the following.

### 2.5.1.6. DYNAMIC MOKE EXPERIMENT

The time-resolved measurements have been realized using the synchronized stroboscopic pump-probe technique already described in section 2.1. The experimental setup is schematically presented in figure 2.30.

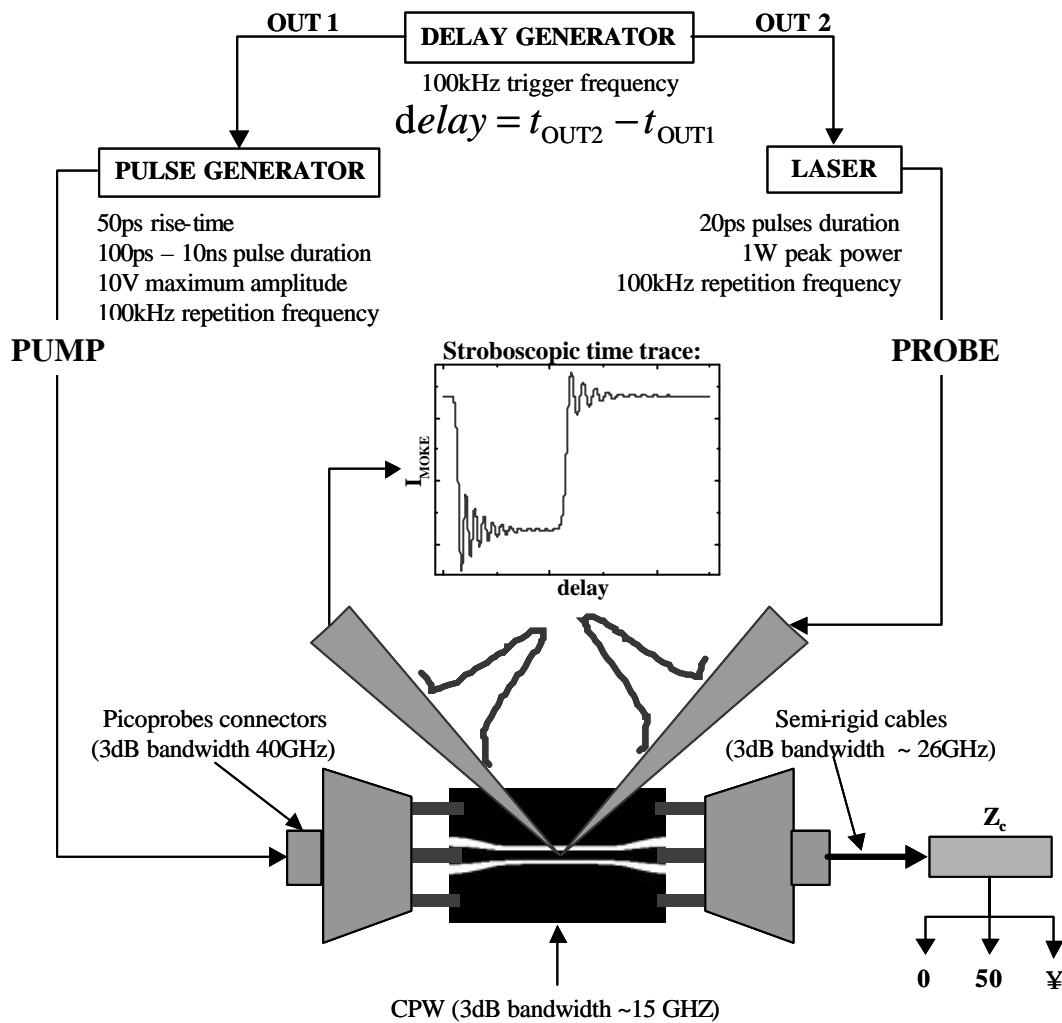


Figure 2.30: Schematic of the dynamic MOKE experimental set-up

The delay between the probe pulses (laser) and the pump pulses (voltage pulse generator) is realized using a commercial delay generator. It synchronizes the pump and probe by delivering two pulses (OUT1 and OUT2), delayed one with respect to the other. These will

serve as external trigger for the laser and the pulse generator. For one pump pulse delivered at time  $T_0$  there is one probe pulse delivered at  $T_0 + Dt_i$  (e.g.  $Dt_i = 0, 10 \text{ ps}, 20 \text{ ps} \dots 10 \text{ ns} \dots$ ). The synchronization between the pump and the probe is characterized by the jitter value, which is less than 10 ps.

One probe pulse (of 20 ps duration) is not enough to realize a measurement for a value  $Dt_i$ . In consequence, the stroboscopic measurement averages the Kerr signal over several probe pulses. As we mentioned before in a static MOKE experiment one measures one point in about 300 ms. During this time, we obtain about  $17.2 \cdot 10^3$  probe pulses. As the pump and probe frequencies are equal, the number of the pump pulses is equal to the number of probe pulses. In consequence, a point on the stroboscopic time trace is averaged over 300 ms (time interval chosen on the lock-in), corresponding to about  $17.2 \cdot 10^3$  dynamic equivalent events.

The pump and probe frequencies are limited by the maximum frequency on the pulse generator that is of 100 KHz.

In this context, we have to mention that a stroboscopic measurement is valid if two conditions are respected: i) the sample has to be in the identical initial magnetic state before each excitation field. This is realized by resetting the system after each pump pulse in the time window of 10  $\mu\text{s}$  and ii) The magnetization vector follows the same trajectory during and after each excitation field pulse.

Using the dynamic MOKE experiment we measured the magnetization dynamics in  $20 \times 40 \mu\text{m}^2$  spin valve systems (see results in chapter 4). Since the laser spot dimensions are large, about  $15 \mu\text{m}^2$  diameter, the measurement of the magnetization dynamics in spin-valves of smaller dimensions ( $4 \times 8 \mu\text{m}^2$  or  $2 \times 4 \mu\text{m}^2$ ) was not possible. In consequence, we used as probe the MR effect for which the experimental setup will be presented in the next section.

## 2.5.2. THE MAGNETO – RESISTIVE PROBE

The MR probe uses the magneto-resistive effect to measure the magnetization dynamics in multilayer magnetic systems. Details of some basic aspects of this effect and the experimental realization of the static and time-resolved measurements will be presented in the following. The realization of the MR experiment connected to the device preparation and further details of the design are presented in chapter 3.

### 2.5.2.1. MAGNETO-RESISTIVE EFFECTS

The magneto – resistance (MR) characterizes the response of the electrical resistance of a system under an external magnetic field. To quantify the magneto-resistive effect, usually one uses the relative changes of resistance ( $\Delta R/R$ ), resistivity ( $\Delta \rho/\rho$ ) or electron mean free path between two scattering processes ( $\Delta \lambda/\lambda$ ).

There are several types of MR effects to be distinguished:

- i) Anisotropic Magneto – Resistive effect (**AMR**);
- ii) Giant Magneto – Resistive effect (**GMR**).

#### A) Anisotropic Magneto – Resistive effect (AMR)

The Anisotropic Magneto – Resistance is an internal property of a sample and it is related to the anisotropy of the atomic charge distribution in magnetic materials. The orbital momentum direction of the charge distribution in an external magnetic field is defined by the spin-orbit coupling. As a function of the relative orientation between the external magnetic field and the current, the electrical resistance of the sample has different values because the conduction electrons have different probabilities of scattering.

The AMR signal is proportional to the magnetization component, which is parallel to the current direction. The *transverse* geometry is characterized by a perpendicular relative orientation between the magnetic field and the current, the minimum value of the resistance corresponds to the saturation magnetic field value when the magnetization becomes perpendicular to the current direction (fig. 2.31a). In a *longitudinal* configuration, characterized by parallel relative orientations between the magnetic field and the current, the saturated magnetic state corresponds to a maximum value of the resistance as the magnetization is aligned parallel to the current direction (fig. 2.31b). In both cases, the

maximum (fig. 2.31a) or minimum (fig. 2.31b) on the curves corresponds to the magnetic coercive field value where the magnetic state of the sample is characterized by total spin disorientation.

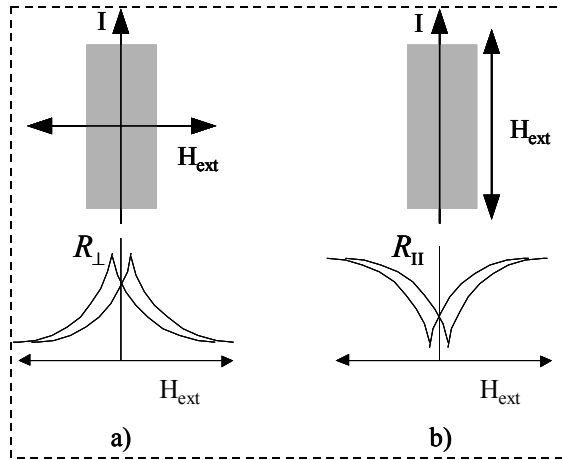


Figure 2.31:  
AMR variation as a function of the external field value and direction; (a) the transversal and (b) the longitudinal configurations

The amplitude of the AMR effect is about 1% and it can reach 3% in the case of permalloy ( $\text{Ni}_{0.8}\text{Fe}_{0.2}$ ). The AMR is defined as:

$$AMR(\%) = \frac{\Delta R}{R_0} = \frac{R_{\perp} - R_{\parallel}}{R_0} \text{ where } R_0 = \frac{R_{\parallel}}{3} + \frac{2R_{\perp}}{3} \quad (2.54)$$

where  $R_0$  represents the resistance in a zero magnetic field supposing total disorder.

### B) Giant Magneto – Resistive effect (GMR)

The GMR is defined as the variation of the electrical resistance of a multilayer system (minimum two ferromagnetic layers separated by a non-magnetic one), as a function of the relative orientation between the layer magnetizations. Parallel (antiparallel) relative orientation of the magnetizations of the two layers corresponds to a minimum (maximum) value of the electrical resistance (fig.2.32).

The electrical resistances equivalent to parallel and anti-parallel states are (fig. 2.32):

$$R_{\uparrow\uparrow} = \frac{2rR}{R+r} \text{ and } R_{\uparrow\downarrow} = \frac{R+r}{2} \quad (2.55)$$

where  $r$  (respectively  $R$ ) is the electrical resistance corresponding to the electron with a spin parallel (respectively anti-parallel) to the layer magnetization.

The magneto-resistance is defined as:

$$\frac{\Delta R}{R} = \frac{R_{\uparrow\downarrow} - R_{\uparrow\uparrow}}{R_{\uparrow\downarrow}} = \left( \frac{R-r}{R+r} \right)^2 \quad (2.56)$$

Magneto-resistive measurements on spin-valves or tunnel junctions yield informations on the magnetization orientation of the free layer with respect to the pinned layer.

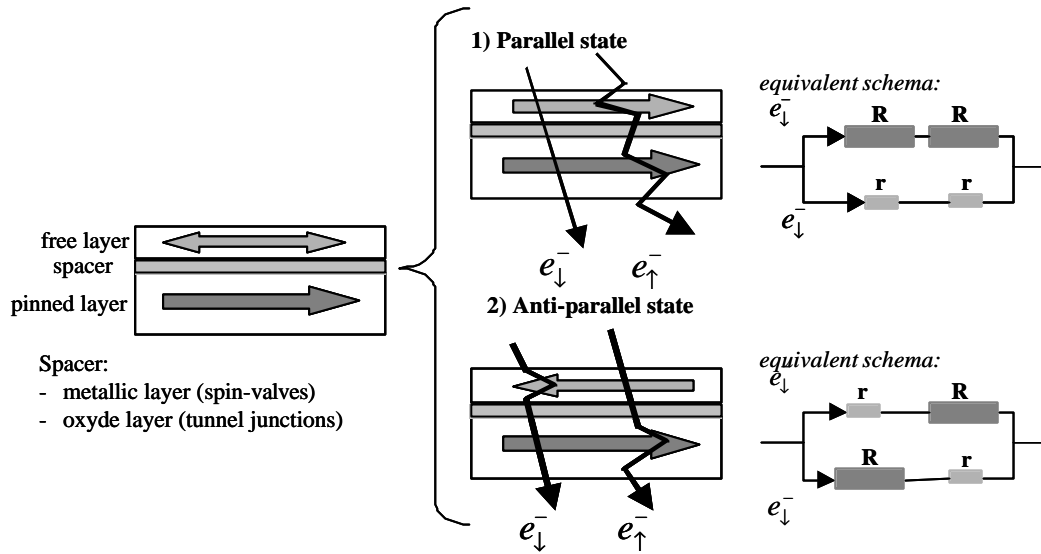


Figure 2.32:

Electron trajectories and equivalent electric circuit for parallel and antiparallel states in a magnetic multilayer sample (CPP geometry).

In the following, our experimental setup is described for static and dynamic magneto-resistive measurements.

#### 2.5.2.2. MAGNETO-RESISTIVE EXPERIMENTAL SETUP

The Magneto-Resistive measurements were realized on micron-sized magnetic samples (spin valves or tunnel junctions) patterned on the centerline of a coplanar waveguide, the pump line. The probe line measures the variation of the CIP (Current In Plane) magneto-resistance in a two-point contact configuration (see figure 2.33). This is realized by using a Keithley multi-meter to deliver a constant current to the sample and to measure the voltage changes.

In total, the dynamic MR device is characterized by 4-ports. Static measurements are performed using the two contacts represented by port 3 and 4. A DC current is sent in the probe line at port 3 ( $P_3$ ) and the voltage is read on the same port for different terminations ( $0\Omega$  or  $50\Omega$ ) at port 4 ( $P_4$ ).

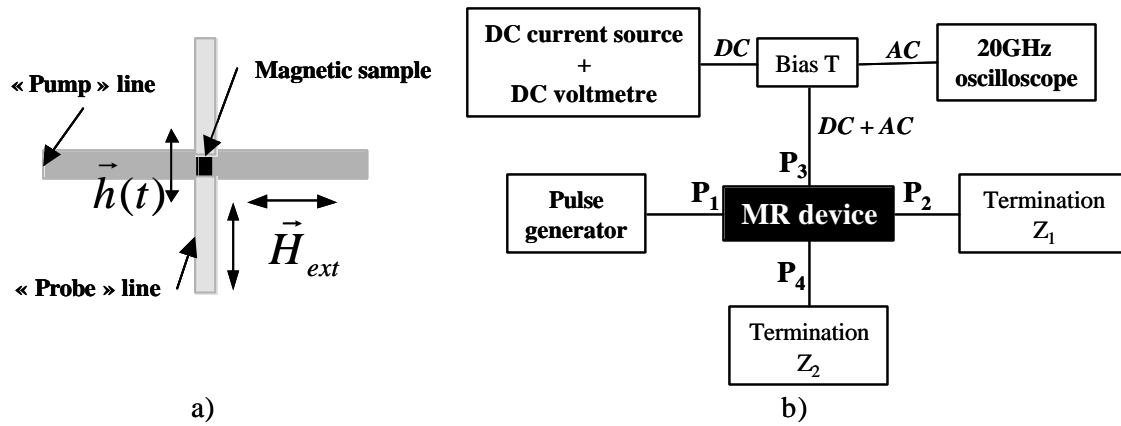


Figure 2.33:

“Pump” and “probe” transmission lines (a) and the experimental setup used in static and dynamic MR measurements

Dynamic measurements are realized using the configuration represented in figure 2.33b. The pulse generator is connected to P<sub>1</sub> and applies a voltage pulse to the pump line, creating an excitation field. The termination Z<sub>1</sub> at port 2 (P<sub>2</sub>) determines whether there is a second pulse traveling back. For 50 Ω there is no reflected pulse, while for short (open) circuit one obtains a reflected voltage pulse of opposed (same) polarity. A Keithley current generator and the 20 GHz oscilloscope are connected through a Bias T to P<sub>3</sub>. The termination Z<sub>2</sub>, (generally 50 Ω), is connected to P<sub>4</sub>. The Bias T is used as well to separate the alternative (AC) signal and the continuous one (DC) from the total voltage signal (AC + DC) measured on the probe line, port P<sub>3</sub>. The DC voltage signal contains the static MR response while the dynamic MR response is measured on the 20 GHz oscilloscope. The oscilloscope is a sampling oscilloscope realizing “stroboscopic” measurement. The voltage resolution is about 20 μV that can be improved by realizing averaging over several time traces.

Usually for MR values about 1% and for resistance values of about 30 Ω (for a spin-valve), we expect a variation of the resistance about 0.3 Ω. For a current value about 5mA this corresponds to a voltage variation of 1.5 mV.

### 2.5.3. THE INDUCTIVE PROBE

During this work, we have developed the inductive effect to characterize the linear magnetization dynamics in magnetic systems. This will be detailed in the following.

In this case the probe corresponds to transmitted power of the incident high frequency pump pulse applied to a CPW. The sample is positioned on top of this CPW. The measurement can be realized in frequency as well as in time domain as a function of the external magnetic field or of the pump field frequency. Here I will present some aspects of the theory of inductive effect, as well as on the experimental setup.

#### 2.5.3.1. INDUCTIVE EFFECT

The inductive effect appears in the magnetic materials as a consequence of a transient external magnetic field:  $\vec{H}(t)$ . It is described by the Faraday law:

$$\nabla \times \vec{E} = -\frac{\partial \vec{B}}{\partial t} \quad (2.57)$$

where  $\vec{B} = \mu_0(\vec{H} + \vec{M})$  and  $\vec{M}$  is the magnetic sample magnetization.

The magnetic fields in the  $x$ ,  $y$  and  $z$  directions produced by a current density  $J$  that traverses a rectangular stripline of volume  $V$  in the  $x$ -direction, has the components (see Annexe 1):

$$\begin{aligned} H_x(\vec{r}) &= 0 \\ H_y(\vec{r}) &= \frac{\mu_0 J}{4\pi} \int_V \frac{\partial}{\partial z} \left( \frac{d\vec{r}'}{|\vec{r} - \vec{r}'|} \right) \\ H_z(\vec{r}) &= -\frac{\mu_0 J}{4\pi} \int_V \frac{\partial}{\partial y} \left( \frac{d\vec{r}'}{|\vec{r} - \vec{r}'|} \right) \end{aligned} \quad (2.58)$$

where the  $\vec{r}$ ,  $\vec{r}'$  represent the vectors corresponding to the coordinates where the magnetic field is calculated and the coordinates of the stripline, respectively and  $d\vec{r}' = dx dy dz$ .

Silva et al [Silva 1999] presented magnetic field solutions deduced from the reciprocity theorem adapted to gap recording heads [Bertram 1994]. Neglecting the  $z$ -component of the magnetic field,  $H_z$ , since it is too weak to cause the magnetization to go out of the plane, *the magnetic flux* that winds around the waveguide center conductor from a magnetic sample of thickness  $t$ , length  $l$ , and width  $w$ , may be calculated as [Mallinson 1993, Bertram 1994]:

$$\Phi = \frac{\mu_0}{l} \iiint_{sample} H_y(I, x, y, z) M_y(x, y, z) d\vec{r}' \quad (2.59)$$



The inductive voltage is produced by the change in flux:

$$V = -\frac{d\Phi}{dt} \quad (2.60)$$

Experimentally, one measures, in the presence of a magnetic field, the inductive voltage that is proportional to the variation of the magnetization component that is parallel to the magnetic pump field. In the following, we describe the experimental setup developed during this work to measure the magnetization component that is parallel to a high-frequency magnetic field.

### 2.5.3.2. EXPERIMENTAL SETUP

The measurement is realized by connecting Port 1 of the coplanar waveguide to the pulse generator and Port 2 to the 20 GHz digital oscilloscope for time domain measurements (TDR or TDT). In the frequency domain technique, ports 1 and 2 are connected to a network analyzer which provides a continuous wave voltage at a given frequency and which measures the transmitted power (fig.2.2).

In the time-domain, the oscilloscope detects only the pulse that traverses the line in the same direction as the driving voltage pulse.

From 2.59 and 2.60 we obtain:

$$V_p = \text{const} \cdot \frac{d}{dt} \left( \int_{-w/2}^{w/2} M_y(y) dy \right) = \text{const} \cdot \frac{d\bar{M}_y}{dt} \quad (2.61)$$

where the constant depends on the line electrical resistance ( $R_{DC}$ ):  $\text{const} = \frac{Z_0}{Z_0 + 0.5 \cdot R_{DC}}$ .

By integrating the measured voltage pulse, the average value of the magnetization that rotates can be estimated:

$$\bar{M}_y = \text{const}^{-1} \cdot \int V_p dt \quad (2.62)$$

From 2.62 it is obvious that we are sensitive to the magnetization component that is parallel to the excitation magnetic field.

In the frequency domain the network analyzer is used both to pump and probe the signal absorption. This can be realized by varying the signal frequency and the external magnetic field.

For the studies presented in Chapter 4, the inductive technique has not been used. Therefore, Fig. 2.34 shows representatively the results obtained for a  $2 \times 100 \mu\text{m}^2$  FeNi wire that has been deposited on top of a 2.8 wide CPW centerline.

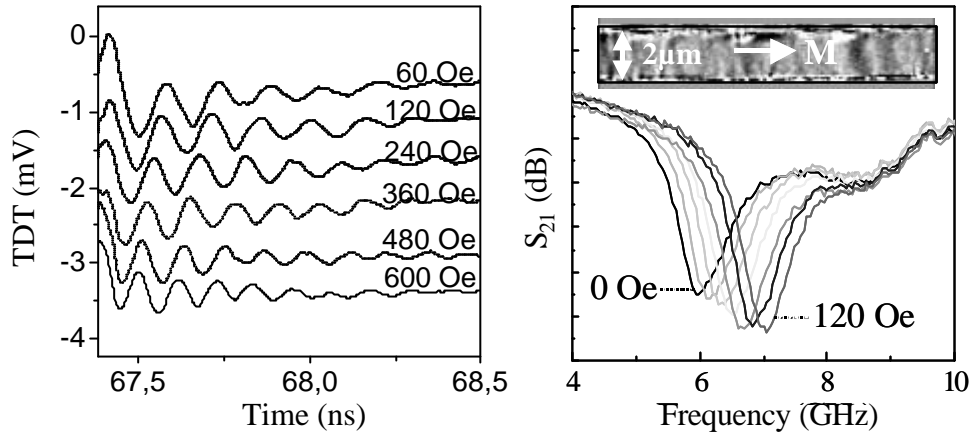


Fig. 2.34: Time domain traces and frequency domain absorption spectra for a FeNi wire obtained with the inductive technique.

## 2.6. PUMP-PROBE TECHNIQUE – STATE-OF-ART

In the following, a short overview it is presented over different magnetization dynamics experiments, presented in the literature that use the pump-probe technique.

Freeman et al [Freeman 1991, Freeman 1992, Elezzabi 1996, Freeman 1996, Freeman 1997B] were the first to realize pump-probe experiments to study the magnetization dynamics in magnetic systems with a sub-nanosecond time resolution. They used as pump the magnetic field pulses induced in coplanar waveguide traversed by electric pulses obtained by a photoconductive switch in a GaAs semiconductor (fig.2.35a). As probe they used both the Faraday effect to determine the magnetic field profile induced in the CPW (fig.2.35b) as well as the Kerr effect with a spatial resolution of some micrometers. The pump and probe laser pulses had durations in hundreds of femto-seconds range.

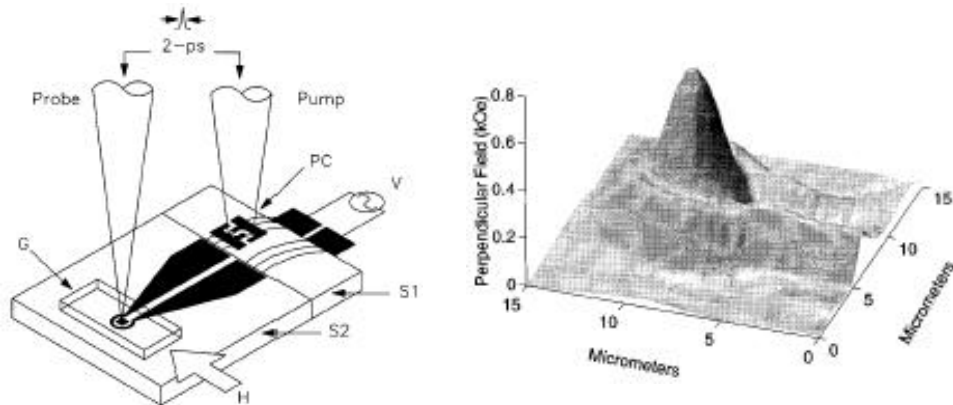


Figure 2.35

a) The experimental setup; b) The 2D magnetic image scan of the transmission line coil taken at 70 ps after optical excitation [Elezzabi 1996]

Similar pump-probe experiments were used to characterize the magnetization dynamics in permalloy elements [Gerrits 2002, Gerrits 2002B]. They showed that the pump-pulse could be tailored by using two independent triggered GaAs photoswitches excited Ti-sapphire laser pulses of 150 fs duration (fig.2.36). Both pulses are of opposite sign and slightly delayed one with respect to the other. In this case, the in-plane magnetization components are measured by Magnetization induced Second Harmonic Generation (MSHG) while the polar component is measured using the linear polar magneto-optical Kerr effect. The spatial resolution was determined by the laser spot dimensions equal to  $3\mu\text{m}$  by  $5\mu\text{m}$ .

Crawford et al [Crawford 1999] used as pump voltage pulses from a pulse generator and as probe the second harmonic magneto-optic Kerr measurements.

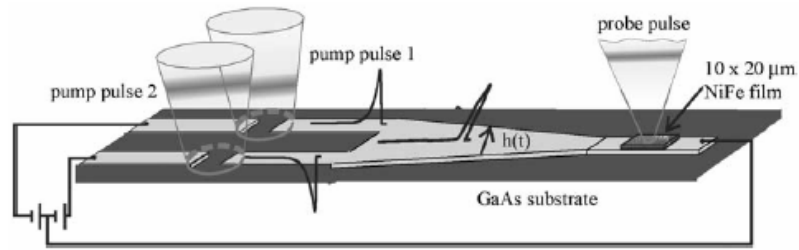


Figure 2.36

Pump1- pump2 – probe experimental scheme [Gerrits 2002B]

Using as pump the ultrashort magnetic field pulses of duration 0.2 – 4 ns, obtained by applying voltage pulses from a commercial generator through a 50  $\Omega$  adapted coplanar waveguide Schumacher et al studied the magnetization dynamics in  $1\mu\text{m} \times 4\mu\text{m}$  GMR devices using as probe the MR effect [Schumacher 2002, Schumacher 2003]. Similar measurements but on tunnel magnetic junctions have been realized by Koch et al [Koch 1998].

Using the inductive effect as probe and pulses or steps (5 V amplitude and 80 ps rise-times, 200 ps pulses width) obtained by a photoconductive switch on a commercial InGaAs photodiode, Silva et al [Silva 1999] studied the magnetization dynamics in thin-film permalloy. The inductive effect was measured in time-domain using a 18 GHz bandwidth oscilloscope. The experimental setup is presented in figure 2.37.

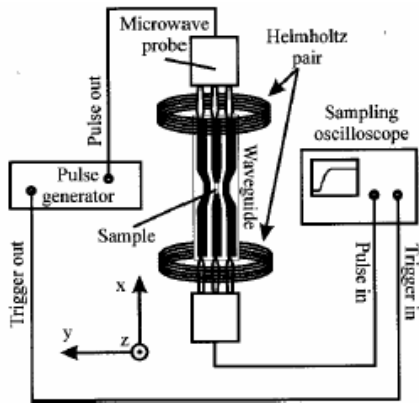


Figure 2.37

Experimental setup for the inductive measurement [Silva 1999].

Finally I would like to mention that Bonfim et al [Bonfim 2001] realized measurements of the magnetization dynamics using as probe the XMCD and as pump magnetic pulses induced in a copper microcoil [Mackay 2000], which are synchronized with the x-ray photon pulses at the repetition frequency of the ESRF (357 KHz in a single bunch mode), obtaining a time resolution in the nanosecond range.



**CHAPTER 3:**  
**EXPERIMENTAL TECHNIQUES**  
**FOR SAMPLE PREPARATION AND CHARACTERIZATION**



### **Abstract**

*In this chapter we present the experimental techniques and the major steps during the preparation of experimental devices. These devices are composed of: i) the transmission line, ii) the magnetic sample patterned on the transmission line and iii) the “read” line (for the magneto-resistive device). We used preparation techniques such as: the ultraviolet (UV) or the deep ultraviolet (DUV) lithography, the ion beam etching, the reactive etching, the sputtering technique. The characterization of the intermediate steps was realized using the atomic force microscopy (AFM), the magnetic force microscopy (MFM), or the scanning electron microscopy (SEM). These yield us information on the topographic and magnetic structure of micron-sized magnetic samples ( $20 \times 40 \mu\text{m}^2$ ,  $4 \times 8 \mu\text{m}^2$ ) and on the quality of the insulating layer between the “read” and “write” lines. We propose some improvements of devices used for magneto-resistive measurements, which can be envisaged in the future.*

### **Résumé**

*Dans ce chapitre nous présentons les techniques expérimentales ainsi que les principales étapes de la préparation des dispositifs expérimentales. Ces dispositifs de mesure sont composés par: i) la ligne de transmission, ii) l'échantillon magnétique fixé sur la ligne de transmission et iii) la ligne de lecture (pour le dispositif prévu pour les mesures magnéto-resistives). Ils ont été réalisés en utilisant comme techniques de préparation : la lithographie UV et UV profond, la gravure ionique et réactive, le dépôt par pulvérisation cathodique. Pour caractériser les étapes intermédiaires nous avons utilisé la microscopie à force atomique et magnétique et la microscopie électronique à balayage. Ils nous ont fourni des informations sur la couche isolante entre les lignes d'écriture et de lecture ainsi que sur la structure magnétique des échantillons de taille micronique ( $20 \times 40 \mu\text{m}^2$ ,  $4 \times 8 \mu\text{m}^2$ ). Des améliorations dans la structure des certains dispositifs envisageable dans le futur, sont proposés.*



### 3.1. INTRODUCTION

The realization of devices used in time-resolved magnetization measurements requires the use of different preparation techniques. These will be presented in this chapter along with the actual fabrication of the devices studied during this work.

Two to three steps can be distinguished in the sample preparation, which are presented in figure 3.1:

- i) The patterning of the coplanar wave-guide pump-line using Ultra-Violet (UV) lithography for centerline width values between  $2\mu\text{m}$  and up to  $50\mu\text{m}$ . Figure 3.1a, presents the images of two coplanar waveguides, with  $50\mu\text{m}$  and respective  $10\mu\text{m}$  centerline width.
- ii) The patterning of the magnetic sample on top of the centerline. The size of these samples varies between  $20 \times 40\mu\text{m}^2$ ,  $4 \times 8\mu\text{m}^2$  and down to  $2 \times 4\mu\text{m}^2$ . Figure 3.1b presents the images of two samples: a  $20 \times 40\mu\text{m}^2$  NiO based spin-valve and a  $4 \times 8\mu\text{m}^2$  IrMn based spin-valve. An insulating layer was always deposited between the magnetic layers and the pump line.

For the magneto-optic and inductive probes, the sample preparation is finished after these first two steps. For static and dynamic MR measurements, we need a supplementary step that consists of:

- iii) The patterning of the high frequency electrical contacts onto the magnetic sample surface as shown in figure 3.1c. Here, a special attention was given to the electrical insulation between the pump and probe lines.

This chapter is divided into three parts:

- I. The first part of this chapter focuses on the description of the experimental techniques that have been used for the device preparation and which are commonly used for the patterning of micron-sized elements. These are Ultra-Violet (UV) and Deep-UV (DUV) lithography, Reactive Ion Etching (RIE), Ion Beam Etching (IBE), lift-off, and thin film sputtering.
- II. In the second part the techniques used for the device characterization during and after the patterning process, are presented. The topography/magnetic contrast of the samples were measured with the Atomic / Magnetic Force Microscope (AFM / MFM). The quality of the oxide between the pump-line and the magnetic sample or the probe line is analyzed by conductive AFM. Scanning Electron Microscopy (SEM) was used

to measure and analyze the edge roughness of the surfaces etched in a reactive process (RIE).

III. The third part is focused on the actual sample preparation and characterization.

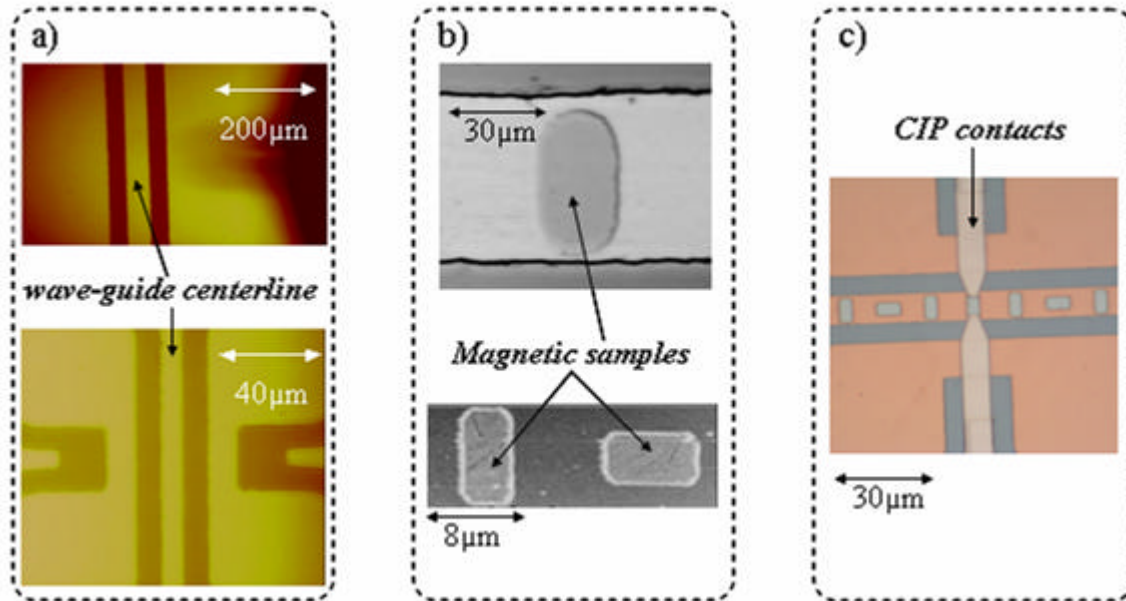


Figure 3.1: Optical photographs showing different steps in the sample preparation: a) Coplanar waveguide, (b) Magnetic samples and (c) CIP contacts patterning.

## 3.2. SAMPLE PREPARATION TECHNIQUES

### 3.2.1. SPUTTERING TECHNIQUE

The sample preparation contains steps during which metallic or oxide thin films have been deposited by sputtering<sup>1</sup>.

The sputtering technique belongs to the category of plasma deposition [Parsons1991], [Richardt1997], [Vossen1991]. It is used for a wide variety of applications like magneto-optical storage media, compact discs, conductors and barriers for large-scale integrated circuits, different kinds of coatings, etc. The main advantages of using a sputtering device are:

- Versatility. Since the sputter process is based on the momentum transfer and not on a chemical or thermal reaction, virtually any kind of material can be sputtered;

<sup>1</sup> For this, different sputtering machines have been available at CEA/DRFMC, CEA/LETI and Louis Neel Laboratory/CNRS in Grenoble.

- Film uniformity over large areas;
- Surface smoothness and thickness control;
- High deposition rates.

We consider two electrodes in a vacuum chamber and an external high voltage power supply (fig. 3.2). The material to be deposited, the *target*, is fixed to the cathode and the substrates to the anode. Considering that 2V is the applied bias between the anode and the cathode, the electric field would be  $2V/d$ , where  $d$  the distance between the anode and the cathode. An electric discharge between the anode and cathode is formed in the presence of the argon gas introduced in the vacuum chamber at a low-pressure ( $2.7 \cdot 10^{-3}$  mbar). This will partially ionize the gas and the ions may strike the cathode with sufficient energy to cause the ejection of surface atoms and the emission of secondary electrons, which will cause further ionization of the gas. Very rapidly, a condition known as *breakdown* is installed and the plasma is stabilized. The principal source of electrons to sustain the plasma is the secondary electron emission caused by the bombardment of the cathode by the ions. DC and RF sources are equally used nowadays to power the plasma. In a general sense, the RF-powered discharge operates in the same way as the dc-powered. In both cases, a voltage is applied between the cathode and the anode, a breakdown occurs and plasma is formed and sustained. RF power, though, allows the use of insulating materials as sputtering targets and it increases the level of ionization in the plasma.

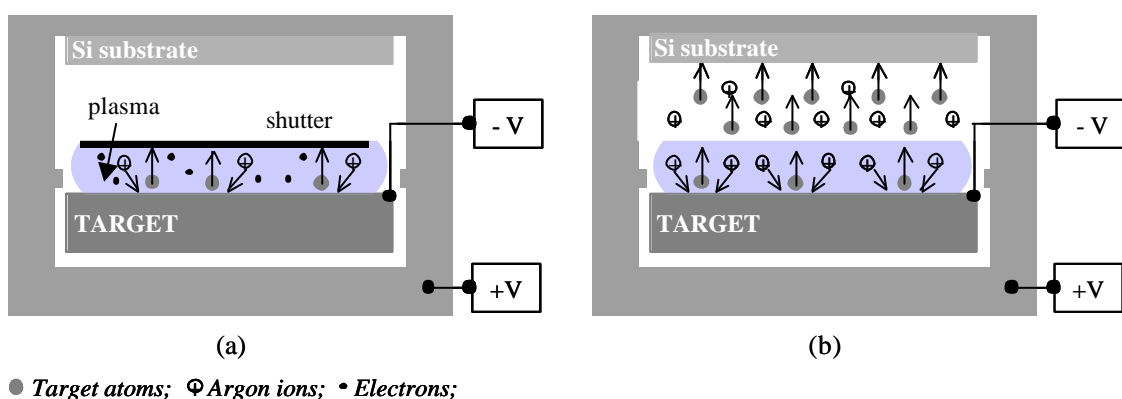


Figure 3.2: Sputtering device: (a) plasma is switched near the target surface; the argon ions are striking the target and create the ejection of target atoms, shutter position is closed; (b) the shutter opens, the target atoms are sputtered on the substrate.

During this study, single layers and multilayers have been deposited using magnetron sputter sources. Magnetrons below the target create a magnetic field parallel to the target surface. Combined with the electric field, it causes a drift of the secondary electrons in closed orbits in front of the target surface. This spatial confinement of the secondary electrons close to the target enhances the efficiency of the plasma, so that a magnetron can operate in lower gas pressures and voltages compared to non-magnetron sources. Different target configurations exist. In particular, we used the two kind of target geometries: i) two targets placed with their surface parallel to the substrate holder (plane targets) and ii) two targets forming a  $45^\circ$  angle with respect to the plane of the substrate holder (convergent targets). The sputtering rate, generally controlled by the DC or RF applied bias and the gas pressure, is also modified by the geometric arrangement of the targets.

Most deposition processes of magnetic layers, oxide layers, metallic non-magnetic layers, have been realized in the sputtering machines of CEA/DRFMC/SP2M – Grenoble. In general, all sputtered magnetic layers were characterized by an induced anisotropy. Its direction was not known for the sputtering installation used in our sample preparation since the magnetrons were changed quite regularly, during the time of this study. The maximum thickness of oxide sputtered was 50nm, its value being limited by the deposition time (50nm in 10min). A longer time for oxide deposition ( $> 1$  hour) induced instabilities in the installation functionality.

### 3.2.2. OPTICAL LITHOGRAPHY TECHNIQUE

The optical lithography was realized at Siemens in Erlangen, Germany<sup>2</sup> and Nanofab laboratory in Grenoble, France<sup>3</sup>.

This is a special technique used to transfer a pattern designed on a mask, onto a photosensitive resist that covers the sample. Here, the three steps necessary for the lithography process are described (fig.3.3).

a) The first step corresponds to the coating of the cleaned sample surface with a thin ( $0.3\mu\text{m} - 3\mu\text{m}$ ) layer of a photosensitive substance called photo-resist, as shown in figure 3.3.a. To ensure homogeneity and continuity of the photo-resist layer, this is realized on a spinning vacuum chuck.

---

<sup>2</sup> Siemens AG, ZT MF 1, Paul-Gossen-Strasse 100, 91034 Erlangen, Germany

<sup>3</sup> Nanofab – CNRS, 25, Av.des Martyrs, 38042, Grenoble, French

b) In the second step, which is presented in figure 3.3.b, the resist is irradiated with Ultra-Violet (UV) or Deep- Ultra-Violet (DUV) radiation through a physical mask. The mask is a glass or plastic plate, onto which the patterns that we want to transfer on the sample are designed as a succession of transparent and opaque surfaces. It can be negative or positive. A positive mask corresponds to opaque regions associated to the designed geometries. The wavelength value of the incident irradiation, the thickness of the resist and the performance of the mask aligner limit the spatial resolution of the process. The UV ( $\lambda_{UV} = 360nm$ ) mask aligner, has a minimum spatial resolution of  $10\mu m$ , while, for the DUV ( $\lambda_{UV} = 250nm$ ), characterized by a smaller wavelength, the minimum spatial resolution is about  $0.5\mu m$ .

c) The third step in the lithographical process corresponds to the development of the resist. As a function of the resist used (positive or negative), the lithographic process leads to a positive respectively negative reaction between the photosensitive substance and the UV irradiation (figure 3.3c). After a positive reaction, the resist that has been irradiated is developed while in a negative one the non-irradiated region is developed. Consequently, as a function of the mask polarity and of the resist type we have two situations: i) a positive mask and a positive resist is equivalent to a negative mask and a negative resist, and ii) a positive mask and a negative resist is equivalent to a negative mask and a positive resist.

The resists used in the UV lithography were *S-1818* for positive reaction and *UI-310* for negative reaction.

The resists used in the DUV lithography were *UV-3* for positive reaction and *UVN-2* for negative reaction.

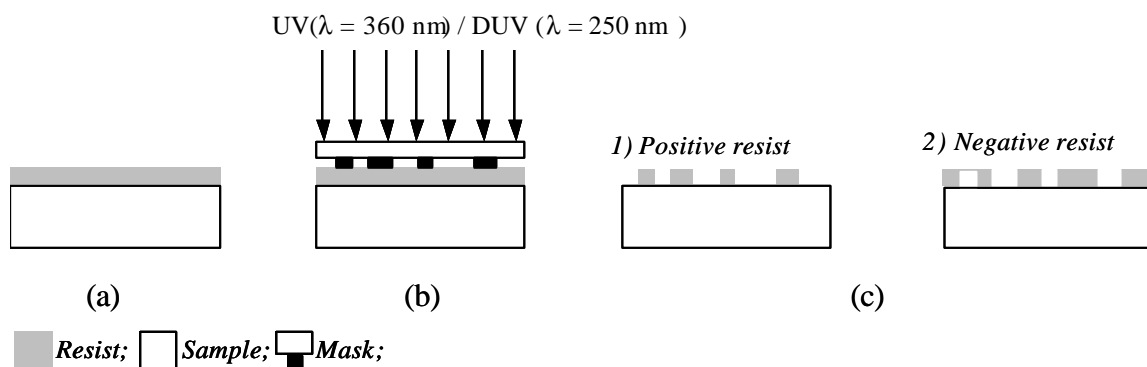


Figure 3.3:

Lithography processes: resist coating on the sample surface (a); UV/UVI irradiation of the resist through a physical mask (b); development for positive or negative resist (c)

There are two alternative techniques that are generally used to obtain patterned samples: i) etching and/or ii) lift-off techniques. These are presented in figure 3.4.

### *The etching technique*

In the first case, the initial sample, substrate-S (Si in our case), is entirely covered by a thin film of the material to be patterned, the sputtered layer (SL). In the next step, a photo-resist is spun onto the film and the mask design is transferred on the photo-resist using a positive process (positive mask + positive lithography or negative mask + negative lithography). In the third step, the entire sample surface is etched resulting in non-etched regions, which were covered with resist, and etched regions, with no resist. After etching metallic film, the resist is dissolved in acetone in an ultrasonic bath.

#### 1) Etching technique:

##### 1a) S + SL



##### 1b) S + SL + positive patterned resist :



IBE  
or  
RIE

##### 1c) S + patterned (SL+ positive resist) :



Acetone  
+  
ultrasounds

##### 1d) S + patterned SL:



#### 2) Lift-off technique:

##### 2a) S :



##### 2b) S + negative patterned resist :



sputtering

##### 2c) S + patterned negative resist + SL:



Acetone  
+  
ultrasounds

##### 2d) S + patterned SL:



Figure 3.4:  
Etching / Lift-off techniques

### *The lift-off technique*

In the second case, a negative patterned resist (negative mask + positive lithography or positive mask + negative lithography) is obtained directly on the substrate (S). In the next step, the thin layer is sputtered on the entire sample. Then, the surfaces covered with resist and the deposited film, are cleaned in acetone in an ultrasonic bath obtaining the similar patterned sample as in the first case.

### **3.2.3. ION BEAM ETCHING (IBE)**

A schematic representation of the Ion Beam Etching (IBE) device is presented in figure 3.5. The gas used for the plasma creation is argon (Ar). The source consists of a discharge chamber with a hot filament cathode (usually of Tungsten) and an anode. When the filament is heated electrons are emitted and accelerated towards the anode. Under appropriate pressure conditions dense plasma is created by the ionization of the Ar gas inside the chamber. The ions produced in the discharge chamber are moving in a stochastic manner.

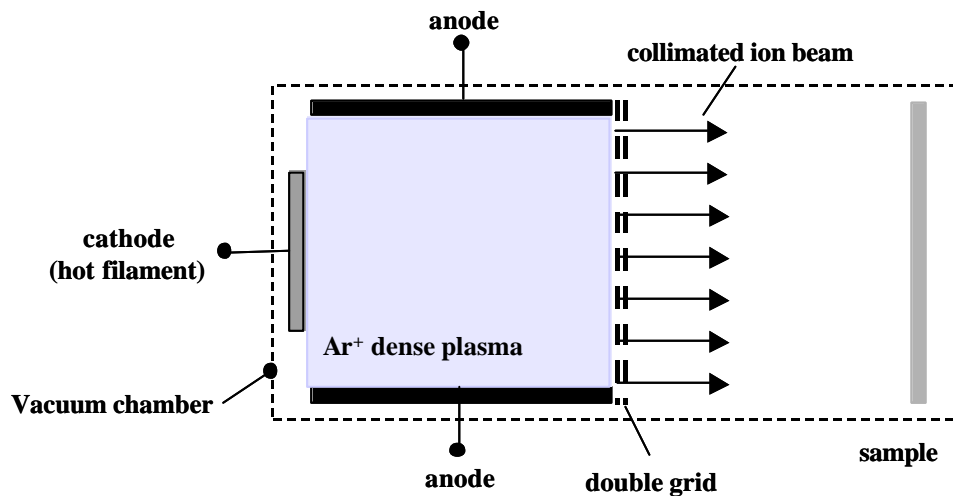


Figure 3.5: The Ion Beam-Etching (IEB) device

In order to produce a collimated beam of these ions, one side of the chamber is equipped with a pair of grids that are aligned. The first grid is positively biased. Thus, the plasma cannot penetrate the grid. Individual ions, however, may travel through the holes of the first grid. If they do so, then they experience a strong accelerating field due to the negative biasing of the second grid and they travel in the form of a monochromatic ion beam towards the target, which is kept at ground potential. The etching rate of the ion beam depends drastically on the material.

We use this etching technique to pattern the CPW. The major disadvantage of one of the available installation (available at CNRS – Grenoble) was the impossibility to obtain a good etching calibration since the etching rates were changing from one process to another. Furthermore, the process was not uniform over the entire surface of the sample. In consequence, only the steps where an over-etch was not critical were realized with this equipment. Most of the magnetic sample etching was realized using the etching equipment available at CEA/LETI - Grenoble.

### 3.2.4. REACTIVE ION ETCHING (RIE)

In a Reactive Ion Etching (RIE) device, presented in figure 3.6, a reactive gas, such as  $\text{SF}_6$ ,  $\text{CHF}_3$ , or  $\text{O}_2$  is introduced into the grounded chamber. In our case we used the  $\text{SF}_6$  to etch Si. The substrate to be etched is placed on an electrode, which is supplied by an RF source. When the RF plasma is formed, the gas molecules are broken down in fragments and radicals.

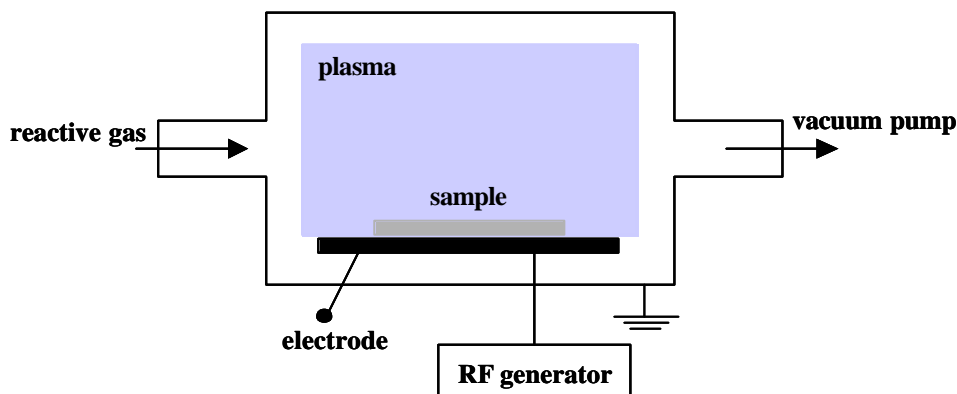


*Figure 3.6:*  
The Reactive Ion Etching (RIE) device

A significant number of these radicals are ionized (positive ions) and they bombard the substrate (negatively polarized due to the more mobile electrons of the plasma). During the reactive etching, gaseous species from the plasma react with surface atoms to form compounds or molecules. In our case, we used  $\text{SF}_6$  to etch the Si substrate. Due to the formation of reactive gaseous species in the plasma, the etching rate is much higher than in a gaseous medium without plasma. RIE is material selective as the etching rate depends on the chemical reaction of the gaseous species with the materials existent on the wafer surface. The chemical effect (formation of reactive gases) introduces an isotropic etching while the physical effect (sample bombardment) creates an anisotropic etching. To obtain vertical edges



during the reactive etching, it is necessary to keep equilibrium between etching parameters: gas debit, pressure, etching time and RF power.

We used this process to etch Si substrate since it is characterized by a larger etching rate (2 min for 300 nm Si) than the IBE technique for Si (~ tens of minutes for 300 nm Si) and it is uniform over the sample surface.

During this study, we have used both the etching and the lift-off techniques to obtain micron-sized patterned samples. The lift-off was generally used to obtain the transmission lines, the CIP contacts, single-layer magnetic patterned samples, and  $20 \times 40 \mu\text{m}^2$  spin-valve samples, while the smaller spin-valves were patterned using the IBE. It is possible to use the lift-off technique to pattern samples smaller than  $20 \times 40 \mu\text{m}^2$  but in this case the appearance of over-flanks at the sample would destroy the magnetic properties of the spin-valve realizing a direct contact between the soft and hard magnetic layers.

### 3.3. SAMPLE CHARACTERIZATION TECHNIQUES

Topographic characterization of the samples was realized using Atomic Force and Scanning Electron Microscopes (AFM and SEM). A qualitative study of the magnetic contrast in samples with in-plane anisotropy was realized using Magnetic Force Microscopy (MFM) measurements. The conductive AFM (C-AFM) was used to perform measurements on the oxide between two conductors: the pump line and respectively the probe line.

The AFM, MFM, and C-AFM measurements were realized using the Dimension 3100 Scanning Probe Microscope with a Nanoscope IV controller. The SEM images were realized at LETI – Grenoble.

#### 3.3.1. ATOMIC FORCE MICROSCOPY (AFM)

Atomic force microscopy [Binnig1986] is a powerful technique for probing the surface of the thin film layers and deducing valuable information of its topological features, fast and accurately. AFM operates by scanning a very sharp and tiny tip attached to the end of a cantilever across the sample surface (fig. 3.7). The tip approaches the surface of the sample and interacts with it via Van der Waals forces. The interaction translates in a cantilever deflection or a change in the cantilever's oscillating frequency, depending on the operational mode of the AFM: *contact* or *tapping*. The deflection or the frequency changes of the cantilever are detected by an optical system consisting of a laser beam, which is reflected on

the cantilever. The vertical and the horizontal deflection are measured using a split photodiode detector that analyses the reflected beam. The displacement of the cantilever in the three directions is done by means of a piezoelectric scanner, combining independently operated piezo-electrodes for X, Y and Z direction into a single tube. The two operating modes that have been used, *contact – AFM* and *tapping – AFM*, are described in more detail in the following.

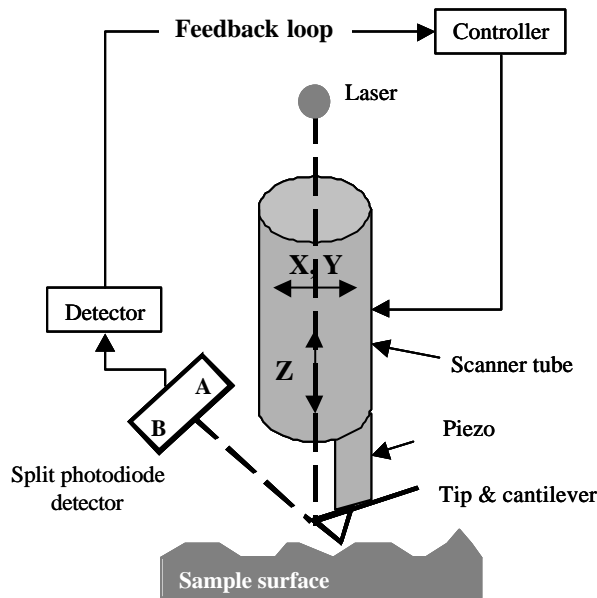


Figure 3.7:  
Atomic Force Microscope

### Contact mode AFM

As we have mentioned the changes in the cantilever's deflection are monitored with a split photodiode detector as the tip is scanning the sample surface [Martin1987]. A feedback loop maintains a constant deflection between the cantilever and the sample by vertically moving the scanner at each data point to maintain a 'set-point' deflection. By maintaining a constant cantilever deflection, the force between the tip and the sample remains constant. The force  $F$  is calculated from Hook's law:  $\vec{F} = -k\vec{x}$ , where  $k$  is the spring constant and  $x$  the deflection. Spring constants usually range from 0.01 to 1.0 N/m, resulting in forces ranging from nN to  $\mu$ N. The distance the scanner moves vertically at each point  $(x,y)$  is stored by the computer to form the topographic image of the surface.

### Tapping mode AFM

In the tapping operational mode the cantilever is oscillated near its resonance frequency with the amplitude ranging typically from 20 to 100 nm. The tip lightly 'taps' the surface

while scanning, contacting the surface at the bottom of its swing. The feedback loop maintains constant oscillation amplitude by maintaining a constant RMS of the oscillation signal acquired by the split photodiode detector. In order to maintain a constant oscillation amplitude the scanner has to move vertically at each point  $(x,y)$ . The vertical position of the scanner is stored by the computer, to form the topographic image of the sample surface.

### **3.3.2. MAGNETIC FORCE MICROSCOPY (MFM)**

The magnetic force imaging is a feature provided by the atomic force microscope. In MFM we use a tapping mode cantilever equipped with a special magnetic tip [Rugar1990, Boef1990]. The tip is first scanned over the sample in order to obtain the topographic information. After each scan line, the feedback is turned off and the tip is raised above the sample to a user-defined height (20-100nm) to perform a second scan of the surface measuring any far field contribution, such as magnetic forces (at that height only long range forces can be detected while Van der Waals forces related to the topography are negligible). This feature of the Dimension 3100 microscope is called Interleave mode. The topography data acquired during the first scan are used to maintain the tip at a constant height. The existence of magnetic forces shifts the resonant frequency of the cantilever by an amount proportional to vertical gradients in the magnetic forces on the tip. Resonant frequency shifts are very small (from 1 to 5 Hz for a resonant frequency of about 100 Hz) and can be detected either by phase detection mode or by amplitude detection mode. Phase detection measures the cantilever's oscillation phase relative to the piezo-drive, and amplitude detection measures the oscillation amplitude. In both cases, the measured signal is proportional to the second derivative of the stray field emanated from the sample [Grütter1995]. Phase detection is much superior than amplitude detection and has been used in this thesis to measure samples with very low net magnetic moment with in-plane magnetisation.

### **3.3.3. CONDUCTIVE AFM**

The Conductive AFM (C-AFM) mode of the microscope realizes maps of currents, corresponding to the sample surface, by keeping the sample at a bias voltage and scanning the sample surface in contact mode with a conductive tip connected to ground (fig.3.8). A linear amplifier with a range of 1pA to 1 $\mu$ A senses the current passing through the sample. The

topography and current image of the sample surface are measured simultaneously, enabling the direct correlation of sample local topography with its electrical properties. In this study, C-AFM was used to characterize the resistivity of the oxide between the pump and the probe line of a MR-device during sample preparation.

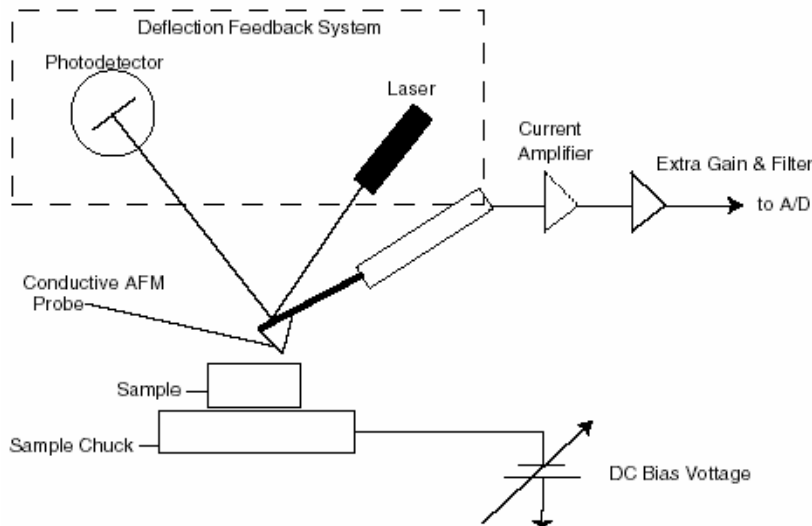


Figure 3.8:  
Conductive AFM

### 3.3.4. SCANNING ELECTRON MICROSCOPY (SEM)

*Scanning Electron Microscopy (SEM)* is used for characterizing surface topography, measuring line widths, and determining material properties [Kittel1966, www1].

In a SEM, a fine beam of high-energy electrons coming from an electron gun is scanned across the sample by scan coils, while a detector counts the number of low energy secondary electrons or back-scattered electrons given off from each point on the scanned surface. The signal obtained from these types of electrons conveys information on the topology of the sample.

We used SEM to calibrate the RIE and to estimate the quality of the steps formed in Si after the reactive etching.

### 3.4. SAMPLE PREPARATION AND CHARACTERIZATION

This section details the actual preparation and characterization of samples and devices used to realize high-frequency time-resolved experiments.

We present first in section 3.4.1. the coplanar wave-guide micro-fabrication and in section 3.4.2. the magnetic sample patterning using the two alternative methods: etching and lift-off. The MOKE and inductive studies require micron-sized magnetic samples (simple magnetic layers or multilayers) directly deposited on the pump CPW. The MR measurements were realized on similar micron-sized magnetic samples embedded in MR devices as presented in section 3.4.3. We present the different steps in MR device realization and its characterization. Then we discuss the disadvantages of the design resulting from the poor isolation between the pump and probe lines. Finally, we present two alternatives for the MR device fabrication, as perspectives for an improved MR device.

#### 3.4.1. COPLANAR WAVE-GUIDES PREPARATION

As mentioned in chapter 2, we used as transmission line the coplanar wave-guide (CPW) of micron-sized dimensions composed of metallic multilayers of the structure: [Ta(5nm)/Cu(50nm)] x 4 or x 5. They have been patterned on silicon substrate of high resistivity ( $5 \cdot 10^3$  and  $10^4 \Omega\text{cm}$ ) using UV and DUV lithography. The micron-sized CPW have been realized using both the etching and the lift-off technique (see section 3.2.2). Both processes use the same mask.

For the etching technique, the initial sample is the Si-substrate onto which continuous metallic layers have been deposited. The CPW were patterned by UV positive lithography and IBE.

For the lift-off technique, the initial sample is the Si-substrate. The CPW were patterned by UV negative lithography and metallic layer sputtering followed by lift-off.

The principal steps in the sample patterning are detailed in figure 3.9a.

We realized two CPW using these techniques, characterized by  $20\mu\text{m}$  centerline width by etching and respective  $50\mu\text{m}$  centerline width by lift-off. The border roughness was larger for  $20\mu\text{m}$  than for the  $50\mu\text{m}$  centerline width (see images from figure 3.9b). After several

experimental trials, we deduced that it was due to the UV lithography resolution (mask<sup>1</sup> + aligner) and was independent of the technique used.

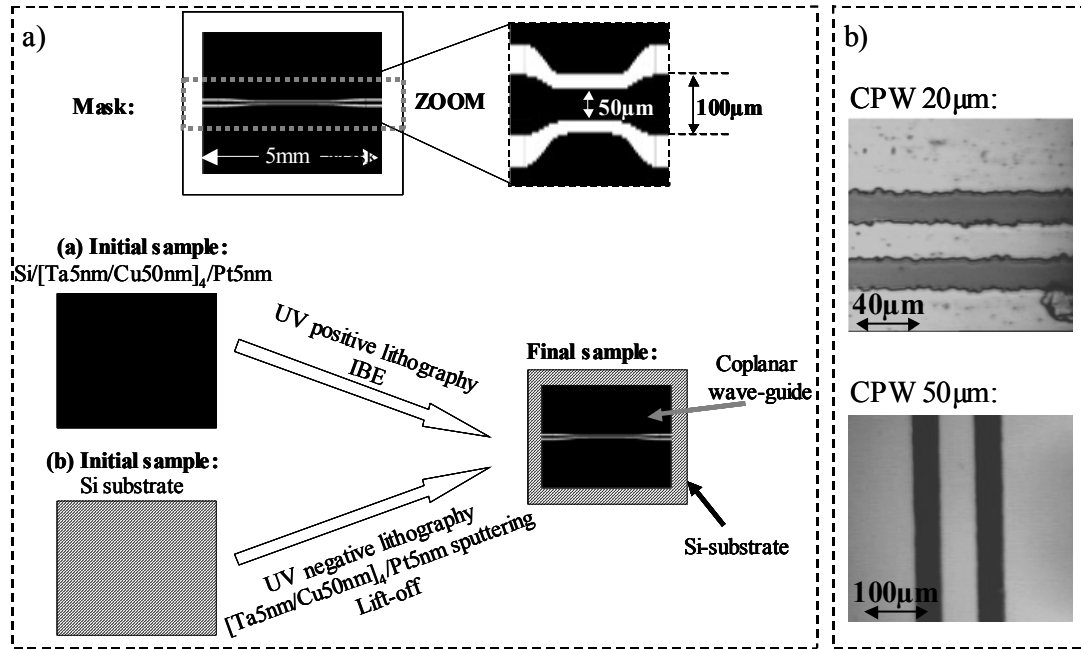


Figure 3.9

a) Coplanar waveguides patterning; b) AFM images of two CPW of 20 μm and respective 50 μm centerline width

### 3.4.2. MAGNETIC SAMPLE ELABORATION

All samples were directly grown on top of the [Ta5nm/Cu50nm]<sub>x</sub>n/Pt5nm buffer used in the coplanar waveguide elaboration. These samples, studied in MOKE or MR experiments, were either single magnetic thin films and spin-valves samples with a NiO or IrMn anti-ferromagnetic pinning layer.

#### a) MOKE samples

Single magnetic layers (NiFe) or NiO-based bottom spin valves samples of 20x40 μm<sup>2</sup> dimensions were patterned by lift-off on top of the CPW surface with a centerline of 50 μm width.

<sup>1</sup> The UV lithography was realized using masks printed on a latex substrate; the masque had already some irregularities on the line borders on the original design (in the range of some μm) and furthermore the resolution on the final mask depends on the width of the writing-line during the printing process of the mask (this was about 10 μm).

Four sets of magnetic structures were realized:

- (i) Single continuous NiFe layer: NiFe(5nm);
- (ii) A spin-valve structure: NiO(44nm)/Co(2.7nm)/Cu(3nm)/Co(0.2nm)/NiFe(10nm).
- (iii) The hard layer of the spin valve: NiO(44nm)/Co(2.7nm)/Cu(3nm);
- (iv) The soft layer of the spin valve: Cu(1nm)/Co(0.2nm)/NiFe(10nm);

Figure 3.10a presents the preparation processes and the mask used in the sample micro-fabrication. With a positive mask, and a negative UV resist, the micron-sized pattern of the mask was transferred on the centerline of a CPW. The sample was defined then by lift-off after the layer deposition by sputtering.

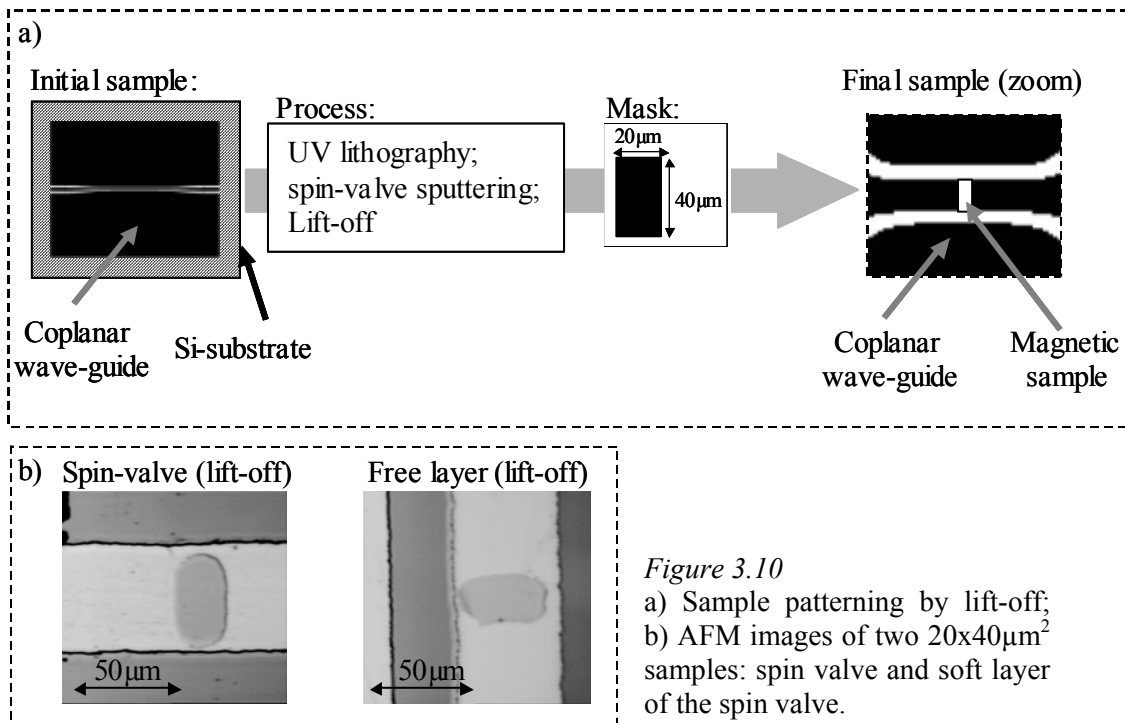


Figure 3.10

a) Sample patterning by lift-off;  
b) AFM images of two  $20 \times 40 \mu\text{m}^2$  samples: spin valve and soft layer of the spin valve.

In figure 3.10b, we present two AFM images obtained on two  $20 \times 40 \mu\text{m}^2$  samples, the spin valve, and soft layer of the spin valve.

The samples were deposited by sputtering at room temperature in Ar atmosphere at a pressure of  $2.7 \cdot 10^{-3}$  mbar. Prior to the deposition of magnetic layers an oxide layer ( $\text{Al}_2\text{O}_3$ ) of 40 nm thickness was deposited by sputtering.

#### b) MR magnetic samples

MR experiments were realized on IrMn based spin valves of  $4 \times 8 \mu\text{m}^2$  and  $2 \times 4 \mu\text{m}^2$ . The MR device requires two superposed transmission lines, realized at two levels, both

matched for the wave transmission in the 10 GHz range. One corresponds to the pump using sharp magnetic field pulses to excite the magnetic sample. The other line is to probe the static or dynamic MR signal.

The superposition of the two lines at a distance equal to the oxide thickness that is sputtered between them (about 50 nm), determines the presence of a RLC coupling between these lines as shown in figure 3.11. Parallel respectively perpendicular relative orientation of the two high frequency CPW determines different types of the coupling between the two lines:

- i) Resistive coupling determined by a direct contact between the two lines in the case when the oxide is not continuous;
- ii) Inductive coupling if a voltage pulse applied on the pump line induces a voltage in the probe line based on the induction law of Faraday.
- iii) Capacitive coupling due to the oxide between the two conductors.

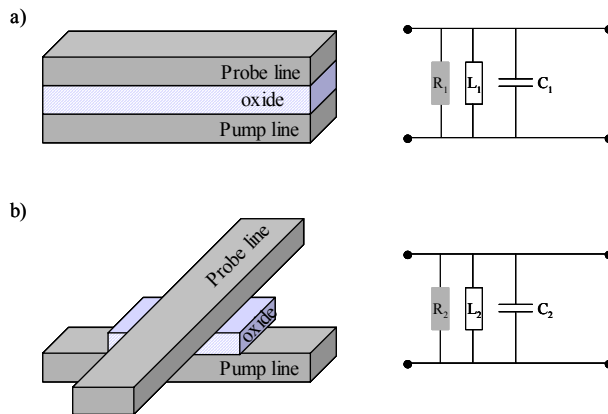


Figure 3.11

The RLC coupling between the pump and probe lines in a MR device

To minimize the coupling we have to decrease the inductance,  $L$ , and the capacitance  $C$ , and to increase the resistance,  $R$ . This is better achieved for a perpendicular geometry between the two lines. In this geometry, the inductance,  $L$ , is decreased since the magnetic field created by one line is parallel to the other. On the other hand, the capacitance values are decreased and the resistance values are increased by decreasing the superposed surface between the two conductors ( $C \sim S$ ,  $R \sim 1/S$ ). Increasing the oxide thickness will determine a decrease of  $L$  and  $C$  values, and an increase of  $R$ .

Calculations realized for coplanar waveguides [using software such as Txline and Serenade] have shown that the two lines should be isolated by a dielectric of large permittivity ( $\epsilon_r = 12.9$ ), a reduced loss tangent (0.001), and thickness larger than 1  $\mu\text{m}$ . If the isolation layer thickness is smaller than 1  $\mu\text{m}$  one can induce a strong electromagnetic coupling (“cross-talk”) between the two transmission-lines, which disturbs both the pump magnetic



field and the probed signal. As mentioned above a decrease of the *cross talk* was obtained by patterning the probe-line perpendicularly to the pump-line.

Different approaches for the fabrication of the insulating layer between the pump and probe lines have been tested in order to minimize the RLC coupling.

In the first approach, the insulating layer is deposited on top of the CPW (fig.3.12). However, several difficulties, which are described in the following, rendered this method less suited.

#### *SiO<sub>2</sub> - insulating layer*

We realized two similar processes to deposit SiO<sub>2</sub> on top of the CPW on a large surface equal to 4 x 5 mm<sup>2</sup> (fig.3.12).

In the first process – A (fig.3.12A), the SiO<sub>2</sub> is directly deposited on top of the patterned CPW. In this case, the insulating layer follows the pump-line profile, with large variations equal to the pump-line thickness (~250 nm). Furthermore, these large inhomogeneities of the sample surface propagate to the probe-line, inducing large variations in the probe-line cross-section that can be sources of reflections of high-frequency wave transmission.

In the second process – B (fig.3.12B), a quasi-uniform isolation between the two lines is obtained if the oxide thickness is thicker than the pump-line thickness ( $t_{\text{oxide}} \gg 250$  nm). The solution was to fill the gap of the pump-line with the insulating layer using the lift-off technique (see figure 3.4), before the deposition of further insulating layer on the entire surface of the sample, as shown in figure 3.12-B.

The difficulty of these two approaches (A and B) is given by the long time needed to realize the oxide deposition by sputtering (for a rate deposition of 3.4 nm/min the time necessary to deposit 250 nm is about 74 min!) on the available equipment during this thesis. Furthermore, the adherence of very thick oxide layers on metallic layers such as Pt or Cu was poor resulting in a damaged oxide layer for the subsequent preparation processes.

#### *Pyrallin-insulating layers*

A second approach was to replace the oxide-insulating layer obtained by magnetron sputtering with a special resin named Pyrallin. The advantage of this method consisted in the possibility to obtain a very thick insulating layer (about 5  $\mu\text{m}$  thickness) in a very short time by spin coating. Furthermore, after annealing of the resist at temperature and times following the sequences:

- 27 °C – 200 °C (4°/min) in air

- 200 °C – 30 min. in air
- 200 °C – 350 °C (2.5 °C/min) in nitrogen;
- 350 °C – 60 min. in nitrogen;
- gradually cooling to room temperature

the resist layer becomes insoluble in acetone or other solvents. This is a necessary condition for the subsequent preparation processes. Unfortunately, during the next step of sample elaboration, the Pyralin layer adherence proved to be bad and it partially came off the substrate surface.

In conclusion, the deposition of an insulating layer directly on the CPW over a large surface of 4 x 5mm was not optimum in this case.

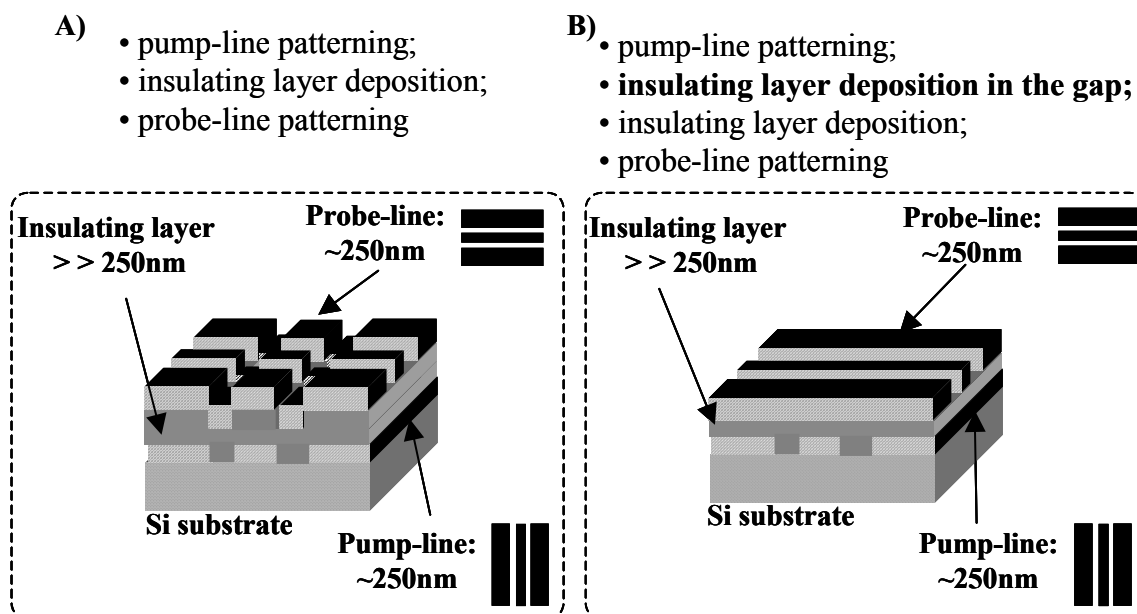


*Figure 3.12*  
First concept in MR sample preparation

The solutions chosen to optimize the sample preparation are discussed in the following.

### *Unique-ground plane*

Firstly, to obtain the sample planarization before the deposition of the probe-CPW, instead of depositing an oxide layer in the pump-CPW gap as presented above in figure 3.12B we have chosen to embed the pump-CPW and the oxide layer in Si substrate<sup>2</sup>.

Secondly, to improve the insulating layer adherence to the metallic surface, we minimized the surface where the pump-CPW and probe-CPW were superposed. This was achieved by using a unique ground plane.

This process has 4 steps (see figure 3.13) which are presented in the following.

- i) The pump-CPW that contains the unique ground plane for both pump and probe CPW and the terminations of the probe-CPW centerline are embedded in Si (figure 3.13-1).
- ii) The micron-sized samples of dimensions:  $2 \times 4 \mu\text{m}^2$  and  $4 \times 8 \mu\text{m}^2$ , are obtained by IBE as shown in figure 3.13 – 2.
- iii) The etching (ionic or reactive) of the contact regions “to open” the contacts (fig. 3.13 – 3).
- iv) CIP contacts patterning by lift-off as shown in figure fig. 3.13 – 4.

In the following section, each step of this procedure and its step-by-step characterization are described more in detail.

---

<sup>2</sup> Ideally we should embed completely the pump-CPW and the oxide layer in Si. In reality, when we are depositing the stack 1 (see process steps presented in figure 3.13) it is possible that i) a part of the thickness of the oxide is outside the Si (if  $t_{\text{pump-line}} < t_{\text{RIE}} < t_{\text{pump-line}} + t_{\text{oxide}}$ ) or ii) a part of the magnetic stack is also embedded in Si (if  $t_{\text{pump-line}} + t_{\text{oxide}} < t_{\text{RIE}} < t_{\text{pump-line}} + t_{\text{oxide}} + t_{\text{spin-valve}}$ ).

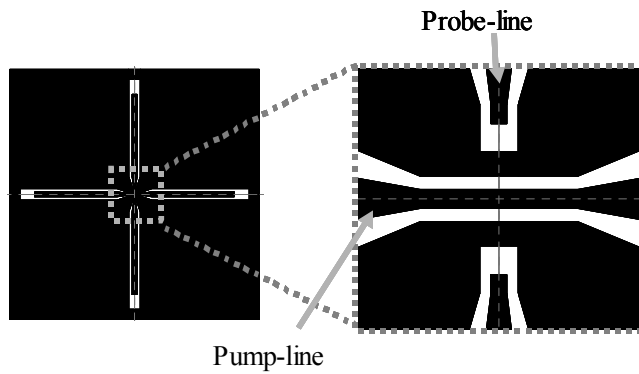
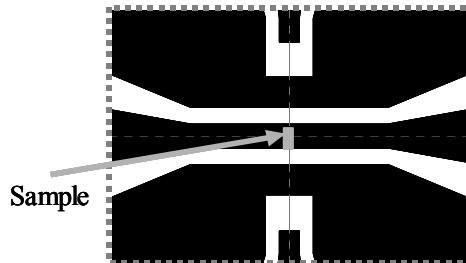
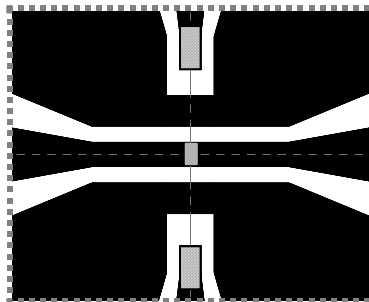
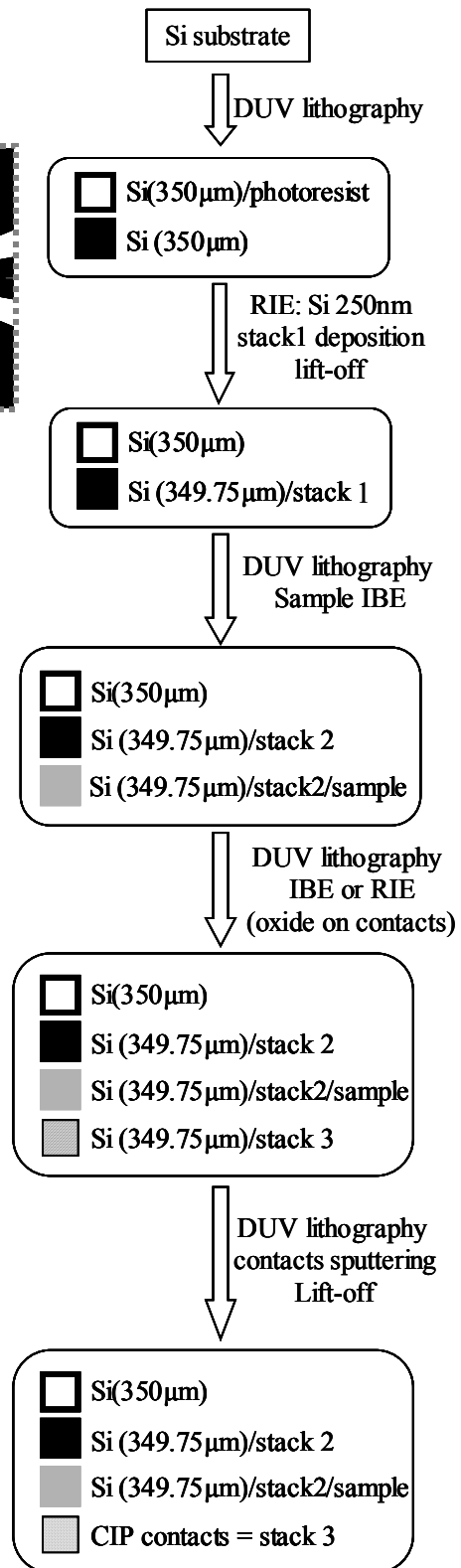
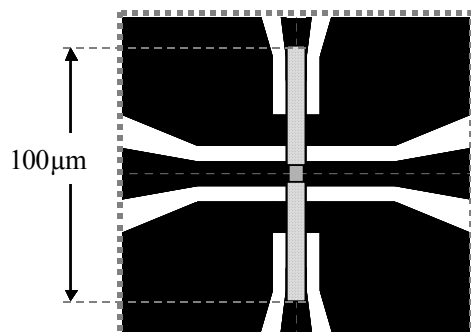
Step no.1Step no.2Step no.3Step no.4

Figure 3.13 Lithographical procedure in MR sample elaboration

**Stack 1:** [Ta5nm/Cu50nm]<sub>5</sub>/SiO<sub>2</sub>50nm/Ta5nm/NiFe3nm/IrMn7nm/Co3nm/Cu2.5nm/Co1nm/NiFe4nm/Pt2nm

**Stack 2:** [Ta5nm/Cu50nm]<sub>5</sub>/SiO<sub>2</sub>50nm;

**Stack 3:** [Ta5nm/Cu50nm]<sub>5</sub>;

### 3.4.3. SAMPLES PREPARATION FOR DYNAMIC MR MEASUREMENTS

#### Step no.1: CPW embedding in Si substrate (fig. 3.13 – 1)

The pattern transfer of the CPW in Si is realized using the DUV negative lithography on a UVN2 photo-resist through a positive mask<sup>3</sup>. The CPW profile has been obtained with a negative contrast (i.e. the Si substrate that is not-covered with the resist corresponds to the CPW). In the next step the samples were introduced in the vacuum chamber of the RIE installation. We have experimented two RIE processes using as reactive gases either ( $\text{SF}_6 + \text{O}_2$ ) or ( $\text{SF}_6$ ). SEM images (presented in figure 3.14) were obtained on the etched samples, after the cleaning of the sample surface of the resist in acetone in an ultrasonic bath.

RIE with respect to IBE yields an *isotropic* etching. This means that the etching process may occur under the photo-resist layer, which normally is used to protect the surfaces that it covers. Thus for long etching times and for a ratio: etched width / etched depth  $< 1$  the profiles of the walls might become oblique. To avoid this, usually, oxygen can be mixed with  $\text{SF}_6$  as the reactive gas at low pressure. The inconvenience is the large value of the etching velocity of the resist by oxygen<sup>4</sup>.  $\text{SF}_6$  etches also the resist but with a reduced etching rate. In our case, the resist thickness is equal to the etching depth (about  $0.3\ \mu\text{m}$ ). As we are interested in keeping the resist on the sample surface after the RIE process, we had to make a compromise between the gasses to use and the etching time.

Several RIE procedures were tested.

The first one corresponds to an etching time of about 64 minutes in  $\text{SF}_6$ . We observed that after etching there was no resist on the sample surface, the etching time being much longer than the resist etching time. The complete etching of the resist layer was not good for the next two processes: the deposition of stack1 and its subsequent lift-off (that are presented in the next paragraphs). However, the etching depth was about  $3.55\ \mu\text{m}$  and the walls were vertical and very well defined as we can observe on the image from figure. 3.14A.

The second case corresponds to a smaller etching time, about 2 minutes in  $\text{SF}_6$ . The image presented in figure 3.14B shows that the etched depth was about  $0.32\ \mu\text{m}$  with well-defined vertical walls. Moreover, the resist was not completely etched.

In the third case, for the same etching time but using an ( $\text{SF}_6 + \text{O}_2$ ) atmosphere, the etched depth was of about  $0.4\ \mu\text{m}$  as shown in figure 3.14C.

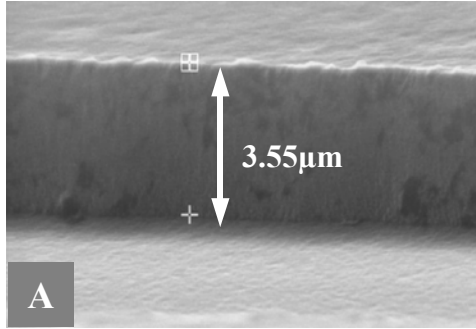
---

<sup>3</sup> All the masks have a positive contrast;

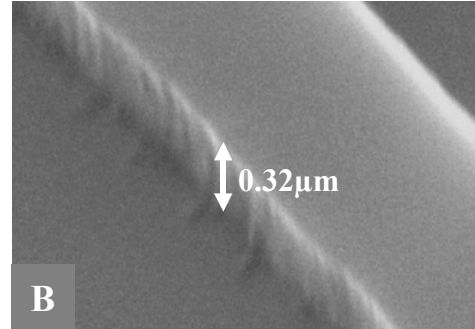
<sup>4</sup> Oxygen is often used to clean the samples surfaces of resist residues

No difference between the wall profiles corresponding to the absence or presence of oxygen in the etching chamber was observed. Thus, we decided to use only  $\text{SF}_6$  as etching reactive gas for 2 minutes as etching time.

$T_{\text{RIE}} = 64\text{min}; \text{SF}_6$



$T_{\text{RIE}} = 2\text{min}; \text{SF}_6$



$T_{\text{RIE}} = 2\text{min}; \text{SF}_6 + \text{O}_2$

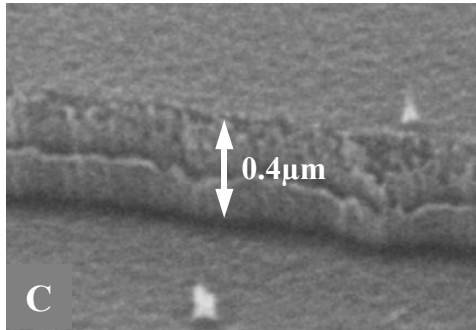


Figure 3.14  
SEM images on etched Si substrates using RIE

The next process of step no.1 (fig.3.13) consists in the deposition by sputtering of the wave-guide metallic layers, the  $\text{SiO}_2$  - insulating layer and spin-valve magnetic layers:

$$[\text{Ta}5\text{nm}/\text{Cu}50\text{nm}]_s/$$

$$\text{SiO}_2 50\text{nm}/\text{Ta}5\text{nm}/\text{NiFe}3\text{nm}/\text{IrMn}7\text{nm}/\text{Co}3\text{nm}/\text{Cu}2.5\text{nm}/\text{Co}1\text{nm}/\text{NiFe}4\text{nm}/\text{Pt}2\text{nm}$$

on the entire surface without removing the resist that remains in the CPW gap regions.

The last process of step no.1 corresponds to the lift-off. One of the conditions to accomplish is:

$$\text{Total sputtered thickness} < \text{etching depth} + \text{resist thickness}$$

In our case, this condition is fulfilled since the total sputtered thickness was about 352.5 nm, the etching depth about 320 nm, and the resist thickness larger than 100 nm<sup>5</sup>. Compared to the usual case the lift-off process required a longer time in acetone plus ultrasonic bath because the resist was hardened during the RIE and sputtering deposition.

<sup>5</sup> Here, we have the case:  $t_{\text{pump-line}} (275\text{nm}) < t_{\text{RIE}} (320\text{nm}) < t_{\text{pump-line}} (275\text{nm}) + t_{\text{oxide}} (50\text{nm})$  when a part of the oxide layer thickness is not embedded.

For a perfect planarization, before the sputtering of the CIP contacts, the difference between the deposition level and Si-level should be zero. We measured this level using the tapping AFM technique. For a sample with a 2  $\mu\text{m}$  wide centerline, the difference between the Si and sputtered layer levels was about 3.5 nm (fig. 3.15A). For a sample with 10  $\mu\text{m}$  width of the CPW centerline, this difference was about -6.8 nm (fig. 3.15B). The difference between the two cases is probably due to the calibration precision of the RIE process that introduces discrepancies larger than 10 nm. These values (3.5 nm or 6.8 nm) are much smaller than the CIP contacts thickness (275 nm) that will be deposited in the last step. Hence a relatively good planarization is obtained with this method. The peaks observed in figure 3.15 correspond to holes on the sample surface located at the line borders between the deposited stack and Si. These could induce contacts between the pump and the probe lines. This aspect has been characterized after the next step of the process (*magnetic sample patterning*) and will be discussed in the next paragraphs.

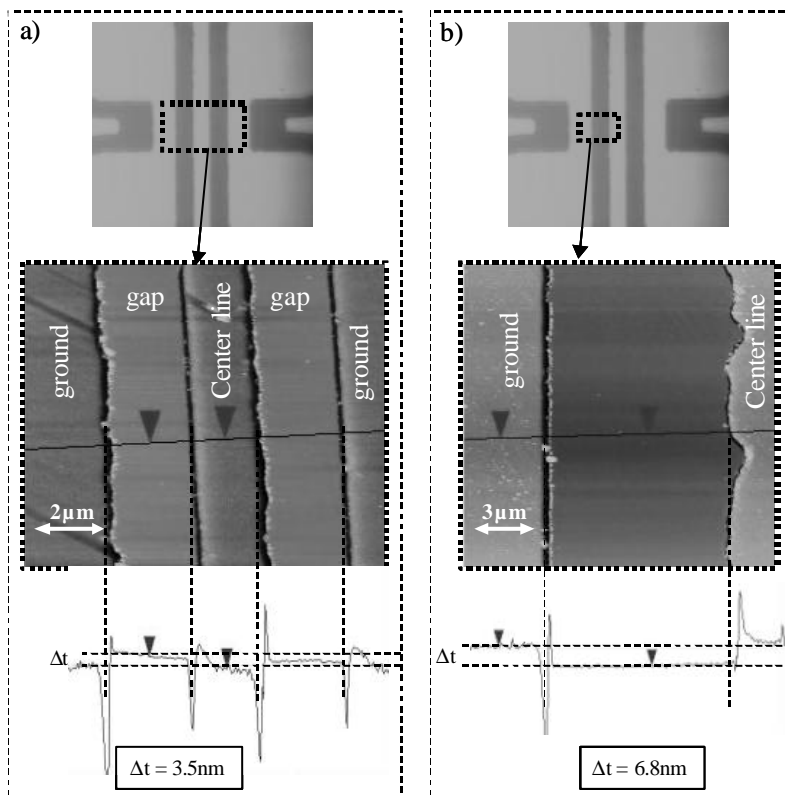


*Figure 3.15*  
Sample analysis after step no.1  
using the tapping AFM  
technique

*Step no.2: Magnetic sample patterning (fig 3.13-2)*

The magnetic sample patterning contains two processes: the positive DUV lithography to define the sample geometry and Ion Beam Etching. The lithography was realized by using the positive photo-resist: UV3.

The resolution of the lithographic process using this resist with DUV radiation is about 0.5  $\mu\text{m}$ . In our case, the minimum sample dimensions that are designed on the masks are about  $1 \times 2 \mu\text{m}^2$ . All the lithography steps were realized after the alignment between two successive masks. Since the microscope objective of the aligner had an insufficient spatial resolution, the alignment of a  $1 \times 2 \mu\text{m}^2$  dot on a 2  $\mu\text{m}$ -width line was not possible. In conclusion, the resolution of the entire process limits the size of devices designed for MR measurements to about  $2 \times 4 \mu\text{m}^2$ .

In order to limit the material re-deposition on the sample borders during the IBE, the sample substrate is rotating in a plane inclined with  $30^\circ$  with respect to the vertical direction. The calibration of the IBE need to be very exact since the etching should be stopped at the 50 nm oxide layer. This is a very important condition to respect because this oxide represents the insulating layer between the pump- and probe- line.

The oxide layer was characterized in contact-AFM experiments. The images presented in figure 3.16 show the oxide conductivity map, obtained with the conductive AFM technique, in comparison with the topographic map.

Considering a bias voltage of 45,67 mV between the ground plane of the CPW and the AFM conductive tip, the 333 pA current peak shows a decrease of the electrical resistance at the border between the ground plane of the CPW and the silicon of about 137  $\text{M}\Omega$ . This is equivalent to a short circuit between the ground plane of the CPW and the tip through the oxide layer. On the topographic image, we observe that the region of reduced resistance corresponds to a “hole”, of about 125 nm depth and 156 nm width, which is due to the non-uniform deposition of the entire stack near the etched borders.

In order to reduce the possibility of a short circuit between the CIP contacts and the lower CPW, an additional oxide layer of 30 nm was deposited using the lift-off technique, keeping the resist on the sample<sup>6</sup>.

---

<sup>6</sup> The resist used to etch the magnetic sample.



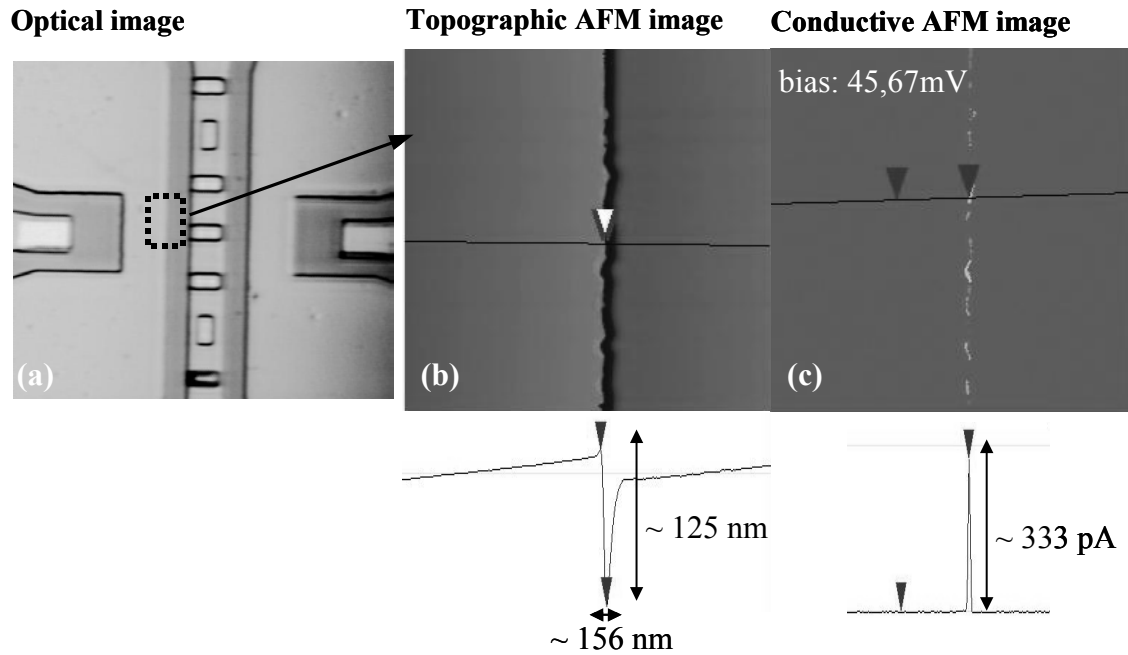


Figure 3.16

(a) Optical image of the sample obtained with the AFM optical microscope; (b) Topographic and (c) conductive AFM images corresponding to the edges between the waveguide gap and its ground plane.

Step no.3: Oxide etching to define the contacts on the probe-line (fig 3.13-3)

After step 2 the sample is completely covered with 80 nm of  $\text{SiO}_2$  except the spin valve sample. The next step consists in opening windows in the oxide in order to define the CIP contact regions. Consequently, this step contains a negative DUV lithography and an IBE process. This requires a precise calibration in order to be sure to etch the entire oxide layer (etched thickness  $\gg 80$  nm). Tapping AFM images have been realized in order to measure the etching depth. In figure 3.17 we observe that there is a difference of about 131 nm between the oxide and etched levels. This means that the metallic layers have been over-etched by a depth equal to 51 nm. Since the total thickness of the metal thickness is 275 nm, 50 nm less is not important and will be filled by subsequent deposition of the CIP contacts.

Measuring the misalignment between the contact hole and the probe-line observed in figure 3.18, we can estimate the alignment precision during the DUV lithography, which in this case is between 1  $\mu\text{m}$  and 2  $\mu\text{m}$ .

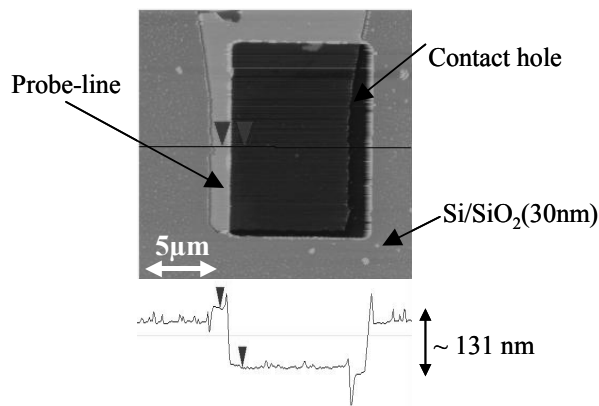
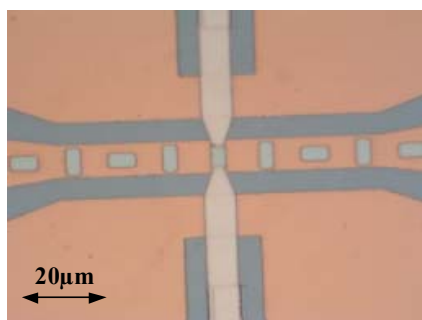


*Figure 3.17*  
AFM characterization of the etched depth during the third step

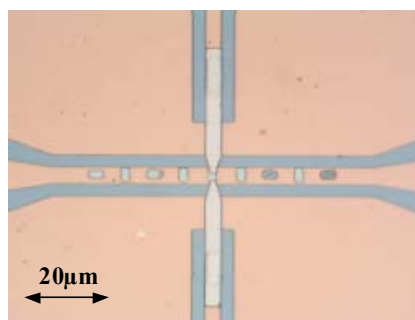
Step no.4: CIP contact deposition (fig 3.13-4)

This step contains the DUV negative lithography that defines the CIP contact lines, the sputtering deposition of the multilayer:  $5 \times [\text{Ta}(5\text{nm})/\text{Cu}(50\text{nm})]/\text{Pt}(2\text{nm})$  and the lift-off. In this case, the alignment is very important since the overlap region between the probe line and the sample is  $1 \mu\text{m}$  long. Figure 3.18 presents optical images of the final samples.

The process presented above for the preparation of MR devices has some disadvantages mostly related to the RLC coupling between the pump and probe line. This coupling is determined on the one hand by the direct contact between the lines and on the other hand by the low thickness of the insulating layer. This can be corrected by inverting and improving several steps as is presented in the following two alternatives.



$4 \times 8 \mu\text{m}^2$  samples dimensions;  
 $10 \mu\text{m}$  centerline width;  
 $6 \mu\text{m}$  gap between the contacts on the sample.



$2 \times 4 \mu\text{m}^2$  samples dimensions;  
 $5 \mu\text{m}$  centerline width;  
 $3 \mu\text{m}$  gap between the contacts on the sample.

*Figure 3.18*  
Optical images of the final samples previewed for MR measurements

#### **3.4.4. FIRST ALTERNATIVE PREPARATION PROCESS FOR DYNAMIC MR DEVICES**

This alternative is very similar to the previous one and it contains an improved isolation between the pump and probe line. It is currently being tested in collaboration with LETI – CEA, Grenoble and has not been realized throughout this work.

The main idea is to realize the complete embedding of the metallic CPW in silicium. This is realized using step 1 of the previous process (fig.3.13) but with a stack 1 consisting of [Ta/Cu]<sub>5</sub>. In step 2 a thick oxide layer (thicker than 500 nm) is deposited on the entire surface. The third step corresponds to the sample preparation by lift-off. This requires a deposition of the spin-valve and then its etching. Since the magnetic properties of the spin valve are influenced by the oxide roughness, before step 3 the entire surface of the oxide is planarized up to a roughness value similar to the one of the initial substrate (RMS ~ 1-2 Å). Step 4 consists in the opening of the contacts in the oxide and the final step corresponds to the CIP contact deposition by lift-off.

#### **3.4.5. SECOND ALTERNATIVE PREPARATION PROCESS FOR DYNAMIC MR DEVICES**

The second alternative corresponds to an inversion of the steps presented in figure 3.13. and is about to be tested in collaboration with LETI – CEA, Grenoble.

The first step corresponds to the magnetic sample preparation by lift-off directly onto the substrate. In step no. 2, the CIP contacts are deposited by lift-off on the sample. The third step consists in the deposition of a thick layer of oxide on the entire sample. In the fourth and fifth steps the pump line, the probe lines and the ground plane are deposited by lift off realizing the contacts on the lower CIP contacts. In this way, the non-uniformities that appear between the metallic surfaces and the Si in the first process are avoided.

## **CHAPTER 4:**

### ***MAGNETIZATION DYNAMICS***

#### ***IN MICRON-SIZED SPIN VALVE ELEMENTS***



**Abstract**

*In this chapter, we present experimental results obtained with time-resolved pump-probe techniques. The probe consists of longitudinal and transversal Magneto-Optical Kerr Effect (MOKE) and the MR effect. The samples consist of NiO and IrMn based spin-valves and NiFe magnetic thin films.*

*We obtained the magnetization reversal by precession in  $20 \times 40 \mu\text{m}^2$ - sized NiO based spin-valves and NiFe continuous magnetic thin films deposited on a glass substrate. FMR-type experiments were realized to measure the uniaxial anisotropy field.*

*Quasi-static measurements were realized using both MOKE and MR effect. Similar results have been obtained on NiO and IrMn based spin-valve samples. These were influenced by a very complex magnetic structure of the free layer of the spin valves.*

*Macrospin simulations have been realized to explain some aspects of the magnetization precessional movement.*

**Résumé**

*Dans ce chapitre, nous présentons les résultats expérimentaux obtenus en utilisant les techniques pompe-sonde résolue en temps. Comme sonde, nous avons utilisé l'effet Kerr magnéto-optique dans les configurations longitudinale et transversale et l'effet magnéto-résistif. Nous avons ainsi étudié des structures de type vanne de spin (couches continues et plots de taille micrométrique) et des couches continues de NiFe déposées sur un substrat de verre.*

*Nous avons obtenu le renversement par précession dans des plots de  $20 \times 40 \mu\text{m}^2$  (avec un empilement de type vanne de spin ou seulement une couche libre) et dans les couches continues de NiFe déposées sur verre. Des mesures de type RFM nous ont permis de mesurer le champ d'anisotropie uniaxiale.*

*En utilisant l'effet Kerr et l'effet magnéto-résistif, nous avons réalisé des mesures quasi-statiques. Les résultats sont similaires sur différents échantillons (vannes de spin avec NiO ou IrMn comme couche antiferromagnétique) en étant influencés par la structure magnétique très complexe de la couche libre.*

*Des simulations macrospin ont été réalisées pour expliquer certains aspects liés au mouvement précessionnel de l'aimantation.*

## 4.1. INTRODUCTION

In this chapter, experimental results obtained using the time-resolved longitudinal and transversal MOKE and the MR effect are presented. The samples consist of NiO and IrMn based spin-valve elements of micron-size.

The results are organized as follows.

Section 4.2 is dedicated to the static characterization of micron-sized NiO-spin valves. From the static hysteresis loops obtained with MOKE the anisotropy and the coercive field values are deduced, while MFM imaging is used to characterize the magnetic homogeneity of the sample. In section 4.3 the dynamic response to easy axis and hard axis field pulses is presented using the time-resolved stroboscopic MOKE. The dynamic response for weak pulses is used to study the damped oscillations towards equilibrium from which the ferromagnetic resonance frequency is deduced. Subsequently, the reversal under strong field pulses is investigated (precessional switching). The characteristic parameters of the precessional switching are deduced by comparing the experimental results with the results obtained from macrospin simulations.

In section 4.4 results on the static and dynamic MR measurements are presented for IrMn based spin-valve structures. Quasi-static MR experiments evidenced the partial switching by precession of the sample magnetization. The low signal/noise ratio did not allow us to obtain a time resolved signal from these structures. This has been caused by an important cross-talk between the read and write line as well as by the low value of the magnetic field pulse amplitude obtained with the MR device. In consequence, the MR device was characterized in order to distinguish the sources of the cross-talk, and the possibilities to minimize it.

Section 4.5 presents preliminary results on the precessional reversal obtained in continuous films of permalloy deposited on a glass substrate.

## 4.2. STATIC MOKE MEASUREMENTS OF NiO-BASED SPIN VALVES

Both continuous films and micron-sized lithographically patterned spin valve elements have been statically and dynamically characterized using the Magneto-Optic Kerr Effect (MOKE).

The NiO-based bottom spin valve structure is:

$$\text{NiO}(25\text{nm})/\text{Co}(2.7\text{nm})/\text{Cu}(3\text{nm})/\text{Co}(0.2\text{nm})/\text{NiFe}(10\text{nm})$$

The micron-sized elements were patterned by optical lithography to a size of  $20 \times 40 \mu\text{m}^2$  on top of the centerline of a  $[\text{Ta}(5\text{nm})/\text{Cu}(50\text{nm})] \times 4/\text{Pt}(5\text{nm})$  coplanar waveguide of  $50 \mu\text{m}$  width. The fabrication of these samples has been described in chapter 3.

This spin-valve is composed of the magnetic soft bi-layers:  $\text{Co}(0.2\text{nm})/\text{NiFe}(10\text{nm})$  and the hard bi-layers:  $\text{NiO}(25\text{nm})/\text{Co}(2.7\text{nm})$  separated by a non-magnetic spacer of  $\text{Cu}(3\text{nm})$ . The  $\text{Co}(2.7\text{nm})$  layer is exchange coupled to the NiO layer that was deposited at oblique incidence to obtain a strong uniaxial anisotropy. In this case, the exchange coupling between the NiO anti-ferromagnetic layer and the adjacent Co layer results in an enhanced coercivity of the pinned Co layer rather than in a shift in the hysteresis loop [Chopra2000, Chopra 2000B, Cartier 2002]. No annealing was performed on these samples. The role of the thin  $\text{Co}(0.2\text{nm})$  layer at the interface between Cu spacer and the free NiFe layer is to obtain the maximum difference in scattering rates of spin “down” and spin “up” electrons at the Co/Cu interfaces. [Parkin1993, Dieny1994]. The Cu-spacer thickness is chosen to be of 3nm. This value is a compromise since a smaller value ( $\sim 1 \text{ nm}$ ) would lead to an increased coupling between the two ferromagnetic layers (due to the presence of pinholes or strong magnetostatic coupling in this range of the spacer thickness) while a larger value decreases the flux of the polarized electrons transmitted from one ferromagnetic layer to the other [Dieny1991].

The hysteresis curves, obtained on continuous films using MOKE and Vibrating Sample Magnetometer (VSM), are presented in figure 4.1.



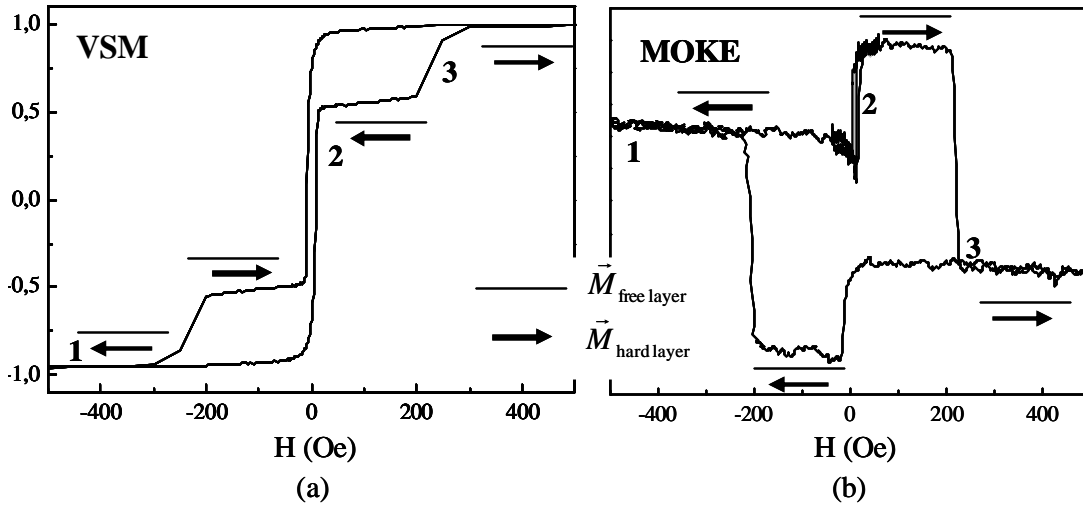


Figure 4.1

(a) VSM and (b) MOKE hysteresis loops obtained on the continuous film of NiO-based bottom spin-valve

The VSM clearly shows the reversal of the soft layer for a coercive field value of about 11 Oe and of the hard layers corresponding to a larger coercive field value of about 250 Oe (fig.4.1a). Similar results were obtained using MOKE (fig.4.1b). The different shapes of the loops obtained by VSM and by MOKE are explained by opposite signs of the Kerr reflectivity of the Co and NiFe layers [Kim 2002]. The minor loop (point 2 in fig 4.1 a) measured with MOKE is shifted by 8 Oe with respect to zero field indicating the existence of a weak orange-peel coupling between the two layers.

As it is shown in figure 4.1, points 1 and 3 correspond to the magnetic state where the magnetization of the soft and the hard layers are *parallel* while the flat region between points 2 and 3 corresponds to the anti-parallel magnetic state. In applications these two distinct magnetic states correspond to the logical value “0” and “1” respectively.

#### 4.2.1. MICRON-SIZED ( $20 \times 40 \mu\text{m}^2$ ) RECTANGULAR ELEMENTS

The static characterization of micron-sized NiO-based spin-valves has been realized using MFM and MOKE experiments. Three different magnetic samples of the same lateral dimensions ( $20 \times 40 \mu\text{m}^2$ ) but different multilayer structures have been lithographically patterned on top of a CPW with  $50 \mu\text{m}$  centerline width (fig.4.2).

- i) The first sample corresponds to the soft layer:

$$\text{Cu}(3\text{nm})/\text{Co}(0.2\text{nm})/\text{NiFe}(10\text{nm})$$

- ii) The second one represents the hard layer:

$$\text{NiO}(44\text{nm})/\text{Co}(2.7\text{nm})/\text{Cu}(3\text{nm})$$

iii) The third is the entire spin-valve structure:

$$\text{NiO}(25\text{nm})/\text{Co}(2.7\text{nm})/\text{Cu}(3\text{nm})/\text{Co}(0.2\text{nm})/\text{NiFe}(10\text{nm})$$

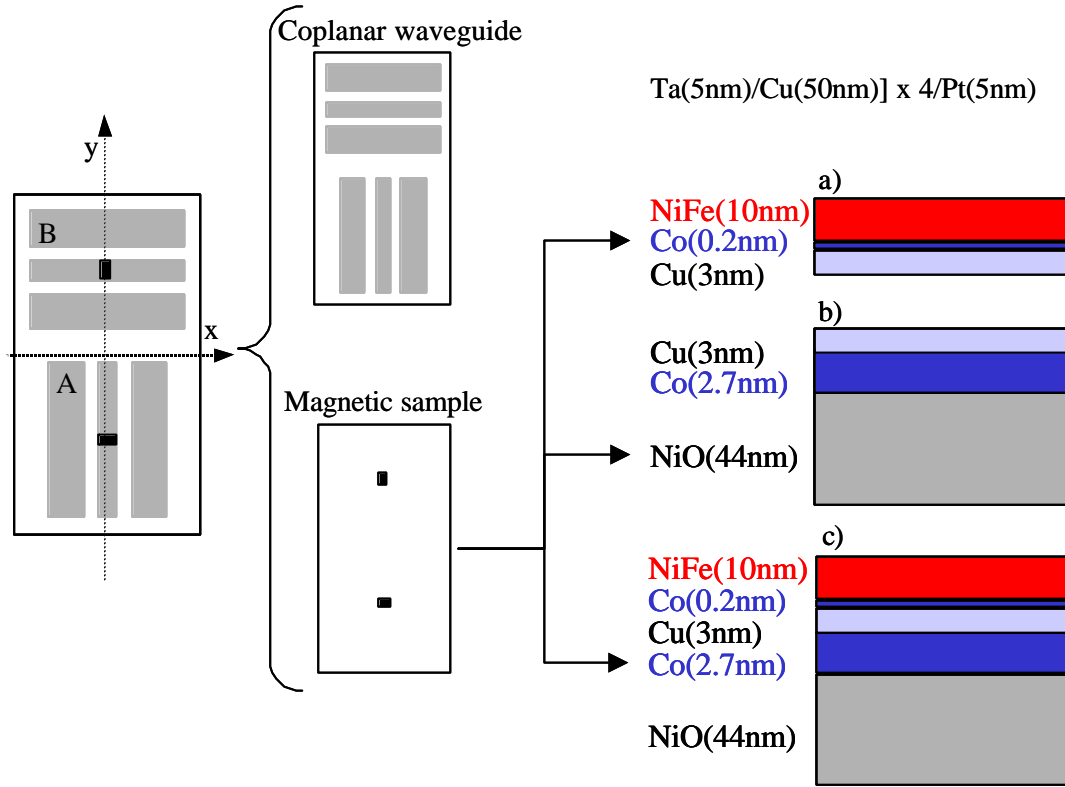


Figure 4.2.

Micron-sized NiO-based samples derived from the spin valve structure: (a) soft layer; (b) hard layer; and (c) the entire NiO-based spin-valve

All these samples have been deposited by sputtering. A uniaxial anisotropy has been induced parallel to the  $oy$ -direction as shown in figure 4.2. Two types of geometries have been realized for each of the three magnetic samples presented above (i, ii and iii). These two geometries differ by the orientation of the element long axis as well as the orientation of the easy axis with respect to the stripline. Notably, for

- sample geometry (A), the easy axis (E.A) is perpendicular to the magnetic field pulse ( $h_p$ ),
- sample geometry (B), the easy axis (E.A) is parallel to the magnetic field pulse ( $h_p$ ).

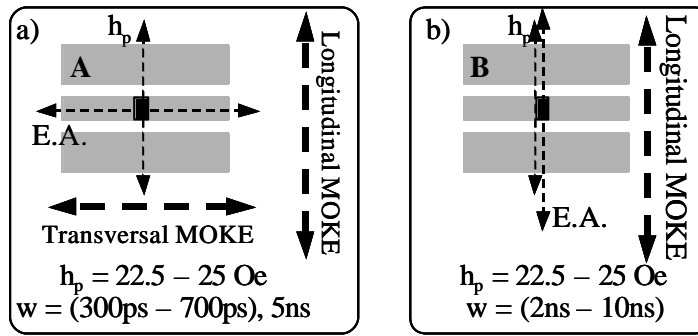


Figure 4.3  
Measurement configurations in the MOKE experiment

#### 4.2.2. STATIC MFM CHARACTERIZATION

Magnetic Force Microscopy (MFM) was used to characterize the magnetic domain structure of the samples. MFM images of the isolated free layer (fig.4.4) reveal a magnetic contrast similar to a magnetization ripple structure [Hoffman 1968, Hubert 1998], which reflects the irregular polycrystalline nature of the films deposited by sputtering.

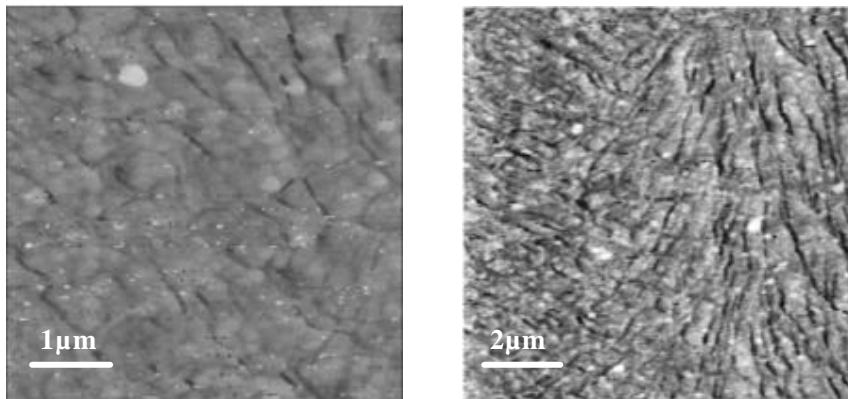
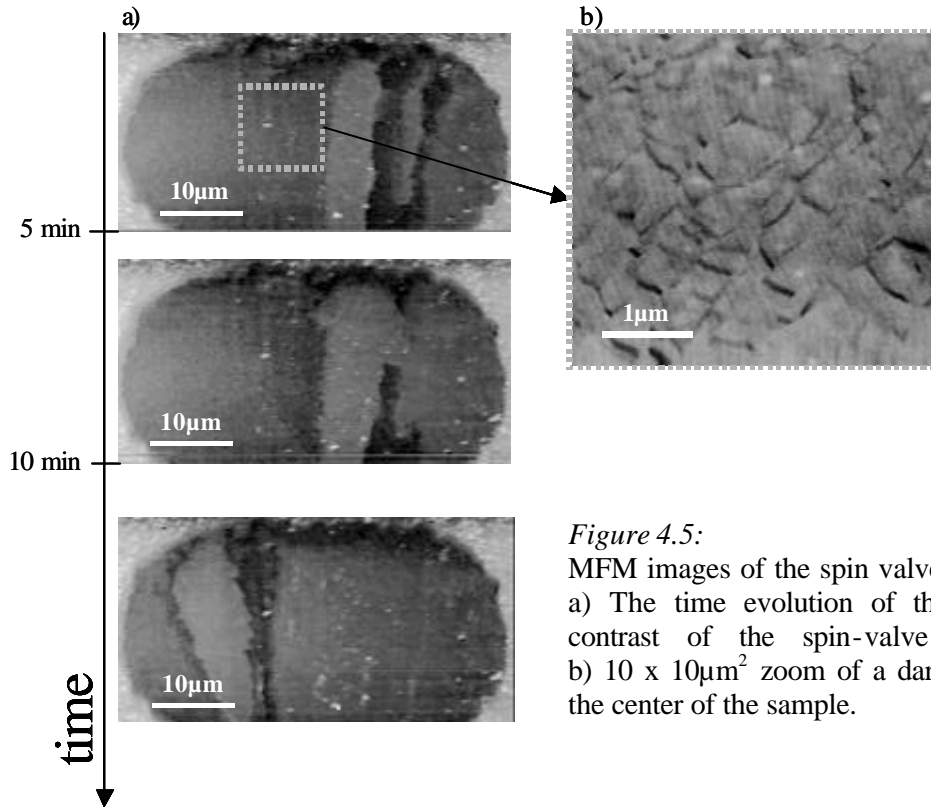


Figure 4.4:  
MFM images of the isolated free layer in the center of the rectangular sample

The corresponding images in figure 4.5a of the entire spin-valve rectangle reveal the existence of “white” and “black” regions. The white regions increase its surface in time most likely due to the MFM tip stray field upon scanning across the element (no external field has been applied). A zoom reveals that the two regions correspond to two “magnetic domains” where the ripple magnetic structure is more or less dense. For example, the zoom in figure 4.5b of a dark region shows a dense ripple contrast, similar to the contrast of the isolated free layer of figure 4.4.



*Figure 4.5:*  
MFM images of the spin valve rectangle:  
a) The time evolution of the magnetic contrast of the spin-valve rectangle;  
b) 10 x 10 μm<sup>2</sup> zoom of a dark region in the center of the sample.

#### 4.2.3. STATIC MOKE MEASUREMENTS

Static MOKE measurements were performed on 20 x 40 μm<sup>2</sup> magnetic samples along the easy and hard axis direction. From this, the easy axis coercivity and the in-plane uniaxial anisotropy field values are estimated. It is reminded that the spatial resolution is of 15 x 15 μm<sup>2</sup> determined by the laser spot diameter. The hysteresis loops, measured for all samples presented above, are given in figure 4.6.

The coercive fields of the isolated (Co/NiFe) soft layer are about 3.5 Oe for sample A and 3.8 Oe for sample B, while the corresponding anisotropy fields are 20 Oe for sample A and 15 Oe for sample B.

The coercive fields of the isolated hard layer are about 175 Oe for sample A and 140 Oe for sample B, while the corresponding anisotropy fields are greater than 600 Oe.

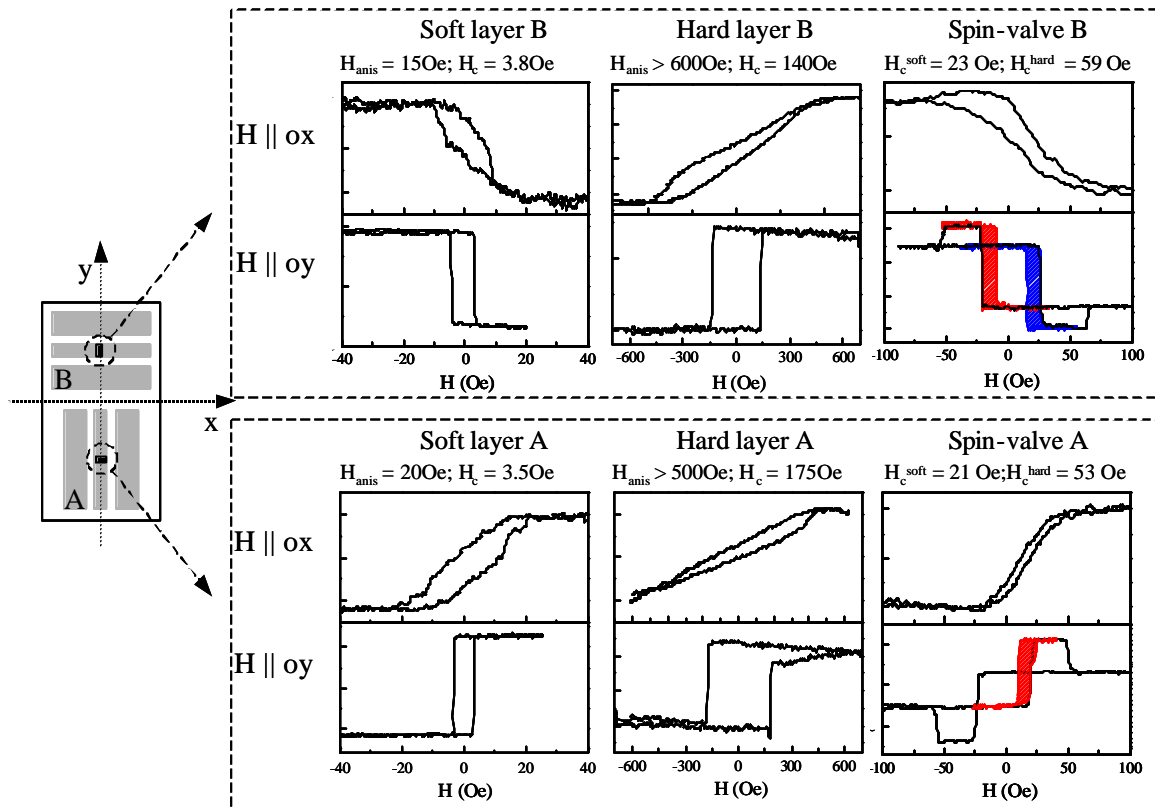


Figure 4.6:

MOKE hysteresis loops for micron-sized samples for external fields applied parallel to the  $ox$ - and  $oy$ - axis respectively; the minor hysteresis loops for the spin-valve samples correspond to the filled-color regions.

On the hysteresis loops of the entire spin valves, we observe a coercive field of about 21 Oe (sample A) and 23 Oe (sample B) for the soft layer and 53 Oe (sample A) and 59 Oe (sample B) for the hard layer. The minor hysteresis loop of the integrated soft Co/FeNi layer is shifted by 17 Oe, which is attributed to a dipolar coupling between the hard and the soft layer.

### 4.3. DYNAMIC MOKE STUDIES OF NiO-BASED SPIN VALVES

The study of different dynamical processes (precessional reversal, relaxational processes and small angles precessions) has been realized using both the longitudinal and the transversal MOKE configurations on both sample A and sample B, as shown in figure 4.3.

Samples of type A are oriented such that the magnetic field pulse is perpendicular to the easy axis. This corresponds to the configuration necessary to induce the precessional reversal as well as small angle oscillations. The small amplitude oscillations have been followed using the longitudinal Kerr effect to probe the magnetization component perpendicular to the easy axis. For the precessional reversal both the longitudinal and transverse Kerr effect have been used.

Samples of type B are oriented such that the magnetic field pulse is parallel to the easy axis. (fig.4.3b). For these structures, only partial reversal followed by relaxational processes were observed. We used as pump magnetic field pulses parallel to the easy axis with durations between 2 ns and 10 ns, and as probe, the longitudinal MOKE, sensitive to the magnetization component parallel to the pump magnetic field.

In all cases, the maximum voltage fixed on the pulse generator, 10 V, determined the amplitude of the magnetic field. Experimentally we observed that for the same amplitude, 10 V, pulses shorter than 500 ps have a real amplitude that is smaller than 10 V. For instance, a pulse of 200 ps duration and of  $U_0 = 10$  V has an amplitude of about  $90\% * U_0$ , i.e. 9 V. The magnetic field values corresponding to pulse amplitudes between 9 V and 10 V, vary between 22.5 Oe and 25 Oe <sup>1</sup>.

---

<sup>1</sup> In these calculations, we neglected the skin depth (equal to 22 $\mu$ m in Cu for 20GHz) since the CPW thickness has a much smaller value (0.225 $\mu$ m).

### 4.3.1. FMR TYPE MEASUREMENTS IN THE TIME DOMAIN

The magnetization oscillations around the equilibrium effective field can be studied upon application of short field pulses. This has been realized using the time resolved longitudinal MOKE measurements on the isolated soft layer, sample A. Magnetic field pulses of 20 Oe amplitude and of 500 ps duration have been applied for different bias fields oriented parallel to the hard axis. The oscillations of the magnetization component parallel to the hard axis are presented in figure 4.7A.

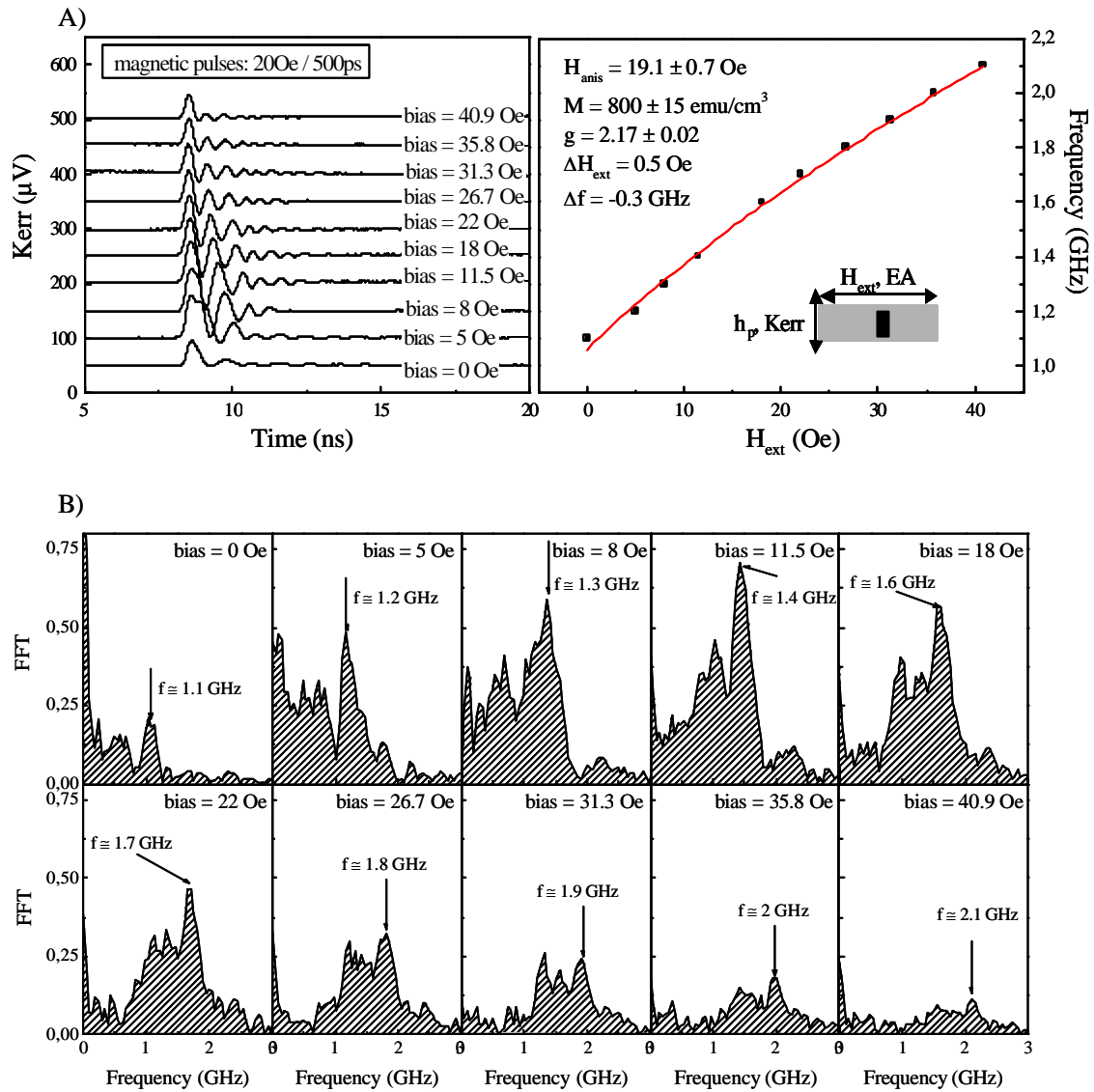


Figure 4.7

A) FMR measurements and Kittel dispersion for the isolated soft layer;

B) Fast Fourier Transformations (FFT) from which the resonance frequency was deduced with a certain precision (precision defined by  $Df$ ).

Increasing the bias field values from 0 Oe to 40.9 Oe, the oscillation frequencies increase from 1.1 GHz to 2.1 GHz. The frequency values have been estimated after calculating the Fast Fourier Transformation (FFT) of each experimental time-trace. The initial FFT spectrum (which is not presented here) was characterized by a large peak. Eliminating the first oscillation from the experimental time traces we have distinguished more precisely the characteristic frequency corresponding to each bias. Nevertheless, the calculation of the characteristic frequency is not precise because of the non-zero width of the peak on the FFT spectra. In consequence we included a certain “error” for the frequency calculation ( $f = f_0 \pm Df$ ).

In figure 4.7A we present the calculated frequency values as a function of the bias field.

Using the Kittel dispersion equation<sup>2</sup>:

$$f = \frac{g}{2p} \sqrt{(H_{anis} + H_{ext})(H_{anis} + H_{ext} + M_S)} \quad (4.1)$$

we can fit this variation as a function of five parameters: i) the anisotropy field,  $H_{anis}$ , ii) the  $M_S$  value, iii) the  $g$  value<sup>3</sup>, iv) the error corresponding to the external magnetic field values ( $DH_{ext}$ )<sup>4</sup> and v) the error corresponding to the resonance frequency ( $Df$ ).

Using the formula:  $f = Df + (g * const * sqrt((H_{anis} + H_{ext} + DH_{ext}) * (H_{anis} + H_{ext} + DH_{ext} + M_S)))$  the experimental data are well fitted for an anisotropy field about 19 Oe, a saturation magnetization of about 800 emu/cm<sup>3</sup>, a  $g$  value of 2.17, an external field error of 0.5 Oe, and a resonance frequency error of -0.3 GHz. We observe that the anisotropy value obtained from the fit (20.17 Oe – fig.4.7) has the same value as the one obtained in the static measurements (20 Oe – fig. 4.6). The values obtained for  $g$  and  $M$  are in agreement with the values obtained in the literature [Silva1999, Lopusnik2003, Nibarger 2003].

It should be noted that time traces calculated from a macrospin model which uses the values of parameters deduced above, do not fit all the experimental oscillations of figure 4.7. We suppose that the magnetic field pulse excites several frequencies in the magnetic samples due to either a relatively strong field pulse or the finite sample size and sample inhomogeneity of the magnetic state. In this case further investigations are required in order to determine more exactly the characteristic frequencies of the magnetic system and the above analysis corresponds to an average behavior.

<sup>2</sup> equation written in the International System of Unities;

<sup>3</sup>  $g = \hbar/\mu_B$

<sup>4</sup> During measurements, the magnetic field values have been recorded with a certain precision ( $\pm DH_{ext}$ ), which, in this case, is taken into account.



### 4.3.2. HYSTERESIS LOOPS IN THE PRESENCE OF SHARP MAGNETIC FIELD PULSES

Magnetization hysteresis loops of the type A spin-valve element as well as of the isolated soft layer element ( $20 \times 40 \mu\text{m}^2$ ) have been recorded in the presence and in the absence of magnetic field pulses. This has been done for easy and hard axis hysteresis loops with the external field applied parallel to the transversal ( $H_{\text{transversal}}$ ) respective longitudinal ( $H_{\text{longitudinal}}$ ) directions (see sample configurations on figures 4.3 and 4.8). The transversal and respective longitudinal directions have been defined with respect to the experimental MOKE configurations (see chapter 2). More precisely, the transversal (longitudinal) direction corresponds to the direction that is perpendicular (parallel) to the pulse magnetic field as indicated in figure 4.8.

#### External field parallel to the transversal direction

##### *20 x 40 $\mu\text{m}^2$ sized spin valves*

Figures 4.8a1 and 4.8b1 present respectively the transversal and the longitudinal Kerr easy axis hysteresis loops obtained in the absence of pulsed magnetic fields.

The transversal loop (fig.4.8a1) presents the variation of the magnetization component that is parallel to the external field  $\vec{H}_{\text{ext}}$ <sup>5</sup>. We can clearly observe the magnetization reversal corresponding to the free and hard layer of the spin – valve with a coercive field value of about 25 Oe for the free layer and of 53 Oe for the hard layer.

The longitudinal loop (fig.4.8b1) presents the variation of the magnetization component that is perpendicular to the external field. This component should be zero at saturation, when the magnetization is aligned parallel to the external field. For magnetic fields smaller than the saturation field, processes such as domain nucleation, domain wall displacements and coherent/incoherent rotation may occur determining, for an external field equal to the coercive field, the magnetization reversal. On the experimental curve we observe two peaks that correspond to the coercive magnetic states of the free layer and a small variation corresponding to the hard layer. The amplitudes of these peaks are related to the variation of the magnetization component that is perpendicular to the external field during the magnetization reversal dominated by the magnetization incoherent rotations. Supposing that the magnetization at the positive saturation ( $H_{\text{sat}} > 0$ ) is orientated to the right, the positive and

---

<sup>5</sup> Inversed shape as in figure 4.1b

respective negative peaks correspond to the anti-clock-wise rotation of the magnetization. On the longitudinal loop the Kerr-intensity values at saturation (positive and negative) should be the same since the longitudinal component of the magnetization is zero. In this case we observe a certain difference between the Kerr intensities at positive and negative saturation, which can be explained as a misalignment between the incidence plane of the Kerr experimental set-up and the external field direction.

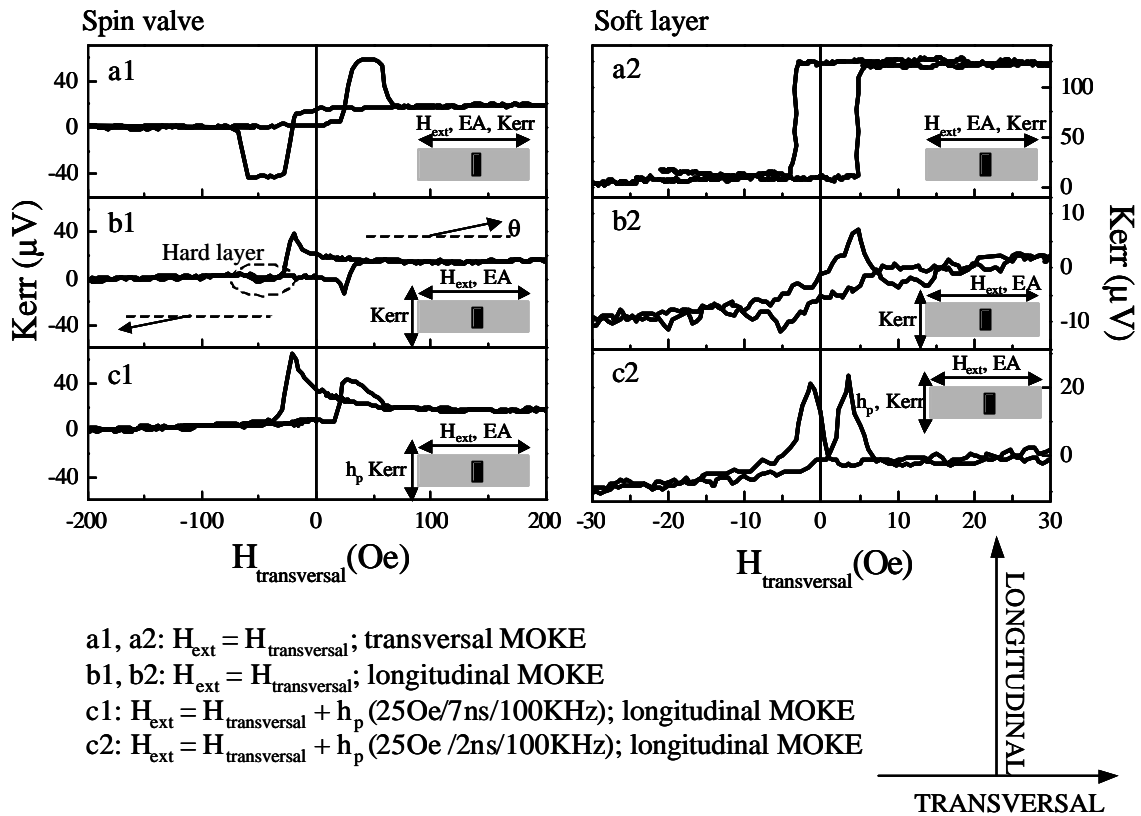


Figure 4.8

Longitudinal and transversal hysteresis loops obtained in the absence and presence of magnetic field pulses.

We realized the same measurement in the presence of magnetic field pulses, applied perpendicular to the external field (and thus along the hard axis). These field pulses have an amplitude of 25 Oe, with a duration of 7 ns and a repetition rate of 100 KHz. It is noted that the signal for each field value on the hysteresis loop is averaged over 300 ms (time constant of the lock-in), while a single magnetic pulse is applied every 10  $\mu$ s. This yields tens of thousands of pulses per measured point. It is furthermore noted, that the time between each pulse (10 $\mu$ s) is considerably longer than the magnetic relaxation time of a few ns, see for example figure 4.7.

On the longitudinal loop, we observe two positive peaks (fig.4.8c1) instead of one positive and a negative one as in figure 4.8b1. Furthermore, the amplitude of the two peaks is larger in the presence of magnetic field pulses (fig.4.8c1) than the amplitude of the two peaks in the absence of magnetic field pulses (fig.4.8b1). This is explained by the presence of pulsed field, which provides a bias during the magnetization rotation. From positive to negative saturation the magnetization executes an anti-clock-wise rotation while from the negative to positive saturation the magnetization executes a clock-wise rotation, favoring an intermediate orientation for the magnetization that is parallel to the excitation magnetic field pulse.

Similar experiments have been performed on the isolated  $20 \times 40 \mu\text{m}^2$  – sized soft layer. The results are presented in figure 4.8a2, b2 and c2 in the absence and respective presence of magnetic field pulses. In the presence of perpendicular pulsed fields, the longitudinal loops reveal two positive peaks. It is furthermore noted that, in this case, the value of the coercive field decreases from 5 Oe in the absence of magnetic field pulses to about 3 Oe in the presence of magnetic field pulses.

In order to explain this decrease of the coercive field of a micron-sized sample, characterized by a complex magnetic structure, we will compare the equilibrium states of a macrospin system with the equilibrium states of a complex magnetic system in the presence of excitation magnetic field pulses.

#### *Macrospin system*

Successive magnetic pulses of 2 ns duration, delayed by 10  $\mu\text{s}$ , determine a decrease of the barrier height between two minima, during the time of the pulse, and an increase of the barrier height during the interval between pulses (see figure 4.9 and figure 1.10 from chapter 1). The decrease/increase of the barrier height is reversible in the macrospin model.

#### *Complex magnetic system*

In the case of a magnetic system, characterized by a very complex magnetic structure (e.g. magnetization ripple structure and inhomogeneous demagnetizing fields from sample edges), in the presence of magnetic field pulses of duration  $d$  and delayed by  $Dt$ , one can define two magnetic states corresponding to the intervals  $d$  and  $Dt$ . The variation of the energy of this magnetic system between the two states is not always reversible (as for a macrospin system) because of multiple irreversible processes that may occur (e.g. the irreversible processes due to impurities or defects that act as blocking centers on the domain wall propagation). Furthermore, successive pulses of the same polarity would propagate

domain walls by always increasing the favored domains, if the magnetization in these domains is parallel to the magnetic field. Thus, it is possible that after the first magnetic field pulse the system will not completely relax toward its initial state. The second pulse will induce a new irreversible state, and so on. Furthermore, considering that the amplitude of the magnetic field pulses (20 Oe - 25 Oe) is comparable to the uniaxial anisotropy field (20 Oe), we can suppose that certain magnetic field pulses might locally induce reversed magnetic domains and initiate the reversal at a lower coercive field.

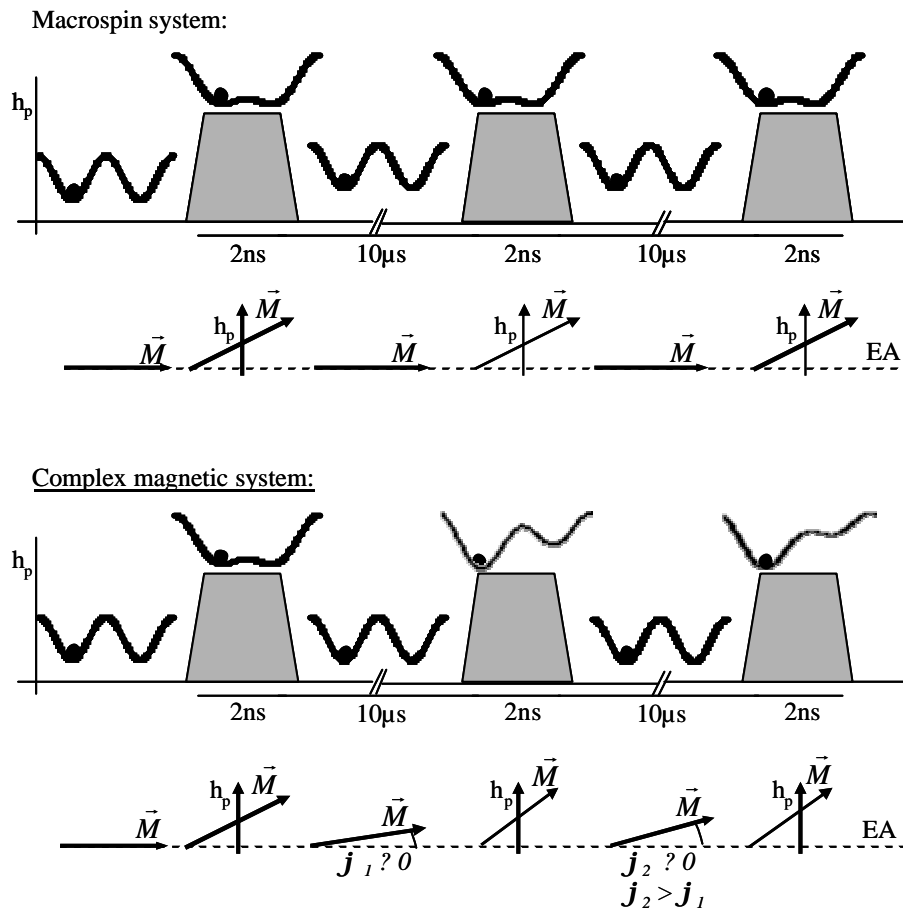


Figure 4.9: The influence of successive pulses applied perpendicular to the EA on a macrospin system or on magnetic systems characterized by a more complex structure (e.g. ripple magnetic structure)

Furthermore, after tens of thousands of similar irreversible processes induced by thousands of magnetic field pulses, the static hysteresis loop characterizes the variation of an “averaged magnetization vector”<sup>6</sup> that is oriented away from the uniaxial easy axis direction. Due to this deviation, the angle between the magnetization orientation and the external field is

<sup>6</sup> averaged over tens of thousands pulses

smaller than  $180^\circ$ , and in consequence, the coercive field decreases (with respect to the case of a  $180^\circ$  angle between the magnetization and the external field as in the absence of magnetic field pulses).

#### External field parallel to the longitudinal direction

A similar decrease of the coercive field, was observed on the same sample but for an external magnetic field perpendicular to the easy axis and parallel to the pulsed magnetic field. This decrease is explained similarly as described above.

Applying an external magnetic field parallel to the hard axis of the sample (longitudinal direction) we evidenced a decrease of the coercive field value in the presence of magnetic field pulses of 16 Oe amplitude, 2 ns duration and 100 KHz repetition rate (fig.4.10) from 8 Oe to about 2 Oe. The decrease of the coercive field can be explained as above.

This configuration has been used to measure time-traces corresponding to the magnetization dynamics induced by pulses of 25 Oe amplitude and 5 ns duration.

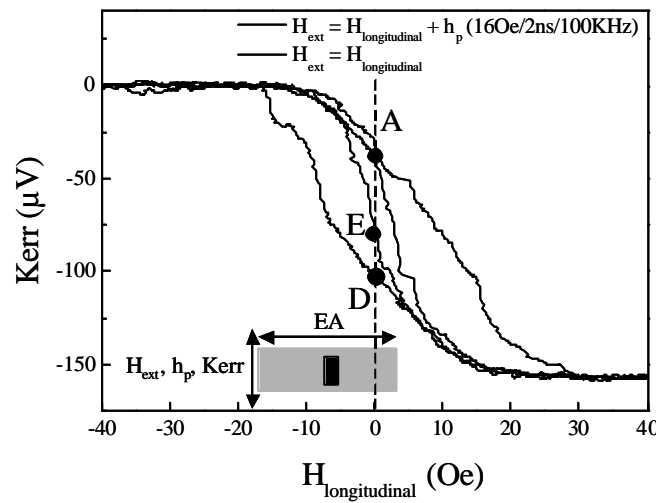


*Figure 4.10*  
Hard axis hysteresis loops obtained in the absence and presence of magnetic field pulses obtained with the longitudinal MOKE.

In the following, we present time-resolved MOKE results obtained on samples A and B. The first result corresponds to the magnetization large angle deviation observed for pulse amplitude of 25 Oe and durations larger than 2ns.

### 4.3.3. LARGE-ANGLE MAGNETIZATION ROTATIONS OBSERVED WITH THE TIME-RESOLVED STROBOSCOPIC MOKE

#### *Sample A – spin valve*

In order to investigate large angle rotations without reversal, we recorded stroboscopic time traces on  $20 \times 40 \mu\text{m}^2$  spin valves whose uniaxial the easy axis is oriented perpendicular to the magnetic field pulses. Both static and dynamic experiments were performed using the longitudinal MOKE where one measures the magnetization component parallel to the pulsed magnetic field (see the insets of figures 4.11 – 4.13).

The static hysteresis loop with a field applied perpendicular to the easy axis reveals a typical hard axis loop, see figure 4.11. The reversal of the soft and respectively hard layer of the spin valve are not resolved and we can only deduce the anisotropy field of the entire spin valve which is about 55 Oe.

The dynamic measurements were realized in zero-bias field that corresponds to two possible remanent states. On the hysteresis loop these are represented by points B and A obtained after sample saturation in respectively positive and negative external fields. (fig. 4.11).

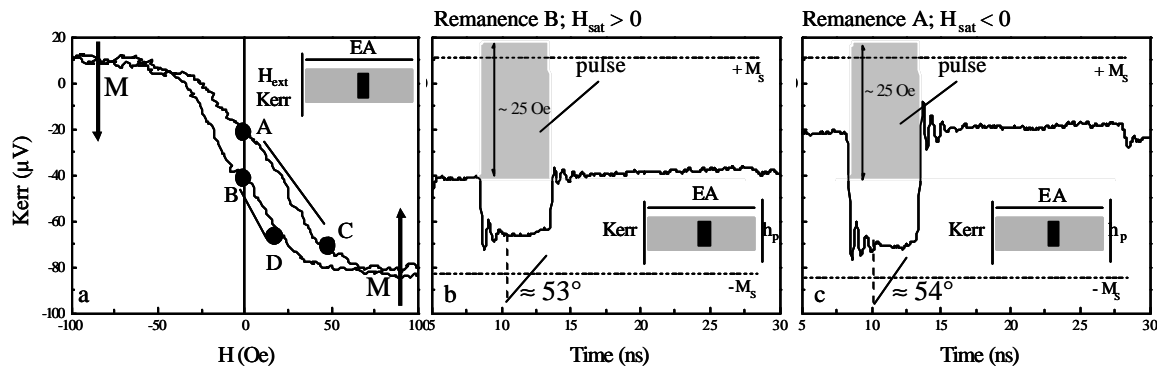


Figure 4.11: Large angle magnetization deviation and small angle oscillations induced by large magnetic pulses 25Oe/5ns

On figure 4.11b and c, the time traces obtained for magnetic pulses of 25 Oe amplitude and 5 ns duration are shown for both remanent states. Due to the relatively large amplitude of the pulsed field and the long duration, the magnetization reorients during pulse application into its new effective field direction, determined by the vectorial superposition of the anisotropy field and the pulsed field. This reorientation induces a variation of the Kerr signal from point A to C and from point B to D for the two remanent states respectively. We observe that for the same pulse amplitude we obtain a larger variation of the signal in case A

(fig.4.11c) than in case B (fig.4.11b),. However the final signal level is the same corresponding to a longitudinal magnetization component with a value of about  $0.6 M_S$ . Assuming coherent rotation of the magnetization from, this state would correspond to a deviation of the magnetization with respect to the longitudinal axis of about  $53^\circ$  or  $54^\circ$  as shown in figures 4.11b and c.

The alignment of the magnetization parallel to the effective field (during the pulse duration – 5 ns – and after the pulse is stopped) is realized by small angle attenuated precessions of the magnetization around the effective field direction that takes about 3 ns. On figure 4.11b and c these precessions appear as small amplitude oscillations of the longitudinal component of the magnetization. These are characterized by frequencies around 1.15 GHz.

Similar experiments were realized on spin valves characterized by an easy axis parallel to the pulsed magnetic field (sample B). Time-resolved results obtained in the longitudinal MOKE configuration are presented in the following.

#### *Sample B – spin valve*

Static and time-resolved stroboscopic measurements were realized on  $20 \times 40 \mu\text{m}^2$  spin-valves – sample B. As in the previous case, we measured the magnetization component parallel to the pulsed magnetic field. We used pulses of 25 Oe amplitude and durations equal to 2 ns, 5 ns, 8 ns and 10 ns.

On the static hysteresis loop, fig. 4.12a, one distinguishes between the reversal of the soft and hard layers. The static measurements on the spin valve sample reveal a major hysteresis loop centered in zero field and two minor loops that are shifted by about  $\pm 17.5$  Oe (fig.4.12a – loops I and II).

The dynamic measurements were realized for a bias field of about  $-17.5$  Oe corresponding to point A on figure 4.12a. In order to have the same initial magnetic state before each excitation, we used an open termination of the CPW that determined two magnetic pulses of opposite polarity. The delay between the two pulses was about 17 ns.

Due to the geometry, the pulsed field is now parallel to the easy axis and will not induce a precessional reversal. However, since the pulsed field amplitude is larger than the static coercive field, a reversal or partial reversal can be induced [Choi2001, Choi2001B, Koch1998]. The time-traces in fig. 4.12a reveal a partial reversal of the magnetization for all the pulse widths (2 ns, 5 ns, 8 ns and 10 ns).

The incident magnetic pulse has not sufficient amplitude and width to realize the complete reversal of the magnetization.

All traces are characterized by a fast rising edge of the magnetization, which reaches about the same signal level, followed by a relaxation, where the signal level slowly decreases. Hence upon increasing pulse width from 2 ns to 5 ns, the total Kerr signal variation is larger. A likely process might be a partial reversal of the magnetization (by either rotation or wall nucleation) and a subsequent wall propagation under the pulsed field, which tends to increase the reversed domain volume [Choi2001, Choi2001B, Koch1998]. For the back reversal we observe a similar effect, however the relaxation is much slower. Unfortunately, there was no possibility to increase the magnetic pulse amplitude since we used the maximum voltage delivered by the pulse generator of 10V.

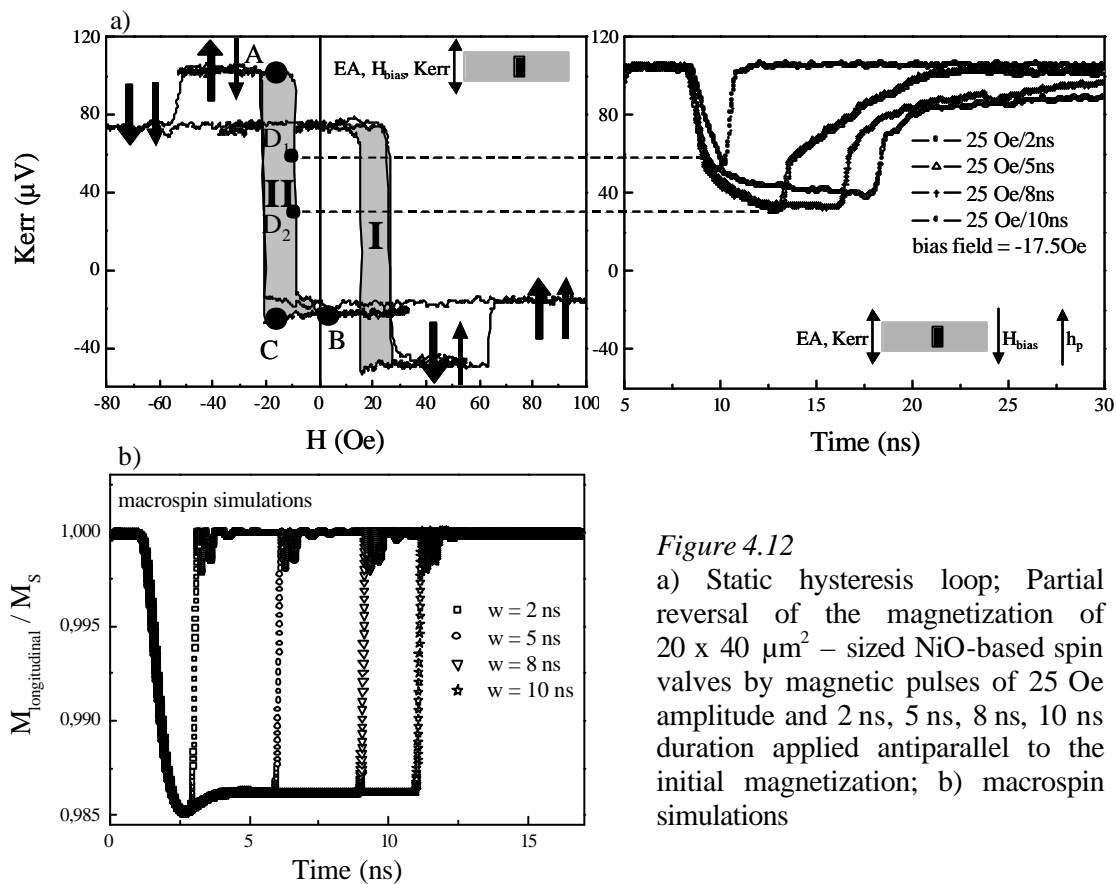


Figure 4.12

a) Static hysteresis loop; Partial reversal of the magnetization of  $20 \times 40 \mu\text{m}^2$  – sized NiO-based spin valves by magnetic pulses of 25 Oe amplitude and 2 ns, 5 ns, 8 ns, 10 ns duration applied antiparallel to the initial magnetization; b) macrospin simulations

In order to analyze the fast rising edge, we compared the experimental results to the macrospin simulation (details see section 4.2.7.4.) upon using the following parameters:

- Damping constant  $\alpha = 0.02$ , Landé factor  $g = 2.18$ , in-plane demagnetizing factors:  $N_x = 0.0012$  and  $N_y = 0.0006$  0006 (corresponding to an ellipsoid of  $20 \times 40 \mu\text{m}^2$ )



- The uniaxial anisotropy field and the initial magnetization quasi-parallel to the longitudinal axis (there is a small misalignment  $\sim 1^\circ$  between the initial direction of the magnetization and the longitudinal axis);  $H_u = 21.5 \text{ Oe}$ ;  $M = 800.4 \text{ emu/cm}^3$ .
- Incident magnetic field pulse of 25 Oe amplitude and 2 ns, 5 ns, 8 ns and 10 ns durations applied anti-parallel to the initial magnetization direction;

The results are presented in figure 4.12b. For the macrospin simulations, we have chosen a large anisotropy field (21.5 Oe) in order to obtain partial reversal of the magnetization. Lower values for the anisotropy field lead to a complete reversal of the longitudinal magnetization.

From the macrospin simulations when the pulse is stopped, the magnetization returns to the initial direction very rapidly obtaining a very sharp transition.

On the experimental time-traces obtained for pulse width of 5 ns, 8 ns and 10 ns just after the pulses are stopped we observe sharp variation of the magnetization as in the macrospin model followed by relaxational processes corresponding most likely to domain wall displacements.

On the experimentally time-trace corresponding to magnetic pulses of 2 ns width, the relaxational processes do not appear because the pulse width is too short to induce an observable relaxation effect.

#### *Sample B – isolated soft layer*

Similar results have been obtained for the isolated Co/NiFe free bi-layer (fig.4.13).

In this case, we used only one magnetic field pulse, obtained with a  $50 \Omega$  termination on the CPW. To assure the same magnetic state before each pulse, we kept a bias field between  $-10 \text{ Oe}$  and  $-7 \text{ Oe}$ . Pulses of  $20 \text{ Oe}$  amplitude,  $5 \text{ ns}$  widths and two different bias fields, partially reverse the magnetization from point A to B or C. Pulses of  $10 \text{ ns}$  width induce a larger variation of the Kerr signal (from point A to D) that determines a longer relaxation time ( $\sim 50 \text{ ns}$ ).

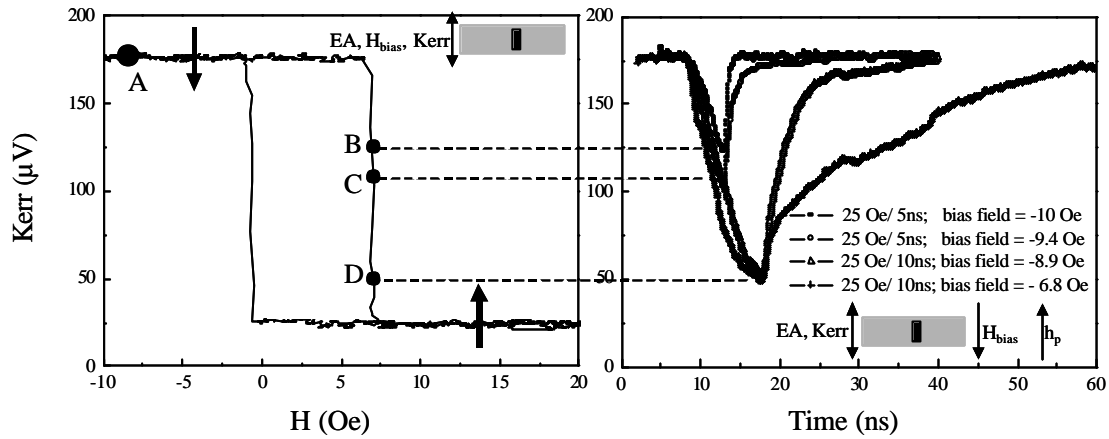


Figure 4.13

Partial reversal of the magnetization of  $20 \times 40 \mu\text{m}^2$  – sized soft layer by magnetic pulses of 25 Oe amplitude and 5 ns, 10 ns durations applied antiparallel to the initial magnetization

In conclusion, sections 4.3.2. and 4.3.3 represent the validation of the dynamic experimental setup by measuring time-traces characterized by a time resolution of tens of picoseconds using the stroboscopic Kerr effect for different configurations of the field pulse with respect to the uniaxial anisotropy direction. Furthermore, we evidenced the decrease of the coercive field in the presence of magnetic field pulses and partial reversal of the magnetization induced by pulses of several nanoseconds duration.

In the following we present the time resolved magnetic response of sample de type A to shorter magnetic field pulses of duration of some hundreds of picoseconds, applied perpendicular to the easy axis.

#### 4.3.4. PRECESSIONAL REVERSAL

##### 4.3.4.1. EXPERIMENTAL EVIDENCE FOR PRECESSIONAL REVERSAL

The precessional reversal consists in the magnetization switching in half of a precession cycle induced by short magnetic field pulses applied perpendicular to the easy axis (see chapter 1, section 1.7.3). In this case, the magnetic field pulse acts like a “*trigger*” of the precessional motion, while the demagnetizing field is the “*motor*” of the reversal.

As pump, we used short magnetic pulses, of some hundreds of picosecond duration and of maximum 25 Oe amplitude. These are applied perpendicular to the easy axis of a  $20 \times 40 \mu\text{m}^2$  – sized isolated soft layer or spin-valve structure (samples A in figure 4.2). The time-resolved measurements of the magnetization dynamics were realized using the transverse MOKE, stroboscopically synchronized to the pump as detailed in chapter 2. Transverse MOKE corresponds here to the measurement of the magnetization component perpendicular to the pump magnetic field as shown in figure 4.3. In a stroboscopic measurement, the magnetic state of the sample before each pump and probe pulse must be the same. In our case, supposing that the first pump pulse realizes the magnetization switching from  $+M$  to  $-M$ , we need a second pulse to reverse the magnetization back to  $+M$ , before the following probe pulse is triggered. In consequence, the second magnetic pulse has to be triggered in the interval between two successive laser-probe pulses. Experimentally, we realized this using a short-ended CPW that produces a reflected magnetic pulse of the same polarity, but that is delayed with respect to the incident magnetic pulse by about 15 ns (fig. 4.14A). The delay value is given by the length of the cable between the CPW-end and the short-circuit. Since the resistance of the CPW is not negligible ( $R \sim 15 \Omega$ ), some part of the incident power is lost in the line by Joule dissipation. In consequence, the reflected pulse has a smaller amplitude with respect to the amplitudes of the incident pulse ( $h_p^r \approx 0.85 \cdot h_p^i$  from TDR measurements).

The effect of the incident and the reflected magnetic pulses on the transverse magnetization component is summarized in figure 4.14B for the isolated soft layer for different values of the pulse widths (300ps, 350ps, 400ps, 450ps, 500ps, 600ps, 650ps and 700ps) and amplitude of about 25Oe. Each of these curves is the average of at least eight time traces.

First, we consider the time trace obtained for pulse width of 400ps (fig.4.14 - 3). For the initial magnetization,  $\vec{M}_1$ , oriented to the left in figure 4.14 – 3 the incident magnetic pulse,  $\vec{h}_p^i$ , perpendicular to  $\vec{M}_1$ , induces a transition from  $\vec{M}_1$  to  $\vec{M}_2$ , while the second pulse resets the magnetization from  $\vec{M}_2$  to  $\vec{M}_1$ . Comparing this variation with the static magnetic curve, we conclude that  $\vec{M}_2$  corresponds to a complete reversal of the magnetization.

To demonstrate this as a reversal by precession, we have to consider the characteristic parameters of this type of switching (see figure 1.12 from chapter 1):

1. The precessional switching is characteristic to in-plane magnetized thin magnetic films, capable of creating large demagnetizing fields ( $h_d \gg H_u$ ) along one direction;
2. The magnetic films are characterized by a uniaxial anisotropy, that stabilizes the magnetization direction;
3. The pump magnetic field is perpendicular or quasi-perpendicular to the initial direction of the magnetization (or the easy axis – EA);
4. The pulse width ( $Dt$ ) should have values in the same range as the precession period  $T$ , in order to induce reversal in plane in a half-precession period. Increasing the pulse width, the magnetic states induced change from reversed to non-reversed states. The influence of the pulse amplitude and width on the magnetization switching was evidenced in 2003 by Schumacher et al. [Schumacher2003].

The first three points are accomplished by the experiment since these results have been obtained on a permalloy thin film element of 10 nm thickness with a uniaxial anisotropy field about 20 Oe and magnetic field pulses of 25 Oe applied perpendicular to the easy axis. The demagnetizing factor corresponding to the film thickness is close to 1, determining a very high demagnetizing field for a low value of the magnetization component perpendicular to the film thickness. As mentioned in chapter 1, an out of plane deviation of  $1^\circ$  of the magnetization corresponds to a demagnetizing field perpendicular to the film plane: of 183Oe for  $M_S^{\text{NiFe}} = 853 \text{ emu/cm}^3$ , a value that is much larger than the anisotropy field value, 20Oe<sup>1</sup>.

As we have shown in section 4.2.4, the FMR frequencies in this sample lies between 1.1 GHz and 2.1GHz for bias fields between 0 and 41Oe. The frequency values correspond to complete precession periods between 500ps and 900ps. From the Kittel equation of dispersion (eq.4.1), the precession times decrease for higher fields (for 430Oe the extrapolated

---

<sup>1</sup> Macrospin simulations (see section 4.2.7.3) revealed an initial deviation out-of-plane of the magnetization of about  $2.5^\circ$  that determines demagnetizing field about 430Oe.

frequencies are 6.3GHz that corresponds to precession periods of 160ps). The third point is accomplished using pulse widths values in the same range as the precession periods (pulse widths  $\in$  300ps – 700ps in figure 4.14).

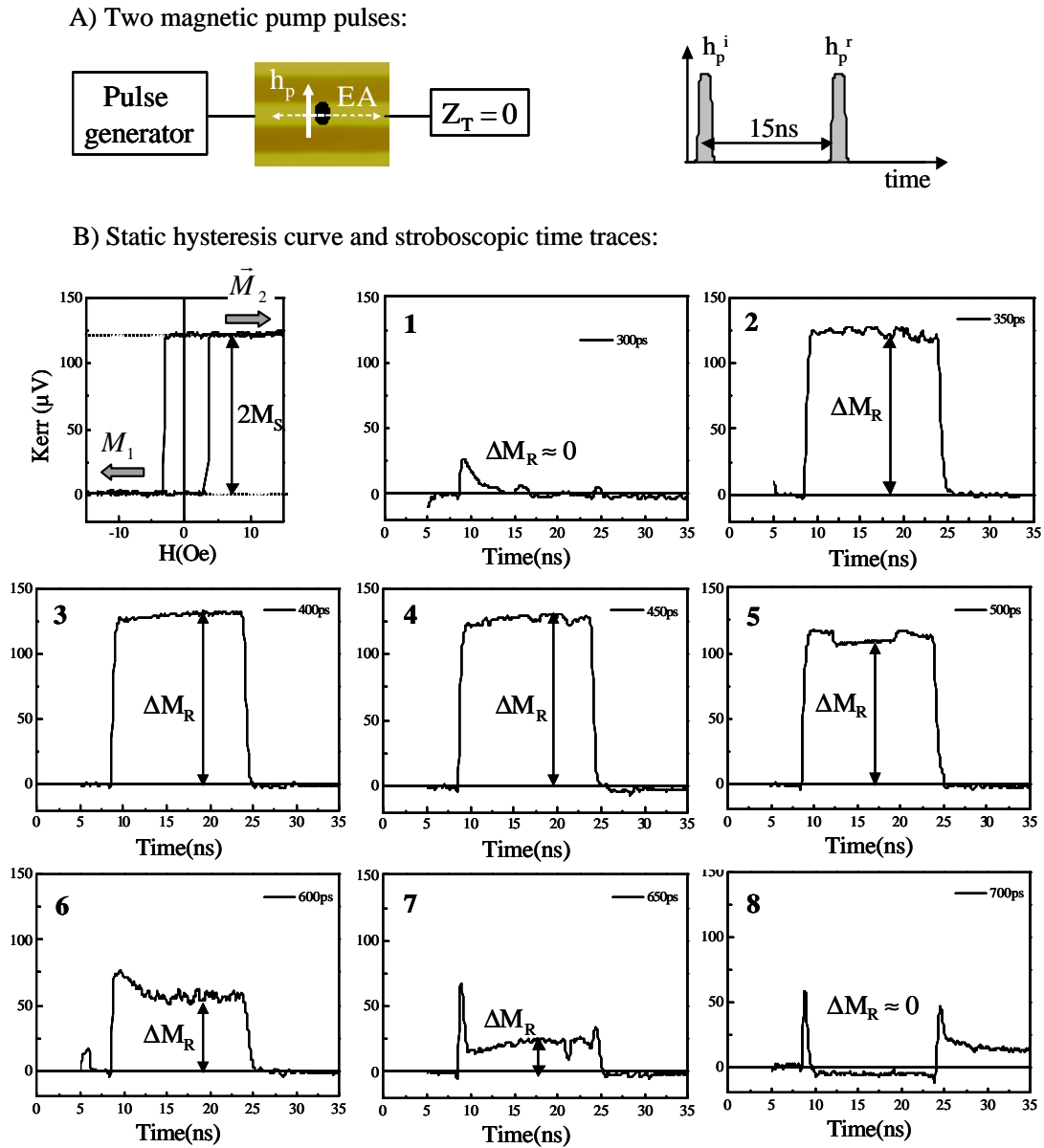


Figure 4.14

Transversal MOKE measurements that evidenced the precessional reversal in the isolated free layer of the spin valve structure

For pulse width of 300ps (fig.4.14 – 1), we observe no switching. The pulse width or amplitude, is not large enough to induce the magnetization reversal. In consequence, after the pulse is stopped, the magnetization relaxes back to its initial state. For larger pulse widths, 350ps, 400ps and 450ps (fig.4.14 – 2, 3 and 4) and 25Oe amplitude, we observe that the

magnetization switches between the two levels,  $\vec{M}_1$  and  $\vec{M}_2$ , by a process that corresponds to the magnetization reversal by precession, as justified above.

The precessional reversal, at least for a macrospin system, is characterized by two discrete remanent states corresponding to non-reversal and to complete reversal. In contrast to this, larger widths of the pulses resulted in our experiments in intermediate magnetic states defined by the ratio:  $0 < \Delta M_R / M_S < 1$  (0 corresponds to non-reversal and 1 to reversal), that were observed for pulse durations of 500ps, 600ps, 650ps and 700ps (fig.4.14 – 5, 6 and 7). Here,  $\Delta M_R$  corresponds to the difference of the signal levels before and after the incident pulse. In order to understand this *reduced remanence* we have to consider that one point on the experimental stroboscopic time-trace represents an average value over tens of thousands of individual switching events. In this context, one question is: *What happened after one single switching event?*

To answer this, quasi-static experiments were realized to measure the remanent state of the magnetic sample after successive field pulses. These will be detailed in the following.

#### 4.3.4.2. REDUCED REMANENCE

We have statically measured the remanent state after single switching events, induced by pulses of 25 Oe amplitude delayed by 5 seconds, using the transversal MOKE. These ‘single shot’ measurements were realized for the same bias field, pulse width and amplitudes as in the stroboscopic measurements, but with a 50  $\Omega$  termination to suppress the reflected pulse. The results are presented in figure 4.15 for three different pulse widths of 100ps, 300ps, and 400ps.

This type of experiment characterizes more generally the switching probability and stability of a device. The remanent state in the stroboscopic data, defined by  $\Delta M_R$  in figure 4.14, can be deduced from the quasi-static measurements as the average value of the remanent states,  $M_R^i$  (fig.4.15), after single switching events using the formula:

$$\Delta M_R = \frac{1}{N} \cdot \sum_{i=1}^N \Delta M_R^i \quad (4.3)$$

For pulse width of 400ps, the switching is quasi-perfect, the value of  $\Delta M_R^i$ , being equal to  $2M_S$  for each pulse<sup>2</sup>. In this case, the switching probability of 72 events (in the interval of

---

<sup>2</sup> The magnetization varies between  $M_S$  (reversal) to  $-M_S$  (non-reversal) after each pulse.

measurement of about 6 minutes) is about 100%. The average value of the remanent magnetization is:  $\Delta M_R = 2M_S$ , a result that has also been obtained with the stroboscopic measurements (see figure 4.14-3).

The switching stability is characterized by the magnetization stability in the time-interval between two successive magnetic field pulses, which in our case is 5 sec. During this time, the magnetization value does not change.

For pulse widths of 300 ps, and 100 ps we observe switching events with  $\Delta M_R$  smaller than  $2M_S$ . This effect is more pronounced for 100 ps than for 300 ps or 400 ps. Quasi-static measurements realized for larger widths of the pump pulses (500ps, 600ps, etc.), yield a similar result as the ones presented for 100ps or 300ps in figure 4.15. To explain this, we have to consider the complex magnetic structure that was observed on the MFM images (fig.4.4 and 4.5). In this context, we can consider that before each magnetic field pulse the local magnetization is characterized by a distribution of its orientation with respect to the magnetic field direction. Macrospin simulations, which will be presented in section 4.2.7.4, lead to the conclusion that the switching depends strongly on the value of the angle between the initial orientation of the magnetization and the perpendicular direction to the pulsed magnetic field. In consequence, partial switching processes occur only in those regions where the magnetization is almost perpendicular to the magnetic field pulses.

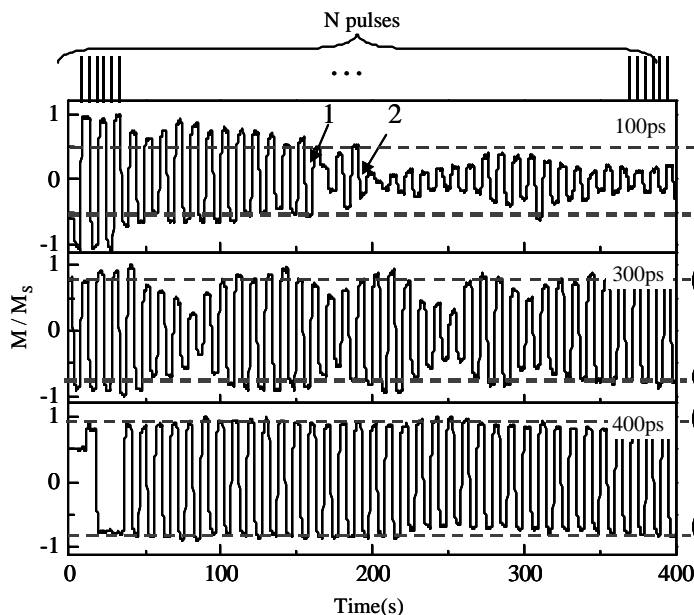


Figure 4.15

Quasi-static measurements of the remanent state of the  $20 \times 40 \mu\text{m}^2$  sized isolated soft layer after successive pulses delayed by 5 seconds

The reduced remanence observed on the stroboscopic time-traces presented above (fig.4.14) can be also a consequence of the switching failure that is obvious for pulses of 100ps durations (points 1 and 2 on the figure 4.15). Considering that, initially the odd pulses

switch the magnetization toward the +1 state, and that the incident pulses sample the transition to the positive remanent state +1, one switching failure will determine a sampling of a negative remanence instead, until the next switching failure occurs. One switching failure in the middle of the time-measurement (~300ms) determines zero signal in a stroboscopic measurement. As a consequence, the average value in the stroboscopic experiment will be much reduced, even though the sample might have more or less completely switched. The presence of strong fluctuations as well as the probability for a switching failure to occur is larger in the transition range from reversal to non-reversal. In this context, it is interesting to note that for pulse widths of 100ps the quasi-static measurements (fig.4.15) show that the complete reversal can be induced although the stroboscopic measurement indicated zero remanent value ( $\Delta M_R = 0$ ).

In conclusion, the reduced remanent state observed on the stroboscopic results corresponds i) to the partial magnetization switching where only a part of the sample volume is reversed, and ii) to the switching failures. An important aspect to retain is that a zero stroboscopic result is not equivalent to the absence of precessional switching processes.

The precessional character of the magnetization switching detailed above is more obvious when one represents the magnetization trajectory. The experimental trajectory of the magnetization will be presented in the following section.

#### 4.3.4.3. MAGNETIZATION TRAJECTORY

We measured the longitudinal and the transverse magnetization components using time-resolved MOKE experiments. The planar representation of the two components yields the magnetization trajectory in the film plane. From this, one evidences the precessional character of the magnetization switching by precession.

The longitudinal and transversal stroboscopic time-traces were obtained using the geometrical configurations presented in figure 4.3a. The results are presented in figure 4.16 for pulse widths values of 300ps, 350ps, 400ps, as well as the magnetization trajectory for 300ps pulse width.

These results show very clearly the magnetization reversal in half-precession cycle. The first pulse,  $\vec{h}_p^i$ , induces the fast magnetization reversal from the left orientation to the right and the reflected pulse,  $\vec{h}_p^r$  from the right to the left.



Furthermore, the two successive field pulses of the same polarity reverse the magnetization along similar trajectories. In particular, the longitudinal magnetization component  $m_l$  is always positive for the initial and the back reversal (fig.4.16). This is due to the fact that the torque  $-\vec{M} \times \vec{h}_p(t)$  exerted by the incident and reflected field pulses induces opposite out of plane magnetization components for the initial and the reversed magnetization. As a consequence, the initial magnetization precesses in a clockwise rotation sense around the out of plane demagnetization field while the reversed magnetization precesses in an anticlockwise rotation sense.

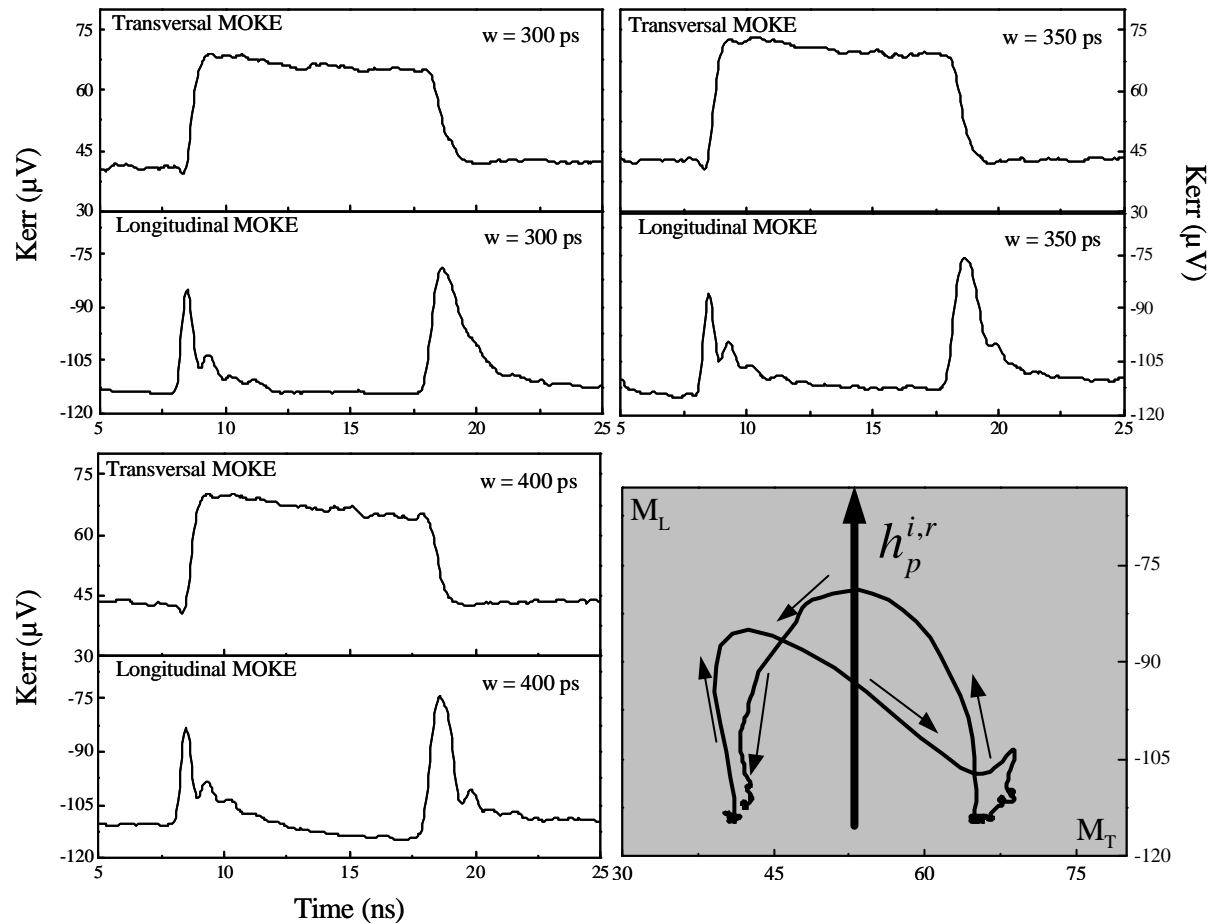


Figure 4.16

The stroboscopic time-traces obtained with time-resolved longitudinal and transversal MOKE for 300ps, 350ps and 400ps. Magnetization trajectory in the precessional switching corresponding to a pulse width of 300ps.

In contrast to the transverse component, the longitudinal component shows weak ringing and a relaxation of a few ns (fig.4.16). The oscillations of the longitudinal component of the magnetization are more visible (these are proportional to  $\cos\mathbf{q}$ , where  $\mathbf{q}$  is the angle between the magnetization and the pulse direction) than the ringing of the transverse component

(which is proportional to  $\sin q$ ). The fact that some ringing is visible might be attributed to the relatively larger oscillation amplitudes.

More observations concerning the results on the precessional reversal have been evidenced from the comparison between the experimental data to macrospin simulations. They will be detailed in the following.

#### 4.3.4.4. MACROSPIN SIMULATIONS

A better understanding of the precessional magnetization dynamics (reversal as well as small angle precession) is possible by comparing results to simulation for a macrospin system solving the Landau-Lifshitz –Gilbert equation (eq.1.18b, chapter1) for.

It is noted that care has to be taken when comparing the experimental results to simulations since the real system is far from being a single macrospin (see MFM image in figure 4.4).

Considering the reduced terms:

$$\vec{m}(m_x, m_y, m_z) = \frac{\vec{M}}{M_S}, \quad \vec{h}(h_x, h_y, h_z) = \frac{\vec{H}_{eff}}{M_S}, \quad \text{and} \quad t = tI M_S \quad (4.4)$$

the Landau-Lifshitz –Gilbert equation transforms to the system:

$$\begin{aligned} \frac{\partial m_x}{\partial t} &= -\frac{1}{1+a^2} \left[ (m_y h_z - m_z h_y) + a \cdot m_y (m_x h_y - m_y h_x) - a \cdot m_z (m_z h_x - m_x h_z) \right] = f_x(m_x, m_y, m_z) \\ \frac{\partial m_y}{\partial t} &= -\frac{1}{1+a^2} \left[ (m_z h_x - m_x h_z) + a \cdot m_z (m_y h_z - m_z h_y) - a \cdot m_x (m_x h_y - m_y h_x) \right] = f_y(m_x, m_y, m_z) \\ \frac{\partial m_z}{\partial t} &= -\frac{1}{1+a^2} \left[ (m_x h_y - m_y h_x) + a \cdot m_x (m_z h_x - m_x h_z) - a \cdot m_y (m_y h_z - m_z h_y) \right] = f_z(m_x, m_y, m_z) \end{aligned} \quad (4.5)$$

The equations 4.5 were integrated using the 4<sup>th</sup> order Runge-Kutta method [*Numerical Recipes*], which is detailed in Annexe 4.

The macrospin simulation results were compared to the experimental time-trace obtained on the isolated micron-sized soft layer (sample A), in a MOKE experiment, for incident pulses of 25 Oe amplitude and 300ps width as shown in figure 4.17<sup>3</sup>. The uniaxial anisotropy is parallel to the *ox*-axis and has a value about 20 Oe as obtained from the static measurements (fig.4.6) and from the FMR results (fig.4.7).

<sup>3</sup> This experiment was realized in a different moment with respect to the one presented in figure 4.14 and different experimental conditions (as the focusing on different regions on the sample) determined changes in the stroboscopic response, as the precessional reversal obtained for smaller pulse widths.

Using the parameters:

$$\mathbf{a} = 0.013, g = 2.18, N_x = 0, N_y = 0;$$

$$H_u = 200\text{e} (// \text{ox});$$

$$h_p = 250\text{e} (// -\text{oy}), \text{ pulse rise-time} = 55\text{ps}, \text{ pulse fall-time} = 60\text{ps}, \text{ pulse width} = 300\text{ps};$$

$$M_s = 800.4 \text{ emu/cm}^3 \text{ (magnetization initial orientation parallel to } (-\text{ox}) \text{ axis);}$$

we obtained the simulated curve presented in figure 4.17.

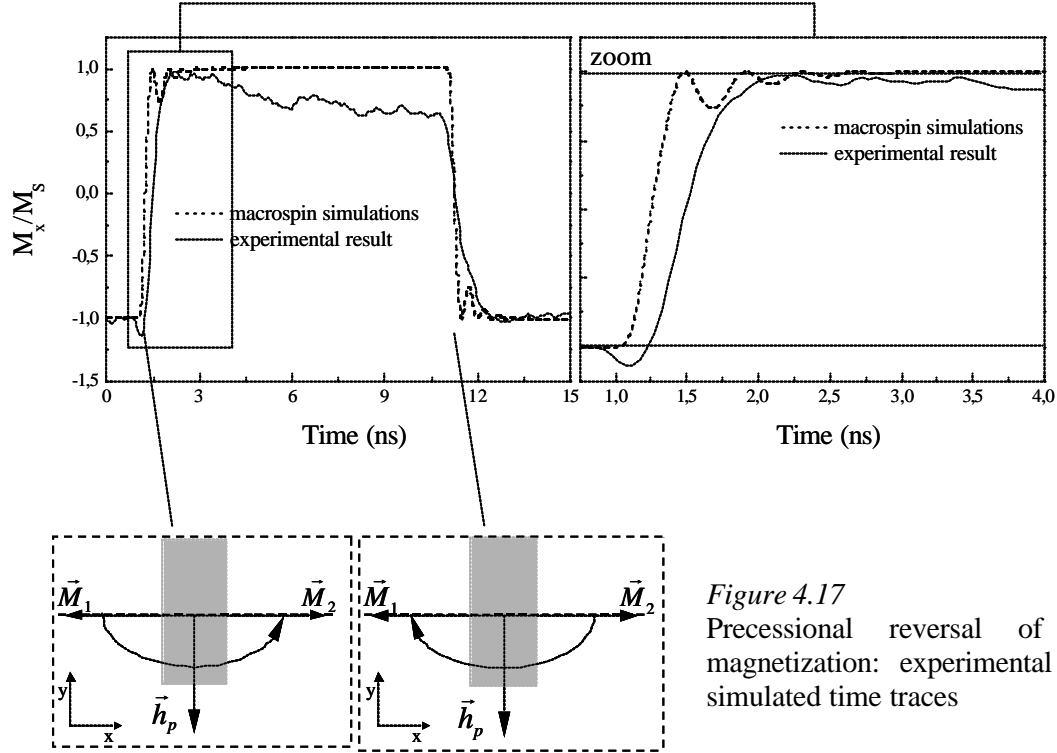


Figure 4.17  
Precessional reversal of the magnetization: experimental and simulated time traces

Comparing the experimental time trace to the simulated curve around the rising edge of the pulse one can distinguish:

- i) A larger switching time in the experimental case ( $\sim 1\text{ns}$ );
- ii) The existence of an undershoot just before the magnetization reversal;
- iii) The absence of the oscillations after the magnetization reversal on the experimental time trace.

In the following, we discuss each of the three aspects mentioned above as a function of the damping,  $\mathbf{a}$ , the anisotropy field,  $H_u$ , the magnetic pulse amplitude  $h_p$ , and width  $w$ , and of the angle  $\mathbf{j}$  between the easy axis and the  $\text{ox}$ -axis (fig.4.17).

### i) The switching time

Due to the undershoot, a 10% - 90% value for the reversal time cannot be defined. Therefore, the estimated value of 1.2 ns for the experimental switching time corresponds to the start of the pulse and the point where the magnetization first reaches its final value. The switching time in the experimental case is larger than in the simulated time trace, which is estimated to be about 0.4ns.

This can be explained considering that the dynamic processes of a very complex magnetic structure introduce a supplementary damping that can be envisaged in the macrospin simulations by the increase of the effective parameter  $\alpha$ .

In the following we will analyze the dependence of switching time on the damping parameter, magnetic pulse amplitude and anisotropy field values.

The values of the other parameters used in the macrospin calculations are:

$$\begin{aligned} g &= 2.18, N_x = 0, N_y = 0; \\ H_u &\parallel ox; \\ h_p &\parallel -oy, \text{ pulse rise-time} = 55\text{ps}, \text{ pulse fall-time} = 60\text{ps}, \text{ pulse width} = 300\text{ps}; \\ M_s &= 800.4 \text{ emu/cm}^3 \text{ (magnetization initial orientation parallel to } -ox \text{ - axis);} \end{aligned}$$

#### *Switching time as a function of effective damping*

Figure 4.18a presents the simulated time-traces for 4 different values of the damping parameter,  $\alpha = 0.013, 0.02, 0.03$ , and  $0.035$ , for an anisotropy field about 20 Oe and pulse amplitude of 25 Oe. Comparing them to the experimental results, we observe that increasing the damping parameter, the switching time of the magnetization is also increased. This is due to a slower response of the magnetization to the excitation pulse. We observe that for about  $\alpha = 0.02$  the inclinations of the experimental and simulated time-traces are about the same. Nevertheless, because of the undershoot just before the magnetization reversal, the experimental time-trace is shifted with respect to the simulated data by about 250 ps.

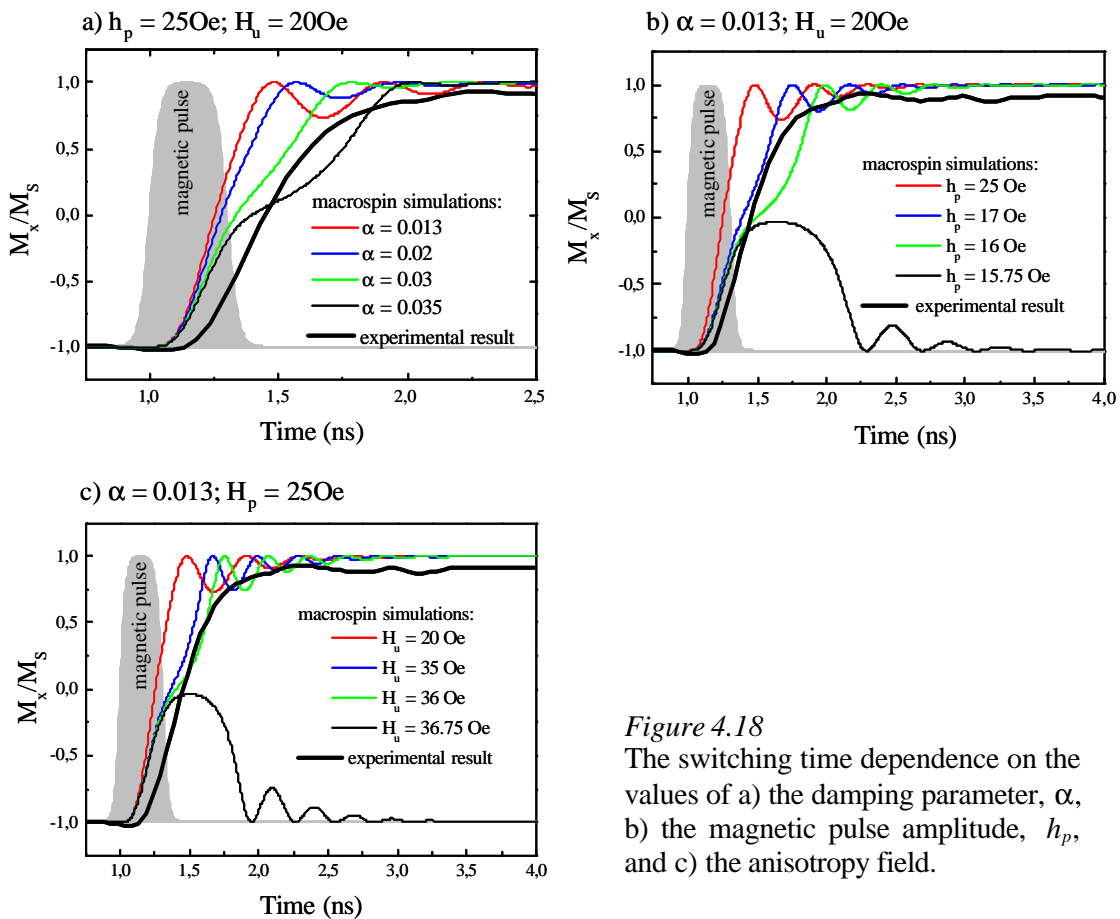
#### *The switching time dependence on the magnetic pulse amplitude ( $h_p$ )*

Figure 4.18b presents the simulated data for 5 different values of the pulsed field amplitudes,  $h_p = 25 \text{ Oe}, 17 \text{ Oe}, 16 \text{ Oe}, 15.75 \text{ Oe}$  for an anisotropy field of about 20 Oe and a damping parameter of 0.013. We observe that decreasing the pump amplitude, the system response is longer, and consequently, the switching time is increased. For a small value of the pulse amplitude (16 Oe) the switching time is very long ( $>1 \text{ ns}$ ). In this case, the magnetization motion is delayed after a rotation of  $90^\circ$  and finally relaxes parallel to the

reversed state. Decreasing the amplitude to 15.75 Oe the magnetization reaches the 90° deviation and finally relaxes to the non-reversed orientation.

*The switching time dependence on the magnetic anisotropy ( $H_u$ )*

Similar results have been obtained increasing the magnetic anisotropy value. Figure 4.18c presents the simulated curves for 5 values of the anisotropy field, 20 Oe, 35 Oe, 36 Oe, 36.75 Oe. For an anisotropy field about 36.75 Oe the magnetization deviates by about 90° and then relaxes to the non-reversed state. For values about 35 Oe or 40 Oe we obtained longer switching times but the shift between the experimental and the simulated traces is about the same as in the previous cases.



**Figure 4.18**  
The switching time dependence on the values of a) the damping parameter,  $\alpha$ , b) the magnetic pulse amplitude,  $h_p$ , and c) the anisotropy field.

In conclusion, the reversal is produced if the energy given to the system by the external magnetic pulse is sufficiently high to pass the potential barrier corresponding to the precessional switching. By increasing the damping parameter, and the anisotropy field or by decreasing the pulse amplitude, the ratio: pulse energy over the damping in the magnetic system is decreased and for certain values of these parameters, the switching fails.

We analyzed the dependence of the magnetization switching on the ratio  $h_p/H_u$  for four values of the damping parameters (0.013, 0.02, 0.03 and 0.035). For this, pulse amplitude – anisotropy field diagrams have been calculated using the macrospin model. The results are presented in figure 4.19. The light-gray or dark-gray regions correspond respectively to the  $(h_p, H_u)$  values for which the magnetization is reversed (R) or non-reversed (NR). The transition from reversal to non-reversal regions corresponds to the linear dependences:

- for  $\alpha = 0.013$ ;  $h_p^{limit} = 0.55 \cdot H_u + 4.7$
- for  $\alpha = 0.02$ ;  $h_p^{limit} = 0.58 \cdot H_u + 6.5$
- for  $\alpha = 0.03$ ;  $h_p^{limit} = 0.62 \cdot H_u + 9.3$
- for  $\alpha = 0.035$ ;  $h_p^{limit} = 0.63 \cdot H_u + 11$

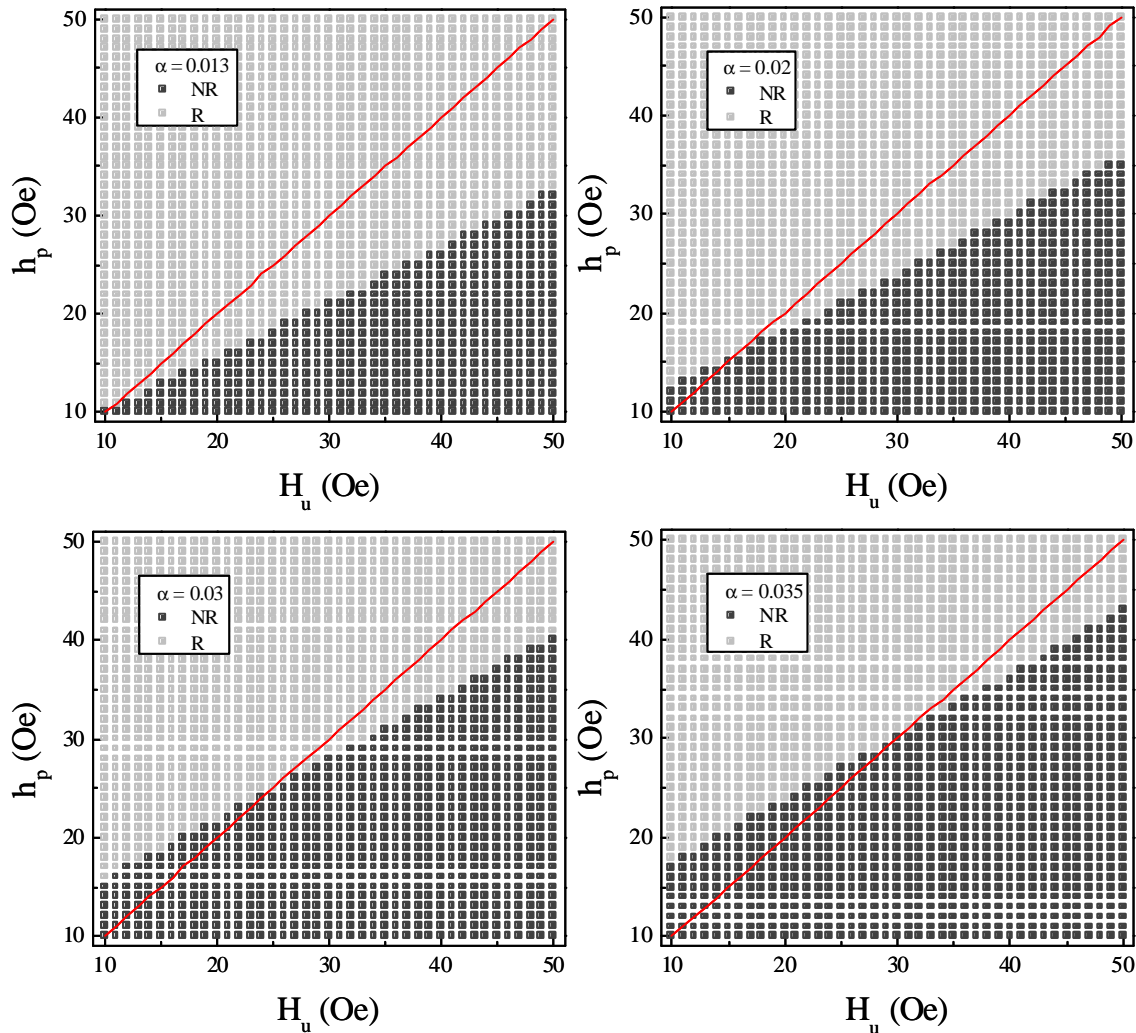


Figure 4.19: Pulse amplitude – anisotropy field switching diagram calculated for  $\alpha = 0.013, 0.02, 0.03$  and  $0.035$

The ( $h_p$ ,  $H_u$ ) values corresponding to the transition between reversal and non-reversal regions have corresponding time-traces similar to the ones obtained for  $h_p = 15.75$  Oe and for  $H_u = 36.75$  Oe that are presented in figure 4.18b, c.

We observe that increasing the damping parameter while keeping a constant value of the anisotropy field, we need a larger value for the pulsed magnetic field to obtain the reversal.

In conclusion, as a function of  $a$ ,  $h_p$  and  $H_u$  values, the switching time may vary between 0.4ps to 1ns as shown in the examples presented above. Nevertheless, an important point that remains to be explained is the undershoot.

## ii) The undershoot

### *The misalignment between the easy axis and ox-axis*

We will show that a misalignment between the easy axis and the  $ox$ -axis may result in an undershoot of the transversal magnetization component variation just before the switching.

We realized macrospin simulations using an anisotropy field of about 20 Oe, pump pulses of 25 Oe amplitude, deviation angles  $\mathbf{j}$  between the easy axis and the  $ox$ -axis equal to  $20^\circ$ ,  $-15^\circ$ ,  $-10^\circ$ ,  $-5^\circ$  and  $0^\circ$  (see figure 4.20) and 4 different values for the damping parameter,  $\alpha = 0.013$ , 0.02, 0.03, and 0.035. Considering the following values for the parameters used in the macrospin simulations:

$$\begin{aligned} g &= 2.18, N_x = 0, N_y = 0; H_u = 20 \text{ Oe} \\ h_p &\parallel -oy, \text{ pulse rise-time} = 55\text{ps}, \text{ pulse fall-time} = 60\text{ps}, \text{ pulse width} = 300\text{ps}; \\ M_s &= 800.4 \text{ emu/cm}^3 \end{aligned}$$

we obtained the results presented in figure 4.20.

Firstly, we observe that the undershoot amplitude increases by increasing the value of the deviation angle. Among the results presented here (fig.4.20), the largest undershoot amplitude was obtained for a deviation of  $(-20^\circ)$ . The undershoot obtained in the experimental measurements is comparable to the simulated one for deviation comparable to  $(-15^\circ)$  and  $(-20^\circ)$ , being quasi-zero for  $(-5^\circ)$  or  $(-10^\circ)$ .

Secondly, we observe that for:

- i)  $\phi = -5^\circ$  and  $\alpha = 0.035$ ,
- i)  $\phi = -10^\circ, -15^\circ$  and  $\alpha = 0.03$  and  $0.035$ ,
- ii)  $\phi = -20^\circ$  and  $\alpha = 0.02, 0.03$  and  $0.035$ ,

the magnetization switching induced by the reflected pulse fails (fig.4.20)

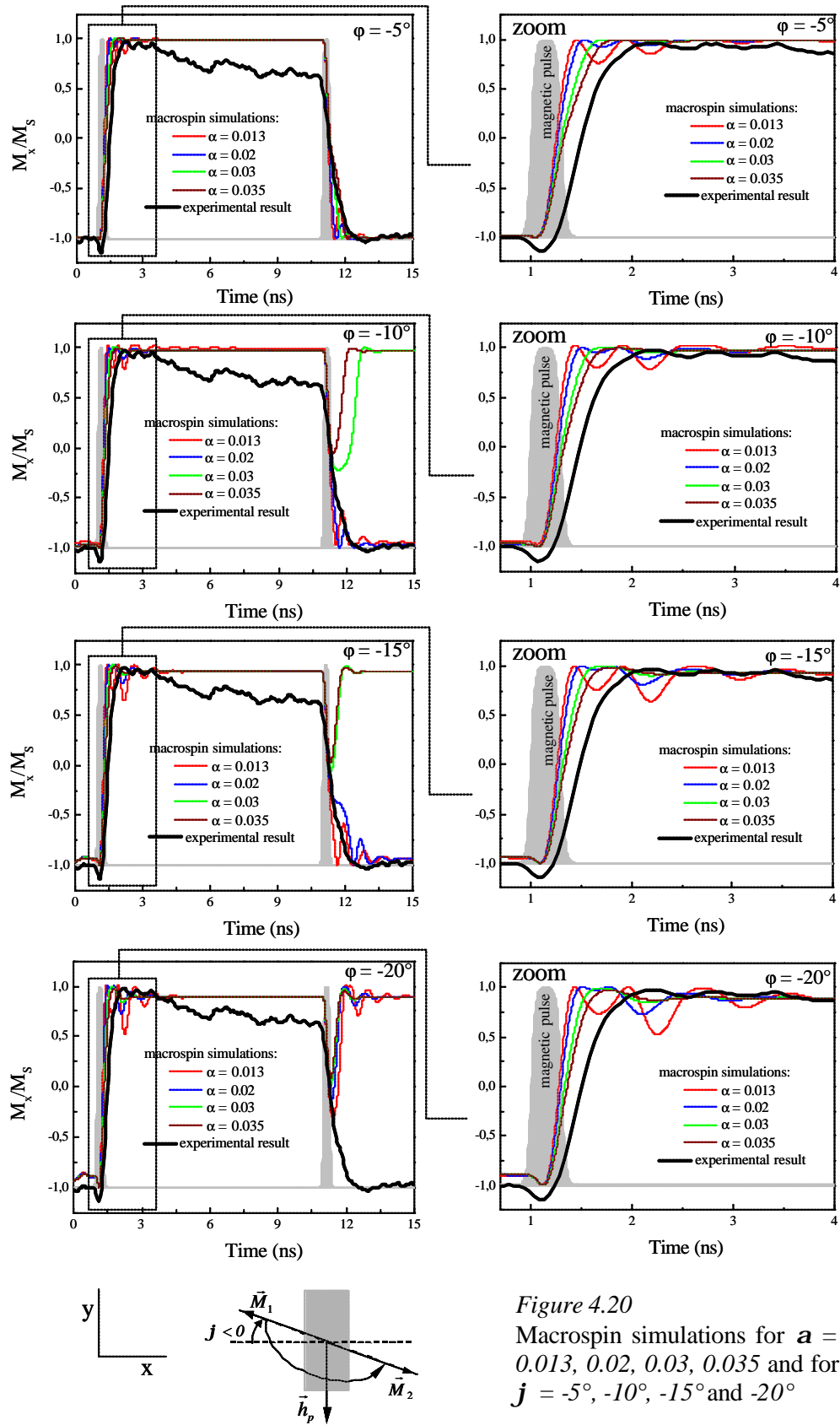


Figure 4.20

Macrospin simulations for  $\alpha = 0.013, 0.02, 0.03, 0.035$  and for  $j = -5^\circ, -10^\circ, -15^\circ$  and  $-20^\circ$



In consequence, increasing  $\phi$  (the angle between the initial magnetization and the  $ox$ -axis), the damping value, for which the magnetization switching fails, decreases. For example, for  $a = 0.3$  the switching induced by the reflected pulse fails for initial deviation angles larger than  $10^\circ$ . This behavior does not correspond to the experimental result where the magnetization switches for both the incident and the reflected magnetic pulse.

In conclusion, the undershoot cannot be explained entirely by the deviation of the easy axis with respect to the  $ox$ -axis. Small deviations (up to  $-10^\circ$ ) can be always envisaged since the magnetic sample is characterized by a complex magnetic configuration, similar to the magnetization ripple structure, as observed on the MFM images previously presented, but, the undershoot due to this misalignment is smaller than the one obtained on the experimental time-trace.

The second possible explanation of the undershoot is related to the Kerr measurement configuration and it is detailed in the following.

#### *Longitudinal and polar contributions in the transversal MOKE signal*

As mentioned in chapter 2, in a time-resolved transversal MOKE experiment the Kerr intensity ( $DI$ ) contains informations on all the three components of the magnetization. This is expressed by the linear dependence<sup>4</sup>:  $\Delta I_{Kerr}^{transversal} = P_1 + P_2 m_l + P_3 m_t + P_4 m_p$ , where  $P_1 = 0.1235$ ,  $P_2 = 2.2 \cdot 10^{-4}$ ,  $P_3 = 1.41 \cdot 10^{-3}$  and  $P_4 = 4.71 \cdot 10^{-3}$ .

In figures 4.21a and b we present the time variation of  $DI$  calculated as a function of  $m_l$ ,  $m_t$  and  $m_p$ , which were obtained from the macrospin simulations for  $a = 0.013$ ,  $0.02$ ,  $0.03$  or  $0.035$ ,  $j = 0^\circ$ ,  $h_p = 25$  Oe and  $H_u = 20$  Oe. The other parameters used in the macrospin simulations were the same as above.

Figure 4.21d, presents the traces corresponding to  $P_2 m_l$ ,  $P_3 m_t$ , and  $P_4 m_p$ . We observe that both longitudinal and polar contributions present negative peaks corresponding to the incident pulse just before the magnetization reversal and peaks of opposite signs corresponding to the reflected pulse. On the simulated  $DI$  trace we can distinguish an undershoot corresponding to the incident pulse and an overshoot (fig. 4.21c) corresponding to the reflected pulse. The undershoot and the overshoot are determined by the sum and respective, difference, between the amplitudes of the polar and longitudinal peaks, corresponding to the incident and reflected magnetic pulses. The overshoot has smaller amplitude than the undershoot since their amplitudes can be expressed as:

---

<sup>4</sup> For the set of parameters  $(n, Q)$  specified in chapter 2

$$\begin{aligned}\Delta I_{undershoot} &= P_2 m_l + P_4 m_p \\ \Delta I_{overshoot} &= -P_2 m_l + P_4 m_p\end{aligned}\quad (4.6)$$

In consequence from equations 4.6 it is possible to determine the longitudinal and the polar components corresponding to the undershoot and respective overshoot using:

$$\begin{aligned}m_p &= \frac{\Delta I_{undershoot} + \Delta I_{overshoot}}{P_4} \\ m_l &= \frac{\Delta I_{undershoot} - \Delta I_{overshoot}}{P_2}\end{aligned}\quad (4.7)$$

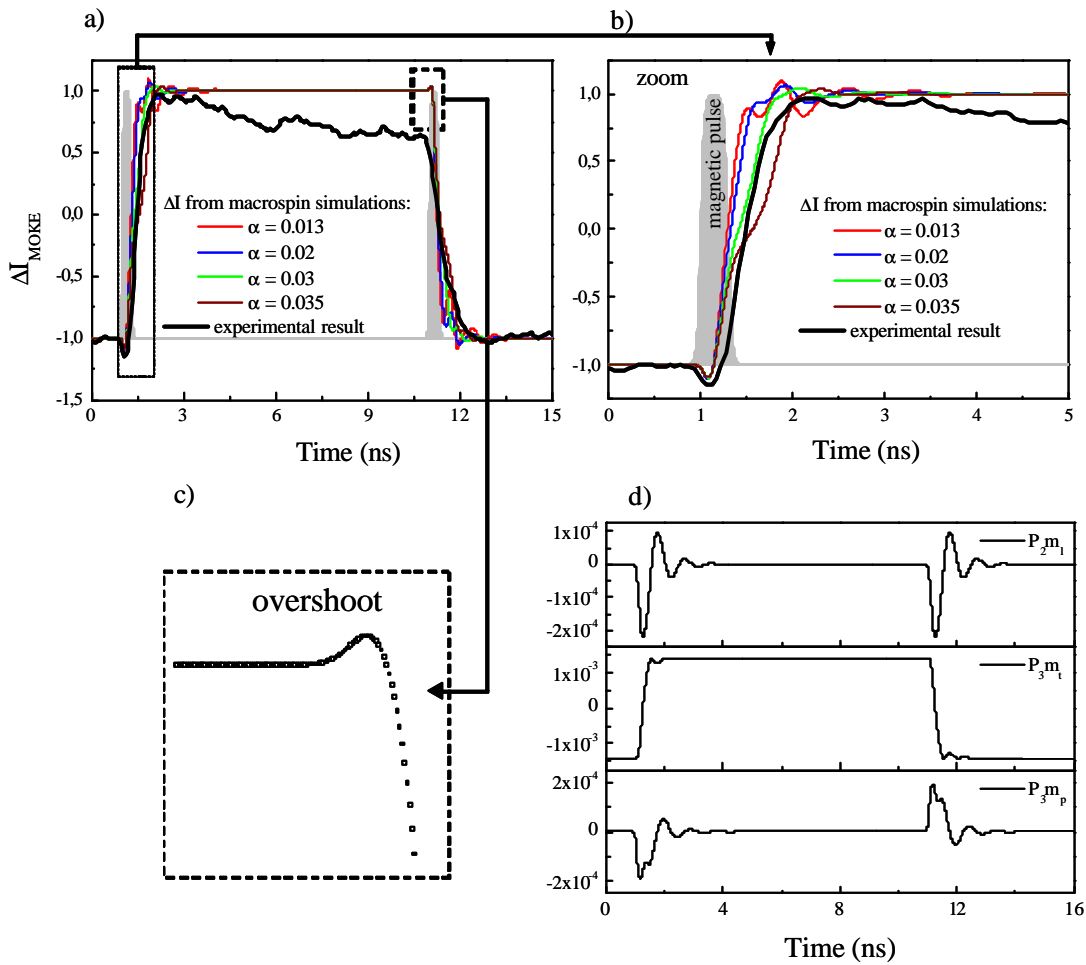


Figure 4.21: The undershoot due to the polar and longitudinal components of the magnetization for  $\alpha = 0.013, 0.02, 0.03$ , and  $0.035$ .

On the experimental time trace presented in figure 4.21a, the overshoot is not obvious since during the time interval between the incident and the reflected pulse one observes a magnetization relaxation. This might be due to domain wall propagation in such magnetic systems characterized by complex magnetic structure as shown on the MFM images (fig.4.4).

Furthermore, the overshoot is not visible on all the experimental time-traces since its amplitude becomes comparable to the experimental noise.

In conclusion the undershoot is mostly determined by the polar and longitudinal magnetization component but this does not exclude a possible misalignment between the easy axis of the magnetic sample and the  $ox$ -axis.

### iii) The absence of oscillations on the experimental time-trace

In order to understand the absence of oscillations, it has to be noted, that the stroboscopic technique measures the average response of a large number of reversal cycles (approx. 70000). This requires a high correlation, and hence a high level of reproducibility of the magnetization configuration between all switching events [Freeman 2002].

The absence of oscillations on the experimental trace can be explained by the fluctuations of the remanent state values observed in the quasi-static measurements (fig.4.15). More precisely, different remanent states correspond to different magnetic configurations on the sample and thus different oscillation modes, which are uncorrelated from one switching event to the next. Consequently, the magnetization oscillations, which are excited during and after the main reversal and which relax the energy acquired from the field pulse, will not be well correlated, from one switching event to the next. Therefore, an average over all these events reduces the oscillation amplitudes.

It is furthermore noted, that even for ideal reversal ( $\Delta M_R/2M_s=1$ ), it has been calculated [Miltat 2000] for the case of sub-micron rectangles, that the finite size effect induces inhomogeneous magnetization oscillations throughout the sample, which leads to rather irregular variations in the average magnetization component instead of correlated periodic oscillations.

In this context, we also would like to draw attention to the role which the effective damping factor might play for the visibility of the ringing effect for a macrospin or equivalently for the coherent oscillations averaged over the sample as probed by the experiment. The amplitude of the ringing oscillations of the transversal component are reduced by almost a factor of ten when increasing  $\alpha$  for instance from 0.013 to 0.035 (see figures 4.18a and 4.20). This strong decrease with a modest increase in  $\alpha$  is due to the exponential decay law, which describes the variation of the oscillation amplitudes [Silva 1999].

### The switching failure

We observed from the simulations that for certain parameters ( $\mathbf{a}$ ,  $h_p$ ,  $H_u$ ,  $\mathbf{j} \neq 0$ ), the reflected pulse does not induce the magnetization switching even though the incident pulse reverses the magnetization (fig. 4.20). In the following, we discuss this aspect and its influence on the stroboscopic result.

For magnetization deviation angles  $\mathbf{j} \neq 0$ , the relative orientation of the magnetizations with respect to the incident and respective the reflected pulse, are not equivalent ( $|\mathbf{f}_1| \neq |\mathbf{f}_2|$ , fig.4.22). This determines non-equivalent switching processes induced by the incident and by the reflected magnetic field pulses. In consequence, in certain configurations, the magnetization is reversed by the incident pulse, while the switching fails after the reflected pulse.

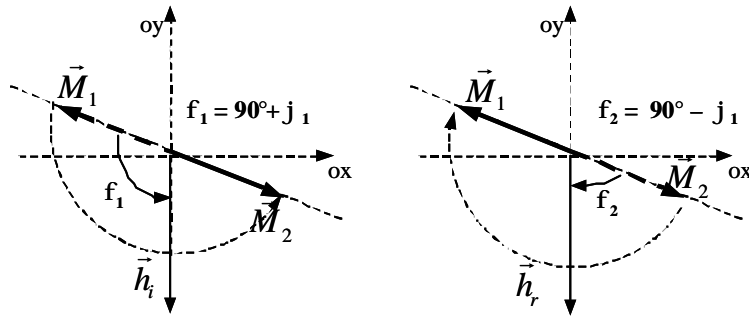


Figure 4.22

The initial orientations of the magnetizations  $\vec{M}_1$  and  $\vec{M}_2$  with respect to the incident and respective reflected pulse ( $\vec{h}_i$  and  $\vec{h}_r$ ) are characterized by different angles  $\phi_1 \neq \phi_2$ .

This can explain a local switching failure, which is one of the mechanisms of the reduction of the remanent state observed on the quasi-static measurements. The experimental evidence of these were obtained and are presented on the figure 4.15, points 1 and 2.

### Switching diagrams

The switching diagram represents a bi-dimensional representation of the reversed (R)- or non-reversed (NR) regions, which are defined by the points (X, Y) where X and Y coordinates are represented by parameters such as pulse amplitude, pulse width, or the angle  $\phi$  between the magnetization and the ox-axis, etc. One of the disadvantages of these diagrams is that they contain no information on the ringing after reversal.

In the following we present a) the pulse amplitude versus the pulse width diagram for 4 values of the damping parameter,  $\mathbf{a} = 0.013, 0.02, 0.03$ , and  $0.035$  and b) deviation  $\phi$  versus pulse width diagram for  $\mathbf{a} = 0.02$ .

a) *The amplitude/width diagram*

Using the macrospin simulation code, we calculated the pulse amplitude versus pulse width diagram, such diagrams have been realized and experimentally confirmed by Schumacher et al. [Schumacher 2003].

For the macrospin simulations, we used the parameters:

$$g = 2.18, N_x = 0, N_y = 0;$$

$$H_u = 20 \text{ Oe}$$

$$h_p \hat{\mathbf{I}} (10 - 100) \text{ Oe} \parallel -oy; \text{ pulse rise-time} = 55\text{ps}, \text{ pulse fall-time} = 60\text{ps}, \text{ pulse width } \hat{\mathbf{I}} (50\text{ps} - 1\text{ns});$$

$$M_S = 800.4 \text{ emu/cm}^3$$

The diagrams are presented in figure 4.23 for pulse widths between 50ps and 1ns and amplitudes from 10 Oe to 100 Oe. We observe dark and light gray regions, which correspond to either non-reversal (NR) or respective reversal (R), of the macrospin magnetization.

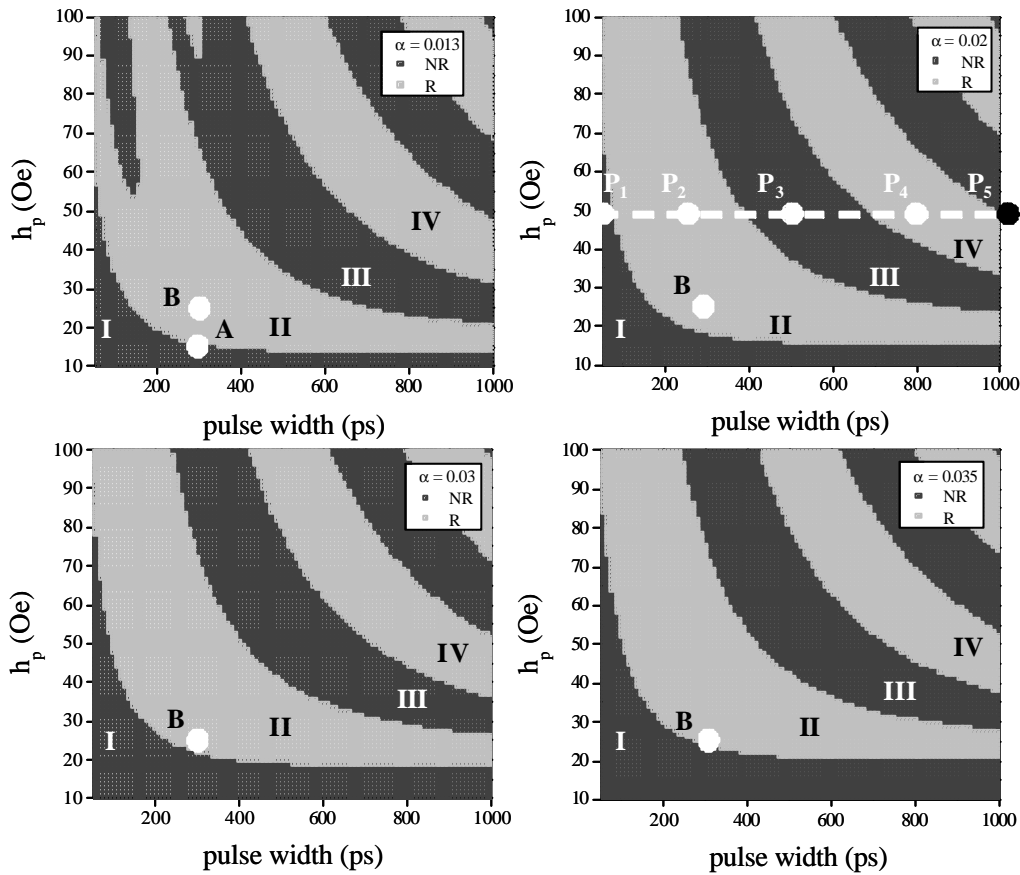


Figure 4.23  
Amplitude-width diagram obtained by macrospin simulations

On these diagrams, the point A corresponds to the transition from non-reversal to reversal. The corresponding time trace is presented in figure 4.18b for  $h_p = 15.75$  Oe. For the entire first dark-gray region (I), the magnetization is not reversed even for large widths of the

pulses. For larger damping values, the “islands” observed for  $a = 0.013$  are shifted to higher magnetic pulses (larger than 100Oe for  $a > 0.02$ ). Also, increasing the damping parameter, the points B, on all diagrams, become closer to the lower dark region (I). The time traces corresponding to these points can be observed on figure 4.18a.

On all diagrams, for constant magnetic field pulse amplitude, increasing the pulse width one passes from dark-gray to light-gray regions, or from non-reversed to reversed orientations.

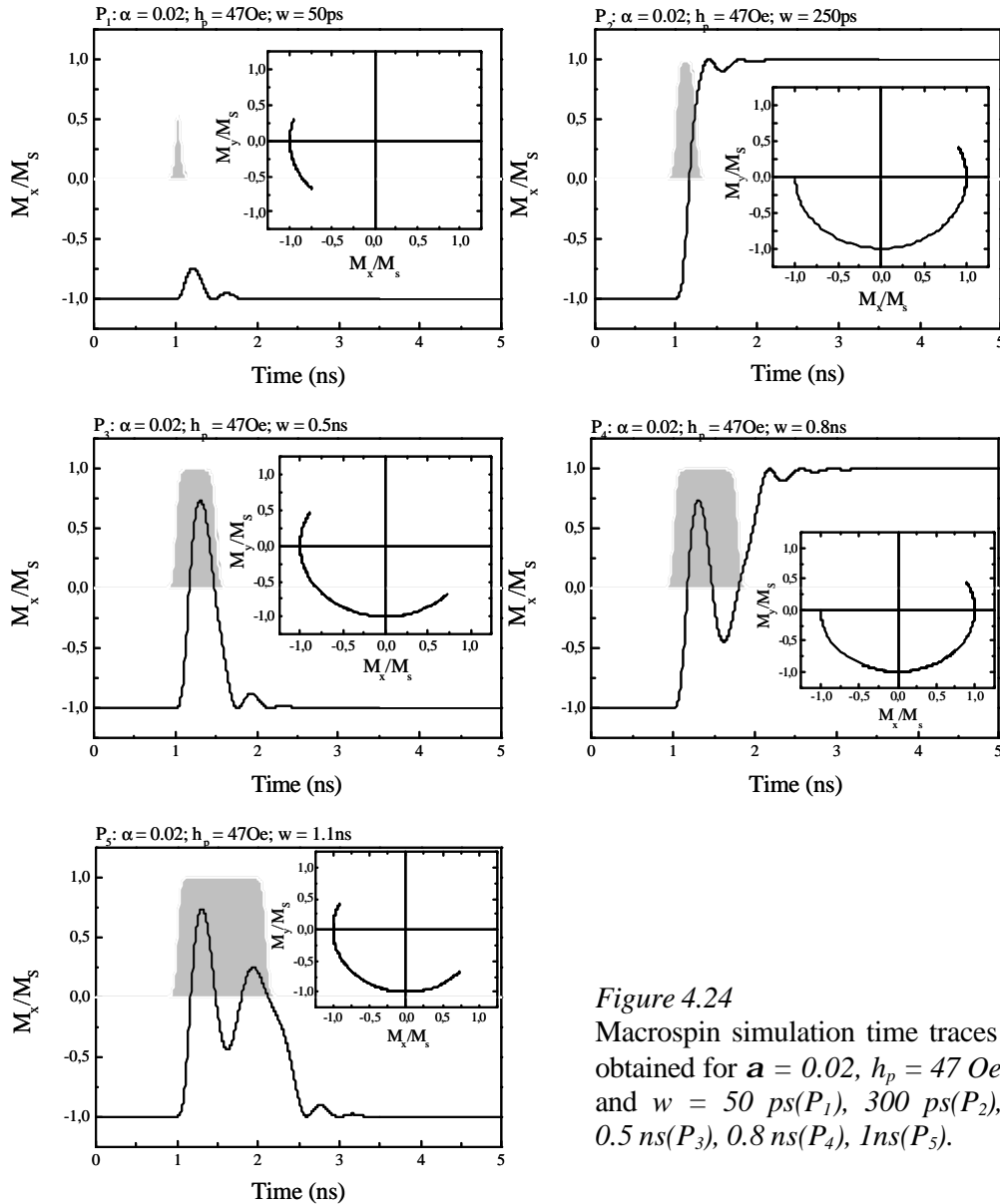


Figure 4.24

Macrospin simulation time traces obtained for  $a = 0.02$ ,  $h_p = 47$  Oe and  $w = 50$  ps ( $P_1$ ), 300 ps ( $P_2$ ), 0.5 ns ( $P_3$ ), 0.8 ns ( $P_4$ ), 1 ns ( $P_5$ ).

To better understand this transition from one reversed region to a non-reversed one, we obtained the macrospin time-traces corresponding to five points on the diagram for  $a = 0.02$ . They correspond to  $h_p = 47$  Oe and pulse widths of 50 ps ( $P_1$ ), 250 ps ( $P_2$ ), 0.5 ns ( $P_3$ ), 0.8 ns

( $P_4$ ) and 1.1ns ( $P_5$ ). The time-traces and the magnetization trajectories in the  $xy$ -plane are presented in figure 4.24.

The first point ( $P_1$ ) characterizes the first dark-gray region (I) where the reversal is not obtained. The magnetic field pulse induces deviations of the magnetization vector smaller than  $90^\circ$  (in this example the magnetization rotation angle is about  $60^\circ$ ).

The second point ( $P_2$ ) corresponds to the magnetization reversal by precession and it characterizes the first light-gray region (II).

Increasing the pulse duration, we obtain the time-trace corresponding to the third point ( $P_3$ ). At the third point it is noted that the magnetization does not completely reverse and after the pulse stops it returns toward its initial state. In this case, we obtain a non-reversal state (second dark-gray region (III)) but not as a consequence of a  $360^\circ$  complete precession. Smaller damping or larger pulse amplitude should lead to a larger angle deviation and eventually to a deviation larger than  $180^\circ$ .

Continuing to increase the pulse duration, the magnetization starts an oscillation around the  $90^\circ$ -deviation direction as we can observe for the durations of 800ps ( $P_4$ ) and 1ns( $P_5$ ). For 800ps pulse width, after one entire precession around the pulse direction, the magnetization relaxes parallel to the reversed orientation. For larger pulses, e.g. 1.1ns duration, the oscillating motion of the magnetization takes a longer time, and, finally the magnetization relaxes parallel to the non-reversed direction.

### *The angle/width diagram*

In the analysis of the results obtained on magnetic systems characterized by a complex magnetic structure, it is important to have a reversal diagram of the pulse width,  $w$ , as a function of the magnetization deviation angle,  $\mathbf{j}$ .

We have obtained the pulse width versus deviation angle diagram using the parameters:

$$\begin{aligned} g &= 2.18, N_x = 0, N_y = 0; \mathbf{a} = 0.013 \\ H_u &= 20 \text{ Oe}, \mathbf{j} \hat{\mathbf{I}} (0^\circ - 360^\circ) \\ h_p &= 25 \text{ Oe} // -oy; \text{pulse rise-time} = 55\text{ps}, \text{pulse fall-time} = 60\text{ps}, \text{pulse width } \hat{\mathbf{I}} (50\text{ps} - 1\text{ns}); \\ M_s &= 800.4 \text{ emu/cm}^3; \mathbf{j} \hat{\mathbf{I}} (0^\circ - 360^\circ); \end{aligned}$$

It is presented in figure 4.25 in polar coordinates.

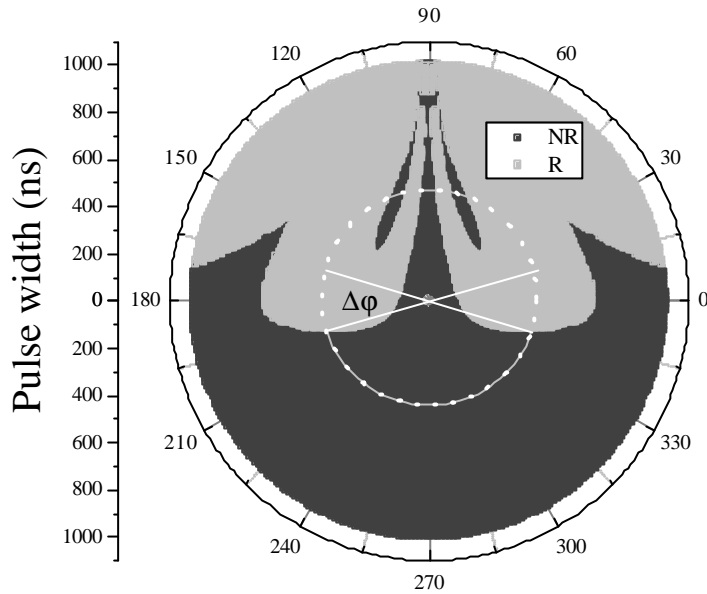


Figure 4.25

Polar representation of the switching diagram that represents the pulse width as a function of the magnetization deviation angle  $\mathbf{j}$ .

In this particular case, one can define the conditions for the magnetization switching for both the incident and the reflected pulse. Considering a given pulse width ( $w$ ) represented in the diagram by the white circle, the magnetization that has the orientation inside the angle ( $D\mathbf{j}$ ) (see figure 4.25), and which is characterized by a pulse width corresponding to a light gray region, reverse for both incident and reflected magnetic field pulses. We call this *the critical switching angle*. In all the other cases, the magnetization does not switch or switch only once. On figure 4.25,  $\Delta\mathbf{j} = 20^\circ$ , that determines a deviation angle of the magnetization of maximum  $10^\circ$ .



#### 4.3.4.5. PRECESSIONAL MAGNETIZATION SWITCHING - CONCLUSIONS

During this work, we obtained similar precessional reversal results on the isolated and integrated soft layer Co/FeNi. These are summarized in figure 4.26a and 4.26b, which represents the ratios  $\Delta M_R / 2M_S$  obtained for the two magnetic samples.

Different stroboscopic time traces correspond to measurements realized at different positions on the sample. In consequence, here we present 2 (4.26a) or 4 (fig.4.26b) traces that correspond to different measurements. From these, we deduced an interval for the pulse widths, of approximately 300 ps to 550 ps, where precessional reversal of the magnetization was experimentally obtained on both samples. The simulated values for the reversal correspond to a larger interval for the widths (150 ps to 550 ps) for 25 Oe pulse amplitude as shown on figure 4.23.

This can be explained considering:

- The precessional reversal events of fluctuating amplitude were obtained for widths smaller than 300 ps during the quasi-static measurements (fig.4.15) even if on the stroboscopic curves the response was zero.
- On the amplitude-width switching diagram presented in figure 4.23, increasing the effective damping parameter, the value of the pulse duration for which the reversal is obtained increases.
- Considering the angle-width switching diagram presented in figure 4.25, we observe that for non-zero deviations of the easy axis with respect to  $ox$ -axis (e.g.  $\mathbf{j} = 190^\circ$ ), the pulse duration interval corresponding to reversal decreases.

In consequence, including an increased effective damping parameter (due to sample inhomogeneities or internal field inhomogeneities) and a deviation angle  $\phi$  of the initial magnetization we obtain the calculated diagram represented in figure 4.26c that corresponds to the experimental pulse width interval for which the magnetization switching is obtained. The diagram amplitude-width was obtained for  $\mathbf{j} = 187^\circ$  and  $\mathbf{a} = 0.025$ . The others parameters used in the macrospin calculations were:

$$\begin{aligned} g &= 2.18, N_x = 0, N_y = 0; \\ H_u &= 20 \text{ Oe}; \\ h_p \hat{\mathbf{I}} &(20-30) \text{ Oe} \parallel -oy, \text{ pulse rise-time} = 55 \text{ ps}, \text{ pulse fall-time} = 60 \text{ ps}; \text{ width } w \hat{\mathbf{I}} (50 \text{ ps} - 1 \text{ ns}) \\ M_S &= 800.4 \text{ emu/cm}^3; \end{aligned}$$

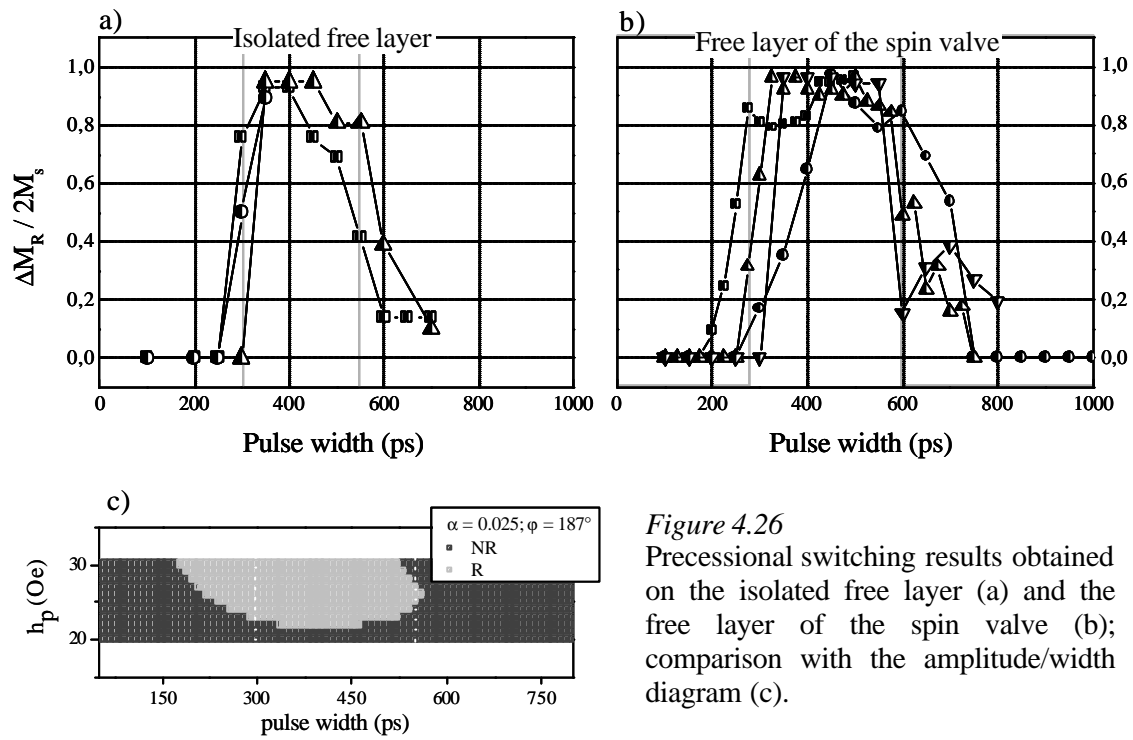


Figure 4.26

Precessional switching results obtained on the isolated free layer (a) and the free layer of the spin valve (b); comparison with the amplitude/width diagram (c).

#### 4.4. PRECESSIONAL REVERSAL ON MICRON-SIZED IRMN-BASED SPIN VALVES

Magneto-Resistive (MR) static and dynamic measurements were realized on IrMn-based bottom spin valves of structure:

**Ta(5nm)/NiFe(3nm)/IrMn(7nm)/Co(3nm)/Cu(2.5nm)/Co(1nm)/NiFe(4nm)/Pt(2nm)**

The sample preparation for dynamic MR measurements is more complex than for optical measurements since the electrical contacts necessary for **Current-In-Plane** (CIP) or **Current-Perpendicular to -Plane** (CPP) demand supplementary preparation and characterization steps. All details concerning the sample preparation are described in chapter 3. The optical photograph of a finalized device realized for CIP-MR measurements, is presented in figure 4.27. It consists of:

- i) The **coplanar waveguide** (CPW) used to obtain high frequency magnetic field excitations;
- ii) The micron-sized magnetic sample etched on top of the centerline of the CPW, isolated from the metal surface by a SiO<sub>2</sub> layer of 50nm thickness;
- iii) The CIP contacts deposited on top of the magnetic sample and isolated from the bottom CPW by a SiO<sub>2</sub> layer of 50nm thickness.

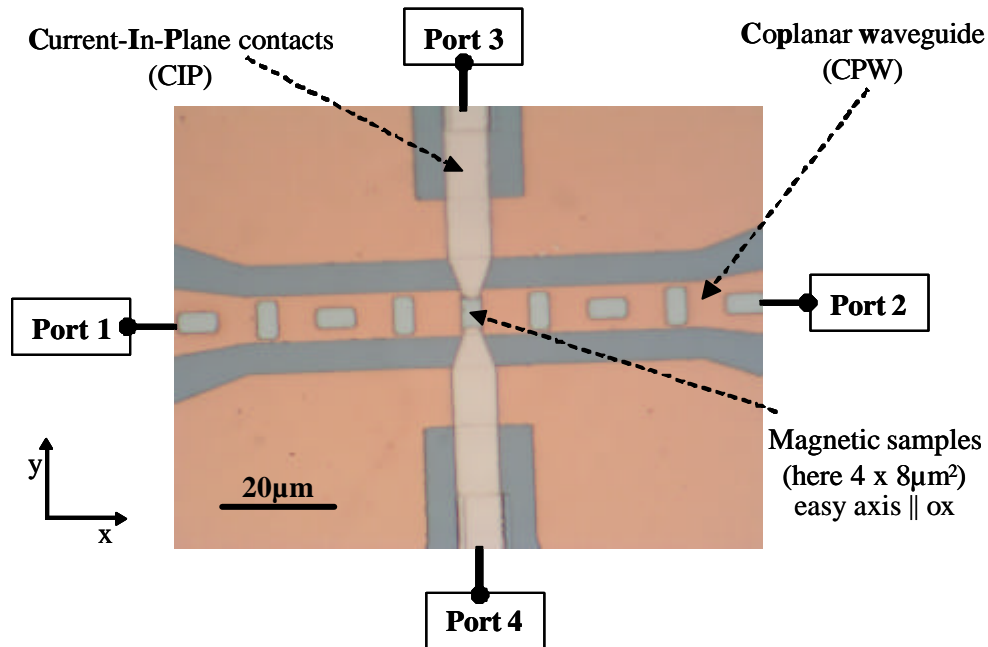


*Figure 4.27*

The optical photograph of a MR sample composed by the CPW, magnetic samples, and CIP contacts

Nine magnetic samples have been patterned on the centerline of the waveguide but only the one in the middle was used to measure the MR effect. The other samples have been patterned for future static and dynamic MOKE measurements. Actually, the laser spot is larger than  $4 \times 8 \mu\text{m}^2$  and the Kerr signal has a very large noise because of diffusive reflection of the incident light on the sample borders.

Three different MR-devices have been designed for the MR dynamic measurements:

- i) Of  $10 \mu\text{m}$  centerline width and magnetic sample dimensions of  $4 \times 8 \mu\text{m}^2$ ;
- ii) Of  $5 \mu\text{m}$  centerline width and magnetic sample dimensions of  $2 \times 4 \mu\text{m}^2$ ;
- iii) Of  $2 \mu\text{m}$  centerline width and magnetic sample dimensions of  $1 \times 2 \mu\text{m}^2$ .

Because of the poor spatial resolution of the lithography process (see chapter 3), we finalized only the first two devices. For the third device, it was impossible to pattern the CIP contacts on the magnetic sample surface.

#### 4.4.1. STATIC MAGNETO-RESISTIVE CHARACTERIZATION

The IrMn based bottom spin valve consists of a pinned layer: IrMn/Co and a soft layer Co/NiFe separated by a Cu spacer. The pinning direction of the hard Co layer was defined by annealing at  $150^\circ\text{C}$  for 30min in the presence of an external magnetic field applied parallel to the short axis of these elements. The exchange coupling between the IrMn anti-ferromagnetic layer and the Co ferromagnetic layer will determine the displacement of the hysteresis loop of the pinned layer with respect to zero field. Due to orange peel coupling between the hard and the free layer [Néel1962], the minor loop is also shifted from zero fields.

The static characterization of the spin-valve was realized by measuring the MR effect in the longitudinal ( $I \parallel H$ ) and the transverse ( $I \perp H$ ) configuration (as detailed in the chapter 2) using the two points contact in CIP geometry (CIP contacts on figure 4.27).

The dynamic MR-device is characterized by 4 ports: the first and the second for the pump line, and the third and the fourth for the probe line (fig.4.27).

The static MR measurements were realized by applying a constant current ( $I = 0.3\text{mA}$ ) to port 3, varying the external magnetic field, and measuring the variation of the voltage in the magnetic sample. The corresponding MR hysteresis loop is presented in figure 4.28. Because the measurement is realized in two point contacts mode, the total resistance value of about  $96\Omega$  include besides the spin valve, the line, and the termination resistances.

In general, the MR signal is a superposition of the AMR and GMR effect. As shown in chapter 2, the AMR is at maximum (minimum) when the current is parallel (perpendicular) to

the magnetization direction. In the transverse configuration, where the external field is perpendicular to the current, at saturation, the AMR is minimum, and, it becomes maximum around the coercive field. From the transverse loop, (fig.4.28), we deduce a coercive field value of about 10 Oe for the free layer and around 300 Oe for the hard layer. On the longitudinal loop, we observe two minima corresponding to the coercive field values of the soft layers that are due to the AMR effect. In this case, the AMR is maximum for saturation.

The sample dimensions are small enough to induce a non-negligible demagnetizing field, which tries to keep the magnetization parallel to the long dimension of the sample. The estimated value for the averaged demagnetizing field for an elliptical shape of  $4\mu\text{m} \times 8\mu\text{m} \times 5\text{nm}$  is about 8 Oe. The competition between the uniaxial anisotropy induced during the sample deposition and annealing ( $\parallel$  to the short axis of the magnetic sample) and the shape anisotropy ( $\parallel$  to the long axis of the magnetic sample), will favor the creation of magnetic domains.

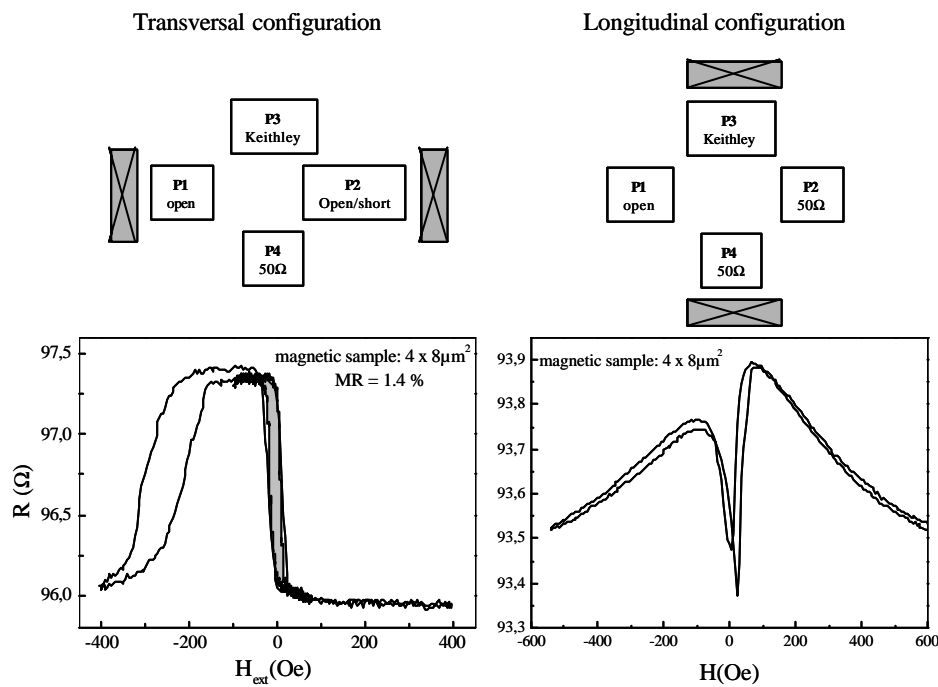
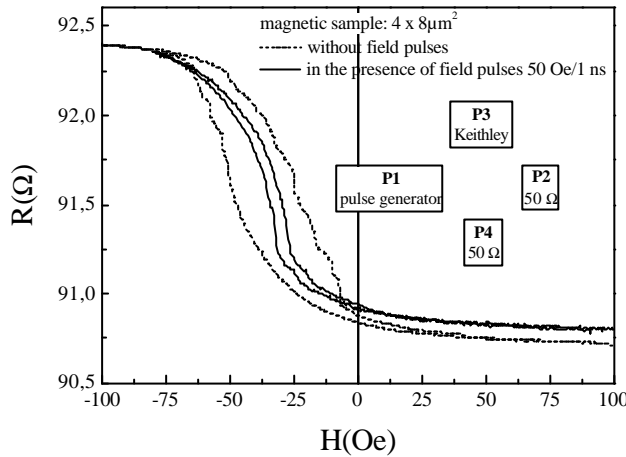


Figure 4.28

The transversal and longitudinal MR measurements of  $4 \times 8\mu\text{m}^2$  IrMn-based bottom spin valve

The measurements realized in the transverse configuration (fig.4.28), for the external magnetic field parallel to the short dimension of the magnetic sample ( $4\mu\text{m}$ ), reveal a coercive field of 10 Oe. Comparing the longitudinal and transversal measurements, we conclude that the axis parallel to the short element direction is an easier magnetic direction.

Static minor loops realized in the presence of short magnetic pulses are characterized by a smaller coercive value as compared to the one when the pulses are absent, as shown in figure 4.29. These results are similar to those obtained on NiO-based spin valve samples using MOKE (see section 4.2.5).



*Figure 4.29*  
The minor hysteresis loops of IrMn-based bottom spin-valve in the presence and absence of magnetic field pulses of 50Oe amplitude and 1ns duration.

#### 4.4.2. THE CHARACTERIZATION OF THE ELECTRONIC DEVICE

Using a 50Ω termination connected at port 4 of the MR device we realized MR measurements for three different terminations connected at port 2: short-circuit, 50Ω and open circuit. Port 1 is connected to the pulse generator.

An ideal MR-device should have similar resistance values in the three cases, and consequently, similar MR responses. In our case, we obtained three different values for the electrical resistances as measured with the Keithley:

- For a short termination of port 2 we obtained a value of 11.4 Ω;
- For a 50Ω termination of port 2 we obtained a value of 36 Ω;
- For an open-termination of port 2 we obtained a value of 73.6 Ω.

Furthermore, the MR hysteresis loops look quite different as we can observe in figure 4.30 and the MR values vary between 0% for a short termination at P<sub>2</sub> to 0.7% for a 50Ω termination at P<sub>2</sub> and 1.78% for an open termination at P<sub>2</sub>.

These results can be explained considering the existence of short-circuits between the pump line and probe line and/or the lower ground plane. In this case, one measures not only the probe line and sample resistance but also the resistance connected in parallel due to the pump line and/or to the lower ground plane.

The resistance value of the sample was estimated to about  $2\Omega$ , and of the probe line to about  $15\Omega$ . A  $50\Omega$  termination at port 4 should give a resistance about  $R_{\text{sample}} + R_{\text{probe-line}} + 50\Omega = 67\Omega$ .

A short termination at port 2 determines a significant part of the current to pass in the pump line or the ground plane, explaining the lower value of the resistance,  $11.4\Omega$ , on figure 4.30a.

A  $50\Omega$  termination at port 2 determines an equivalent resistance of about  $36\Omega$ . In this case, using the estimated value of the probe line and the sample of about  $67\Omega$  we should have an equivalent resistance value about  $R_{\text{equivalent}} = \frac{67\Omega \cdot 50\Omega}{67\Omega + 50\Omega} = 28.6\Omega$ .

An open termination determines no short circuit and the equivalent resistance was about  $73.6\Omega$ . In this case, we should measure the probe line and the sample resistance ( $67\Omega$ ).

The experimental values of the resistances are larger than the estimated ones by about  $7\Omega$ . This difference originates from the contact resistances, which can be more or less important as a function of the contacts quality on the probe line surface.

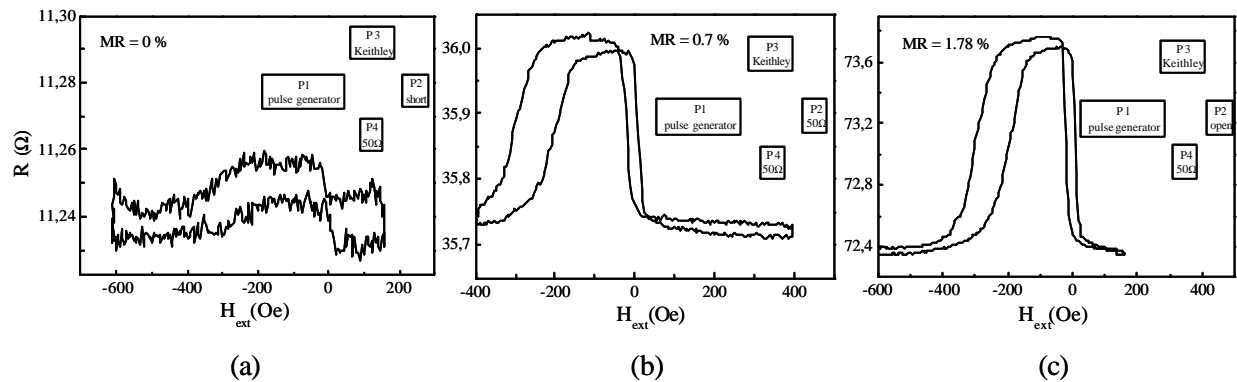


Figure 4.30

The variation of the MR-device resistance as a function of the termination to port 2 for a device characterized by a short circuit between the pump and probe lines

In the following, we discuss the equivalent DC circuit of the MR device in the ideal and the real cases.

#### DC equivalent circuits of the MR-device

As mentioned above, in the ideal case, the pump, and probe lines should be perfectly isolated from each other. Each element of the device has an equivalent resistance value:  $R_{\text{CPW}}$  for the pump line,  $R_{\text{CIP}}$  for the CIP contacts, and  $R_{\text{sample}}$  for the magnetic

sample. The equivalent circuit is presented in figure 4.31, taking only ohmic resistances into account. We suppose that the two lines are impedance matched to  $50\Omega$  over all their length.

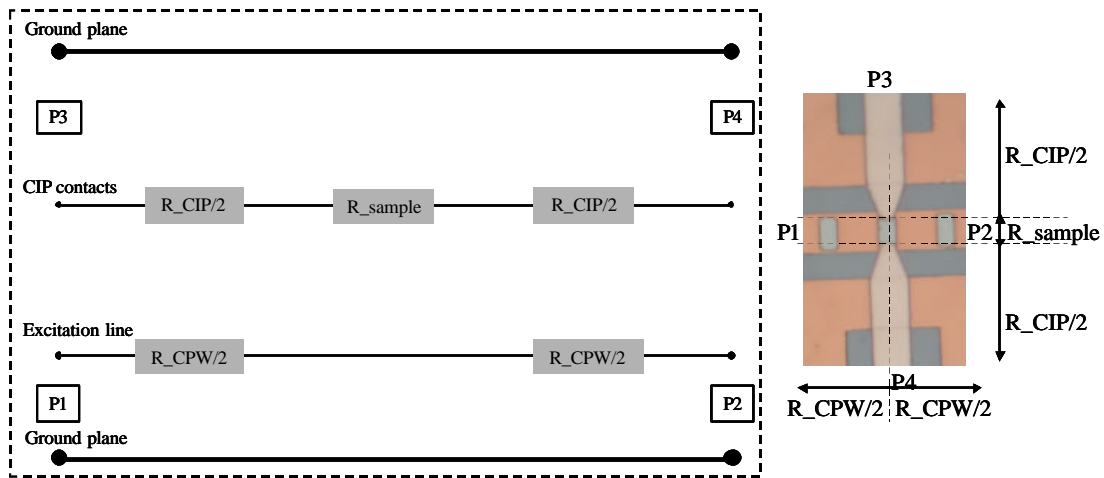


Figure 4.31

The equivalent circuit of an ideal MR device

The equivalent DC circuit for the real case is presented in the figure 4.32.

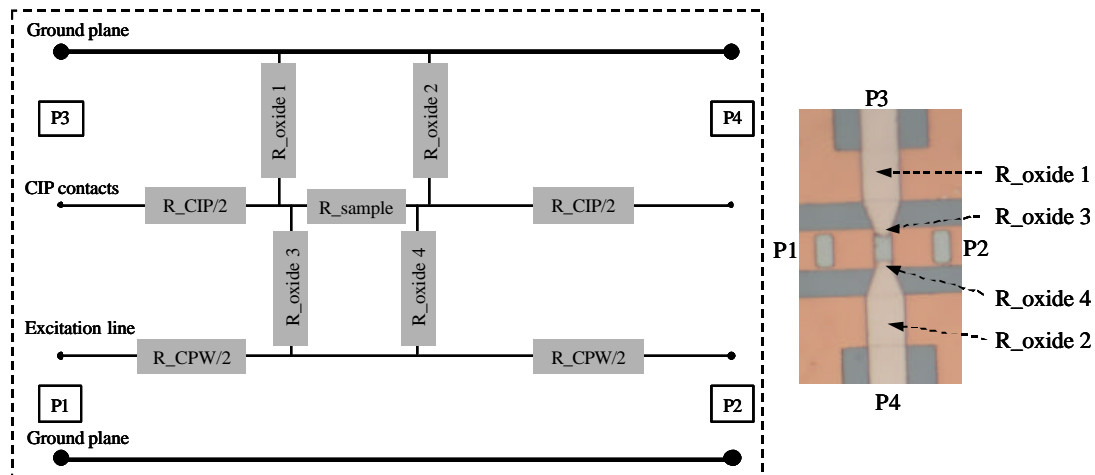


Figure 4.32

The equivalent circuit of a real MR device

As we have already mentioned in chapter 3, C-AFM images evidenced that the borders of the metallic pump line and of the ground plane are characterized by a reduced resistance of the oxide. We consider that these regions most probably will develop short circuits to the lower pump line or ground plane during the measurements. On the DC equivalent circuit (fig.4.32) these are defined by the resistances:  $R_{oxide\ 1}$ ,  $R_{oxide\ 2}$ ,  $R_{oxide\ 3}$  and  $R_{oxide\ 4}$ . The results presented in figure 4.30 are a consequence of the values of these resistances.



The short circuits mentioned above amplify the cross-talk between the two lines, making it more difficult to measure low signals obtained in the dynamic measurements. Important voltage oscillations have been recorded in the CIP contacts as a consequence of the LC coupling between the two lines. Figure 4.33, presents the high-frequency signal (the cross-talk) induced in the CIP contacts by voltage pulses of 5V amplitude and 5ns duration applied on the lower pump CPW. The measurement was realized with a 20GHz oscilloscope connected to port 3, with two 50 $\Omega$ -terminations at port 2 and 4. The pulse generator was connected to port 1 and delivered pulses with a frequency of 100 KHz.

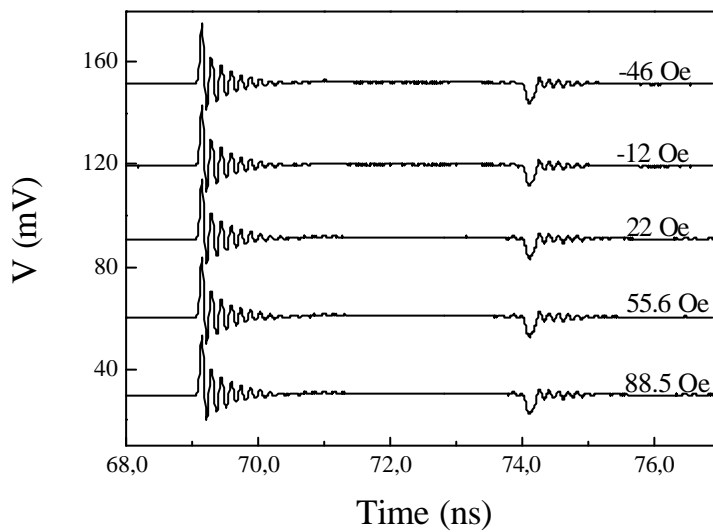


Figure 4.33

The cross-talk due to the LC coupling between the probe-line (CIP contacts) and the pump-line;

Varying the external magnetic field, we have not found any modification of the oscillation frequency, as expected if they had been due to the magnetization changes in the sample. Furthermore, the oscillation frequency, about 7 GHz, is larger than the typical frequencies of the magnetization precessions ( $\sim 1$  GHz).

As the cross-talk was important, the first MR experiments realized on these devices consisted in quasi-static MR measurement of the remanent magnetic states induced by successive magnetic field pulses delayed by several seconds. The results obtained for pulses of different amplitudes (28 Oe, 38 Oe and 48 Oe) and durations from 150 ps to 500 ps are presented in the following.

#### 4.4.3. REMANENCE MAGNETO-RESISTIVE MEASUREMENTS

Similar measurements to the ones presented in section 4.2.7.2. of this chapter were realized on IrMn-based bottom spin valves using the MR effect. These consist on the measurements of the magneto-resistance of the spin valve induced by successive magnetic field pulses of the same polarity.

These MR measurements were realized for 100 $\mu$ A DC current through the CIP contacts and about 30Oe bias field in order to center the minor loop in zero field (see MR static hysteresis loop presented in figure 4.34a). Quasi-static MR results obtained for magnetic field pulses of the same polarity (obtained with a 50 $\Omega$  termination at port 2) and delayed by about 10 seconds are presented in figure 4.34b. In the first 80 seconds the external magnetic field was varied from -100 Oe to +100 Oe to measure the maximum and minimum resistance levels,  $R_{max}$  and  $R_{min}$ . We adjust the bias field,  $H_{ext}$ , so that the sample is in the remanent point A in order to compensate the shift of the soft layer hysteresis loop originated from the exchange interaction between the pinned layer and the free layer. Then, magnetic field pulses of 48 Oe amplitude and 150ps width were applied to the magnetic sample every 10seconds. The amplitude of 48Oe was calculated for a constant excitation voltage of 5V applied to CPW of 10 $\mu$ m centerline width. Taking into account that the pulse duration is very short (150ps) for a rise-time or fall time about 55ps, the real amplitude of the voltage pulse is about 4.5V. The skin depth effects were not considered here since the CPW thickness (0.275 $\mu$ m) is smaller than the skin depths (some  $\mu$ m).

Referring to the precessional reversal process detailed in chapter 1, fig.1.8, each magnetic field pulse should realize a transition between the two extreme levels represented by  $R_{min}$  and  $R_{max}$ . This result was not obtained, but we observed that the MR signal toggles between two relatively well-defined levels, defined by the resistances of points C and D on the static hysteresis loop (see figure 4.34a and b).

Magnetic force microscopy (MFM) imaging was performed using an external bias field of about 30Oe, which corresponds to the remanent configuration of the soft Co/NiFe layer, compare point (A) in figure 4.34a. The complex contrast of the MFM image corresponds to a disordered magnetization configuration, where the magnetization orientation varies locally.

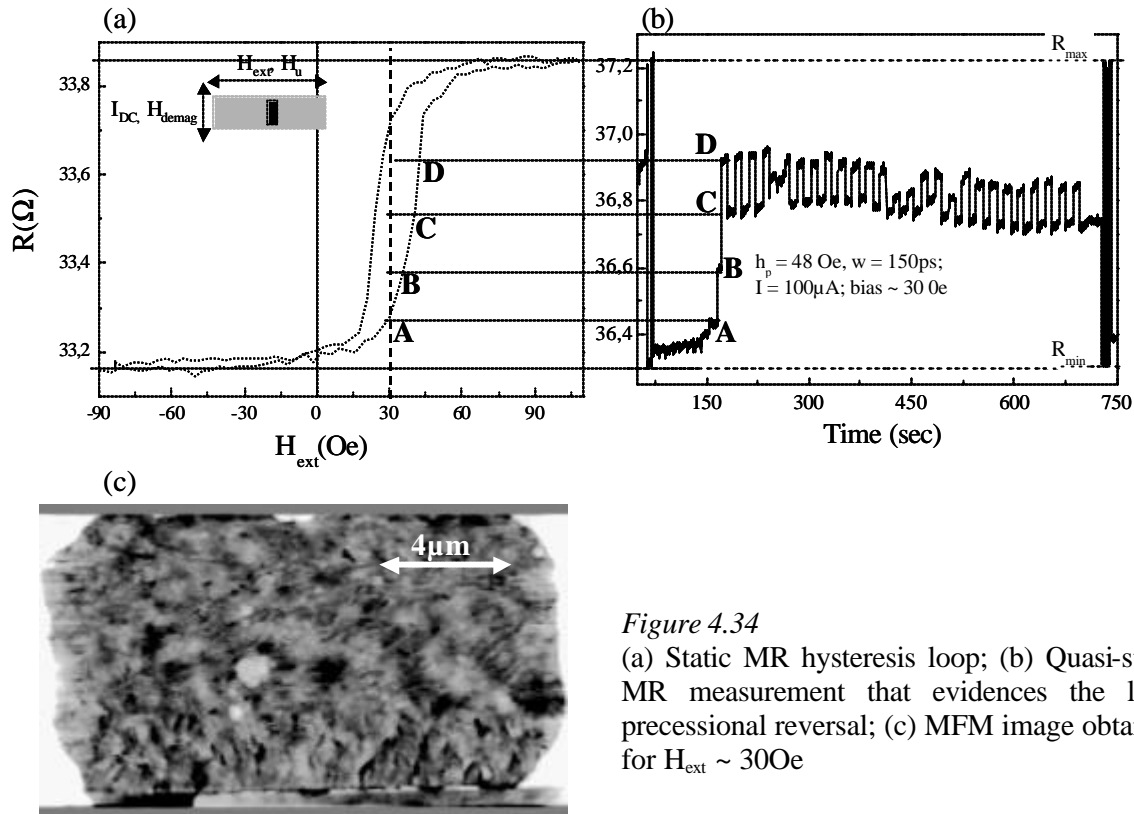


Figure 4.34

(a) Static MR hysteresis loop; (b) Quasi-static MR measurement that evidences the local precessional reversal; (c) MFM image obtained for  $H_{ext} \sim 30\text{Oe}$

Similar measurements were realized for different pulse amplitudes (28Oe and 38Oe) and widths (between 200ps and 500ps). The results are presented in figure 4.35.

Figure 4.35A shows that a decrease of the pulse amplitude from 38Oe to 28Oe for the same duration of the magnetic pulse (200ps), determined a decrease of the amplitude of the resistance variation and an increase of the number of the switching failures (fig.4.35A). Furthermore, changing the pulse width, as shown in figures 4.35 B, C, D, the resistance variation changes its amplitude and becomes even zero for pulses of 38Oe amplitude and 500ps width. Switching failures, as observed in MOKE experiments (see figure 4.15 from section 4.2.7.2) can be observed on the results presented in figure 4.35C.

All these results can be interpreted considering that the alternation in the MR level is the consequence of reversal of the local magnetization by precession. It would be inconsistent with a domain wall propagation process, since successive field pulses of the same polarity would propagate a wall by always increasing the favored domain, thus successively increasing the MR. Furthermore, wall propagation would be less sensitive to the pulse width, while precessional reversal is only realized for certain values of the pulse width, matched to the pulse amplitude and the internal fields of the sample. The much lower MR ratio of 0.4%

of this local reversal as compared to the MR value of 2% for the full reversal (fig.4.34) is explained by the dispersion of the magnetization direction throughout the sample.

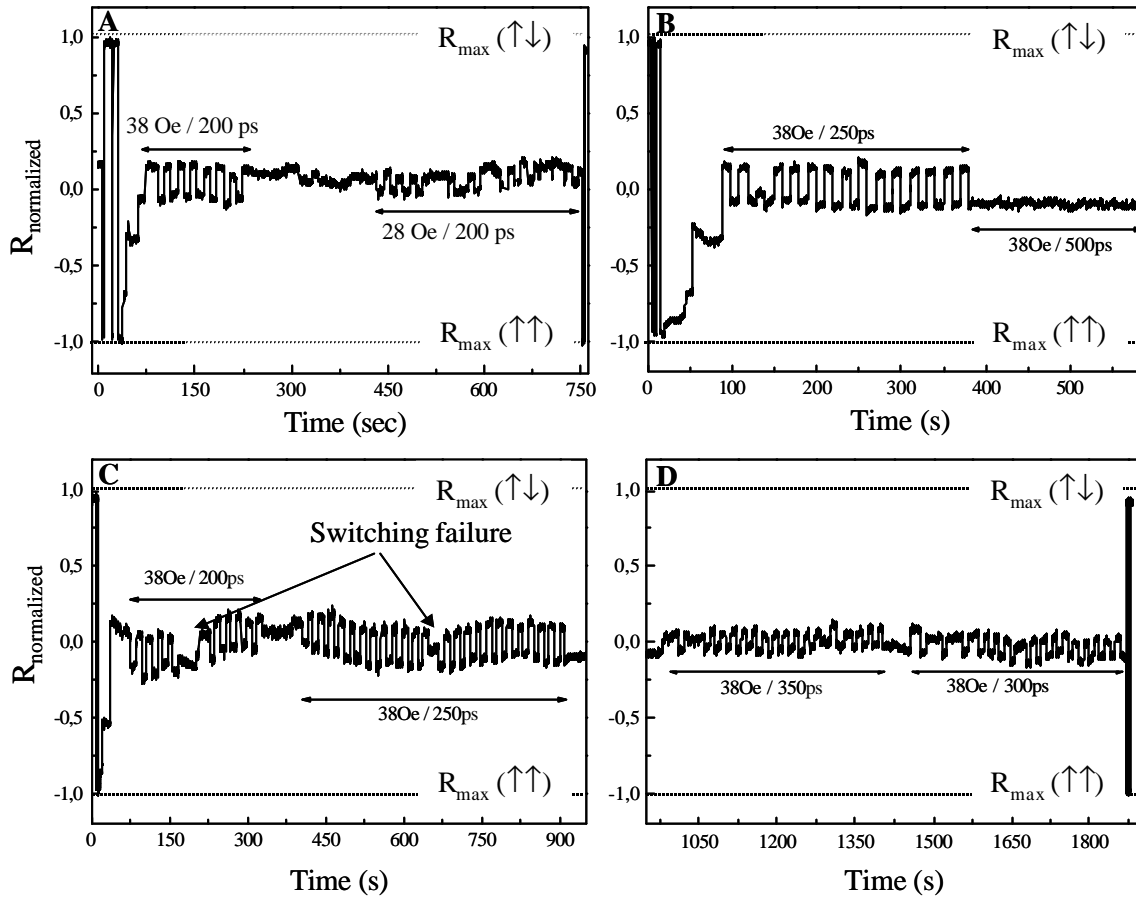


Figure 4.35

MR quasi-static measurements that evidence the local precessional reversal for two values of the magnetic pulse amplitudes (38Oe and 48Oe) and variable duration

Let us suppose that an angle/width diagram similar to the one presented in figure 4.25 can be associated to the magnetic system. Considering a uniform distribution of the angles  $\mathbf{j}$  in the magnetic sample, the critical angle  $\mathbf{q}_c$ , (see section 4.2.7.4 – switching diagrams), is proportional to the value of the partial variation of the magneto-resistance ( $MR_{local}$ ). In consequence, the partial variation of the MR signal ( $MR_{local}$ ) can be estimated by:

$$\frac{MR_{local}}{MR_{max\,imum}} = \frac{\mathbf{q}_c}{180^\circ} \cdot 100(\%) \quad (4.8)$$

In our case the distribution of the angles  $\mathbf{j}$ , is not uniform since the sample is characterized by a relatively easy axis. If the easy axis is characterized by an angle (in our case  $0^\circ$ ), which is smaller than the critical angle,  $\mathbf{q}_c$ , the ratio defined above (eq.4.8) is larger.

The precessional character of the local magnetization switching was further verified by quasi-static measurements obtained for two different terminations for the pump-line at port 2:  $50\Omega$  that determined one single magnetic pulse and the short circuit to induce in the pump line a reflected magnetic pulse of the same polarity. The results presented in figure 4.36 show very clearly that for one magnetic field pulse of 48Oe amplitude and 150ps width, about 16% of the total magnetization switches by precession, while two successive magnetic pulses of the same polarity determine two half-precessions obtaining a final non-reversed final state.

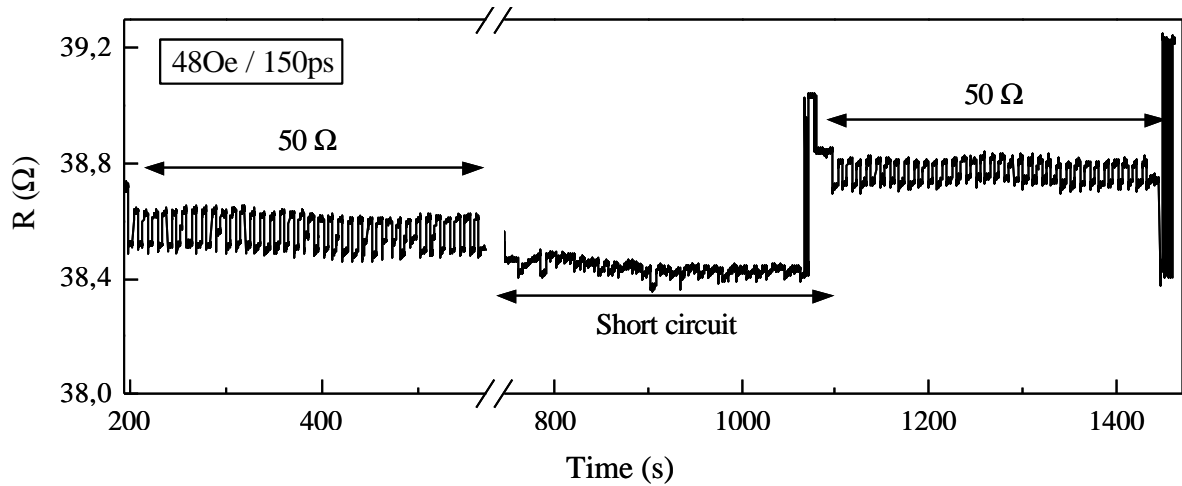


Figure 4.36:

MR quasi-static measurements that evidence the local precessional reversal for two different terminations of the pump CPW ( $50\Omega$  and short circuit)

In conclusion, we evidenced the local magnetization reversal by precession characterized by a MR of 0.4% which is smaller than the 2% corresponding to the entire MR signal obtained on the minor hysteresis loop. For a DC current of  $100\mu\text{A}$ , the partial MR variation should correspond to a voltage variation of

$$\Delta V = \Delta R \cdot I = 13.4 \mu\text{V} \quad (4.9)$$

In consequence, the dynamic MR measurements should reveal, a variation of the MR signal of about  $13.4\mu\text{V}$  (similar to the stroboscopic MOKE results presented in section 4.2.7.1). In the following, we present some aspects on the dynamic MR experiments as: cross-talk and its minimization and voltage resolution during these measurements.

#### 4.4.4. DYNAMIC MAGNETO-RESISTIVE MEASUREMENTS

The stroboscopic measurements were realized using the experimental setup presented in figure 4.37. Port 1 is connected to the pulse generator and port 2 to the termination impedance  $Z_2$ . One or two magnetic pulses can be obtained as already mentioned in chapter 2. The MR effect has two contributions: the static MR (DC) that is proportional to the voltage changes measured by a Keithley after applying a constant current in the probe line and the dynamic MR (AC) that is proportional to the high frequency variation of the magnetization and captured on the 20GHz oscilloscope. The two components AC and DC are separated by a bias T connected to port 3. Usually we used  $50\Omega$  for the termination connected to port 4, but this can be changed to a short circuit. Here we have to mention that for a short termination at port 4 the oscilloscope records the high-frequency signal (composed by MR dynamic response, cross talk, inductive effect) and its reflection. The open circuit cannot be envisaged for port 4 since in this case the DC current is zero.

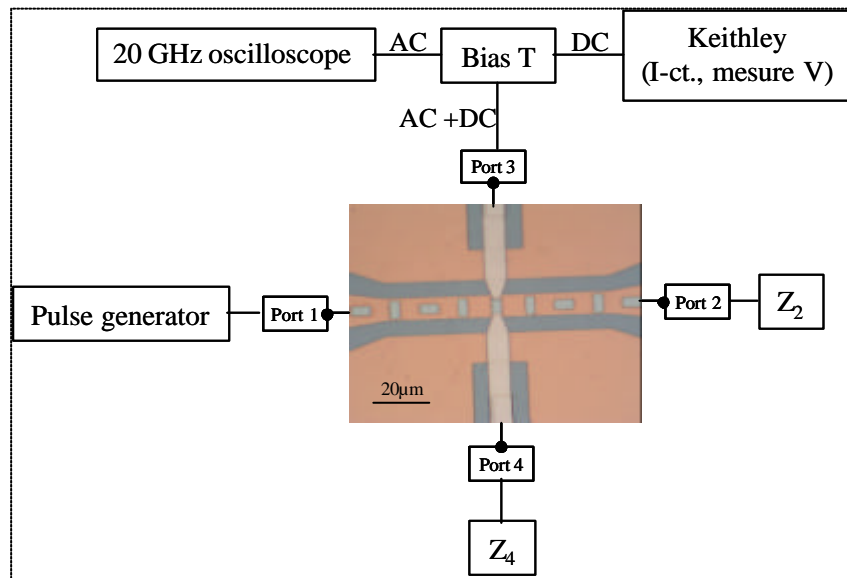


*Figure 4.37*  
Experimental setup of the dynamic MR measurement

An important cross talk may appear and results in a decrease of the transmitted power in the excitation line. This, in consequence, decreases the amplitude of the induced magnetic field. Furthermore, the existence of a cross talk is equivalent to an un-matched line, which results in a distortion of the magnetic field pulse. In consequence, the characterization of the

cross-talk is important. For this we considered two MR devices: MR1 with a relatively good isolation between the two lines (see schematics in figure 4.31) and MR2 that contains a short circuit between the pump and probe CPW (see schematics in figure 4.32).

In both cases, three measurements were realized:

- i) The incident pulse measurement. The pulse generator is connected directly to the oscilloscope.
- ii) The transmitted pulse recorded at port 2. The pulse generator is connected to port 1 and the oscilloscope at port 2.  $50\Omega$ -terminations are connected at ports 3 and 4.
- iii) The cross-talk measurement at port 3. The pulse generator is connected to port 1 and the oscilloscope at port 3.  $50\Omega$ -terminations are connected at ports 2 and 4.

All signals are equally attenuated on the oscilloscope input by two attenuators of 3dB and 20dB. In consequence, the incident pulse amplitude is attenuated from 1V down to 71mV.

The results are presented in figure 4.38 for MR1 for incident voltage pulses of 1V amplitude and 2ns duration.

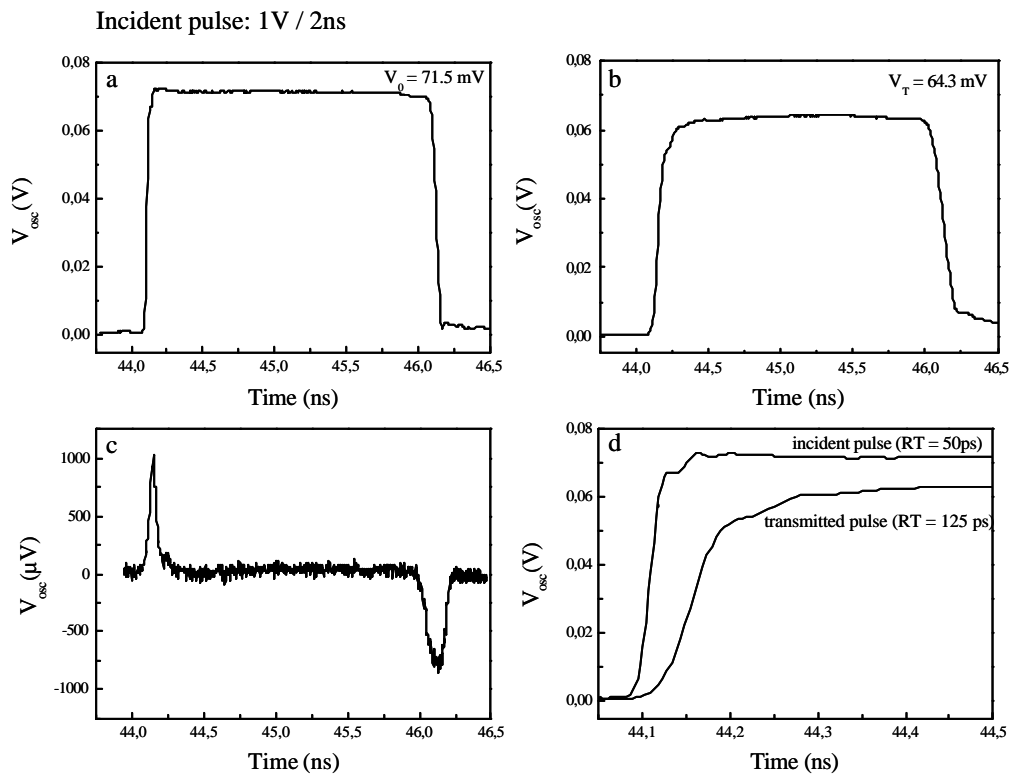


Figure 4.38

MR1 device characterization: a) the incident pulse; b) the transmitted pulse; c) the cross-talk; d) the rise-times of the incident and transmitted pulses

The transmitted pulse in the pump-line of the first device has a smaller amplitude (64.3mV) with respect to the incident pulse (71.5mV). This is due to the Joule losses in the line and to the cross-talk (fig.4.38 a and b). As seen in figure 4.38c, the cross-talk is zero during the pulse width and presents two peaks of about 1mV that corresponds to the incident pulse rise-time and fall-time. The coupling between the two lines can be resistive, capacitive, and inductive due to the electrical resistance ( $R$ ), capacitance ( $C$ ), and inductance ( $L$ ), between the pump and probe lines. In this case, the coupling is not resistive since the amplitude of the cross-talk is zero but the high-frequency components of the incident pulse are decreased by the LC coupling between the pump and probe lines. This is a consequence of the relatively thin oxide layer between the pump and probe line, a thickness which is not matched to  $50\Omega$  impedance. Txline calculations [Txline] have shown that a good isolation between the two lines is obtained for oxide layers thicker than  $1\mu\text{m}$ . The cross-talk signal determines the increase of the transmitted pulse rise-time (RT) from the initial value of 50ps to 125ps as is observed in figure 4.38d.

The results obtained on MR2 for incident pulses of 2V amplitude and 5ns duration are presented in figure 4.39.

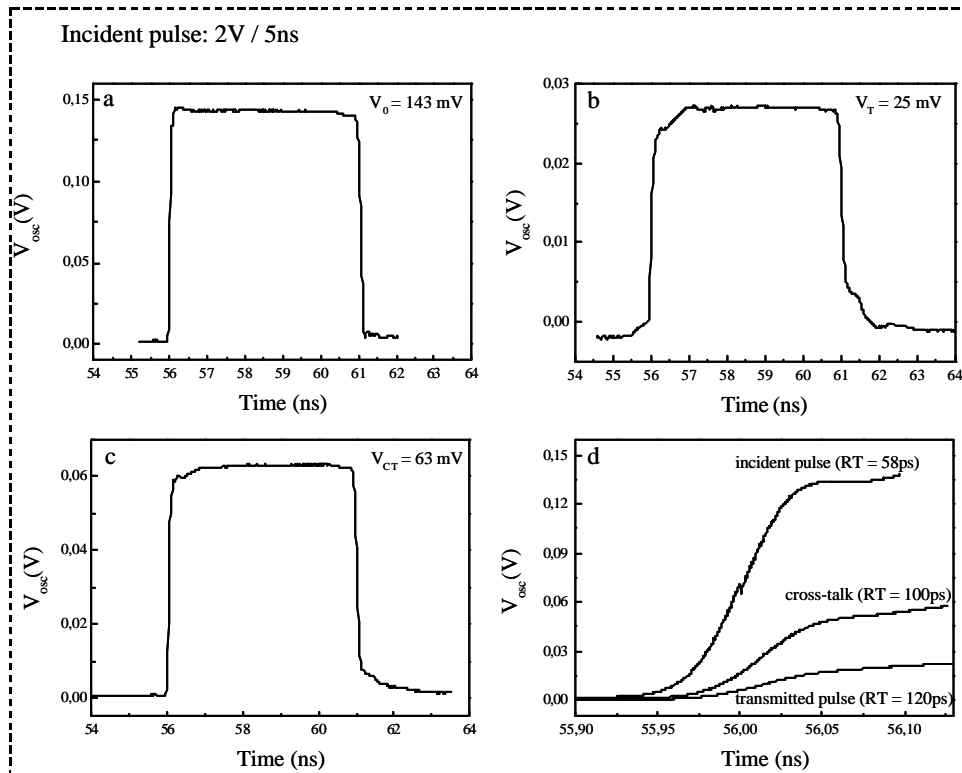


Figure 4.39

MR2 device characterization: a) the incident pulse; b) the transmitted pulse; c) the cross-talk; d) the rise-times of the incident and transmitted pulses



This is characterized by a short circuit between the pump and the probe lines determining an RLC coupling. The resistive coupling is equivalent to large amplitudes of the cross-talk signal (63mV that corresponds to 44% from the incident pulse of 143mV) and consequently a low value of the transmitted pulse amplitude (25mV) (fig.4.39a, b, and c). The consequences of the LC coupling are an increased rise-time of the transmitted pulse (120ps) with respect to the incident pulse rise-time (58ps) as we can see in figure 4.39d.

During the dynamic MR measurements, the signal measured at port 3 on the oscilloscope as a function of the external magnetic field has two contributions that originate from the inductive effect due to the cross-talk signal and due to the magneto-resistive effect.

The inductive effect was characterized with TDR measurements in the probe-line as a function of the external field. The oscilloscope was connected to port 3, the pulse generator to port 1 and 50 $\Omega$  terminations to ports 2 and 4. Voltage pulses of 5V amplitude and 1ns durations were applied on the CPW. On the oscilloscope, we recorded the cross-talk as a function of the external magnetic field. The results are presented in figure 4.40a for nine values of the external magnetic field in the interval between -90Oe and 80Oe. Figure 4.40b presents the traces from which we subtracted the trace obtained for  $H_{\text{ext}} = -90$  Oe ( $\Delta V = V_{H_{\text{ext}}} - V_{-90\text{Oe}}$ ) in order to evidence more clearly the effect of the external field on the cross-talk. We observe a maximum variation of the pulse amplitude as a function of the external field of about 500 $\mu$ V obtained for 80Oe.

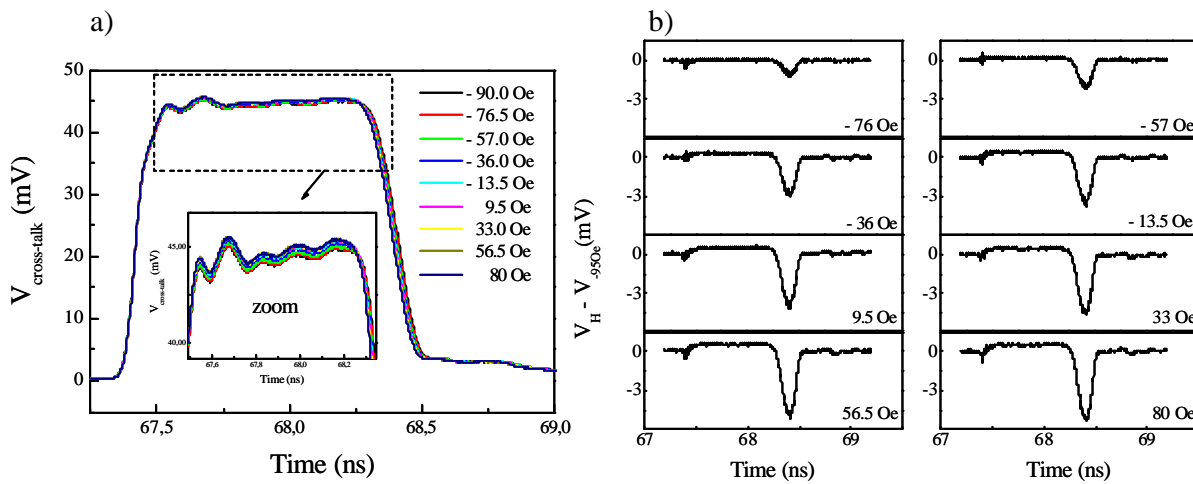


Figure 4.40: a) Cross-talk signal variation as a function of the external magnetic field; b) The subtracted cross-talk signal:  $\Delta V = V_{H_{\text{ext}}} - V_{-90\text{Oe}}$ .

The inductive effect induced by the cross-talk in the magnetic sample determines the variation of the cross-talk amplitude (e.g.  $\Delta V_{80\text{ Oe}} = V_{80\text{ Oe}} - V_{90\text{ Oe}}$  is about  $500\mu\text{V}$ ) and of the cross-talk fall-time (evidenced by the negative peaks corresponding in figure 4.40b). This measurement was realized on a device was characterized by an important RLC coupling.

As mentioned above, in the dynamic experiments we expect a dynamic MR variation about  $14\mu\text{V}$ , a value that is much smaller than the inductive effect.

The inductive effect may be subtracted from the MR result considering that for two DC currents in the probe line (that are used to measure the MR effect) of the same value but different signs ( $I_{\text{pos}}$  and  $I_{\text{neg}}$ ) the MR effect has opposite signs while the inductive effect has the same sign. This is expressed as:

$$\begin{aligned} V(I_{DC} > 0) &= V_{MR} + V_{\text{inductive}} \\ V(I_{DC} < 0) &= -V_{MR} + V_{\text{inductive}} \end{aligned} \quad (4.10)$$

In consequence, the MR effect can be expressed as:

$$V_{MR} = V(I_{DC} > 0) - V(I_{DC} < 0) \quad (4.11)$$

Figure 4.41 presents the time traces obtained on the oscilloscope in a dynamic MR measurement induced by the excitation pulse of  $100\text{Oe}$  amplitude and  $350\text{ps}$  width in the probe line for a zero external field and  $\pm 5\text{mA}$  DC current delivered by the Keithley multimeter. This MR device is characterized by a LC coupling that determines two peaks corresponding to the rise and fall times of the pump pulses. On the time traces obtained for positive respectively negative DC currents –  $V(I_{DC} > 0)$  and  $V(I_{DC} < 0)$ , we can observe some oscillations characterized by a frequency of about  $0.4\text{GHz}$  as shown in figures 4.41a and b. On the MR trace, these oscillations due to the inductive effect in the MR device, have been subtracted (fig. 4.41c).

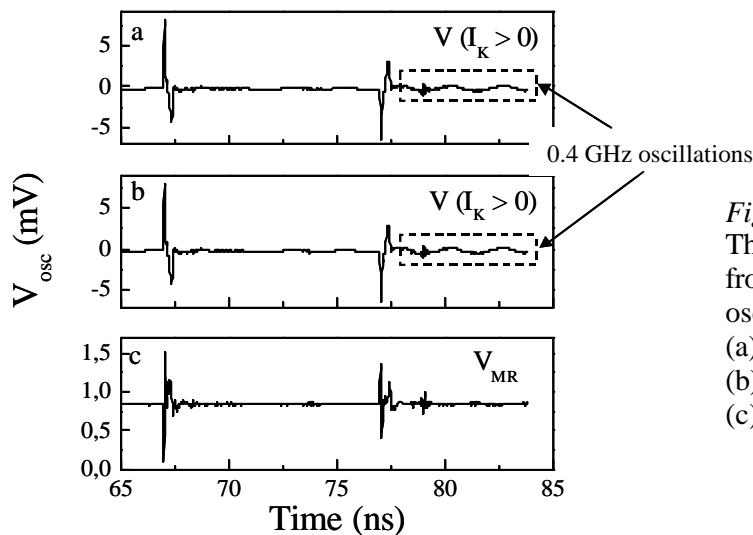


Figure 4.41

The subtraction of the inductive effect from the total signal  $V$  on the oscilloscope:

(a)  $V(I_{DC} > 0)$

(b)  $V(I_{DC} < 0)$

(c)  $V_{MR} = V(I_{DC} > 0) - V(I_{DC} < 0)$

Dynamic measurements were realized on samples characterized by the LC coupling for which the incident, transmitted and the cross-talk signals were similar to those presented in figure 4.38 using the experimental scheme shown in figure 4.37.

The MR experimental device is very sensitive to the amplitude of the pump voltage pulses applied on the excitation line, and, to the repetition frequency of voltage pulses. We observed that amplitudes larger than 1V (corresponding to 10 Oe for a 10 $\mu$ m CPW line width) determined short circuits in the device for repetition frequencies of 100KHz and, consequently, the increase of the cross-talk signal. Larger pulse amplitudes are possible but only in the quasi-static experiments where the pulses repetition rate was about 0.1Hz (1pulse each 10seconds).

In conclusion, due to experimental limitations (that determined a maximum pulse amplitude of 10 Oe) it has not been possible to obtain a time-resolved signal of the precessional switching that was previously obtained in quasi-static measurements for pulse amplitudes of 28 Oe, 38 Oe, and 48 Oe.

In the following, we present preliminary results on the precessional reversal obtained on magnetic continuous films deposited on a glass substrate.

#### **4.5. PRECESSIONAL REVERSAL ON CONTINUOUS MAGNETIC FILMS – PRELIMINARY RESULTS**

Stroboscopic dynamic MOKE measurements were realized on continuous thin magnetic films, of NiFe of 30nm thickness, deposited on a glass substrate. The sample was fixed on the CPW with the magnetic layer in contact to the pump line. The laser is focused through the glass substrate on the magnetic sample that is in contact with the centerline of the CPW. The dynamic time-traces for two excitation pulses of the same polarity and delayed by 10ns are presented in figure 4.42a. The pulses were characterized by 200ps, 300ps, 400ps, and 600ps width and 70Oe nominal amplitude. Similar to the MOKE results obtained on micron-sized magnetic dots, in this case, the magnetization is reversed by precession by the incident pulse, and then, the reflected pulse is used to return the magnetization to the initial state. Comparing the stroboscopic traces with the static MOKE loop we observe that the Kerr signal variation induced by the first pulse corresponds to a complete reversal of the region of the continuous magnetic film where the laser spot was focused.

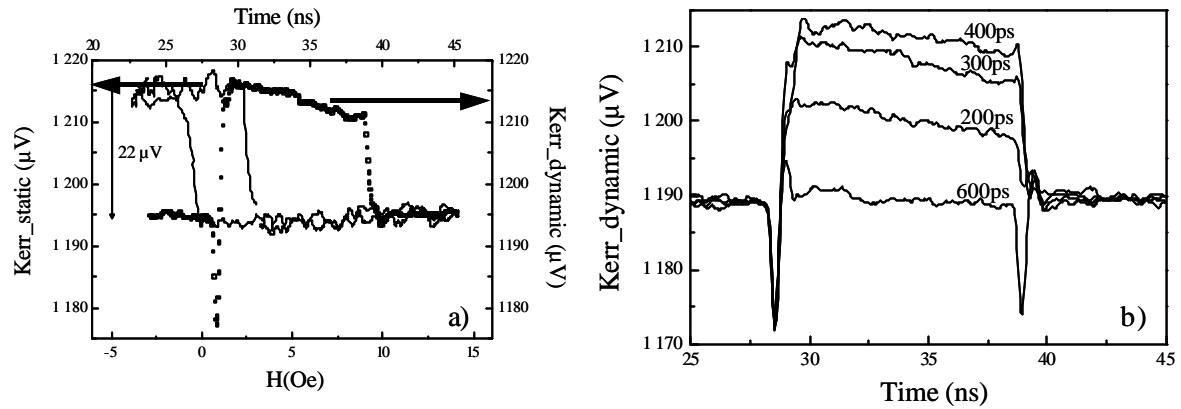


Figure 4.42: MOKE measurements on continuous NiFe magnetic thin films of 30nm thickness deposited on a glass substrate a) Static and dynamic MOKE results; b) Dynamic MOKE results obtained for pulse amplitude of 70 Oe amplitude and 200 ps, 300 ps, 400 ps and 600 ps durations

Furthermore, we observe a negative peak just before and after the reversal, which has very large amplitude, comparable to  $M_S$ . We explain this as a consequence of the Faraday and Voigt effects in the glass substrate (see chapter 2) induced by the magnetic fields pulse but needs further investigations. The first peak is observed in all traces and the second peak appears only for 100ps, 150ps, 450ps, 550ps, 600ps and 650ps values of the pulse widths (fig.4.43). Both peaks are clearly observed in cases where the precessional reversal is not obtained (for pulse widths of 100ps, 550ps, 600ps, 650ps) or when the magnetic state relaxes toward the initial magnetic state after the reversal induced by the first pulse (150ps, 450ps).

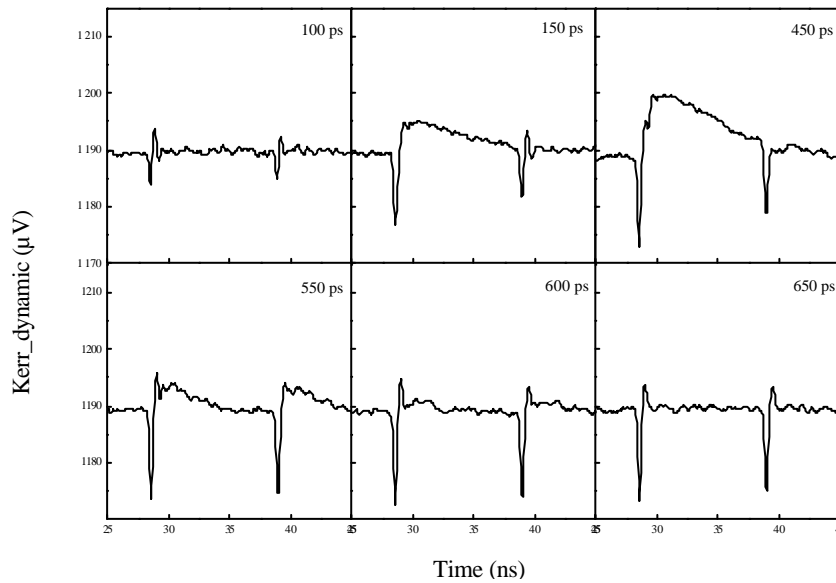


Figure 4.43  
Dynamic MOKE results obtained on continuous NiFe films of 30nm thickness for pulses of 70 Oe amplitude and durations of 100 ps, 150 ps, 450 ps, 550 ps, 600 ps and 650 ps

For pulse widths of 200ps, 300ps, 400ps for which the magnetization is maintained in the reversed position, the second peak is not visible. In this case, Faraday and Kerr effects have the same variation in the negative sense and we consider that the Faraday effect cannot be distinguished. Further experiments will be realized on these continuous films to better characterize the precessional reversal in these systems and also to study the magnetization small angle oscillations using both longitudinal and transversal MOKE.

**CONCLUSIONS**  
**AND**  
**PERSPECTIVES**



## CONCLUSIONS

Time-resolved measurements of the magnetization dynamics were used to characterize processes such as small angle magnetization precessions, magnetization reversal by precession and relaxational processes due to the nucleation or domain wall propagations, in the picosecond time scales.

My work can be divided in three distinct parts. One concerns the conception and the elaboration of the experimental setup in a pump-probe configuration, for time-resolved magnetometric measurements with time resolution of sub-nanoseconds. The second consisted on the elaboration of the magnetic devices to measure (magnetic samples patterned on top of coplanar waveguides for magneto-optical measurements and contacted with CIP contacts for MR measurements). The third was the characterization of the magnetization dynamics in several magnetic systems using the magneto-optic Kerr and the magneto-resistive effects.

Of great importance and complexity was the realization of the pump-probe technique matched for high-frequency experiments. The pump consists of high-frequency magnetic field pulses with rise-times sufficiently small to realize adiabatic excitations. These field pulses are obtained by applying voltage pulses onto a high bandwidth ( $> 20$  GHz) coplanar waveguide (CPW) matched to an impedance of  $50\Omega$ . The voltage pulses are delivered by a commercial pulse generator and the contacts on the coplanar waveguide are realized with high-frequency matched microprobe connectors. We used the Magneto-Optic Kerr Effect (MOKE) as probe in two different configurations: longitudinal and transversal. The analysis of these configurations revealed the presence in the recorded Kerr intensity of all the magnetization components: longitudinal, transversal, and polar. Considering a magnetic sample with in-plane anisotropy, the polar component is negligible during static measurement. Each perturbation of the magnetization is followed in the next nanoseconds by the magnetization precessions with a non-negligible value of the polar component. As a consequence, the Kerr polar contribution becomes important in the stroboscopic Kerr time-trace, the measured signal being a mixture of polar, transversal and longitudinal components.

The samples studied in this work were prepared using UV and DUV lithography processes and were characterized by AFM, MFM, SEM, VSM, MOKE, and MR. A special device was needed for dynamic MR measurements: particular attention was given to the high-frequency insulation between the pump and the probe lines.



Magnetization dynamics results were obtained recording stroboscopic time-traces on NiO-based spin valve micron-sized magnetic samples using the magneto-optical Kerr as probes. The magnetic sample size that can be measured by MOKE experiments is given by the collimated laser spot-size (15 $\mu\text{m}$  diameter), while in a MR experiment the sample size can be smaller than 1 $\mu\text{m}$ .

For the NiO-based spin valves, two different geometries were used, with the in-plane easy axis parallel or perpendicular to the pulsed magnetic field (sample B and respective A, in chapter 4, figure 4.3). We evidenced the magnetization reversal by precession both in the soft layer and in the entire spin valve in configuration A. For certain values of the pulse duration, the precessional switching is characterized by a reduced remanence. By quasi-static experiments, the magnetic state was measured after successive magnetic field pulsed delayed by about 5 seconds, and it was demonstrated that the reduced remanence is due to non-repetitive reversal events. This is due to magnetization and internal field inhomogeneities, giving rise to a local misalignment between the magnetization vector and the pulsed magnetic field. These explain the occurrence of switching failures which reduce the average magnetization value measured in the stroboscopic time trace, which averages over tens of thousands events.

For the IrMn-based spin valves, quasi-static MR measurements revealed local magnetization reversal by precession. Due to the very complex magnetic structure, only the magnetic domains that have the magnetization quasi-perpendicular to the pulsed magnetic field reverse. So far, dynamic MR measurements have not been possible because of the cross-talk signal and because the pulsed magnetic field amplitude was too low for the given device.

For a better understanding of the phenomena underlying the magnetization dynamics (precession), an important part of my work was dedicated to macrospin simulations. In this way, switching diagrams can be defined describing reversed vs. non-reversed magnetic states as a function different parameters of interest: the pulse amplitude and width, the uniaxial anisotropy field and the angle  $\mathbf{j}$ . Each specific case was treated in this manner, the macrospin simulation being an important and useful tool to characterize the precessional reversal.

## PERSPECTIVES

There are still few aspects needing further studies and improvements.

Firstly, I would like to mention the minimization of the laser spot (better collimating optics) and the realization of dynamic measurements on smaller samples (nanometer scale).

Secondly, the MR-device should be improved using the lithographical procedures specified in chapter 3. The short-circuits sources could be minimized by inter-changing the lithographical steps and depositing thicker insulating layers ( $> 1\mu\text{m}$ ) between the two lines.



**REFERENCES:**

- [ASHCROFT 1976] N.W. Ashcroft, N.D. Mermin, D. Mermin, *Solid State Physics*, Saunders 1976
- [ATKINSON] R. Atkinson, N.F. Kubrakov,  
<http://www.research.salford.ac.uk/MONET/Kubrakov.ppt>
- [AUSTON 1974] D.H. Auston, C.V. Shank, Phys.Rev.Lett., 32, 1120, (1974)
- [BACK 1998] C.H. Back, D. Weller, J. Heidmann, D. Mauri, D. Guarisco, E.L. Garwin, H.C. Siegman, Phys.Rev.Lett., 81, 3251, (1998)
- [BACK 1999] C. H. Back, R. Allenspach, W. Weber, S. S. P. Parkin, D. Weller, E. L. Garwin, H. C; Siegmman, Science 285, 864 (1999)
- [BAILLEUL2002] M. Bailleul, PhD thesis, (2002)
- [BARKHAUSEN 1919] H. Barkhausen, Phys.Z, 20, 401-403, (1919)
- [BAUER 2000] M. Bauer, J. Fassbender, B. Hillebrands, R.L. Stamps, Phys.Rev.B, 61, 3410, (2000)
- [BEAUREPAIRE 1996] E. Beaurepaire, J.C. Merle, A. Daunois, J.Y. Bigot, Phys.Rev.Lett., 76, 22, 4250, (1996)
- [BEAUREPAIRE 1998] E. Beaurepaire, M. Maret, V. Halte, J.C. Merle, A. Daunois, J.Y. Bigot, Phys.Rev.B, 58, 18, 12 134, (1998)
- [BERTRAM 1994] H. N. Bertram, *Theory of Magnetic Recording* (Cambridge University Press), Cambridge, 1994
- [BINNIG 1986] G. Binnig, C.F. Quate and G. Gerber, Phys. Rev. Lett. 56, 930 (1986)
- [BINNS 2003] C. Binns, F. Sirotti, H. Cruguel, S.H. Baker, P. Prieto, J.D. Bellier, S.C. Thornton, J.Phys.Cond.Matt., 15, 4287, (2003)
- [BLOCH 1932] F. Bloch, Z.Phys. 74, 295-335 (1932)
- [BLOIS 1955] M.S. Blois, J.Appl.Phys., 26, 975, 1955
- [BOEF 1990] A.J. den Boef, Appl. Phys. Lett. 56, 2045 (1990)
- [BONET 1999] E. Bonet, W. Wernsdorfer, B. Barbara, A. Benoît, D. Mailly, A. Thiaville, Phys.Rev.Lett., 83, 20, (1999)
- [BONFIM 2001] M. Bonfim, G. Ghiringhelli, F. Montaigne, S. Pizzini, N.B. Brooks, F. Petroff, J. Vogel, J. Camarero, A. Fontaine, Phys.Rev.Lett., 86, 16, 3646, (2001)
- [BROWN 1963] J. F. Brown, Jr. : *Micromagnetics*, Interscience Publishers, J. Wiley and Sons, New York (1963)

- [CAMARERO2001] J.Camarero, Y.Pennec, M.Bonfim, J.Vogel, S.Pizzini, A.Fontaine, J.Appl.Phys., 89, 6585, (2001)
- [CARTIER 2002] M. Cartier, S. Auffret, P. Bayle-Guillemaud, F. Ernult, F. Fetta, B. Dieny, J.Appl.Phys., 91, 3, 1436, (2002)
- [CELINSKI 1997] Celinski Z, Urquhart K-B and Heinrich B, J. Magn. Magn. Mater., 166, 6, (1997)
- [CHIKAZUMI 1997] S. Chikazumi, C.D. Graham, *Physics of Ferromagnetism*, Oxford University Press Inc., New York (1997)
- [CHOI 2001] B.C. Choi, M. Belov, W.K. Hiebert, G.E. Ballentine, M.R. Freeman, Phys.Rev.Lett., 86, 4, 728, (2001)
- [CHOI 2001B] B.C. Choi, G.E. Ballentine, M. Belov, M.R. Freeman, Phys.Rev.B, 64, 144418, (2001)
- [CHOPRA 2000] H.D. Chopra, D.X. Yang, P.J. Chen, H.J. Brown, L.J. Swartzendruber, W.F. Egelhoff, Jr., Phys.Rev.B, 61, 22, 15312, (2000)
- [CHOPRA 2000B] H.D. Chopra, D.X. Yang, P.J. Chen, D.C. Parks, W.F. Egelhoff, Jr., Phys.Rev.B, 61, 14, 9642, (2000)
- [COCHRAN 1995] J.F. Cochran, *Magnetic Ultrathin Films*, Vol.II, B. Heinrich, J.A.C. Bland (Eds.) (Springer, Berlin, Heidelberg 1995) pp. 222-257
- [CONGER 1955] R.L. Conger, Phys.Rev., 98, 1752, (1955)
- [CRAWFORD 1996] T.M. Crawford, C.T. Rogers, T.J. Silva, Y.K. Kim, Appl.Phys.Lett., 68, no.11, (1996)
- [CRAWFORD 1999] T.M. Crawford, T.J. Silva, C.W. Teplin, C.T. Rogers, Appl.Phys.Lett., 74, no.22, (1999)
- [CRAWFORD 2000] T.M. Crawford, P. Kabos, T.J. Silva, Appl.Phys.Lett., 76, no.15, 2000
- [DIENY 1991] B. Dieny, V.S. Speriosu, S.S.P. Parkin, B.A. Gurney, D.R. Wilhoit, and D. Mauri, Phys.Rev.B, 43, 1, 1297 (1991)
- [DIENY 1994] B. Dieny, J.M.M.M., 136, 335-359 (1994)
- [DIENY 2000] B. Dieny, M. Li, S; H.S Liao, C. Horng, K. Ju, J.Appl.Phys., 88, 4140, (2000)
- [DIETRICH 2000] W. Dietrich, W.E. Proebster, P. Wolf, IBM J.Res.Develop. 44, no. 1/2, (2000)
- [DOYLE 1993] W.D. Doyle, L. He, IEEE Trans.Magn, 29, no.6, 3634, (1993)
- [DOYLE 1998] W.D. Doyle, S.M. Stinnett, C. Dawson, and L. He, J. Magn. Soc. Jpn., 22, 92, (1998)

- [ELEZZABI 1996] A.Y. Elezzabi, M.R. Freeman, Appl.Phys.Lett., 68, no.25, (1996)
- [FARLE 1998] Farle M, Rep.Prog.Phys, 61, 755-826, (1998)
- [FERRE 1997] J. Ferré, V. Golier, P. Meyer, S. Lemerle, A. Maziewski, E. Stefanowicz, S.V. Tarasenko, V.V. Tarasenko, M. Kisielewski, D. Renard, Phys.Rev.B, 55, 15092, (1997)
- [FREEMAN 1991] M.R. Freeman, R.R. Ruf, R.J. Gambino, IEEE Trans.Magn, 27, no.6, 4840, (1991)
- [FREEMAN 1992] M.R. Freeman, M.J. Brady, J.F. Smith, Appl.Phys.Lett., 60, no.20, 2555 (1992)
- [FREEMAN 1996] M.R. Freeman, J.F. Smith, J.Appl.Phys, 79, no.8, 5898,(1996)
- [FREEMAN 1997] M.R. Freeman, A.Y. Elezzabi, G.M. Steeves, G. Nunes,Jr., Surface Science, 386, 290, (1997)
- [FREEMAN 1997B] M.R. Freeman, A.Y. Elezzabi, J.A.H. Stotz, J.Appl.Phys., 81, 8, 4516 (1997)
- [FREEMAN 1998] M.R. Freeman, W.K. Hiebert, A. Stankiewicz, J.Appl.Phys., 83, 11, (1998)
- [FREEMAN 2000] M.R. Freeman, R.W. Hunt, G.M. Steeves, Appl.Phys.Lett., 77, 5, 717, (2000)
- [FREEMAN 2002] M.R. Freeman, G.M.Steeves, G.E. Ballentines, and A. Krichevsky, J. Appl. Phys. 91, 7326 (2002)
- [FUJIWARA 1995] H. Fujiwara, IEEE Trans.Magn, 31, no.6, 4112, (1995)
- [GERRITS 2002] Th. Gerrits, H.A.M. van den Berg, J. Hohlfeld, L. Bär, Th. Rasing, Nature, 418, (2002)
- [GERRITS 2002B] Th. Gerrits, H.A.M. van den Berg, J. Hohlfeld, O. Gielkens, L. Bär, Th. Rasing, JMMM, 240, 283 (2002)
- [GILBERT 1955] T. L. Gilbert, Phys. Rev. 100, 1243 (1955)
- [GRÜTTER 1995] P. Grütter, H.J. Mamin and D. Rugar, *Scanning Tunnelling Microscopy II, Further Applications and Related Scanning Techniques*, 2nd ed., edited by R. Wiesendanger and H.-J. Guntherodt (Springer, Berlin, 1995), p.151.
- [GUIDONI 2002] L. Guidoni, E. Beaurepaire, J-Y. Bigot, Phys.Rev.Lett, 89, 1, (2002)
- [GUPTA 1996] K.C. Gupta, R. Garg, I. Bahl, P. Bhartia, *“Microstrip Lines and Slotlines”*, 1996
- [HE 1994] L. He, W.D. Doyle, H. Fujiwara, IEEE Trans.Magn, 30, no.6, 4086, (1994)

- [HEINRICH 1995] B. Heinrich, *Magnetic Ultrathin Films*, Vol.II, B. Heinrich, J.A.C. Bland (Eds.) (Springer, Berlin, Heidelberg 1995) pp. 195-222
- [HIEBERT 1997] W.K. Hiebert, A. Stankiewicz, M.R. Freeman, Phys.Rev.Lett., 79, 6, 1134, (1997)
- [HILLEBRANDS 1995] B. Hillebrands, *Magnetic Ultrathin Films*, Vol.II, B. Heinrich, J.A.C. Bland (Eds.) (Springer, Berlin, Heidelberg 1995) pp. 258-290
- [HOFFMAN 1968] H. Hoffmann, IEEE Trans. Mag. 4, 32 (1968)
- [HUBERT 1998] A. Hubert, R. Schäfer, *Magnetic Domains*, Springer (1998)
- [KABOS 2000] P. Kabos, S. Kaka, S. Russek, T. Silva, IEEE Trans.Magn, 36, 5, 3050 (2000)
- [KAKA 2000] S. Kaka, S. Russek, J.Appl.Phys., 87, 9, 6391, (2000)
- [KAKA 2002B] S. Kaka, S. E; Russek, Appl. Phys. Lett. 80, 2958 (2002)
- [KANG 2000] S.J.Kang et al., "Simultaneous Measurement of the Two Components of the Magnetization by using the Magneto-optic Kerr Effect", J. Kor.Phys.Soc., vol.37, 414, 2000
- [KIM 2002] S.K. Kim, J.W. Lee, S.C. Shin, J.Appl.Phys., 91, 5, 3099 (2002)
- [KITTEL 1947] C. Kittel, Phys. Rev., 71, 270, (1947)
- [KITTEL1966] C. Kittel, *Introduction to Solid State Physics*, John Wiley and Sons, 1966
- [KOCH 1998] R.H. Koch, J.G. Deak, D.W. Abraham, P.L. Trouilloud, R.A. Altman, Yu Lu, W.J. Gallagher, R.E. Scheuerlein, K.P. Roche, S.S.P. Parkin, Phys.Rev.Lett., 81, 20, 4512, (1998)
- [LANDAU & LIFSHITZ 1935] L. Landau, E. Lifschitz, Phys. Z. Sowjetunion 8, 153 (1935)
- [LEE 2000] J.-W. Lee, J.-R. Jeong, D.-H. Kim, J.-S. Ahn, J. Kim, and S.-C. Shin, Rev.Sci. Instrum. 71, 3801, (2000)
- [LOPUSNIK 2003] R. Lopusnik, J.P. Nibarger, T.J. Silva and Z. Celinski, Appl.Phys.Lett.83, 93, (2003)
- [MACKAY 2000] K. Mackay, M. Bonfim, D. Givord, A. Fontaine, J. Appl.Phys., 87, 1996-2002, (2000)
- [MALLINSON 1987] J. Mallinson, IEEE Trans. Magn. MAG-23 2003 (1987)
- [MALLINSON 1993] J. C. Mallinson, *The Foundations of Magnetic Recording*, 2nd ed. (Academic, San Diego, CA, 1993)
- [MALOZEMOFF [1979] A.P. Malozemoff and J.C. Slonczewski, *Magnetic domain walls in bubble materials*, R. Wolfe (Eds.), 1979

- [MARTIN 1987] Y. Martin, H.K. Wickramasinghe, Appl. Phys. Lett. 50, 1455 (1987)
- [MILTAT 1994] J. Miltat, in Applied Magnetism, R. Gerber, C. D. Wright and G. Asti (Eds.), NATO ASI Series (Kluwer, Dordrecht), 221 (1994)
- [MILTAT2002] J. Miltat, G. Albuquerque, A. Thiaville, *Spin dynamics in confined magnetic structures I*, B. Hillebrands, K. Ounadjela (Eds.), Springer (2002)
- [NÉEL 1947] L. Néel, C. R. Acad. Science, Paris, 224, 1550 (1947)
- [NÉEL 1962] L. Néel, C.R. Acad. Sci. 255, 1676 (1962)
- [NIBARGER 2003] J.P. Nibarger, R. Lopusnik, Z. Celinski and T.J. Silva, Appl.Phys.Lett.83, 96, (2003)
- [NUMERICAL\_RECIPES] <http://www.nr.com/>
- [PALMER 1996] S.B. Palmer, M.S. Rogalski, *Advanced University Physics*, Gordon and Breach Publishers, 1996
- [PARKIN 1993] S.S.P. Parkin, Phys.Rev.Lett., 71, 1641 (1993)
- [PARSONS 1991] R. Parsons, *Sputter Deposition Processes*, Academic Press (1991)
- [POZAR 1998] D.M.Pozar, “*Microwave Engineering*”, eds. John Wiley and Sons, Inc., 1998
- [RADO 1963] G.T. Rado and H. Suhl, Magnetism, vol 3, ch.11 (E.M. Gyorgy), Academic Press (1963)
- [RICHARDT 1997] A. Richardt and Anne-Marie Durand, *Les Interaction Ion Énergétiques-Solides*, In fine (1997)
- [RIZZO 2000] N.D. Rizzo, T.J. Silva, A.B. Kos, IEEE Trans.Magn., 36, 1, 159, (2000)
- [RUGAR 1990] D. Rugar, H.J. Mamin, P. Guethner, S.E. Lambert, J.E. Stern, I. Fayden, T. Yogi, J. Appl. Phys. 68, 1169 (1990)
- [RUSSEK 2000] S. Russek, S. Kaka, M. Donahue, J.Appl.Phys., 87, 9, 7070, (2000)
- [RUSSEK 2000B] S. Russek, S. Kaka, IEEE Trans.Magn., 36, 5, 2560, (2000)
- [SANDLER 1999] G.M. Sandler, H.N. Bertram, T.J. Silva, T.M. Crawford, J. Appl.Phys., 85, 8, (5080, 1999)
- [SCHABES 1987] M. E. Schabes and A. Aharoni, IEEE Trans. Magn., vol. Mag-23, no. 6, 1987
- [SCHUMACHER 2002] H.W. Schumacher, C. Chapert, P. Crozat, R.C. Sousa, P.P. Freitas, M. Bauer, Appl.Phys.Lett., 80, 20, 3781, (2002)



- [SCHUMACHER 2002B] H.W. Schumacher, C. Chapert, P. Crozat, R.C. Sousa, P.P. Freitas, J.Appl.Phys, 91, 10, 8043 (2002)
- [SCHUMACHER 2003] H.W. Schumacher, C. Chapert, P. Crozat, R.C. Sousa, P.P. Freitas, J. Miltat, J. Fassbender, B. Hillebrands, Phys.Rev.Lett., 90, 1, 017201-1 (2003)
- [SCHUMACHER 2003B] H.W. Schumacher, C. Chapert, R.C. Sousa, P.P. Freitas, J. Miltat, Phys.Rev.Lett., 90, 1, 017204-1 (2003)
- [SHAPIRO 1977] S. Shapiro, Ultrashort Light Pulses: Picosecond Techniques and Applications, Springer, New York, (1977)
- [SIEGMANN 1995] H.C. Siegmann, E.L. Garwin, C.Y. Prescott, J. Heidmann, D. Mauri, D. Weller, R. Allenspach, W. Weber, JMMM, 151, L8, (1995)
- [SILVA 1999] T.J. Silva, C.S. Lee, T.M. Crawford, C.T. Rogers, J.Appl.Phys., 85,11,7849,1999
- [SIXTUS 1931] K.J. Sixtus, L.Tonks, Phys.Rev. 37, 930-958 (1931)
- [SLONCZEWSKI 1991] J.C. Slonczewski, IEEE Trans.Magn. 27, 4, 3532, (1991)
- [ST.-W 1948] E. C. Stoner and E. P. Wohlfarth, Philos. Trans. London Ser. A, 240, 599 (1948)
- [STAMPS 1999A] R.L. Stamps, R.E. Camley, Phys.Rev.B, 60, 16, (1999)
- [STAMPS 1999B] R.L. Stamps, R.E. Camley, Phys.Rev.B, 60, 17, (1999)
- [STANKIEWICZ 1998] A. Stankiewicz, W.K. Hiebert, G.E. Ballentine, K.W. Marsh, M.R. Freeman, IEEE Trans.Magn, 34, no.4, 1003, (1998)
- [THIRION 2002] C. Thirion, W. Wernsdorfer, M. Jamet, V. Dupuis, P. Melinon, A. Perez, D. Mailly, J.Appl. Phys., 91, 10, 7062, (2002)
- [TÖPLER 1867] A. Töpler, Ann.Phys.Chem., 131, 180, (1867)
- [TXLINE] <http://www.txline.com>
- [VOSSEN 1991] J.L. Vossen and W. Kern, *Thin Film Processes II*, Academic Press (1991)
- [WERNSDORFER 1995] W. Wernsdorfer, K. Hasselbach, A. Benoît, G. Cernicchiaro, D. Mailly, B. Barbara, L. Thomas, JMMM, 151, 38, (1995)
- [WERNSDORFER 1996] W. Wernsdorfer, PhD thesis, (1996)
- [WERNSDORFER 2001] W. Wernsdorfer, Advances in Chemical Physics, “*Classical and quantum magnetization reversal studied in nano-meter sized particles and clusters*”, John Wiley and Sons, 2001
- [WILLIAMS 1950] H.J. Williams, W. Shockley, C. Kittel, Phys.Rev., 80, 6, 1090, (1950)

- [WWW 1] <http://www.techniques-ingenieur.fr/affichage/DispIntro.asp?nGcmId=P865&introID=811153&pdfID=811154>
- [ZHANG 1997] S. Zhang, S.A. Oliver, N.E. Israeloff, C. Vittoria, Appl.Phys.Lett., 70, 20, 2756, (1997)
- [ZHANG 1997B] S. Zhang, J.B. Sokoloff, C. Vittoria, J.Appl.Phys., 81, 8, 5076, (1997)



## ANNEXE 1: ANALYTICAL CALCULATION OF THE MAGNETIC FIELD INDUCED BY A DC-CURRENT IN A RECTANGULAR STRIPLINE

We have written a program to calculate the magnetic field created by a DC current of density,  $\vec{J}$ , that traverses a metallic stripline of rectangular section. The solution of the analytical expression of the magnetic field, derived from the Biot-Savart law has been evaluated numerically. Here we present first the analytical expression.

The coordinate system used here is defined by the unity vectors:  $\vec{i}, \vec{j}, \vec{k}$ .

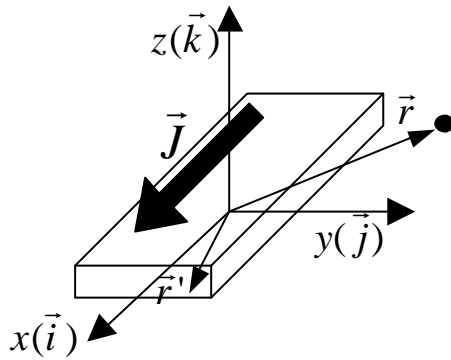


Figure A1.1  
Stripline traversed by a DC-current in xyz - coordinates

### **Step 1: Biot-Savart law**

We consider a metallic stripline parallel to the  $ox$ -axis traversed by a DC current as shown in figure A1.1. The magnetic field created by the current density  $\vec{J} = J \cdot \vec{i}$  is expressed using Biot-Savart's law:

$$\vec{B} = \nabla_{\vec{r}} \times \vec{A} \quad (\text{A1.1})$$

where  $\vec{A}$  represents the magnetic potential vector. This can be calculated by integrating the following expression over the volume  $V = d\vec{r}'$ :

$$\vec{A} = \frac{\mu_0 J}{4\pi} \int_V \frac{\vec{i} \cdot d\vec{r}'}{|\vec{r} - \vec{r}'|} \quad (\text{A1.2})$$

where  $\vec{r}'$  and  $\vec{r}$  are defined on figure A1.1.

Biot-Savart law (expression A1.1) becomes:

$$\vec{B} = \frac{\mu_0 J}{4\pi} \int_V \left( \nabla_{\vec{r}} \times \vec{i} \right) \frac{d\vec{r}'}{|\vec{r} - \vec{r}'|} \quad (\text{A1.3})$$

Since:

$$\nabla_{\vec{r}} \times \vec{i} = \begin{vmatrix} \vec{i} & \vec{j} & \vec{k} \\ \frac{\partial}{\partial x} & \frac{\partial}{\partial y} & \frac{\partial}{\partial z} \\ 1 & 0 & 0 \end{vmatrix} = \vec{i}(0-0) + \vec{j}\left(\frac{\partial}{\partial z} - 0\right) + \vec{k}\left(0 - \frac{\partial}{\partial y}\right) \quad (\text{A1.4})$$

we obtain:

$$\begin{aligned} B_x &= 0 \\ B_y &= \frac{\mu_0 J}{4\mathbf{p}} \int_V \frac{\partial}{\partial z} \left( \frac{d\vec{r}'}{|\vec{r} - \vec{r}'|} \right) \\ B_z &= -\frac{\mu_0 J}{4\mathbf{p}} \int_V \frac{\partial}{\partial y} \left( \frac{d\vec{r}'}{|\vec{r} - \vec{r}'|} \right) \end{aligned} \quad (\text{A1.5})$$

These equations become:

$$\begin{aligned} B_y &= \frac{\mu_0 J}{4\mathbf{p}} \int_V \frac{\partial}{\partial z} \left( \frac{1}{\sqrt{(x-x')^2 + (y-y')^2 + (z-z')^2}} \right) dx' dy' dz' \\ B_z &= -\frac{\mu_0 J}{4\mathbf{p}} \int_V \frac{\partial}{\partial y} \left( \frac{1}{\sqrt{(x-x')^2 + (y-y')^2 + (z-z')^2}} \right) dx' dy' dz' \end{aligned} \quad (\text{A1.6})$$

Considering that:

$$\begin{aligned} \frac{\partial}{\partial z} \left( \frac{1}{\sqrt{(x-x')^2 + (y-y')^2 + (z-z')^2}} \right) &= -\frac{\partial}{\partial z'} \left( \frac{1}{\sqrt{(x-x')^2 + (y-y')^2 + (z-z')^2}} \right) \\ \frac{\partial}{\partial y} \left( \frac{1}{\sqrt{(x-x')^2 + (y-y')^2 + (z-z')^2}} \right) &= -\frac{\partial}{\partial y'} \left( \frac{1}{\sqrt{(x-x')^2 + (y-y')^2 + (z-z')^2}} \right) \end{aligned} \quad (\text{A1.7})$$

we obtain:

$$\begin{aligned} B_y &= -\frac{\mu_0 J}{4\mathbf{p}} \int_{x_1}^{x_2} dx' \int_{y_1}^{y_2} dy' \left[ \frac{1}{\sqrt{(x-x')^2 + (y-y')^2 + (z-z')^2}} \right]_{z'=z_1}^{z'=z_2}; \quad \vec{B}_y = B_y \vec{j} \\ B_z &= +\frac{\mu_0 J}{4\mathbf{p}} \int_{x_1}^{x_2} dx' \int_{z_1}^{z_2} dz' \left[ \frac{1}{\sqrt{(x-x')^2 + (y-y')^2 + (z-z')^2}} \right]_{y'=y_1}^{y'=y_2}; \quad \vec{B}_z = B_z \vec{k} \end{aligned} \quad (\text{A1.8})$$

The expressions A1.8 can be written as:

$$\begin{aligned} B_y &= B_y^{x'y'z_2} - B_y^{x'y'z_1} \\ B_z &= B_z^{x'y_2z'} - B_z^{x'y_1z'} \end{aligned} \quad (\text{A1.9})$$

where:

$$\begin{aligned} B_y^{x'y'z_n} &= -\frac{\mu_0 J}{4p} \int_{x_1}^{x_2} dx' \int_{y_1}^{y_2} dy' \left[ \frac{1}{\sqrt{(x-x')^2 + (y-y')^2 + (z-z_n)^2}} \right]; \quad n=1,2 \\ B_y^{x'y_m z'} &= +\frac{\mu_0 J}{4p} \int_{x_1}^{x_2} dx' \int_{z_1}^{z_2} dz' \left[ \frac{1}{\sqrt{(x-x')^2 + (y-y_m)^2 + (z-z')^2}} \right]; \quad m=1,2 \end{aligned} \quad (A1.10)$$

**Step 2:** The calculation of the terms  $B_y^{x'y'z_n}$  and  $B_z^{x'y_m z'}$

a)  $B_y^{x'y'z_n}$

To calculate the first integral of A1.10 we changed the variables as follows:

$$\begin{cases} x-x'=u \\ y-y'=v \\ z-z_n=w_n \end{cases} \quad \begin{cases} x-x_1=u_1; \quad x-x_2=u_2 \\ y-y_1=v_1; \quad y-y_2=v_2 \\ z-z_1=w_1; \quad z-z_2=w_2 \end{cases} \quad \begin{cases} dx'=-du \\ dy'=-dv \end{cases} \quad (A1.11)$$

In consequence, we obtain:

$$B_y^{x'y'z_n} = -\frac{\mu_0 J}{4p} \int_{u_1}^{u_2} (-du) \int_{v_1}^{v_2} (-dv) \left[ \frac{1}{\sqrt{u^2 + v^2 + w_n^2}} \right]; \quad n=1,2 \quad (A1.12)$$

The second integral can be easily solved obtaining:

$$B_y^{x'y'z_n} = -\frac{\mu_0 J}{4p} \int_{u_1}^{u_2} du \cdot \ln \left( v + \sqrt{u^2 + v^2 + w_n^2} \right) \Big|_{v_1}^{v_2}; \quad n=1,2 \quad (A1.13)$$

The expression A1.13 can be also written as:

$$B_y^{x'y'z_n} = B_y^{x'y_2 z_n} - B_y^{x'y_1 z_n}; \quad n=1,2 \quad (A1.14)$$

where:

$$B_y^{x'y_m z_n} = -\frac{\mu_0 J}{4p} \int_{u_1}^{u_2} du \cdot \ln \left( v_m + \sqrt{u^2 + v_m^2 + w_n^2} \right); \quad n, m=1,2 \quad (A1.15)$$

Using A1.9 and A1.14 we obtain:

$$B_y = \left( B_y^{x'y_2 z_2} - B_y^{x'y_2 z_1} \right) - \left( B_y^{x'y_1 z_2} - B_y^{x'y_1 z_1} \right); \quad n, m=1,2 \quad (A1.16)$$

b)  $B_z^{x'y_m z'}$

Using the variables defined in A1.11, from A1.10 we obtain:

$$B_z^{x'y_m z'} = \frac{\mu_0 J}{4p} \int_{u_1}^{u_2} (-du) \int_{w_1}^{w_2} (-dw) \left[ \frac{1}{\sqrt{u^2 + v^2 + w_n^2}} \right]; \quad (A1.17)$$

The second integral can be easily solved obtaining:

$$B_z^{x'y_m z'} = \frac{\mu_0 J}{4p} \int_{u_1}^{u_2} du \cdot \ln \left( w + \sqrt{u^2 + v_m^2 + w^2} \right) \Big|_{w_1}^{w_2}; \quad m = 1, 2 \quad (A1.18)$$

The short form of the expression A1.18 is:

$$B_z^{x'y_m z'} = B_y^{x'y_m z_2} - B_y^{x'y_m z_1}; \quad m = 1, 2 \quad (A1.19)$$

where:

$$B_z^{x'y_m z_n} = \frac{\mu_0 J}{4p} \int_{u_1}^{u_2} du \cdot \ln \left( w_n + \sqrt{u^2 + v_m^2 + w_n^2} \right); \quad m, n = 1, 2 \quad (A1.20)$$

From A1.9 and A1.20 we obtain:

$$B_z = \left( B_z^{x'y_2 z_2} - B_z^{x'y_1 z_2} \right) - \left( B_z^{x'y_2 z_1} - B_z^{x'y_1 z_1} \right); \quad m, n = 1, 2 \quad (A1.21)$$

In the following, we calculate the terms of the expressions A1.16 and A1.21,  $B_y^{x'y_m z_n}$  and

$B_z^{x'y_m z_n}$

**Step 3:** The calculation of the terms  $B_y^{x'y_m z_n}$  and  $B_z^{x'y_m z_n}$

$$B_y^{x'y_m z_n} = -\frac{\mu_0 J}{4p} \int_{u_1}^{u_2} du \cdot \ln \left( (y - y_m) + \sqrt{u^2 + (y - y_m)^2 + (z - z_n)^2} \right); \quad n, m = 1, 2 \quad (A1.22)$$

The integral from A1.22 can be calculated as [Schabes1987]:

$$\begin{aligned} \int \ln \left[ z + \sqrt{h^2 + z^2 + e^2} \right] dh = & h \cdot \ln \left[ z + \sqrt{h^2 + z^2 + e^2} \right] - h + e \cdot \arctan \left( \frac{h}{e} \right) \\ & - e \cdot \arctan \left( \frac{zh}{e \sqrt{h^2 + z^2 + e^2}} \right) + z \ln \left[ h + \sqrt{h^2 + z^2 + e^2} \right] \end{aligned}$$

Using this result, we obtain:

$$\begin{aligned}
 B_y^{x'y_m z_n} = & -\frac{\mu_0 J}{4p} \left\{ (x-x') \ln \left[ (y-y_m) + \sqrt{(x-x')^2 + (y-y_m)^2 + (z-z_n)^2} \right] - \right. \\
 & - (x-x') + (z-z_n) \arctan \left( \frac{x-x'}{z-z_n} \right) - \\
 & - (z-z_n) \arctan \left[ \frac{(x-x')(y-y_m)}{(z-z_n) \sqrt{(x-x')^2 + (y-y_m)^2 + (z-z_n)^2}} \right] + \\
 & \left. + (y-y_m) \ln \left[ (x-x') + \sqrt{(x-x')^2 + (y-y_m)^2 + (z-z_n)^2} \right] \right\}
 \end{aligned} \tag{A1.23}$$

and, in consequence:

$$B_y = B_y^{x_2 y_m z_2} - B_y^{x_2 y_m z_1} - B_y^{x_1 y_m z_2} + B_y^{x_1 y_m z_1} \tag{A1.24}$$

The final analytical result for  $B_y$  is:

$$\begin{aligned}
 B_y = & B_y^{x_2 y_2 z_2} - B_y^{x_2 y_2 z_1} - B_y^{x_2 y_1 z_2} + B_y^{x_2 y_1 z_1} - B_y^{x_1 y_2 z_2} + B_y^{x_1 y_2 z_1} + B_y^{x_1 y_1 z_2} - B_y^{x_1 y_1 z_1} \\
 B_y^{x_l y_m z_n} = & -\frac{\mu_0 J}{4p} \left\{ (x-x_l) \ln \left[ (y-y_m) + \sqrt{(x-x_l)^2 + (y-y_m)^2 + (z-z_n)^2} \right] - \right. \\
 & - (x-x_l) + (z-z_n) \arctan \left( \frac{x-x_l}{z-z_n} \right) - \\
 & - (z-z_n) \arctan \left[ \frac{(x-x_l)(y-y_m)}{(z-z_n) \sqrt{(x-x_l)^2 + (y-y_m)^2 + (z-z_n)^2}} \right] + \\
 & \left. + (y-y_m) \ln \left[ (x-x_l) + \sqrt{(x-x_l)^2 + (y-y_m)^2 + (z-z_n)^2} \right] \right\}; m, n, l = 1, 2
 \end{aligned} \tag{A1.25}$$

In a similar way, we obtained for  $B_z$  the result:

$$\begin{aligned}
 B_z = & B_z^{x_2 y_2 z_2} - B_z^{x_2 y_2 z_1} - B_z^{x_2 y_1 z_2} + B_z^{x_2 y_1 z_1} - B_z^{x_1 y_2 z_2} + B_z^{x_1 y_2 z_1} + B_z^{x_1 y_1 z_2} - B_z^{x_1 y_1 z_1} \\
 B_z^{x_l y_m z_n} = & \frac{\mu_0 J}{4p} \left\{ (x-x_l) \ln \left[ (z-z_n) + \sqrt{(x-x_l)^2 + (y-y_m)^2 + (z-z_n)^2} \right] - \right. \\
 & - (x-x_l) + (y-y_m) \arctan \left( \frac{x-x_l}{y-y_m} \right) - \\
 & - (y-y_m) \arctan \left[ \frac{(x-x_l)(z-z_n)}{(y-y_m) \sqrt{(x-x_l)^2 + (y-y_m)^2 + (z-z_n)^2}} \right] + \\
 & \left. + (z-z_n) \ln \left[ (x-x_l) + \sqrt{(x-x_l)^2 + (y-y_m)^2 + (z-z_n)^2} \right] \right\}; m, n, l = 1, 2
 \end{aligned} \tag{A1.26}$$



The expressions A1.25 and A1.26 for the magnetic field  $\vec{B}(0, B_y, B_z)$  in different regions around the stripline have been evaluated numerically. It is noted that these calculations are valid for DC-currents and do not take into account the high-frequency effects such as the skin depth.

In the following, we present some fragments of the main program that estimates the two components of the magnetic field  $B_y = B_1$  and  $B_z = B_2$  using the functions  $f1, f2, f3, g1, g2, g3$ .

```
f1(a,b,c)=a*(log(b+sqrt(a**2+b**2+c**2))-1)
f2(a,b,c)=c*atan(a/c)-c*atan((a*b)/(c*sqrt(a**2+b**2+c**2)))
f3(a,b,c)=b*log(a+sqrt(a**2+b**2+c**2))
g1(a,b,c)=a*(log(c+sqrt(a**2+b**2+c**2))-1)
g2(a,b,c)=b*atan(a/b)-b*atan((a*c)/(b*sqrt(a**2+b**2+c**2)))
g3(a,b,c)=c*log(a+sqrt(a**2+b**2+c**2))
```

```
.....
B1=B1+f1(u1,v2,w2)+f2(u1,v2,w2)+f3(u1,v2,w2)
B1=B1-f1(u1,v1,w2)-f2(u1,v1,w2)-f3(u1,v1,w2)
B1=B1-f1(u1,v2,w1)-f2(u1,v2,w1)-f3(u1,v2,w1)
B1=B1+f1(u1,v1,w1)+f2(u1,v1,w1)+f3(u1,v1,w1)
B1=B1-f1(u2,v2,w2)-f2(u2,v2,w2)-f3(u2,v2,w2)
B1=B1+f1(u2,v1,w2)+f2(u2,v1,w2)+f3(u2,v1,w2)
B1=B1+f1(u2,v2,w1)+f2(u2,v2,w1)+f3(u2,v2,w1)
B1=B1-f1(u2,v1,w1)-f2(u2,v1,w1)-f3(u2,v1,w1)
```

```
.....
B2=B2+g1(u1,v2,w1)+g2(u1,v2,w1)+g3(u1,v2,w1)
B2=B2-g1(u1,v2,w2)-g2(u1,v2,w2)-g3(u1,v2,w2)
B2=B2-g1(u1,v1,w1)-g2(u1,v1,w1)-g3(u1,v1,w1)
B2=B2+g1(u1,v1,w2)+g2(u1,v1,w2)+g3(u1,v1,w2)
B2=B2-g1(u2,v2,w1)-g2(u2,v2,w1)-g3(u2,v2,w1)
B2=B2+g1(u2,v2,w2)+g2(u2,v2,w2)+g3(u2,v2,w2)
B2=B2+g1(u2,v1,w1)+g2(u2,v1,w1)+g3(u2,v1,w1)
B2=B2-g1(u2,v1,w2)-g2(u2,v1,w2)-g3(u2,v1,w2)
```

**ANNEXE 2: FOURIER TRANSFORM OF DISCRETELY SAMPLED DATA**

A physical process can be described either in the *time domain*, by the values of some quantity  $h$  as a function of time  $t$ , e.g.,  $h(t)$ , or in the *frequency domain*, where the process is specified by giving its amplitude  $H$  (generally a complex number indicating phase also) as a function of frequency  $f$ , that is  $H(f)$ , with  $-1 < f < 1$ . For many purposes it is useful to think of  $h(t)$  and  $H(f)$  as being two different *representations* of the *same* function. One goes back and forth between these two representations by means of the *Fourier transform* equations:

$$\begin{aligned} H(f) &= \int_{-\infty}^{\infty} h(t) e^{2\pi i f t} dt \\ h(t) &= \int_{-\infty}^{\infty} H(f) e^{-2\pi i f t} df \end{aligned} \quad (\text{A2.1})$$

We have written a program that calculates the Fourier transformation [Numerical Recipes] of a function  $h(t)$  that is sampled at evenly spaced intervals in time. Let  $\mathbf{D}$  denote the time interval between consecutive samples, so that the sequence of sampled values is:

$$h_n = h(n\Delta) \text{ where } n = \dots -3, -2, -1, 0, 1, 2, 3, \dots \quad (\text{A2.2})$$

The reciprocal of the time interval  $\mathbf{D}$  is called the sampling rate; if  $\mathbf{D}$  is measured in seconds, for example, and then the sampling rate is the number of samples recorded per second.

For any sampling interval  $\mathbf{D}$ , there is also a special frequency  $f_c$ , called the *Nyquist critical frequency*, given by

$$f_c = \frac{1}{2\Delta} \quad (\text{A2.3})$$

To estimate the discrete Fourier transform from a finite number of sampled points, we suppose that we have  $N$  consecutive sampled values:

$$h_k \equiv h(t_k), \text{ where } t_k \equiv k\Delta, \text{ for } k = 0, 1, 2, \dots, N-1 \quad (\text{A2.4})$$

We suppose that  $N$  is even. With  $N$  numbers of input (A2.4), we will be able to produce  $N$  independent numbers of output for the discrete values of the frequencies:

$$f_n \equiv \frac{n}{N\Delta}, \text{ where } n = -\frac{N}{2}, \dots, \frac{N}{2} \quad (\text{A2.5})$$

The extreme values of  $n$  in A2.5 correspond exactly to the lower and upper limits of the Nyquist critical frequency range.

The Fourier transform of a discrete function,  $h_k$ , is expressed as a discrete sum that approximates the integral given in A2.1:

$$H(f_n) = \int_{-\infty}^{\infty} h(t) e^{2\pi i f_n t} dt \approx \Delta \sum_{k=0}^{N-1} h_k e^{2\pi i f_n t_k} \quad (\text{A2.6})$$

Denoting:  $H_n = \sum_{k=0}^{N-1} h_k e^{2\pi i f_n t_k}$  the discrete Fourier transform of the  $N$  points of  $h_k$ , is:

$$H(f_n) = \Delta \cdot H_n \quad (\text{A2.7})$$

where  $f_n$  is given by A2.5.

In the following, we present the essential part of the program that calculates the complex Fourier transforms ( $Tc$ ) of a discrete function,  $h(t_n)$  as a function of its real ( $Tr$ ) and imaginary ( $Ti$ ) part:

```

do 200 l=1,N+1
    np=l-1-N/2
    Sr=0.0d0
    Si=0.0d0
    freq(l)=np/(N*delta)
    do 100 i=1,N
        tn(i)=(i-1)*delta
        fn(i)=hp(tn(i)*(1e+9))
        FTr(i,l)=fn(i)*cos(2*PI*(i-1)*np/N)
        FTi(i,l)=fn(i)*sin(2*PI*(i-1)*np/N)
        FTc(i,l)=DCMPLX(FTr(i,l),FTi(i,l))
        Sr=Sr+FTr(i,l)
        Si=Si+FTi(i,l)
100    continue
    Tr(l)=delta*Sr
    Ti(l)=delta*Si
    Tc(l)=DCMPLX(Tr(l),Ti(l))
200    continue

```

### ANNEXE 3: MACROSPIN SIMULATIONS

In this annexe, we present the program that solves the Landau-Lifshitz –Gilbert equation for a macrospin system. As presented in chapter 1, the Landau-Lifshitz equation has the form:

$$\frac{\partial \vec{M}}{\partial t} = -\mathbf{g}(\vec{M} \times \vec{H}_{eff}) + \frac{\mathbf{a}}{M_s} \left( \vec{M} \times \frac{\partial \vec{M}}{\partial t} \right) \quad (\text{A3.1})$$

Considering the reduced terms:

$$\vec{m} = \frac{\vec{M}}{M_s}, \quad \vec{h} = \frac{\vec{H}_T}{M_s}, \quad \text{and} \quad t = t l M_s \quad (\text{A3.2})$$

the Landau-Lifshitz –Gilbert equation transforms to the system:

$$\begin{aligned} \frac{\partial m_x}{\partial t} &= -\frac{1}{1+\mathbf{a}^2} [(m_y h_z - m_z h_y) + \mathbf{a} \cdot m_y (m_x h_y - m_y h_x) - \mathbf{a} \cdot m_z (m_z h_x - m_x h_z)] = f_x(m_x, m_y, m_z) \\ \frac{\partial m_y}{\partial t} &= -\frac{1}{1+\mathbf{a}^2} [(m_z h_x - m_x h_z) + \mathbf{a} \cdot m_z (m_y h_z - m_z h_y) - \mathbf{a} \cdot m_x (m_x h_y - m_y h_x)] = f_y(m_x, m_y, m_z) \\ \frac{\partial m_z}{\partial t} &= -\frac{1}{1+\mathbf{a}^2} [(m_x h_y - m_y h_x) + \mathbf{a} \cdot m_x (m_z h_x - m_x h_z) - \mathbf{a} \cdot m_y (m_y h_z - m_z h_y)] = f_z(m_x, m_y, m_z) \end{aligned} \quad (\text{A3.3})$$

This system is integrated using the 4<sup>th</sup> order Runge-Kutta method [Numerical Recipes].

The solutions can be expressed as:

$$\begin{aligned} m_x &= \frac{k_1^x}{6} + \frac{k_2^x}{3} + \frac{k_3^x}{3} + \frac{k_4^x}{6} \\ m_y &= \frac{k_1^y}{6} + \frac{k_2^y}{3} + \frac{k_3^y}{3} + \frac{k_4^y}{6} \\ m_z &= \frac{k_1^z}{6} + \frac{k_2^z}{3} + \frac{k_3^z}{3} + \frac{k_4^z}{6} \end{aligned} \quad (\text{A3.4})$$

where the integration constants  $k_i^j$ ,  $i = 1, 2, 3$  and  $j = x, y, z$  are defined as:

$$\begin{aligned} k_1^x &= dt \cdot f_x(m_x, m_y, m_z) \\ k_2^x &= dt \cdot f_x\left(m_x + \frac{k_1^x}{2}, m_y, m_z\right) \\ k_3^x &= dt \cdot f_x\left(m_x + \frac{k_2^x}{2}, m_y, m_z\right) \\ k_4^x &= dt \cdot f_x\left(m_x + k_3^x, m_y, m_z\right) \end{aligned} \quad (\text{A3.5a})$$

$$\begin{aligned}
k_1^y &= dt \cdot f_y(m_x, m_y, m_z) \\
k_2^y &= dt \cdot f_y\left(m_x, m_y + \frac{k_1^y}{2}, m_z\right) \\
k_3^y &= dt \cdot f_y\left(m_x, m_y + \frac{k_2^y}{2}, m_z\right) \\
k_4^y &= dt \cdot f_y(m_x, m_y + k_3^y, m_z)
\end{aligned} \tag{A3.5b}$$

and

$$\begin{aligned}
k_1^z &= dt \cdot f_z(m_x, m_y, m_z) \\
k_2^z &= dt \cdot f_z\left(m_x, m_y, m_z + \frac{k_1^z}{2}\right) \\
k_3^z &= dt \cdot f_z\left(m_x, m_y, m_z + \frac{k_2^z}{2}\right) \\
k_4^z &= dt \cdot f_z(m_x, m_y, m_z + k_3^z)
\end{aligned} \tag{A4.5c}$$

In these expressions,  $dt$  is the time-step.

A convergent solution for the calculation was obtained for  $dt = 100fs$ .

#### ANNEXE 4: JONES MATRICES FOR OPTICAL COMPONENTS AND SIMULATIONS OF THE MAGNETO-OPTIC KERR EFFECT

As indicated in chapter 2, section 2.5.1.2., the measured Kerr signal is sensitive to the longitudinal, transversal or polar magnetization components in the different experimental configuration (longitudinal and transverse). In order to characterize the contribution of each of these components to the measured Kerr signal we have written a program to calculate the Kerr signal intensity for each optical component of the experimental setup (magnetic sample, polarizer, analyzer, half wave plate) using the Jones formalism.

In the following, we deduce the Jones matrices of Glan-Thompson and Wollaston polarizing prisms (chapter 2, equation 2.35a and b) and of the half-wave plate (chapter 2, equation 2.36).

##### POLARIZING PRISM

The polarizing prisms are used to obtain two beams of polarizations parallel and respective perpendicular to their axes (see chapter 2, figure 2.22).

Here, we deduce the Jones matrix of the polarizing prisms considering that the prism axis is oriented under a positive angle,  $\theta > 0$ , with respect to the  $P$ -axis (defined in chapter 2, section 2.5.1.2).

Considering that the incident light is characterized by the vector  $\vec{E}_1$ , after the polarizer one obtains a beam with the polarization parallel to the polarizer axis, called here  $P\theta$  (fig. A4.1). We can consider two coordinate axes: i) the  $(P, S)$  – system corresponding to the MOKE configuration and ii) the  $(P\theta, S\theta)$  – system corresponding to the prism.

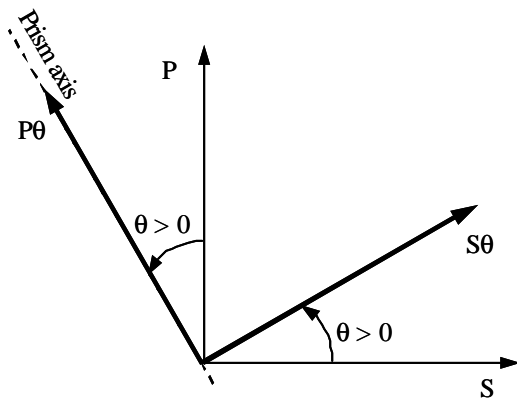


Figure A4.1  
( $P, S$ ) and ( $P\theta, S\theta$ ) coordinate systems

The electric vector,  $\vec{E}_1$  can be expressed in two different coordinate axes using the rotation matrix,  $\mathfrak{R}$ .

Thus, we have:

$$\vec{E}_1 = \begin{bmatrix} E_1^P \\ E_1^S \end{bmatrix} \text{ and } \vec{E}_1 = \begin{bmatrix} E_1^{Pq} \\ E_1^{Sq} \end{bmatrix} \quad (\text{A4.2})$$

$$\text{where } \begin{bmatrix} E_1^{Pq} \\ E_1^{Sq} \end{bmatrix} = \mathfrak{R} \begin{bmatrix} E_1^P \\ E_1^S \end{bmatrix} = \begin{bmatrix} \cos \mathbf{q} & \sin \mathbf{q} \\ -\sin \mathbf{q} & \cos \mathbf{q} \end{bmatrix} \begin{bmatrix} E_1^P \\ E_1^S \end{bmatrix} \quad (\text{A4.3})$$

Since, the two beams refracted from the prism have the polarizations parallel to the axis  $Pq$  and  $Sq$ , for the two beams we obtain the electric vector  $\vec{E}_1$  which in the  $(Pq, Sq)$  coordinate system has the components:

$$\begin{bmatrix} E_2^{Pq} \\ E_2^{Sq} \end{bmatrix} = \begin{bmatrix} E_1^{Pq} \\ E_1^{Sq} \end{bmatrix} \quad (\text{A4.4})$$

The coordinates of the vectors  $E_2^{Pq}$  and  $E_2^{Sq}$  in the  $(P, S)$  coordinate system can be obtained from their coordinates in the  $(Pq, Sq)$  coordinate system after a rotation of the coordinate system by a negative angle,  $\mathbf{q} < 0$ :

$$\begin{bmatrix} (E_2^{Pq})^P \\ (E_2^{Pq})^S \end{bmatrix} = \begin{bmatrix} \cos(-\mathbf{q}) & \sin(-\mathbf{q}) \\ -\sin(-\mathbf{q}) & \cos(-\mathbf{q}) \end{bmatrix} \begin{bmatrix} E_2^{Pq} \\ 0 \end{bmatrix} = \begin{bmatrix} \cos \mathbf{q} & -\sin \mathbf{q} \\ \sin \mathbf{q} & \cos \mathbf{q} \end{bmatrix} \begin{bmatrix} E_2^{Pq} \\ 0 \end{bmatrix} \quad (\text{A4.5a})$$

$$\begin{bmatrix} (E_2^{Sq})^P \\ (E_2^{Sq})^S \end{bmatrix} = \begin{bmatrix} \cos(-\mathbf{q}) & \sin(-\mathbf{q}) \\ -\sin(-\mathbf{q}) & \cos(-\mathbf{q}) \end{bmatrix} \begin{bmatrix} 0 \\ E_2^{Sq} \end{bmatrix} = \begin{bmatrix} \cos \mathbf{q} & -\sin \mathbf{q} \\ \sin \mathbf{q} & \cos \mathbf{q} \end{bmatrix} \begin{bmatrix} 0 \\ E_2^{Sq} \end{bmatrix} \quad (\text{A4.5b})$$

a) In a **Glan-Thompson polarizing prism**, we use only one refracted beam characterized by the expression A4.5a. This expression becomes:

$$\begin{bmatrix} (E_2^{Pq})^P \\ (E_2^{Pq})^S \end{bmatrix} = \begin{bmatrix} \cos \mathbf{q} & -\sin \mathbf{q} \\ \sin \mathbf{q} & \cos \mathbf{q} \end{bmatrix} \begin{bmatrix} E_1^{Pq} \\ 0 \end{bmatrix} = \begin{bmatrix} \cos \mathbf{q} & -\sin \mathbf{q} \\ \sin \mathbf{q} & \cos \mathbf{q} \end{bmatrix} \begin{bmatrix} \cos \mathbf{q} & \sin \mathbf{q} \\ 0 & 0 \end{bmatrix} \begin{bmatrix} E_1^P \\ E_1^S \end{bmatrix} \quad (\text{A4.6})$$

From here, we obtain the Jones matrix for a Glan Thompson polarizing prism,  $JM_{GT}$ :

$$JM_{GT} = \begin{bmatrix} \cos^2 \mathbf{q} & \sin \mathbf{q} \cos \mathbf{q} \\ \sin \mathbf{q} \cos \mathbf{q} & \sin^2 \mathbf{q} \end{bmatrix} \quad (\text{A4.7})$$

b) In a **Wollaston polarizing prism** we use both refracted beams which are characterized by:

$$\begin{bmatrix} (E_2^{Pq})^P \\ (E_2^{Pq})^S \end{bmatrix} = \begin{bmatrix} \cos \mathbf{q} & -\sin \mathbf{q} \\ \sin \mathbf{q} & \cos \mathbf{q} \end{bmatrix} \begin{bmatrix} E_1^{Pq} \\ 0 \end{bmatrix} = \begin{bmatrix} \cos \mathbf{q} & -\sin \mathbf{q} \\ \sin \mathbf{q} & \cos \mathbf{q} \end{bmatrix} \begin{bmatrix} \cos \mathbf{q} & \sin \mathbf{q} \\ 0 & 0 \end{bmatrix} \begin{bmatrix} E_1^P \\ E_1^S \end{bmatrix} \quad (\text{A4.8})$$

which is similar to A4.6 and:

$$\begin{bmatrix} (E_2^{Sq})^P \\ (E_2^{Sq})^S \end{bmatrix} = \begin{bmatrix} \cos \mathbf{q} & -\sin \mathbf{q} \\ \sin \mathbf{q} & \cos \mathbf{q} \end{bmatrix} \begin{bmatrix} 0 \\ E_1^{Sq} \end{bmatrix} = \begin{bmatrix} \cos \mathbf{q} & -\sin \mathbf{q} \\ \sin \mathbf{q} & \cos \mathbf{q} \end{bmatrix} \begin{bmatrix} 0 & 0 \\ -\sin \mathbf{q} & \cos \mathbf{q} \end{bmatrix} \begin{bmatrix} E_1^P \\ E_1^S \end{bmatrix} \quad (\text{A4.9})$$

From A4.8 and A4.9 we obtain:

$$\begin{bmatrix} (E_2^{Pq})^P \\ (E_2^{Pq})^S \end{bmatrix} = \begin{bmatrix} \cos^2 \mathbf{q} & \sin \mathbf{q} \cos \mathbf{q} \\ \sin \mathbf{q} \cos \mathbf{q} & \sin^2 \mathbf{q} \end{bmatrix} \begin{bmatrix} E_1^P \\ E_1^S \end{bmatrix} \quad (\text{A4.10})$$

and

$$\begin{bmatrix} (E_2^{Sq})^P \\ (E_2^{Sq})^S \end{bmatrix} = \begin{bmatrix} \sin^2 \mathbf{q} & -\sin \mathbf{q} \cos \mathbf{q} \\ -\sin \mathbf{q} \cos \mathbf{q} & \cos^2 \mathbf{q} \end{bmatrix} \begin{bmatrix} E_1^P \\ E_1^S \end{bmatrix} \quad (\text{A4.11})$$

During MOKE experiments, we were not interested in the  $P$  and  $S$  components of the electric field refracted by the Wollaston prism, but in the intensity of the two beams that are characterized by  $E_2^{Pq}$  and  $E_2^{Sq}$  defined in A4.3. In consequence, in MOKE calculations we used as Jones matrix for the Wollaston prism (the analyzer) the expression:

$$JM_w = \begin{bmatrix} \cos \mathbf{q} & \sin \mathbf{q} \\ -\sin \mathbf{q} & \cos \mathbf{q} \end{bmatrix} \quad (\text{A4.12})$$

#### HALF WAVE PLATE

The half wave plates rotates the incident electric vector,  $\vec{E}_1$ , by an angle  $2\gamma$  as shown in figure A4.2.

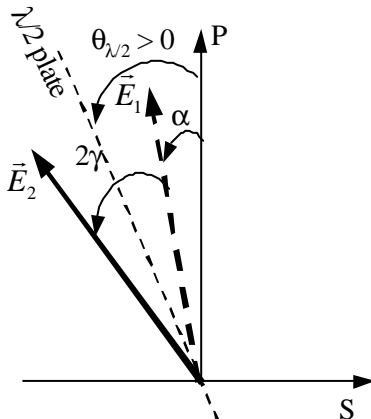


Figure A4.2  
Angle definitions for a half wave plate



Considering a half wave plate characterized by the axis deviated from the  $P$ -axis by the positive angle  $\mathbf{q}_{1/2}$ , we can write the two vectors  $\vec{E}_1$  and  $\vec{E}_2$  as:

$$\begin{aligned}\vec{E}_1 &= \begin{bmatrix} E_1^P \\ E_1^S \end{bmatrix} = E_1 \begin{bmatrix} \cos \mathbf{a} \\ -\sin \mathbf{a} \end{bmatrix} \\ \vec{E}_2 &= \begin{bmatrix} E_2^P \\ E_2^S \end{bmatrix} = E_2 \begin{bmatrix} \cos(\mathbf{a} + 2\mathbf{g}) \\ -\sin(\mathbf{a} + 2\mathbf{g}) \end{bmatrix}\end{aligned}\quad (\text{A4.13})$$

Since  $\mathbf{a} = \mathbf{q}_{1/2} - \mathbf{g}$  these equations becomes:

$$\begin{bmatrix} E_2^P \\ E_2^S \end{bmatrix} = \begin{bmatrix} \cos 2\mathbf{q} & -\sin 2\mathbf{q} \\ \sin 2\mathbf{q} & \cos 2\mathbf{q} \end{bmatrix} \begin{bmatrix} E_1^P \\ E_1^S \end{bmatrix}\quad (\text{A4.14})$$

obtaining the Jones matrix for a half wave plate given by:

$$JM_{1/2} = \begin{bmatrix} \cos 2\mathbf{q} & -\sin 2\mathbf{q} \\ \sin 2\mathbf{q} & \cos 2\mathbf{q} \end{bmatrix}\quad (\text{A4.15})$$

In the MOKE – program the matrices that define the polarizer (Glan-Thompson polarizing prism), the analyzer (Wollaston polarizing prism), the magnetic sample and the half wave plate have been introduced as subroutines:

```

SUBROUTINE POLARISER(th,E1,E2)
  double precision th,E1(2),E2(2),JM(2,2)
  JM(1,1)=cos(th)*cos(th)
  JM(1,2)=sin(th)*cos(th)
  JM(2,1)=sin(th)*cos(th)
  JM(2,2)=sin(th)*sin(th)
  E2(1)=JM(1,1)*E1(1)+JM(1,2)*E1(2)
  E2(2)=JM(2,1)*E1(1)+JM(2,2)*E1(2)
END SUBROUTINE
!*****
SUBROUTINE ANALYSER(th,E4,E5)
  double precision th,JM(2,2)
  double complex E4(2),E5(2)
  JM(1,1)=cos(th)
  JM(1,2)=sin(th)
  JM(2,1)=(-1)*sin(th)
  JM(2,2)=cos(th)
  E5(1)=JM(1,1)*E4(1)+JM(1,2)*E4(2)
  E5(2)=JM(2,1)*E4(1)+JM(2,2)*E4(2)
END SUBROUTINE
!*****
SUBROUTINE MG_SAMPLE(rpp,rps,rsp,rss,E2,E3)
  double precision E2(2)
  double complex rpp,rps,rsp,rss
  double complex E3(2)
  E3(1)=rpp*E2(1)+rps*E2(2)
  E3(2)=rsp*E2(1)+rss*E2(2)
END SUBROUTINE
!*****

```

```

SUBROUTINE HALF_WAVE_PLATE(thl,E3,E4)
    double precision thl,JM(2,2)
    double complex E3(2),E4(2)
    JM(1,1)=cos(2*thl)
    JM(1,2)=(-1)*sin(2*thl)
    JM(2,1)=sin(2*thl)
    JM(2,2)=cos(2*thl)
    E4(1)=JM(1,1)*E3(1)+JM(1,2)*E3(2)
    E4(2)=JM(2,1)*E3(1)+JM(2,2)*E3(2)
END SUBROUTINE
!*****

```

The Jones matrix of the magnetic sample is defined using the Fresnel coefficients (see chapter 2, equations 2.38).

## ANNEXE 5: THE DIELECTRIC TENSOR

The interaction between a crystal and an electric field  $\vec{E}$  is expressed by the relation:

$$\vec{P} = \epsilon_0 (\epsilon_r - 1) \vec{E} = \epsilon_0 \mathbf{c}_e \vec{E} \quad (\text{A5.1})$$

where  $\vec{P}$  is the polarization,  $\epsilon_0 = 8.8542 \times 10^{-12} \text{ (F/m)}$  is the permittivity of free space,  $\epsilon_r$  is the relative permittivity and  $\mathbf{c}_e$  represents the electric susceptibility. For an anisotropic crystal,  $\epsilon_r$  and  $\mathbf{c}_e$  are represented by tensors.

In the following, we deduce the dielectric tensor,  $\hat{\epsilon}_r$ , associated to magneto-optical effects (defined in chapter 2 and [Palmer1996]).

The motion of bound electrons in the presence of both a harmonic field  $\vec{E}(\vec{r}, t) = \vec{E}(\vec{r}) e^{-i\omega t}$  and a static field  $\vec{B}$ , is described by the Lorentz force law:

$$m_e \ddot{\vec{r}} + k_0 \vec{r} = -e \vec{E} e^{-i\omega t} - e \dot{\vec{r}} \times \vec{B} \quad (\text{A5.2})$$

where  $\vec{r}$  is the electron displacement from the equilibrium position,  $k_0 = m_e \omega_0^2$  is the elastic binding force constant (where  $\omega_0$  is called the resonance frequency of the bound electron),  $m_e$  and  $(-e)$  are the electron mass and respective the electron charge. Assuming that the displacement  $\vec{r}$  acquires the same harmonic time dependence as the wave, we obtain the time independent relation:

$$(\omega_0^2 - \omega^2) \vec{r} - i\omega \frac{e}{m_e} (\vec{r} \times \vec{B}) = -\frac{e}{m_e} \vec{E} \quad (\text{A5.3})$$

Considering that the polarization  $\vec{P}$  is defined by:

$$\vec{P} = \frac{1}{V} \sum \vec{p} = -Ne\vec{r} \quad (\text{A5.4})$$

from (A5.3) we obtain:

$$(\omega_0^2 - \omega^2) \vec{P} - i\omega \frac{e}{m_e} (\vec{P} \times \vec{B}) = \frac{Ne^2}{m_e} \vec{E} \quad (\text{A5.5})$$

Considering that the magnetic field is parallel to  $oz$ -axis, we obtain:

$$\vec{P} \times \vec{B} = \begin{vmatrix} \vec{i} & \vec{j} & \vec{k} \\ P_x & P_y & P_z \\ 0 & 0 & B \end{vmatrix} = \vec{i} P_y B - \vec{j} P_x B \quad (\text{A5.6})$$

From (A5.5) and (A5.6) we obtain:

$$\begin{cases} (\omega_0^2 - \omega^2)P_x - i\omega\omega_C P_y = \frac{Ne^2}{m_e} E_x \\ i\omega\omega_C P_x + (\omega_0^2 - \omega^2)P_y = \frac{Ne^2}{m_e} E_y \\ (\omega_0^2 - \omega^2)P_z = \frac{Ne^2}{m_e} E_z \end{cases} \quad (\text{A5.7})$$

where:

$$\omega_C = \frac{eB}{m_e} \quad (\text{A5.8})$$

represents the *cyclotron frequency*.

From (A5.7) we obtain:

$$\begin{cases} P_x = \frac{Ne^2}{m_e} \cdot \frac{1}{(\omega_0^2 - \omega^2)^2 - \omega^2\omega_C^2} \cdot [(\omega_0^2 - \omega^2)E_x + i\omega\omega_C E_y] \\ P_y = \frac{Ne^2}{m_e} \cdot \frac{1}{(\omega_0^2 - \omega^2)^2 - \omega^2\omega_C^2} \cdot [-i\omega\omega_C E_x + (\omega_0^2 - \omega^2)E_y] \\ P_z = \frac{Ne^2}{m_e} \cdot \frac{1}{(\omega_0^2 - \omega^2)} \cdot E_z \end{cases} \quad (\text{A5.9})$$

The equation (A5.1) can be also written as:

$$\begin{bmatrix} P_x \\ P_y \\ P_z \end{bmatrix} = \epsilon_0 \begin{bmatrix} \mathbf{c}_{xx} & \mathbf{c}_{xy} & \mathbf{c}_{xz} \\ \mathbf{c}_{yx} & \mathbf{c}_{yy} & \mathbf{c}_{yz} \\ \mathbf{c}_{zx} & \mathbf{c}_{zy} & \mathbf{c}_{zz} \end{bmatrix} \begin{bmatrix} E_x \\ E_y \\ E_z \end{bmatrix} = \epsilon_0 (\hat{\mathbf{e}}_r - 1) \begin{bmatrix} E_x \\ E_y \\ E_z \end{bmatrix} \quad (\text{A5.10})$$

The dielectric tensor,  $\hat{\mathbf{e}}_r$ , becomes:

$$\hat{\mathbf{e}}_r = \begin{bmatrix} 1 & 0 & 0 \\ 0 & 1 & 0 \\ 0 & 0 & 1 \end{bmatrix} + \begin{bmatrix} \mathbf{c}_{xx} & \mathbf{c}_{xy} & 0 \\ \mathbf{c}_{yx} & \mathbf{c}_{yy} & 0 \\ 0 & 0 & \mathbf{c}_{zz} \end{bmatrix} = \begin{bmatrix} \mathbf{e} & i\mathbf{e}_i & 0 \\ -i\mathbf{e}_i & \mathbf{e} & 0 \\ 0 & 0 & \mathbf{e}_{zz} \end{bmatrix} \quad (\text{A5.11})$$

where:

$$\begin{cases} \mathbf{e} = 1 + \frac{\omega_P^2 \cdot (\omega_0^2 - \omega^2)}{(\omega_0^2 - \omega^2)^2 - \omega^2\omega_C^2} \\ \mathbf{e}_i = \frac{\omega_P^2 \omega \omega_C}{(\omega_0^2 - \omega^2)^2 - \omega^2\omega_C^2} \\ \mathbf{e}_{zz} = 1 + \frac{\omega_P^2}{\omega_0^2 - \omega^2} \end{cases} \quad (\text{A5.12})$$

In these expressions

$$\omega_p = \sqrt{\frac{Ne^2}{m_e \epsilon_0}} \quad (\text{A5.13})$$

defines the *plasma frequency*.

In the case of the Faraday effect, the Verdet constant is expressed as [Palmer1996]:

$$R_v = \frac{pe\omega_p^2\omega}{I_0 n_0 m_e (\omega_0^2 - \omega^2)^2} \quad (\text{A5.14})$$

while the Cotton-Mouton effect (see chapter 2) is defined by [Palmer1996]:

$$k_{\perp} - k_{\parallel} = \frac{e^2 \omega_p^2 \omega^3}{2m_e^2 c (\omega_0^2 - \omega^2)^3} \quad (\text{A5.15})$$

In the expressions presented above we have not taken into account the magneto-optical effects induced by the sample magnetization,  $\vec{M}(M_x, M_y, M_z)$ . Considering in (A5.5) the general expression for the magnetic induction:  $\vec{B} = \mu_0(\vec{H} + \vec{M})$  with an external field parallel to oz-axis,  $\vec{H}(0,0,H_z)$  we can obtain, instead of (A5.7), the following equation system:

$$\hat{A} \cdot \vec{P} = \frac{Ne^2}{m_e} \cdot \vec{E}$$

$$\begin{bmatrix} \omega_0^2 - \omega^2 & -i \frac{we\mu_0}{m_e} (H + M_z) & i \frac{we\mu_0}{m_e} M_y \\ i \frac{we\mu_0}{m_e} (H + M_z) & \omega_0^2 - \omega^2 & -i \frac{we\mu_0}{m_e} M_x \\ -i \frac{we\mu_0}{m_e} M_y & i \frac{we\mu_0}{m_e} M_x & \omega_0^2 - \omega^2 \end{bmatrix} \begin{bmatrix} P_x \\ P_y \\ P_z \end{bmatrix} = \frac{Ne^2}{m_e} \begin{bmatrix} E_x \\ E_y \\ E_z \end{bmatrix} \quad (\text{A5.16})$$

This system can be solved:

$$\vec{P} = \hat{A}^{-1} \cdot \frac{Ne^2}{m_e} \cdot \vec{E} = \epsilon_0 (\hat{\epsilon}_r - \hat{1}) \vec{E} \quad (\text{A5.17})$$

using the inverse of the matrix  $\hat{A}$ ,  $\hat{A}^{-1}$  that is expressed as:

$$\hat{A}^{-1} = \frac{1}{(\mathbf{w}_0^2 - \mathbf{w}^2) \left[ (\mathbf{w}_0^2 - \mathbf{w}^2)^2 - C^2 (M_x^2 + M_y^2 + (H + M_z)^2) \right]} \cdot$$

$$\begin{bmatrix} (\mathbf{w}_0^2 - \mathbf{w}^2) - C^2 M_x^2 & -iC(H + M_z)(\mathbf{w}_0^2 - \mathbf{w}^2) + C^2 M_x M_y & -C^2 M_x (H + M_z) - iC M_y (\mathbf{w}_0^2 - \mathbf{w}^2) \\ iC(H + M_z)(\mathbf{w}_0^2 - \mathbf{w}^2) + C^2 M_x M_y & (\mathbf{w}_0^2 - \mathbf{w}^2) - C^2 M_y^2 & C^2 M_y (H + M_z) - iC M_x (\mathbf{w}_0^2 - \mathbf{w}^2) \\ -C^2 M_x (H + M_z) + iC M_y (\mathbf{w}_0^2 - \mathbf{w}^2) & -C^2 M_y (H + M_z) + iC M_x (\mathbf{w}_0^2 - \mathbf{w}^2) & (\mathbf{w}_0^2 - \mathbf{w}^2) - C^2 (H + M_z)^2 \end{bmatrix}$$

where  $C = \frac{we\mu_0}{m_e}$

(A5.18)

The matrix from (A5.18) represents the sum over two matrices that correspond to the linear magneto-optical effects,  $L$ , and respectively non-linear magneto-optical effects,  $NL$ . The expressions of these matrices are:

$$L = (\mathbf{w}_0^2 - \mathbf{w}^2) \begin{bmatrix} 1 & -iC(H + M_z) & -iC M_y \\ iC(H + M_z) & 1 & -iC M_x \\ iC M_y & iC M_x & 1 \end{bmatrix}$$

$$NL = \begin{bmatrix} -C^2 M_x^2 & C^2 M_x M_y & -C^2 M_x (H + M_z) \\ C^2 M_x M_y & -C^2 M_y^2 & C^2 M_y (H + M_z) \\ -C^2 M_x (H + M_z) & -C^2 M_y (H + M_z) & -C^2 (H + M_z)^2 \end{bmatrix}$$
(A5.19)

Considering only the linear effects (neglecting terms such as  $M_i M_j$ ), for  $H = 0$ , from (A5.17), (A5.18) and (A5.19) we obtain the dielectric tensor:

$$\hat{\epsilon}_r = \begin{bmatrix} 1 & 0 & 0 \\ 0 & 1 & 0 \\ 0 & 0 & 1 \end{bmatrix} + \frac{Ne^2}{m_e \mathbf{e}_0 (\mathbf{w}_0^2 - \mathbf{w}^2)^2} \begin{bmatrix} 1 & -iC M_z & -iC M_y \\ iC M_z & 1 & -iC M_x \\ iC M_y & iC M_x & 1 \end{bmatrix}$$
(A5.20)

This equation is equivalent to:

$$\hat{\epsilon}_r = n^2 \begin{bmatrix} 1 & -iQM_z & iQM_y \\ iQM_z & 1 & -iQM_x \\ -iQM_y & iQM_x & 1 \end{bmatrix}$$
(A5.21)

where:

$$n^2 = 1 + \frac{Ne^2}{m_e \mathbf{e}_0 (\mathbf{w}_0^2 - \mathbf{w}^2)^2}$$

$$Q = \frac{we\mu_0}{m_e} \cdot \frac{Ne^2}{Ne^2 + m_e \mathbf{e}_0 (\mathbf{w}_0^2 - \mathbf{w}^2)^2}$$

$$Q = \frac{we\mu_0}{m_e} \cdot \frac{n^2 - 1}{n^2}$$
(A5.22)

We observe that the permittivity tensors (A5.21) and (2.30) from chapter 2 are equivalent. In chapter 2 we used the normalized values for the magnetization components,  $m_i = M_i / M_s$ .



## **RESUME :**

En utilisant la technique pompe-sonde résolue en temps, nous avons étudié la dynamique de l'aimantation dans des couches minces magnétiques avec une résolution temporelle de 20ps. La pompe est constituée par les champs magnétiques de hautes fréquences induits par des impulsions de tension appliquées sur une ligne coplanaire. Comme sonde, nous avons utilisé l'effet Kerr magnéto-optique et l'effet magnéto-résistif. Nous présentons la préparation des échantillons en utilisant le dépôt de couches minces par pulvérisation cathodique, la lithographie UV, ainsi que différentes techniques de gravure. Les résultats sur la dynamique de l'aimantation correspondent au régime des petites perturbations (de type Résonance Ferromagnétique) et à celui des grandes perturbations (ex. le renversement de l'aimantation). Nous avons mis en évidence le renversement par précession dans des vannes de spin de taille micronique et dans des couches minces continues.

## **ABSTRACT:**

Using a time-resolved “pump-probe” technique, we have studied the magnetization dynamics in magnetic thin films with a time resolution of about 20ps. As pump we used the high-frequency magnetic fields induced by voltage pulses applied on a 50 $\Omega$ -matched coplanar wave-guide. As probe we used the Magneto-Optical Kerr effect and Magneto-Resistive effect. We present the wave-guide and device preparation realized by UV lithography, sputtering and various etching techniques. The magnetization dynamics results concern both small angle perturbations, such as Ferromagnetic Resonance, and large angle perturbations such as the magnetization reversal. For the latter case, we have evidenced the magnetization reversal by precession, in micron-sized spin-valve elements and continuous magnetic films. This process, known as the fastest magnetization reversal process, has direct applications in Magnetic Random Access Memories (MRAM) devices.